INFORMATION TO USERS

This manuscript has been reproduced from the microfilm master. UMI films the text directly from the original or copy submitted. Thus, some thesis and dissertation copies are in typewriter face, while others may be from any type of computer printer.

The quality of this reproduction is dependent upon the quality of the copy submitted. Broken or indistinct print, colored or poor quality illustrations and photographs, print bleedthrough, substandard margins, and improper alignment can adversely affect reproduction.

In the unlikely event that the author did not send UMI a complete manuscript and there are missing pages, these will be noted. Also, if unauthorized copyright material had to be removed, a note will indicate the deletion.

Oversize materials (e.g., maps, drawings, charts) are reproduced by sectioning the original, beginning at the upper left-hand corner and continuing from left to right in equal sections with small overlaps. Each original is also photographed in one exposure and is included in reduced form at the back of the book.

Photographs included in the original manuscript have been reproduced xerographically in this copy. Higher quality 6" x 9" black and white photographic prints are available for any photographs or illustrations appearing in this copy for an additional charge. Contact UMI directly to order.

UMI®

Bell & Howell Information and Learning
300 North Zeeb Road, Ann Arbor, MI 48106-1346 USA
800-521-0600

THE GROWTH AND STRUCTURE OF THIN OXIDE FILMS ON NICKEL SUPERFICIALLY MODIFIED WITH CERIA AND CERIUM

by

Franciszek Czerwinski

A thesis submitted to the Faculty of Graduate Studies and Research in partial fulfilment
of the requirements of the degree of Doctor of Philosophy

Department of Mining and Metallurgical Engineering
McGill University, Montreal, April 1997

0-612-36967-6

ABSTRACT

A small addition of elements with a high affinity to oxygen can have a profound effect on the high temperature oxidation behaviour of many metals and alloys. In order to explain the improvement in oxidation resistance, the research was conducted using Ni-NiO as a model system of cation-diffusing oxides, and Ce as a typical reactive element. Three essential techniques were employed to modify the surface of Ni with Ce and CeO_2: ion implantation, sol-gel technology, and reactive sputtering. The improvement of Ni oxidation resistance was assessed by oxygen uptake measurements mainly during the early stages but also for long-term exposures at temperatures between 873 and 1073 K in pure oxygen, both at low and atmospheric pressures. The variety of oxides produced were examined in detail by several advanced techniques including Rutherford backscattering spectrometry, Auger electron spectroscopy, secondary ion-mass spectrometry, transmission- and scanning-transmission electron microscopy equipped with electron and x-ray analyzers, atomic force microscopy, infrared spectroscopy, and x-ray diffraction techniques. In order to provide direct evidence regarding the mechanism of oxide growth, a sequential oxidation using oxygen isotopes $^{16}O_2/^{18}O_2$ was conducted.

After conversion to the form of ceramic coating, superficially applied CeO_2 sol-gel significantly reduced the Ni oxidation rate as well as changing the NiO morphology and internal microstructure. The extent of the effect depended on coating thickness, size of CeO_2 particles, substrate surface finishing and preoxidation before coating. Under optimum conditions, the reduction in the Ni oxidation rate achieved by sol-gel, reactive sputtering, and ion implantation, was similar. It was found that Ni oxidation resistance is controlled by a well-defined NiO sublayer that is composed of randomly-oriented NiO grains and CeO_2 particles. Moreover, in this sublayer, the Ce^{4+} ions segregate to the NiO grain boundaries. At high temperatures, the Ce^{4+} ions block the outward diffusion of Ni^{2+}

cations along the NiO grain boundaries while allowing the inward diffusion of O^{2-} anions to continue. The "dynamic-segregation mechanism" is proposed in which Ce ions do not statically block the NiO grain boundaries, but actively diffuse along them. It is suggested that the NiO texture and microstructure, which are primarily influenced by the crystallographic orientation of the Ni substrate, are of critical importance for the stability of the reactive element concentration at NiO grain boundaries over the oxidation time.

RÉSUMÉ

L'addition en faible quantité d'éléments ayant une forte affinité avec l'oxygène peut avoir un effet important sur les propriétés oxydantes de nombreux métaux et alliages. Pour expliquer l'amélioration de la résistance à l'oxydation, la diffusion cathodique des oxydes a été étudié sur un systeme Ni-NiO avec du Ce en tant qu'élément réactif. Trois techniques de base ont été employées pour créer la surface du Ni + Ce et CeO_2 : implantation ionique, technologie sol-gel, et craquage réactif. L'amélioration de la résistance à l'oxidation a été quantifiée par une série de mesures effectuées principalement au début de la réaction, mais également pour des durées importantes d'exposition, ceci à des températures comprises entre 873 et 1073K, à hautes et basses pression atmosphériques. La variété des oxydes produits a été etudiée en détail par plusieurs techniques incluant: - les spectroscopies Auger, infrarouge, et ionique; - la microscopie electronique retrodiffuse Rutherford ; - les microscopies à transmission et à balayage équipées d'analyseur d'energie électronique et de rayons X ; - la microscopie à force atomique ; - la diffractomètrie par rayons X. Pour obtenir explicitement les mécanismes contrôlant la croissance des oxydes, une oxydation séquentielle a été faite en utilisant des isotopes d 'oxygène ($^{16}O_2/^{18}O_2$).

Après sa transformation en couche de type céramique, l'application d'un sol-gel de CeO_2 réduit considérablement la vitesse d'oxydation du Ni, et change la nature et la microstructure de la couche d'oxyde NiO. L'étendue des effets dépend de l'épaisseur de la couche, de la taille des particules de CeO_2, de la qualité de surface du dépôt, et de la préoxydation avant revêtement. Dans les conditions optimales, la réduction de la vitesse d'oxydation du Ni était la même quelle que soit la technique de revêtement utilisée (implantation ionique, technologie sol-gel et craquage réactif). La résistance à l'oxydation est contrôlée par une couche interne d'oxyde bien définie, constituée de grains NiO orientés aléatoirement, et de particules de CeO_2. De plus, dans cette couche interne une

ségrégation d'ions Ce^{4+} est observée le long des joints de grains NiO. A haute température, les ions Ce^{4+} bloquent la diffusion des ions Ni^{2+} vers l'extérieur des grain NiO, alors que les ions O^{2-} continuent à diffuser vers l'intérieur. "Le mécanisme de ségrégation dynamique" est proposé pour expliquer comment les ions Ce ne bloquent pas statiquement les joints de grains NiO, mais diffusent activement le long de ces derniers. Il est suggéré que la texture et la microstructure de la couche d'oxyde NiO sont principalement influencées par l'orientation crystallographique du substrat Ni, et que ce sont des paramètres critiques pour la stabilité de la concentration en éléments actifs lors de l'oxydation.

ACKNOWLEDGMENTS

The author wishes to express his sincere gratitude to thesis supervisor, Professor J.A. Szpunar for extensive academic guidance and assistance.

The author is grateful to Professor W.W. Smeltzer and his co-workers at McMaster University for valuable discussions and the use of laboratory facilities.

The author wishes to thank Professor M.J. Graham (National Research Council, Ottawa) for SIMS analysis. Thanks are also due to Mr. S. Poplawski (McGill University) for his assistance with x-ray measurements.

The financial support of this work by the Natural Sciences and Engineering Research Council of Canada, is gratefully acknowledged.

TABLE OF CONTENTS

ABSTRACT ii
RESUME iv
ACKNOWLEDGMENTS vi

LIST OF ABBREVIATIONS xi
LIST OF FIGURES xii
LIST OF TABLES xxi

CHAPTER 1. INTRODUCTION - OBJECTIVES OF THE STUDY 1

CHAPTER 2. LITERATURE REVIEW

2.1. Fundamentals of Ni oxidation 3
    2.1.1. Characterization of Ni oxidation product 3
    2.1.2. Diffusion properties of NiO 5
2.2. Grain-boundary diffusion in oxide growth at high temperatures 8
    2.2.1. Grain boundaries in ionic solids 9
    2.2.2. Theory of oxide growth by lattice and grain boundary diffusion 10
2.3. The reactive element effect in high temperature corrosion 12
    2.3.1. Methods of reactive element addition 13
    2.3.2. Attempts to explain the reactive element effect 15
2.4. Previous work related to the oxidation of the Ni - reactive element system . . . 16

CHAPTER 3. RESEARCH MATERIAL AND EXPERIMENTAL TECHNIQUES

3.1. Description of research material 19
    3.1.1. Substrate material and surface finishing 19
    3.1.2. Surface modification with Ce and CeO_2 20
3.2. Oxidation kinetic measurements 20
3.3. Characterization of the oxides 21
    3.3.1. Analysis of oxide composition 21
    3.3.2. Examination of growth surfaces and cross sections 22
    3.3.3. Thin-foil examination in electron microscopes 22
    3.3.4. X-ray measurements 23

CHAPTER 4. CHARACTERIZATION OF CeO_2 CERAMICS DERIVED FROM SOL-GEL

4.1. Introduction 27
4.2. Thermal decomposition of CeO_2 sol-gel 27
4.3. Evolution of CeO_2 microstructure during annealing 29
4.4. Effect of substrate nature on grain growth in CeO_2 coating during annealing . 30
4.5. Summary 32

CHAPTER 5. EARLY-STAGE OXIDATION KINETICS OF POLYCRYSTALLINE Ni MODIFIED WITH CeO_2 SOL-GEL

5.1. Introduction 39
5.2. Effect of surface finishing and coating thickness 39
5.3. Effect of preoxidation 40
5.4. Effect of oxidation temperature 41
5.5. Effect of CeO_2 particle size 43
5.6. Summary 43

CHAPTER 6. MICROSTRUCTURAL CHARACTERIZATION OF THIN OXIDE FILMS FORMED ON Ni COATED WITH CeO_2 SOL-GEL

6.1. Introduction 50
6.2. Analysis of oxide growth surface 50
    6.2.1. Factors affecting surface morphology 50
    6.2.2. AFM measurements of roughness parameters 51
6.3. Oxide depth composition 53
6.4. The microstructure of thin oxide films 55
    6.4.1. General observations 55
    6.4.2. High-magnification analysis of Ce-rich sublayer of the oxide 56
6.5. Summary

CHAPTER 7. THE INFLUENCE OF THE CRYSTALLOGRAPHIC ORIENTATION OF Ni SURFACE ON THE OXIDATION INHIBITION BY CeO_2 COATINGS

7.1. Introduction 71
7.2. Oxidation kinetics and the reactive element effect 71
7.3. Redistribution of the reactive element within the oxide 72
7.4. The evolution of oxide surface morphology 73
7.5. NiO grain size and calculated oxidation rate 74
7.6. Epitaxy and texture formation in oxide films 75
    7.6.1. Early-stage of oxide growth 75
    7.6.2. Steady-stage of oxide growth 76

7.7. Summary 77

CHAPTER 8. GROWTH AND STRUCTURE OF THIN OXIDE FILMS ON Ni IMPLANTED WITH Ce IONS

8.1. Introduction 88
8.2. Oxide growth kinetics 88
8.3. Surface morphology of oxide films 89
8.4. Ce depth distribution 91
8.5. X-ray diffraction analysis 93
8.6. Analytical electron microscopy analysis of thin oxide films 93
    8.6.1. Oxides formed on Ni directly oxidized after implantation 93
    8.6.2. Oxides formed on Ni vacuum-annealed after implantation 95
8.7. Summary 95

CHAPTER 9. STEADY-STAGE GROWTH OF NiO SCALES ON Ni COATED WITH CeO_2

9.1. Introduction 105
9.2. Oxide growth kinetics at steady-stage 105
9.3. Depth location of reactive element in the oxide 106
9.4. Surface morphology 107
9.5. Oxide microstructure 108
9.6. Summary 110

CHAPTER 10. ANALYSIS OF THE MECHANISM OF NiO GROWTH USING OXYGEN ISOTOPES

10.1. Introduction 117
10.2. Sequential oxidation using $^{16}O_2$ / $^{18}O_2$ isotopes 117
10.3.. Oxygen isotope distribution in oxides 119
    10.3.1. Polycrystalline nickel substrate 119
    10.3.2. Substrate of Ni single crystals 121
10.4. Summary 121

CHAPTER 11. TEXTURE AND GRAIN BOUNDARY CHARACTER IN NiO MODIFIED WITH THE REACTIVE ELEMENT

11.1. Introduction 130
11.2. Phase composition and the texture of oxides formed on Ni 131
    11.2.1. Characterization of polycrystalline Ni substrate 131
    11.2.2. Phase analysis of the oxides 131
    11.2.3. The texture of oxide grown on chemically polished Ni 131
    11.2.4. Texture of oxide grown on mechanically polished Ni 132

11.3. Effect of reactive element on grain boundary character distribution in NiO 133
11.4. Summary 134

CHAPTER 12. DISCUSSION OF RESULTS

12.1. Analysis of factors controlling the protective properties of CeO_2 coatings on Ni 140
12.2. The role of the crystallographic orientation of Ni surface in the microstructural evolution of NiO modified with CeO_2 143
12.3. Analysis of NiO growth on Ce-implanted Ni 145
12.4. Analysis of long-term oxidation behaviour of Ni coated with CeO_2 148
12.5. Texture and grain boundary character distribution in NiO modified with CeO_2
    12.5.1. Texture development in NiO modified with CeO_2 149
    12.5.2. Analysis of grain boundary character distribution in NiO modified with CeO_2 151
12.6. Influence of the reactive element on the diffusion processes within NiO; description of the dynamic segregation mechanism 152

CHAPTER 13. CONCLUSIONS 159

    CONTRIBUTION TO ORIGINAL RESEARCH 163
    SUGGESTIONS FOR FUTURE WORK 165

REFERENCES 167
AUTHOR'S PUBLICATIONS RELATED TO THE THESIS' SUBJECT 172

LIST OF FREQUENTLY USED ABBREVIATIONS

AFM - atomic force microscopy
AES - Auger electron spectroscopy
CBDP - convergent beam electron diffraction pattern
CSL - coincidence site lattice
EDX - energy dispersive x-ray analyzer
EELS - electron energy loss spectroscopy
GBCD - grain boundary character distributions
IR - infrared spectroscopy
FTIR - Fourier transformed infrared spectroscopy
k_p - average value of oxidation rate constant
k_{pi} - instantaneous value of oxidation rate constant
ODF - orientation distribution function of grains
RBS - Rutherford backscattering spectrometry
SAD - selected area electron diffraction pattern
SEM - scanning electron microscopy
SIMS - secondary ion mass spectrometry
STEM - scanning transmission electron microscopy
TGA - thermogravimetric analyzer

LIST OF FIGURES

Fig. 2.1. Formation of metal deficit p-type semiconductor, with cation vacancies and electron holes, by incorporation of oxygen into the "perfect" lattice [Birks and Mayer, 1983]. 4

Fig. 2.2. Diffusion coefficients of Ni and O in the lattice, in dislocations, and along grain boundaries in NiO [Atkinson, 1984]. 6

Fig. 2.3. Diffusion coefficients for some impurities in NiO grain boundaries (at an oxygen pressure of 1 atm) compared with the corresponding lattice diffusivities. The boundary width has been equal to 1 nm [Atkinson and Taylor, 1986]. 8

Fig. 2.4. (a) Relaxed structure at 0 K of the (310) symmetric tilt boundary in NiO seen in projection along the [001] tilt axis [Duffy and Tasker, 1983]; (b) structural models of the same boundary in NiO deducted from high resolution microscopy [Merkle and Smith, 1987]. 10

Fig. 2.5. Schematic of the steady-state of sol-gel dip process [Brinker and Scherer, 1990]. 14

Fig. 2.6. Schematic illustration of mechanism to effect vacancy annihilation in cation-diffusing scales: (a) misfit dislocations at metal/oxide interface with equilibrium separation s°; (b) climb of misfit dislocations into metal and subsequent glide back to the interface, resulting in separation s' [Strawbridge and Rapp, 1994]. 16

Fig. 2.7. Schematic representation of the "poisoned interface" interpretation of the reactive element effect. Large, highly charged reactive element ions segregate to metal/oxide interface, thereby pinning the misfit dislocations and preventing oxide growth by cation diffusion [Pierragi and Rapp, 1993]. 17

Fig. 3.1. Optical micrograph of Ni (99.9% purity) annealed at 1173 K for 1 h and preoxidized at 673 K for 2 h in 760 torr oxygen. Weight gain of 7.7 $\mu g/cm^2$ which corresponds to average NiO thickness of 54 nm. 25

Fig. 3.2. Pole figures of annealed Ni (99.9% purity) used as substrates for oxide growth. 26

Fig. 3.3. Schematic diagram of preparation of the Ni substrates for oxidation experiments. 26

Fig. 4.1. Gravimetric analysis of thermal decomposition of CeO_2 gel: (a) TGA results of weight loss for bulk CeO_2 dried at 293 K for 20 h during continuous heating to 1273 K at a rate of 5 deg/min in argon atmosphere; plot of derivative *dw/dT* (*w* - relative weight loss, *T* - temperature) is shown in the inset; (b) correlation between weight after drying (293 K, 20 h) and after calcination (573 K, 1 h) for coatings with different thicknesses deposited on Pt substrates; line 1 - obtained from fitting to measurements on coatings, line 2 - calculated from TGA analysis of bulk specimens; full symbols indicate two-fold dipping; thickness estimated for coatings after calcination. 33

Fig. 4.2. IR spectroscopy analysis of thermal decomposition of CeO_2 gel: (a) IR reflectance spectra of CeO_2 deposited on Pt substrate after annealing at temperatures indicated; (b) IR reflectance spectrum of CeO_2 powder specimen after annealing at 973 K for 1 h; (c) IR absorbance spectrum of gas evolved during coating annealing at 339 K. 34

Fig. 4.3. TEM bright field images and SAD pattern of CeO_2 coatings stripped from Ni substrate after calcination at 573 K for 1 h (traces of Ni are from the substrate, not completely dissolved during coating stripping): (a) coating thickness of about 20 nm; (b) coating thickness of about 150-200 nm. 35

Fig. 4.4. The morphology of CeO_2 after annealing: (a) 973 K, 1h - AFM surface morphology of 50 nm thick coating on (100)Si substrate; (b) 1173 K, 50 h - SEM fracture cross section of bulk specimen; (c) 2000 K for 5 h - SEM morphology of outer surface of bulk specimen. 36

Fig. 4.5. X-ray diffraction patterns of bulk CeO_2 samples, annealed at temperatures indicated. Analysis "ex situ" at room temperature after cooling. 37

Fig. 4.6. X-ray diffraction patterns of 100-200 nm thick CeO_2 coatings deposited on (100)Si substrate and annealed at temperatures indicated. Analysis "in situ" at reaction temperature. 36

Fig. 4.7. X-ray diffraction patterns of 100-200 nm thick CeO_2 coatings deposited on polycrystalline Ni substrate and annealed at temperatures indicated. Analysis "in situ" at reaction temperature. 38

Fig. 4.8. The growth of grain size of bulk CeO_2 and of 100-200 nm thick coatings deposited on Pt, (100)Si and Ni substrates during annealing for 0.5 h at temperatures indicated. Grain size calculated from x-ray diffraction measurements at room temperature. 38

Fig. 5.1. Effect of CeO_2 coating thickness on oxidation kinetics at 973 K of (a) chemically polished and (b) mechanically polished nickel. Total oxygen uptakes after 4 h for uncoated substrates are 112.4 and 43.8 $\mu g/cm^2$ for mechanical and chemical polishing, respectively. 44

Fig. 5.2. Effect of preoxidation and CeO_2 coatings with thickness of 14 nm on the oxidation kinetics of (a) chemically and (b) mechanically polished nickel. 45

Fig. 5.3. Oxidation kinetics for chemically polished nickel during initial periods of exposure. Heating to oxidation temperature at a rate of 100 K/min in oxygen. Arrows show time when the temperature of 973 K was attained. Coating thickness of 14 nm. 46

Fig. 5.4. Instantaneous parabolic rate constants $2w \cdot dw/dt$ (w - weight gain, t - oxidation time) as a function of time for uncoated and CeO_2 coated nickel (14 nm thick coatings). Plots start when the oxidation temperature was attained. 46

Fig. 5.5. Effect of temperature and CeO_2 coatings with thickness of 14 nm on the oxidation kinetics of (a) chemically, and (b) mechanically polished nickel. 47

Fig. 5.6. Summary of oxidation kinetics data of chemically and mechanically polished uncoated and CeO_2 treated nickel as a function of temperature. Data points indicated by the arrows are: (a) data omitted in the least squares linear fits because after oxidation at this temperature, discrete plates of coating remained on the specimen surface; (b) after coated samples were additionally preoxidized at 973 K for 40 min. 48

Fig. 5.7. (a) Oxidation kinetics at 973 K of nickel coated with 14 nm CeO_2, without and after vacuum annealing at temperatures in the range of 723-923 K for 5 h prior to the exposure to oxygen. (b) Oxygen uptake after 4 h exposure according to Fig. 5.7a plotted as a function of CeO_2 crystallite size in vacuum annealed coatings. Crystallite size measured by x-ray diffraction line broadening. 49

Fig. 6.1. Surface morphology of CeO_2 sol coatings with thickness of 14 nm (a) and 154 nm (b), deposited on chemically polished nickel after calcination at 573 K for 1 h in 760 torr oxygen. Coating with thickness of 14 nm after oxidation at 973 K for 3 min (c) and for 30 min (d). 58

Fig. 6.2. Effect of CeO_2 sol coating thickness on oxide surface morphology after 4 h exposure at 973 K. Chemically polished preoxidized substrate: (a) 7 nm CeO_2, (b) 35 nm CeO_2, (c) 154 nm CeO_2. Mechanically polished preoxidized substrate: (d) 154 nm CeO_2. 59

Fig. 6.3. SEM surface morphology of nickel after oxidation at 973 K for 4 h: (a)

mechanically polished uncoated; (b) chemically polished uncoated;(c) mechanically polished coated; (d) chemically polished coated. CeO_2 coating thickness of 14 nm. 60

Fig. 6.4. AFM surface morphology of oxide grown at 973 K for 4 h on Ni substrate: (a) uncoated surface finished by mechanical polishing, average oxide thickness of 630 nm; (b) uncoated surface finished by chemical polishing, average oxide thickness of 280 nm (grains of Ni substrate beneath the oxide are indicated as A,B and C; (c) 14 nm CeO_2 coated finished by chemical polishing, average oxide thickness of 102 nm. 61

Fig. 6.5. AFM cross-sectional analysis of oxide grown at 973 K for 4 h on: (a) uncoated Ni finished by mechanical polishing, thickness 630 nm and (b) 14 nm CeO_2 coated Ni finished by chemical polishing, thickness of 102 nm. The are shown: planar view image, cross-sectional profile along line shown on the image, distances between markers and roughness parameters. 62

Fig. 6.6. Surface roughness expressed by standard deviation *rms* as a function of oxide thickness and oxidation temperature: (a) uncoated Ni finished by mechanical and chemical polishing, and CeO_2 coated Ni finished by mechanical polishing; (b) CeO_2 coated Ni finished by chemical polishing. 63

Fig. 6.7. The maximum height R_p plotted as a function of oxide thickness. R_p values were averaged over a temperature range 873-1073 K. 64

Fig. 6.8. The ratio of roughness parameters: standard deviation *rms* and maximum height R_p to oxide thickness plotted as a function of oxide thickness. 64

Fig. 6.9. RBS analysis of oxide films formed on CeO_2 coated chemically and mechanically polished nickel: (a) energy spectra of 1 MeV $^4He^+$ ions backscattered from oxide surface; (b) Ce concentration versus depth profiles, as derived from spectra shown in (a); estimated depth resolution is 12.2 nm at 0 deg tilt and 9.3 nm at 45 deg tilt. 65

Fig. 6.10. Composition analysis of oxide films formed on mechanically polished, CeO_2 coated nickel: (a) AES composition-depth profiles for 150 nm thick oxide formed after 6 min oxidation, oxide/metal interface is estimated to be at a sputter time of 23 min; (b) AES composition-depth profile for 486 nm thick oxide formed after 4 h oxidation, oxide/metal interface at a sputter time of about 100 min; (c) SIMS composition-depth profile for oxide analyzed in (b). 66

Fig. 6.11. TEM images and SAD patterns illustrating the effect of substrate finish on the microstructure of pure NiO grown during first minutes oxidation at 973 K: a) mechanical polishing; b) chemical polishing. 67

Fig. 6.12. TEM micrograph and SAD patterns of NiO formed on CeO_2 coated Ni: (a) Ni directly oxidized at 973 K for 4 h after coating; (b) oxidation followed vacuum annealing at 973 K for 5 h, some of the coarse CeO_2 particles are indicated by arrows. 68

Fig. 6.13. (a) High magnification TEM bright field image and SAD pattern of a surface region of oxide formed during 4 h at 973 K on CeO_2 coated nickel; (b) TEM bright-field image and corresponding STEM/EDX analysis of Ce segregation in NiO grain boundary. 69

Fig. 6.14. Results of stereological quantitative analysis of Ce rich portion of oxide shown in Fig. 6.13a: (a) microstructure with elements analyzed: NiO grain boundary network and CeO_2 particles as black phase, (b) distribution of NiO grain diameters, (c) distribution of CeO_2 particle diameters. 70

Fig. 7.1. Oxidation kinetics at 873 K (a) and 973 K (b) of pure and CeO_2 coated Ni crystal faces. 79

Fig. 7.2. Arrhenius plot of the parabolic rate constants for oxide growth on pure and CeO_2-coated Ni crystal faces. Oxygen pressure of 0.005 torr. Values of k_p calculated as w^2/t, where w and t are the oxygen uptake and oxidation time, respectively. Data for polycrystalline Ni are taken from Chapter 5). 80

Fig. 7.3. Depth composition analysis of oxides formed after 4 h oxidation at 973 K on CeO_2-coated Ni: (a) AES - (111)Ni; (b) AES - (100)Ni; (c) SIMS - (100)Ni; arrows indicate the estimated oxide/metal interface. 81

Fig. 7.4. AFM morphology of growth surface of oxides formed on pure and CeO_2-coated Ni crystal faces (1073 K, 15 h): (a) (111)Ni - uncoated; (b) (100)Ni - uncoated; (c) (100)Ni - uncoated - showing the nucleation of new oxide grains at oxide/gas interface; (d) (111)Ni - CeO_2-coated. 82,83

Fig. 7.5. TEM microstructure and SAD pattern for NiO grown at 973 K on pure Ni faces: (a) (100)Ni, beam direction B = [001]; (b) (111)Ni beam direction B = [112], (sample tilted during observation), (c) (111)Ni - two sets of triangular blocks twisted 180 deg with respect to each other are indicated as A and B. 84

Fig. 7.6. Evolution of microstructure of the oxide grown at 973 K on CeO_2 coated (100)Ni: (a) TEM image and SAD pattern of oxide during initial stage of exposure to oxygen (5 min); (b) SEM image of NiO nucleation on the top of CeO_2 coating; (c) TEM image and SAD pattern of oxide at steady stage of growth. 85

Fig. 7.7. X-ray diffraction pattern (a) and pole figures (b) for oxide formed after 15 h at 1073 K on uncoated (100)Ni. 86

Fig. 7.8. Pole figures for oxide formed after 15 h at 1073 K on (100)Ni - CeO_2-coated. 86

Fig. 7.9. X-ray diffraction pattern (a) and pole figures (b) for oxide formed after 15 h at 1073 K on uncoated (111)Ni. 87

Fig. 7.10. X-ray diffraction pattern (a) and pole figures (b) for oxide formed after 15 h at 1073 K on (111)Ni - CeO_2-coated. 87

Fig. 8.1. Oxidation kinetics at 973 K of pure and Ce-implanted nickel. Initial stage of oxidation is shown in the inset. Time when the temperature of 973 K was attained is indicated by the arrow. 97

Fig. 8.2. SEM surface morphology of oxide films grown at 973 K for 4 h on Ni directly oxidized after implantation with Ce (a,b), and oxidized at 973 K for 4 h after post implantation vacuum annealing at 1073 K for 1 h (c). Nodules from implanted part of sample (c) are shown in (d). 98

Fig. 8.3. AFM surface morphology of oxide film formed at 973 K for 4 h on Ni directly oxidized after implantation with Ce. 98

Fig. 8.4. RBS measurements of Ce distribution in Ni and in NiO: (a) energy spectra of backscattered 1MeV $^4He^+$ ions; (b) Ce concentration- depth profiles derived from spectra shown in (a); estimated resolution is 11.5 nm for as-implanted samples (Ni) and 12.2 nm for oxidized samples (NiO). 99

Fig. 8.5. AES analysis of Ce distribution in NiO formed for 4h at 973 K on Ni directly oxidized after implantation (a) and in Ni after implantation and vacuum annealing at 1073 K for 1 h (b). 100

Fig. 8.6. X-ray diffraction patterns of oxides formed on Ni directly oxidized after implantation (a) and oxidized after post implantation vacuum annealing at 1073 K (b), *) diffraction peak of Pt from a thermocouple spot-welded to the specimen. 101

Fig. 8.7. TEM microstructure of outer part of the oxide formed on Ce implanted Ni: (a) bright field image and SAD pattern; (b) EELS spectrum from region shown in (a), high loss-energy part is shown in the inset. 101

Fig. 8.8. TEM microstructure of the middle part of the oxide, foil thickness 66 nm: (a) bright field image of the triple point in the oxide, CeO_2 particles are indicated by arrows; (b) SAD pattern from area shown in (a) and CBDP from a CeO_2 particle, where [013] NiO zone axis are labelled by indices and {111} spots for CeO_2 are indicated by arrows; (c) EELS spectrum, high loss-energy part is shown in the inset; (d) distribution of CeO_2 particle size. 102

Fig. 8.9. Microchemical analysis of the oxide: (a) TEM image showing CeO_2 particles at NiO grain boundary and inside grains, some of them are indicated by arrows; (b) STEM image of area shown in (a); (c) STEM/EDX spectra from CeO_2 particles and NiO matrix; (d) STEM image of grain boundary region; (e) EDX analysis of Ce concentration along line shown in (b,d). 103

Fig. 8.10. TEM image and SAD pattern of near substrate region of NiO grown on Ni directly oxidized after implantation. 104

Fig. 8.11. CeO_2 particles in outer part of oxide grown on Ce implanted Ni, annealed after implantation at 1073 K: (a) bright field image; (b) dark field image of the same area in the illumination of (200) of CeO_2; (c) distribution of CeO_2 particle size. . 104

Fig. 9.1. Oxidation kinetics of bare (uncoated) and CeO_2 coated polycrystalline Ni at 973 K. Each data point represents the individual sample. Weight gain of 1 mg/cm^2 corresponds to 7 μm NiO. 111

Fig. 9.2. RBS measurements of Ce depth profiles in oxides produced after various exposure times at 973 K. The inset illustrates the energy spectrum of backscattered 1-MeV $^4He^+$ions. The estimated depth resolution is about 12 nm. 111

Fig. 9.3. Surface morphology of oxide grown on uncoated Ni: (a) after 38 h exposure at 973 K, optical micrograph showing a pattern caused by colour interference; (b) SEM image of a portion of the oxide shown in (a); (c) SEM image of NiO surface after 125 h exposure at 973 K; (d) fragment of morphology shown in (a). 112

Fig. 9.4. Surface morphology of oxide grown at 973 K on Ni coated with 15 μg CeO_2 /cm^2: (a) optical micrograph of oxide formed after 38 h exposure at 973 K; (b) SEM image of oxide grown after 70 h exposure; (c) faceted morphology of oxide formed on grain A; (d) nodular morphology developed on grain B; (e) globular morphology of oxide formed on grain C; (f) SEM/EDX spectra from regions marked in (b). . . . 113

Fig. 9.5. Taper sections of oxide formed on pure Ni after 110 h exposure at 973 K (weight gain of 0.760 mg/cm^2): (a) nonuniform thickness of the oxide grown on various substrate grains; (b) magnified part of oxide shown in (a); c) SEM image of a part of oxide shown in (a,b) after electrolytical etching. Tilt angle 12°. 114

Fig. 9.6. Taper sections of oxide formed on Ni coated with 15 μg CeO_2 /cm^2 after 75 h exposure at 973 K (weight gain of 0.085 mg/cm^2): (a) non-uniformity of oxide grown on various substrate grains; (b) magnified part of the oxide shown in (a); (c) microstructure of a part of oxide shown in (a,b) after etching, revealing two sublayers. Tilt angle 12°. 114

Fig. 9.7. SEM image of fracture cross-sections of oxide formed after 70 h on pure Ni

(weight gain of 0.625 mg/cm^2) (a), and on Ni coated with 30 μg CeO_2 /cm^2 after 54 h exposure (weight gain of 0.115 mg/cm^2) (b). Arrows indicate some porosity in oxide. 115

Fig. 9.8. TEM analysis of oxide grown at 973 K on Ni coated with 14 nm CeO_2: (a) cross-sectional view of oxide formed after 125 h; (b) bright field image of Ce-rich sublayer inside the oxide after 30 h exposure; (c) dark field image of the region shown in (b) in the illumination of a part of {111} ring of CeO_2, and corresponding SAD pattern (inset); (d) high magnification image showing NiO and CeO_2 phases and CBDP pattern from CeO_2 particle in the NiO matrix (a [233] zone axis for NiO is labelled by indices, arrows indicate two {200} spots for CeO_2). 116

Fig. 10.1. Oxidation kinetics of pure and Ce/CeO_2 modified polycrystalline Ni (a) and Ni crystal faces (b). Continuous lines - sequential oxidation in $^{16}O_2/^{18}O_2$ (time of $^{18}O_2$ admission to the manometric system is indicated by arrow). 122

Fig. 10.2. SIMS composition-depth profiles for a 461 nm thick oxide formed at 973 K after 4 h on polycrystalline mechanically polished nickel, sol coated with 14 nm CeO_2. Oxidation in $^{18}O_2$ only. 123

Fig. 10.3. SIMS composition-depth profiles of a 512 nm thick oxide film formed on mechanically repolished nickel sol coated with 14 nm CeO_2 after oxidation at 973 K in: i) $^{16}O_2$ for 125 min, ii) subsequent oxidation in $^{18}O_2$ for 125 min; oxide thicknesses were 354 and 158 nm respectively. 124

Fig. 10.4. SIMS composition-depth profile of a 195 nm thick oxide film formed on chemically polished nickel implanted with 2x10^{16} Ce^+/cm^2 . Oxidation at 973 K first in $^{16}O_2$ for 240 min and then in $^{18}O_2$ for 120 min; oxide thicknesses were 173 and 22 nm respectively. 125

Fig. 10.5. Composition-depth analyses of oxide film formed on chemically polished nickel, sputter coated with 4 nm CeO_2 after oxidation at 973 K (average thickness of 156 nm): (a) RBS energy spectra of 1MeV $^4He^+$ ions backscattered from surface equal to 100 Ni grains before and after oxidation, and Ce concentration vs depth profile derived from these spectra (b);(c) AES sputter-depth profile of oxide formed on one Ni grain (oxide on this grain was thinner in comparison to that formed on surrounding Ni grains);(d) SIMS profiles after two-stage exposure, first in $^{16}O_2$ for 240 min and then in $^{18}O_2$ for 120 min; oxide thicknesses were 132 and 24 nm respectively. 126,127

Fig. 10.6. SIMS composition- depth profile of a 414 nm thick oxide film formed on (100)Ni sol coated with 14 nm CeO_2 after oxidation at 1073 K first in $^{16}O_2$ for 120 min and then in $^{18}O_2$ for 120 min; oxide thicknesses were 311 and 103 nm, respectively. 128

Fig. 10.7. SIMS composition-depth profile of a 205 nm thick oxide film formed on (111)Ni sol coated with 14 nm CeO_2 after oxidation at 1073 K first in $^{16}O_2$ for 192 min and then in $^{18}O_2$ for 192 min; oxide thicknesses were 152 and 53 nm respectively. 129

Fig. 11.1. Influence of substrate surface finishing and CeO_2 coating on texture of NiO grown at 1073 K for 75 h (760 torr O_2): (a) Ni substrate; (b) chemical polishing, no coating; (c) chemical polishing, CeO_2-coated; (d) mechanical polishing, no coating; (e) mechanical polishing, CeO_2-coated. 136,137

Fig. 11.2. Influence of oxidation time at 1073 K on texture evolution in pure and CeO_2 modified NiO. Results shown as a part of orientation distribution functions for $\phi_2 = 0$ °. Contour levels for all graphs: minimum - 1.2, step - 0.4. 138

Fig. 11.3. Misorientation angle distributions for pure and CeO_2 modified NiO grown for 15 h at 1073 K. 139

Fig. 11.4. Histogram of grain boundary character distributions for Σ up to 27 for pure and CeO_2 modified NiO grown at 1073 K for 15 h. Σ's: 13, 17, 19, 21, 25, and 27 are *a* and *b* type. 139

Fig. 12.1. Factors controlling the effectiveness of CeO_2 sol-gel coatings at high temperatures. 157

Fig. 12.2. Plot of instantaneous rate constant versus time for oxidation of Ni with surface modified with Ce by ion implantation and with CeO_2 by reactive sputtering and sol-gel technology. 157

Fig. 12.3. Schematic diagram of oxide growth on CeO_2-coated and Ce-implanted Ni: (a) before oxidation; (b) initial stage of exposure to oxygen: incorporation of CeO_2 particles into NiO by outward Ni^{2+} diffusion; (c) steady stage of oxide growth by simultaneous Ni^{2+} and O^{2-} ion diffusion. 158

LIST OF TABLES

Table 5.1. Oxygen uptake before onset of the parabolic kinetics for preoxidized uncoated and CeO_2 coated Ni. 42

Table 7.1. The parameters of surface morphology and growth kinetics for selected oxides formed on (100) and (111) Ni crystal faces after 4 h exposure at 1073 K. 75

Table 8.1. Oxygen uptakes and instantaneous values of oxidation rate constants for growth of NiO on unimplanted and Ce-implanted Ni. 91

Table 8.2. AFM analysis of surface morphology of oxides formed on unimplanted and Ce-implanted Ni. 92

Table 9.1. Parabolic rate constants for NiO growth on pure and CeO_2 coated polycrystalline Ni at 973 K and 760 torr oxygen. . . . 106

Table 10.1. Oxidation data for two-stage experiment $^{16}O_2/^{18}O_2$. 118

Table 11.1. Grain boundary character distribution evaluated by numerical analysis of experimental texture data for NiO pure and modified with CeO_2 additions. Oxidation temperature 1073 K. 134

CHAPTER 1. INTRODUCTION - OBJECTIVES OF THE STUDY

The protection of heat-resistant materials against oxidation is provided by the formation of external oxide layers. Good protection requires the oxide to be slow-growing, dense, and resistant to spallation. It was discovered by Pfeil exactly sixty years ago [1937], that these qualities can be drastically enhanced by trace additions of certain elements, having a high affinity to oxygen. Since then, countless observations have been made of this so-called "reactive element effect". Despite the extensive research performed in this area, there is still little agreement, not only about what the effect is but, more importantly, how a small addition of an oxygen active element can have such a profound effect on the oxidation behaviour of many metals and alloys.

The study of the reactive element effect has made substantial progress over the last decade due mainly to the application of more advanced analytical techniques, such as secondary ion-mass spectrometry, Auger electron spectroscopy, field emission gun scanning transmission electron microscopy and atomic force microscopy, which has allowed the examination of the potential reactive element mechanism to move closer to the atomic level. In the research described in this thesis, all these techniques will be used to study the influence of the reactive element on the growth and structure of thin oxide films.

The complexity of oxide growth on multicomponent alloys poses difficulties in the explanation of the mechanism responsible for the increase in oxidation resistance by the reactive elements. Therefore, pure nickel has been chosen for the purpose of this study. Although, as reported by Rapp [1984], the oxidation of nickel is very controversial, it has several advantages as a model system, including the fact that only one oxide (NiO) is formed; structures obtained at intermediate temperatures are coarse enough to permit microscopical examination; and the transport properties in NiO are relatively clearly understood. Cerium was selected as a typical reactive element because of the possibility of applying, using several surface techniques including ion implantation, reactive sputtering and sol-gel technology. The experimental results obtained will significantly advance the understanding of the reactive element effect to the point where a comprehensive theory could be proposed.

The following objectives have been defined for this study:

- to assess the influence of superficially applied Ce on the transport properties and microstructure of NiO thin films formed at high temperatures;

- to establish the role of Ni and NiO textures in oxidation inhibition by a surface applied reactive element;

- to propose a coherent mechanism for improving oxidation resistance of Ni by the surface applied reactive element.

CHAPTER 2. LITERATURE REVIEW

2.1. Fundamentals of Ni oxidation

At high temperatures nickel oxidizes to NiO. The oxidation rate decreases with time, and the oxidation is generally considered to be diffusion controlled. The earlier theory proposed by Wagner and Grunewald [1938], that the single layers of NiO grow at high temperatures by the outward movement of electrons and cations through a metal-deficit p-type oxide, appears to be at least approximately correct. Correspondingly, there is a flow of defects, cation vacancies and electron holes in the opposite direction. As a result, the driving force for the reaction is reflected by the concentration gradient of cation vacancies across the oxide. The nickel vacancies are formed according to the equation:

$$1/2\ O_2 = O_O + 2h\cdot + V_{Ni}'' \qquad (2.1)$$

where: O_O , $2h\cdot$, and V_{Ni}'' represent oxygen ion, an electron hole in valency band, and doubly ionized nickel vacancy, respectively, in the Kroger-Vink notation [Kroger, 1964].

2.1.1. *Characterization of Ni oxidation product*

NiO is the only oxide of nickel which is stable at high temperatures. It has an NaCl structure with a lattice parameter of 4.177 Å and a melting temperature of 2233 K [Neuman et al., 1984]. NiO is approximately stoichiometric at its decomposition pressure, while at higher oxygen pressures the oxide is metal deficient. The predominant point defects in pure NiO are nickel vacancies. By virtue of the energetically close valence states of the cation it is relatively easy for an electron to transfer from Ni^{2+} to Ni^{3+} , thus reversing the charges of the two ions. The site Ni^{3+} is thus seen to offer a low energy position for an electron and is called an "electron hole". The formation of this defect structure can easily be visualised if one considers the interaction of the NiO lattice with oxygen shown in Fig. 2.1. In step (b) the oxygen chemisorps by attracting an electron from a Ni^{2+} site thus forming a Ni^{3+} hole. In step (c) the chemisorped oxygen is fully ionised forming another hole and a Ni^{2+} ion enters the surface to partner the O^{2-} thus forming a vacancy in the cation sub-lattice. Note that this process also forms an extra unit of NiO on the surface of the oxide which should reflect in the density changes if sufficiently sensitive measurements were made.

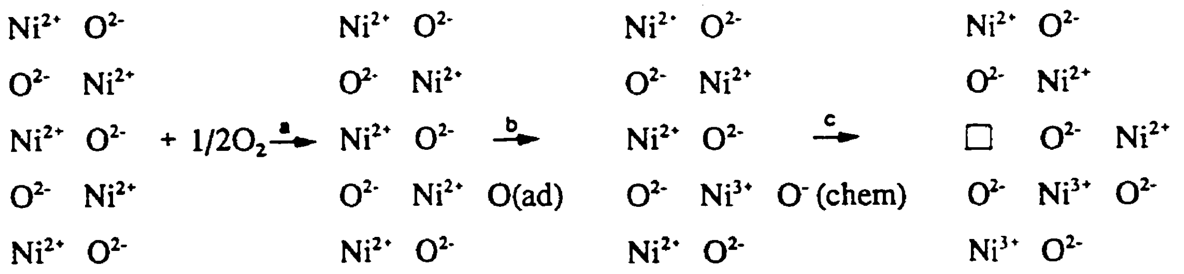

(a) Adsorption: $1/2\ O_2\ (g) = O\ (ad)$
(b) Chemisorption: $O\ (ad) = O^-\ (chem) + h\cdot$
(c) Ionisation: $O^-\ (chem) = O_O + V''_{Ni} + h\cdot$

Overall reaction: $1/2O_2 = O_O + V''_{Ni} + 2h\cdot$

Fig. 2.1. Formation of a metal deficit p-type semiconductor, with cation vacancies and electron holes by the incorporation of oxygen into the "perfect " lattice [Birks and Mayer, 1983].

The process of vacancy formation is represented by equation 2.1 and the equilibrium constant may be written as below, assuming that equation 2.1 represents the only mechanism by which defects form:.

$$C_{h\cdot}^2\ C_{VNi''} = K\ (p_{O2})^{1/2} \qquad (2.2)$$

By stoichiometry $C_{h\cdot} = 2C_{VNi''}$ for electrical neutrality, and thus

$$C_{h\cdot} = \text{const.}\ (p_{O2})^{1/6} \qquad (2.3)$$

The electrical conductivity is expected to vary proportionally to the electron hole concentration and so with the sixth root of the oxygen partial pressure. A further possibility, however, is that a cation vacancy may bond with an electron hole, i.e. in NiO a $Ni^{3\cdot}$ may be permanently attached to the Ni vacancy. In this case, the formation of vacancies and electron holes, on oxidising, may be represented as:

$$1/2\ O_2 = O_O + h\cdot + V_{Ni'} \qquad (2.4)$$

In this case we find

$$C_{h\cdot} = (p_{O2})^{1/4} \qquad (2.5)$$

Experimental results on the variation of electrical conductivity with oxygen partial pressure have confirmed that both types of defect are found in NiO [Eror and Wagner, 1969; Meier and Rapp, 1971; Kofstad, 1972].

As a measure of the nonstoichiometry, y in NiO_{1-y} amounts to approximately y = 10^4 at 1173 K and 1 atm O_2. The temperature dependence of y at 1 atm O_2 can be expressed by the following equation [Kofstad, 1972]:

$$y = \text{Const.} \times \{-80\ 000(\text{J/mol})/RT\} \quad (2.6)$$

Thus, a low level of defects requires the use of high purity Ni substrates during experimental studies, if the effects of impurities on NiO growth rate are to be avoided.

2.1.2. *Diffusion properties of NiO*

The self-diffusion along different paths in NiO has been reviewed in a number of papers [Atkinson, 1984, 1985]. Although the available experimental results are not extensive, they are sufficient for some detailed observations to be made for NiO and some generalisations extended to other oxides. Data for both Ni and O diffusion along dislocations and grain boundaries in NiO are presented in Fig. 2.2 and compared with the corresponding lattice diffusion coefficients.

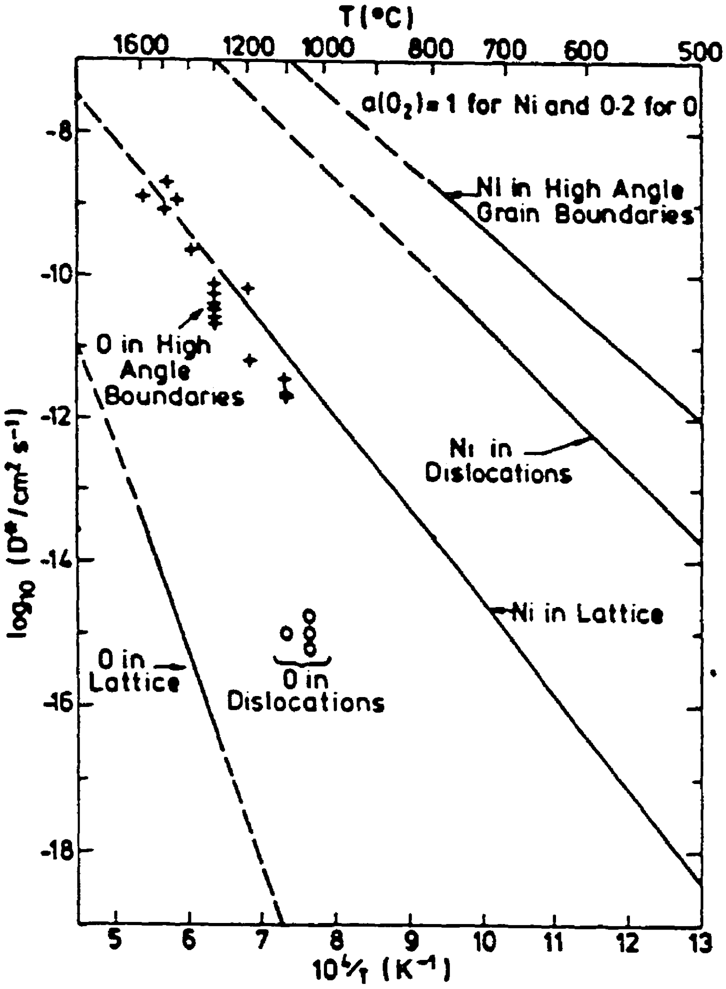

Fig. 2.2. Diffusion coefficients of Ni and O in the lattice, in dislocations and along grain boundaries in NiO [Atkinson, 1984].

In the case of grain boundary diffusion, the parameter which is measured experimentally is the product of the grain boundary diffusion coefficient and the boundary width. In the case of dislocations it is the same parameter measured as for low-angle boundaries. If the mean separation of dislocations in the low-angle boundaries is known, then the parameter $\mathbf{D_d a^2}$ can be deduced, where $\mathbf{D_d}$ is the dislocation diffusion coefficient and **a** is the effective radius of the dislocation, assuming it can be approximated as a cylindrical pipe. In order to compare actual diffusion coefficients, the geometrical parameters and **a** must be measured. Experiments have been carried out to obtain a rough estimate of **a** and δ [Atkinson and Taylor, 1979]. These experiments showed that both the width of the grain boundary and the diameter of the dislocation are approximately 1 nm in NiO. Thus the fast-diffusivity region is essentially confined to the core of the boundary or dislocation and no significant contribution is made by the space charge region which surrounds the boundary in ionic materials. The data in Fig. 2.2 show that diffusivities of both metal and oxygen are enhanced in the boundary with respect to the corresponding lattice diffusivities, but their relative order is maintained, i.e. the faster diffuser in the lattice is also faster in the boundary. Moreover, the degree of diffusion enhancement is relatively great with a typical difference of the order of 10^6.

In order to characterize the impurity diffusion in NiO, elements such as Co, Cr, and Ce were selected. These ions are expected to be in charge states Co^{2+}, Cr^{3+}, and Ce^{4+} and therefore represent a reasonable cross-section of impurity behaviour. They differ widely in their solubility and segregation characteristics. While Co is completely soluble in the NiO lattice and should not segregate appreciably to grain boundaries, Ce has negligible lattice solubility and will dissolve only at grain boundaries. Cr falls between these extremes, having slight lattice solubility and appreciable grain boundary segregation.

The measured grain boundary diffusion coefficients are summarized in Fig 2.3 [Atkinson and Taylor, 1986]. In the case of Co, it has been assumed that segregation to the boundary is negligible and that the boundary width is the same as for Ni diffusion (1 nm). No assumptions were necessary for Ce since it is insoluble in the NiO lattice and therefore its diffusion coefficient in the boundary is measured directly. For Cr the experiments were analyzed in the way which allowed the segregation and diffusion contributions to be separated in a self-consistent way. The diffusion coefficients are in the order $D_{Co} > D_{Ni} > D_{Cr}$ for both lattice and grain boundary diffusion, which reinforces the view that grain boundary and lattice diffusion both take place by a similar mechanism. The atomic characteristics that control impurity diffusion are not understood even for lattice diffusion, but ionic charge is obviously important since, in general, the higher the charge on the ion the more slowly does it tend to diffuse [Hoshino and Peterson, 1984].

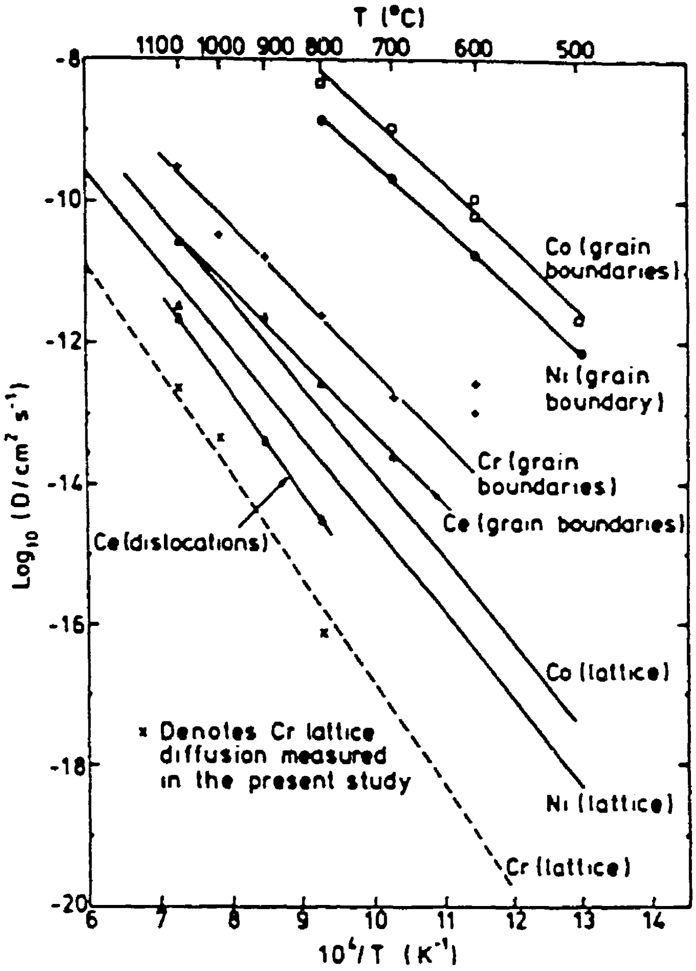

Fig. 2.3. Diffusion coefficients for some impurities in NiO grain boundaries (at an oxygen pressure of 1 atm) compared with the corresponding lattice diffusivities. The boundary width has been assumed equal to 1 nm [Atkinson and Taylor, 1986].

2.2. Grain-boundary diffusion in oxide growth at high temperatures

An extensive amount of data is now available on the oxidation properties of transition metals and their alloys exposed to a corrosive environment at temperatures in the range 600 to 1300 K. One may conclude from this that growth of oxide layers at temperatures of up to half the oxide melting point is often dependent on the higher diffusion of metal and/or oxygen through the grain boundaries than through point defects within the oxide lattice [Smeltzer, 1988].

Although there are no direct experiments which allow the mechanism of grain boundary or dislocation diffusion to be identified, there is now a body of indirect experimental and theoretical evidence to support the concept that a point defect (vacancy or interstitial) is involved which is similar to a lattice defect. In NiO, an increase in oxygen activity leads to an increase in the concentration of vacant sites and hence an increase in the lattice diffusion coefficient for Ni. It is also found that the grain boundary and dislocation diffusion of Ni in NiO increases in a similar way [Atkinson and Taylor, 1979,1981]. This indicates that grain boundary diffusion of Ni in NiO also occurs by a nickel vacancy mechanism and that the concentration and mobility of vacancies is greater in the boundary than in the lattice. Since the grain boundaries are also important in oxides modified with reactive elements, some aspects of their structure and transport properties are discussed below.

2.2.1. *Grain boundaries in ionic solids*

Most of the concepts that have been developed for grain boundaries in metals are also applicable to ionic crystals; however, there are three fundamental differences [Sutton and Balluffi, 1995]. The first is that the repulsive electrostatic interaction between ions of like sign is very strong, and the boundary will undergo relaxations and reconstructions to avoid ions of like sign being nearest neighbours. Secondly, the presence of two or more ionic species introduces the possibility of a greater variety of structures for a particular boundary plane. Finally, the boundary core may acquire a net charge, which must be compensated by space charge layers that can extend considerable distances into the adjoining crystals. The net charge may arise either from imbalances in the formation energies of intrinsic defects [Duffy and Tasker, 1984], or from the segregation of impurities.

Grain boundaries in ionic crystals have not met with the same degree of agreement between experiment and computer simulations as grain boundaries in metals. For example, computer simulations of [001] symmetric tilt boundaries in NiO [Duffy and Tasker, 1983] were found to have very open structure. Fig. 2.4a shows the relaxed structure of the (310) boundary obtained by minimizing the internal energy of the bicrystal at 0 K. It is seen that electrostatic interactions favour ions of the upper grain lying directly above ions with opposite charge in the lower grain, and the resulting structure has large open channels along the tilt axis. Fig. 2.4b shows two distinct structures of the same grain boundary in NiO deducted from high resolution electron microscopy [Merkle and Smith, 1987]. The comparison indicates that neither of the structures observed microscopically in real material (Fig. 2.4b) is the same as that obtained from computer simulation (Fig. 2.4a)

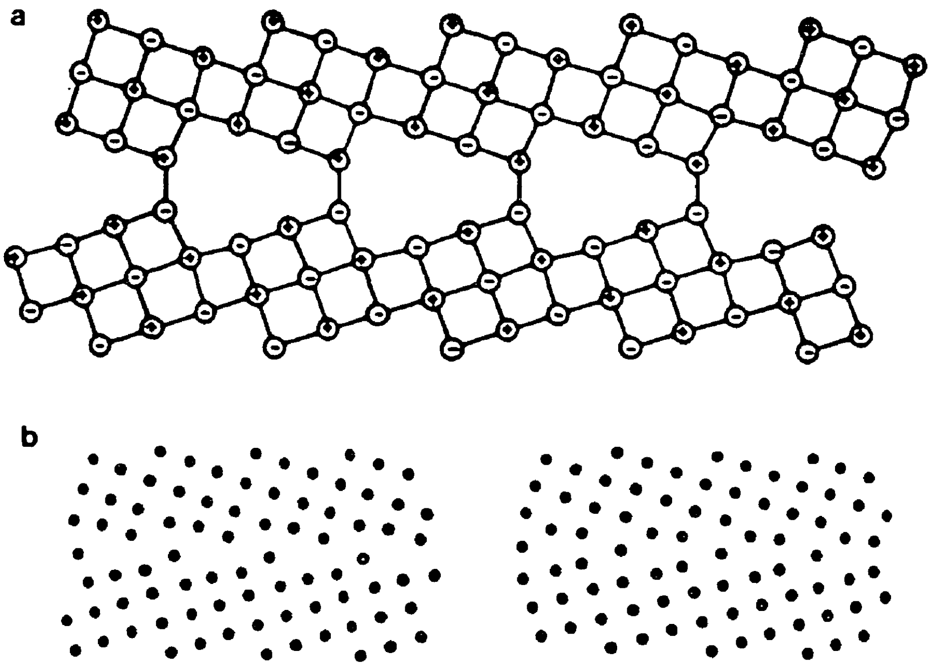

Fig. 2.4. (a) The relaxed structure at 0 K of the (310) symmetric tilt boundary in NiO seen in projection along the [001] tilt axis [Duffy and Tasker, 1983]; (b) structural models of the same boundary in NiO deducted from high resolution microscopy [Merkle and Smith, 1987].

2.2.2. *Theory of oxide growth by lattice and grain-boundary diffusion*

A phenomenological description has been advanced by Smeltzer et al. [1961] and Perrow et al. [1968] to account for the oxidation process based on a model where the reactant migrates through the oxide lattice as in the model for parabolic oxidation. These authors described the increase in scale thickness **X** by a Fick's first law expression:

$$dX/dt = \Omega \ \Delta c \ D_{eff}/X \qquad (2.7)$$

where Ω is the volume of the oxide per reactant ion, Δ**c** is the concentration difference across the scale, and **X** is the layer thickness. Equation 2.7 gives the parabolic rate equation when short-circuit diffusion may be neglected. If the fraction of surface associated with boundaries is virtually constant during the early exposure stages, the initial region of an oxidation curve will conform to a parabolic relationship in which the effective parabolic constant contains terms for grain boundary and lattice diffusion.

When lattice and boundary diffusion contribute to mass transport in a solid containing a random array of short-circuit paths, the effective diffusion coefficient $\mathbf{D_{eff}}$ may be expressed as a weighted sum of the diffusion coefficients for lattice and grain boundary diffusion [Heart, 1957]:

$$D_{eff} = D_L (1 - f) + D_B f \qquad (2.8)$$

where $\mathbf{D_L}$ and $\mathbf{D_B}$ are diffusivities for the lattice and internal boundaries respectively, and **f** is the fraction of the total available diffusion sites lying in the low resistance dislocation and boundary paths. The theory then models parallel outward diffusion of cations over both lattice sites and grain boundary paths. Assuming a cubic grain shape, **f** is given by

$$f = 2\delta \ / \ E_t \qquad (2.9)$$

where $\mathbf{E_t}$ is the grain width at any time, and δ is the boundary width. The further evaluation of the theory involves the substitution of Eqs. (2.8) and (2.9) into (2.7) and subsequent integration; however, experimental observations must provide the functional form for $\mathbf{E_t}$. Perrow et al. [1968] found a parabolic increase in NiO grain size for oxidation of Ni at 773 and 873 K so that

$$E_t^2 - E_o^2 = Gt \qquad (2.10)$$

where $\mathbf{E_o}$ is the original oxide grain width and **G** is a grain growth constant. The parabolic grain coarsening leads to the following rate of oxide thickening:

$$dX/dt = \Omega\ \Delta c/X\ [\ D_L + 2\delta(D_B - D_L)\ /\ (E_o^2 + Gt)^{1/2}] \qquad (2.11)$$

Matsunaga and Homma [1976] have revised and computerized this theory to permit a grain size distribution in the scale, grains with differing boundary widths depending on the grain boundary structure, an incubation time for the onset of scale growth and recrystallization, and a variable n-th power law for grain growth. Examination of Eq. 2.11 shows that a metal may oxidize parabolically when short-circuit diffusion occurs in an oxide layer, providing that the structure and the diffusivities remain time independent.

2.3. The "reactive element effect" in high temperature corrosion

Small additions of an element with a high affinity to oxygen, such as Y, Ce, Hf, Gd, La, Zr, Ti, or Ca, enhance the protective characteristics of oxides on metals and alloys. The reactive elements generally have atomic and ionic sizes which greatly exceed those for metals, so they are not at all or only slightly soluble in metal oxides at high temperatures. At least in the first approximation, the effects generated by various elements are similar, and a typical list includes: i) a reduction in the oxidation rate, ii) an improvement in oxide adhesion or resistance to spallation, and iii) an improvement in the selective oxidation of Cr in chromia formers (i.e. less Cr is required in the alloy to achieve a continuous chromia film). These macroscopic changes are accompanied by: i) a change in oxide growth mechanism, ii) a modification of the oxide microstructure, iii) a prevention of sulphur segregation to the oxide-metal interface, and iv) a reduction of growth stresses.

2.3.1. *Methods of reactive element addition*

In general, reactive elements can be added to the bulk or applied to the surface of a substrate. While alloying would seem to be the simplest way of adding the element to the system, success is limited because of metallurgical difficulties caused by the loss of the reactive element from molten alloy into slag phases, rendering control of composition, low ductility, and cracking during cold working, and low creep resistance at high temperatures [Moon and Bennett, 1989; Stringer, 1989]. A reactive element oxide dispersion, generally provides the best method for introducing the element uniformly throughout the material. It has the additional benefit that the oxide dispersions improve the creep resistance of the material by pinning dislocations [Dieter, 1974]. The drawback of the dispersion is the fabrication. In order to achieve a uniform dispersion, powder metallurgy techniques such as mechanical alloying are necessary [Ikeda et al., 1993].

While prior to the 1970s research was focused mainly on alloy additions, in the last decades an emphasis has been put on other types of reactive element applications, including surface implantation and coatings. Surface implantation has been found to cause the growth of a more uniform scale than alloying. In such a scale, no oxide pegs or other anomalies are found. Although in some cases the radiation damage associated with implantation affects the oxidation behaviour, particularly at intermediate temperatures, in the majority of systems the observed effects derived entirely from the chemical role of the implanted element [Bennett, 1983; Galerie et al., 1985]. There appeared to be a threshold dose for improved oxidation resistance, usually between 10^{15} and 10^{16} ions/cm^2, while maximum inhibition was obtained with doses between $2\text{x}10^{16}$ and 10^{17} ions/cm^2 [Bennett et al., 1982; Hou and Stringer, 1988].

The limited time period of the effectiveness of surface implant has also been occasionally explored. For example, Cotell et al. [1990] found that a Y-implant ($2\text{x}10^{16}$/cm^2) in Cr after 20 h exposure showed signs that the effect was diminishing. It might be expected that in the absence of a continuing reactive element provision from the substrate, the scale growth predominantly by inward oxidant transport provides reactive element free oxide at the scale-substrate interface. Such a growth will result in the eventual breakdown of scale adhesion, as was observed on Y-implanted alumina forming alloys [Bennett et al., 1980; Smeggil and Shuskus, 1987].

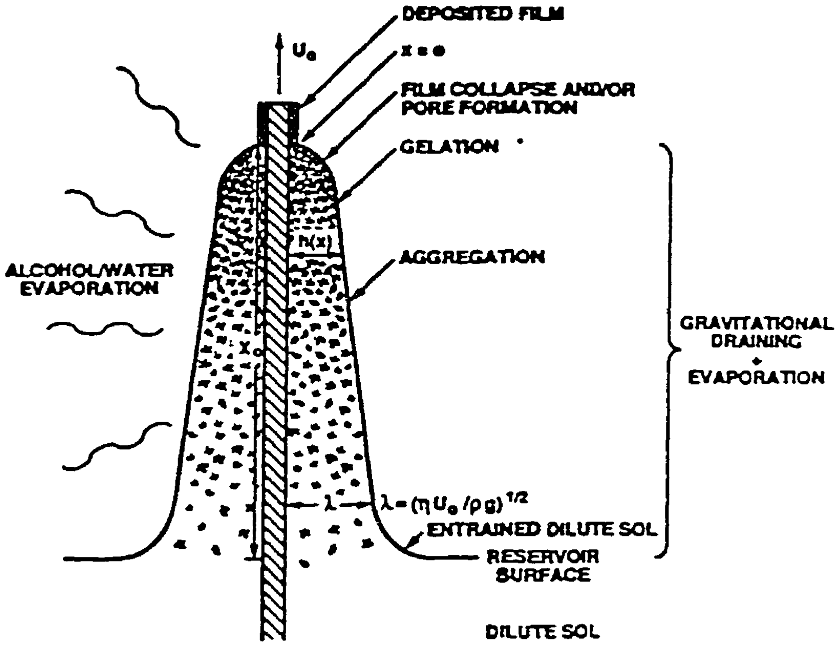

Fig. 2.5. Schematic of the steady state of sol-gel dip process [Brinker and Scherer, 1990].

Coatings of reactive element oxides can be deposited by several techniques. In addition to sputtering [Papaiacovou et al., 1990], some other methods can be used for the same purpose. The reactive element oxide particles can be derived from: i) nitrate salts in solution or molten [Landkof et al., 1985], ii) an oxide slurry in suspension in alcohol [Saito et al., 1987], or an oxide sol [Moon, 1989]. Among the various precursors of reactive-element oxide particles in a coating process, there is increasing interest in sol-gel technology. The fluid sol is ideal for preparing thin coatings on surfaces with complex geometry by dipping, spinning, spraying, or electrophoresis [Cannon et al., 1980; Roy, 1987]. A schematic of the steady state sol-gel dip coating process, showing the sequential stages of structural development that result from draining accompanied by solvent evaporation and continued condensation reactions is given in Fig. 2.5. It should be emphasized that sol-gel coatings were selected as a major technique of Ni-surface modification in this study.

2.3.2. *Attempts to explain the reactive element effect*

Extensive investigations have been carried out during the last decades, and numerous theories have been put forward to explain the reactive element effect, as reviewed by several authors [Whittle and Stringer, 1980; Moon and Bennett, 1989; Stringer, 1989; Saito and Onay, 1990; Pint, 1996]. Consistent with the reviews, the existing interpretations do not provide comprehensive explanations for the observed effects. At present, two major hypotheses are supported by researchers: the segregation theory and the "poisoning interface" model. The first one assumes the change of the relative magnitudes of cation and ion short-circuit diffusion by the reactive element ion segregated to oxide grain boundaries [Przybylski et al., 1988; Cotell et al., 1990]. Details of the mechanism responsible for blocking ion diffusion, related specifically to NiO growth, will be discussed in this study.

The second theory suggests that all of the reactive element effects in chromia formers result from the segregation of reactive element ions to the metal-oxide interface [Pierragi and Rapp, 1988, 1993; Strawbridge and Rapp, 1994]. According to this theory, for the growth of cation-diffusing oxides, the climb of some fraction of the interfacial misfit dislocations into metal, is required. A dislocation at the metal/oxide interface (Fig. 2.6) annihilates cation vacancies or creates interstitial cations to support cation-vacancy diffusion in the scale. If cation-vacancy annihilation, or interstitial-cation creation, is prevented for some reason, then scale growth by cation diffusion cannot occur. In this so called "poisoned interface" model, the relatively large, highly charged reactive element ions segregate to and immobilize the interfacial misfit dislocations (Fig. 2.7) Thus, if the climbs of the misfit dislocations at the metal/oxide interface were sufficiently blocked by the pinning action of the reactive element ions, oxide growth by cation diffusion could be prevented. As a result, the growth would proceed by oxygen diffusion via anion

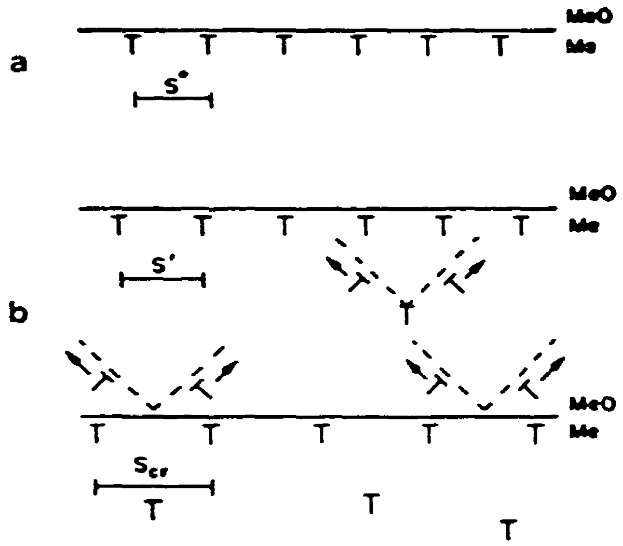

Fig. 2.6. Schematic illustration of the mechanism to effect vacancy annihilation in cation-diffusing scales: (a) misfit dislocations at metal/oxide interface with equilibrium separation s° ; (b) the climb of misfit dislocations into metal and subsequent glide back to the interface, resulting in separation s′ [Strawbridge and Rapp, 1994].

vacancies or interstitials.

There were also other models based on the ability of the reactive element to eliminate sulphur segregation leading to poor adherence at the metal/oxide interface, as demonstrated by Funkenbusch et al. [1985] and supported by Smialek [1987]. However, the role of sulphur is primarily restricted to oxide adherence. The presence or absence of sulphur cannot explain the change in the scale growth mechanism, nor does it appear to affect significantly the scale microstructure [Smialek, 1988]. Other hypotheses about the reactive element effect, based mainly on the interface phenomena, such as the void theory [Stringer, 1966], and the interface bonding model [Anderson et al., 1985) have not been experimentally proven to be fully consistent.

2.4. Previous work related to the oxidation of the Ni-reactive element system

A review of the literature shows that the vast majority of studies concerning the reactive element effect deal with chromia and alumina scales formed on complex alloys [Whittle and Stringer, 1980; Stringer, 1989; Saito and Onay, 1990]. The most extensive research utilizing pure Ni to examine the reactive element effect was conducted by Moon

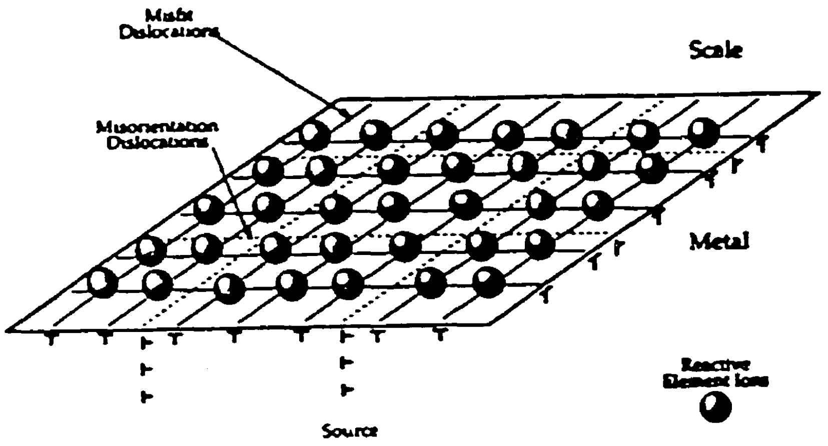

Fig. 2.7. Schematic representation of the "poisoned interface" interpretation of the reactive element effect. Large, highly charged reactive element ions segregate to the metal/oxide interface, thereby pinning the misfit dislocations and preventing oxide growth by cation diffusion [Pierragi and Rapp, 1993].

[1989] (see also Moon and Bennett, 1989). Moon extended the earlier studies by Chadwick and Taylor [1984a,b] and coated Ni with CeO_2 using sol-gel technology developed at Harwell Laboratory (U.K. Atomic Energy Research Establishment). Experiments were conducted at 1173 K in 1 atm O_2 for long periods of time in order to produce thick NiO scales. The major conclusion was that ceria coatings promoted protective scale formation and restricted further attack of the oxidant by inhibiting scale growth and spallation. The important mechanisms for that effect were identified as the scale nucleation at reactive element oxide particles, blocking grain boundary diffusion by reactive element ion-segregants, and reduction of stresses in the scale. At the same time, Moon [1989], investigating oxidation of Ni with alloying addition of 0.6 wt.% Ce, measured an increase in weight gain by 40-50% after 142 h at 1173 K. The large and non-uniformly distributed ceria particles inside the alloy were blamed for a lack of improvement. This is in contrary to experiments by Moosa and Rothman [1985] who found the lower oxidation rate at 773-973 K of the Ni-0.1 wt.% Y alloy as compared to pure Ni. However, the extensive measurements by Moosa et al. [1985] of the diffusion behaviour of NiO formed on the same alloy, led to conclusion that the addition of Y to Ni does not change the grain boundary, sub-boundary and lattice diffusion coefficients of Ni in NiO.

Nath et al. [1985] and George et al. [1989] doped the surface of Ni with Y using ion implantation and observed a significant oxidation inhibition at temperatures between 773 and 1493 K. In all cases after oxidation, the Y implants were located near the oxide/metal interface. An interesting finding of this research was that implants of La, Yb, Ce and Si exerted the same influence on NiO growth at 973 K as Y did. Also Smeggil et al. [1988] found that the Y implants decreased by half the NiO thickness after 620 h at 1173 K. However, the same authors detected Y present approximately in the middle of the NiO scale with a thickness of 18 μm. According to Hampikian et al. [1989], the Y implants after oxidation at 1173 K yielded very uniform NiO which exhibited an absence of the crystallographic relationship between the oxide and the Ni substrate. Moreover, Hampikian et al. [1989] revealed that Y-implanted specimens had a more porous oxide than had unimplanted Ni. This is contrary to the findings of Smeggil et al. [1988], who found the reactive element doped NiO to be less porous than pure NiO. In very recent studies by Strawbridge and Rapp [1994] and Strawbridge et al. [1995], the oxidation inhibition was found to be dependent on the type of the reactive element. For example, 20 times reduction in the parabolic rate constant at 1123 K, was achieved using a 25 nm thick calcium coating deposited on Ni surface. After oxidation the presence of Ca was detected inside the NiO layer.

The review shows that contradictory results were obtained concerning the influence of oxygen active elements on the oxidation inhibition of Ni. The difference in the substrates used by individual authors, especially the surface finishing techniques, substrate purity, texture, dose of the reactive element, and the oxidation conditions unable us to verify the role of specific experimental parameters in the growth of the reactive element modified oxides. In order to achieve this goal, a detailed study performed on the same material and under the same experimental conditions is necessary.

CHAPTER 3. RESEARCH MATERIAL AND EXPERIMENTAL TECHNIQUES

3.1. Description of research material

3.1.1. *Substrate material and surface finishing*

The polycrystalline Ni used for oxidation was in the form of a rod with a diameter of 9.5 mm and purity of 99.99% (A.D. MacKay Inc.). For some experiments, Ni in the form of a sheet with a thickness of 1 mm and purity of 99.5% (Johnson Matthey Inc.) was used, and this material is additionally indicated in the text. Specimens, of 1 mm in thickness, were abraded with 600 grit silicon carbide paper, mechanically polished to 1 μm diamond paste, cleaned ultrasonically, and annealed at 1173 K for 1 h in a vacuum of 10^{-7} torr. The annealed nickel had an average grain size of 100 μm (Fig. 3.1) and grain orientation represented by the pole figures shown in Fig. 3.2. After this process two methods of surface finishing were used: i) chemical polishing for 40 s at 363 K in a solution of 3 parts nitric acid, 1 part sulphuric acid, 1 part orthophosphoric acid, and 5 parts glacial acetic acid [Johnson, 1987], and ii) mechanical repolishing with 1 μm diamond paste for 3 min. Some samples were preoxidized at 673 K for 2 h in flowing oxygen at 760 torr pressure, which produced NiO films having thicknesses of 54 nm for the chemically polished, and of 124 nm for mechanically polished substrates.

The Ni single crystals with (100) and (111) orientations, of an ultra high purity of 99.999%, supplied by Research Crystal Co., after spark cutting were sequentially polished in 60% sulphuric acid and mechanically polished with 1 μm diamond paste. At the final stage of surface finishing, the chemical polishing was performed in a solution consisting of 65 parts of acetic acid, 35 parts of nitric acid and 0.5 parts of hydrochloric acid.

3.1.2. *Surface modification with Ce and CeO_2*

Three different methods of Ni surface modifications with Ce and CeO_2 as a typical reactive element were employed: i) sol-gel coating, ii) reactive sputter coating, and iii) ion implantation. High purity ceria sol having a concentration of 5 g CeO_2/L in 0.1 M nitric acid, was prepared using the 20% colloidal dispersion supplied by Johnson Matthey Ltd. To prevent the coagulation of CeO_2 particles the 25 ml/L of nonionic surfactant, Triton X-100, Aldrich Chemical Co. was added. The coatings were deposited by dipping and draining a cold substrate. During drying for 20 h at room temperature in a desiccator, water between colloidal particles was removed and the sol was converted into gel. To transform the gel to a ceramic material, coatings were calcined at 573 K for 1 h in oxygen at 760 torr pressure. The resulting coatings weighed between 5 and 110 $\mu g/cm^2$. Assuming fully dense CeO_2 and density of 7.1 g/cm^3 [Nelson et al., 1981], it corresponds to a thickness between 7 and 154 nm.

The deposition of CeO_2 coatings by reactive sputtering was conducted using a Ce target sputtered with 8 keV oxygen ions in 3×10^{-3} torr oxygen. The deposition energy was only a few eV, thus causing no sample heating or mixing. Applied coatings had a thickness of 4 nm.

Ion implantation was conducted with 150 keV Ce^+ to a dose of 2×10^{16} ions/cm^2 in a Van de Graaff accelerator. This corresponded to a maximum concentration of 9 atomic % Ce located at a depth of 22 nm. A small part of each sample was not implanted, in order to have a reference surface for the purpose of comparison. To eliminate the effect of radiation damage caused by ion bombardment and to modify the Ce distribution in Ni, some implanted samples were annealed before oxidation at 1073 K for 1 h in vacuum of 10^{-9} torr (1.3×10^{-7} Pa). A schematic diagram of the preparation of Ni substrates for oxidation is shown in Fig. 3.3.

3.2. Oxidation kinetic measurements

Oxidation kinetics under isothermal conditions, at temperatures in the range of 873-1173 K, and for periods up to 4 h were determined using an ultrahigh vacuum (UHV) manometric system. The apparatus employed a sensitive capacitance gauge to follow the pressure decrease with time, during oxidation. The specimen temperature was monitored by a Pt/Pt-Rh thermocouple, which was spot welded to the sample. Experiments were conducted at a total pressure of 5×10^{-3} ±20% torr (0.67 Pa). For the gauge used, MKS Instruments Inc. type 315, the uncertainty in these pressure readings was in the range of 0.5%. Before oxidation the system was evacuated to about 10^{-9} torr and then oxygen was admitted to the system at 1 torr for 2 h to saturate the walls of the chamber. Specimens were heated to the oxidation temperature at a rate of 100 K/min (polycrystals) and 200 K/min (single crystals) in the presence of oxygen. The presence of oxygen was necessary, because the heating of coated specimens in a vacuum led to a coarsening of CeO_2 particles.

Long-term oxidation for time periods up to 125 h was performed in a quartz tube furnace in flowing oxygen at a pressure of 760 torr (10^5 Pa). Weight gains of oxidized samples were measured gravimetrically after cooling to room temperature.

3.3. Characterization of the oxides

Several experimental techniques were employed in order to characterize the oxides through examining the growth surfaces, fracture cross sections, polished taper sections and thin foils.

3.3.1. *Analysis of the depth composition of the oxides*

Three different techniques of the examination of oxide depth composition were employed: i) Rutherford backscattering spectrometry (RBS), ii) Auger electron spectroscopy (AES), and iii) secondary ion mass spectrometry (SIMS):

The depth composition measurements by RBS were performed using 1 MeV $^4He^+$ ions at a scattering angle of 160° [Ziegler et al., 1985]. A maximum current of 2 nA was used to ensure that the detector dead time was less than 1% and that beam-heating effects were negligible. In some cases the samples were tilted through 45° with respect to the analysis beam in order to improve the depth resolution.

Measurements by AES, using a Perkin Elmer PHI 600 system, were performed while simultaneously sputtering the oxide with Ar^+ ions. The beam direction and sputtering angle were 40 and 50° respectively. The sample area analyzed by each of these techniques was essentially different. During the AES measurements the sputtered area was (45 μm)^2 and a small fraction of this region was analyzed, corresponding to oxide grown on one grain of Ni. Using RBS, the analyzed area was about (700 μm)^2. In this case the information was derived from oxide grown on about 100 Ni grains.

For samples sequentially oxidized in $^{16}O_2/^{18}O_2$, polyatomic SIMS analyses were performed with a Physical Electronic SIMS-II system used in conjunction with a differentially pumped ion gun operated with 4 keV xenon at 56° off the specimen normal. The beam was focused over an area of 2x2 mm^2, and was electronically gated to analyze the central 29% of the sputter crater. Fundamentals of RBS, AES, and SIMS techniques can be found elsewhere [Chu et al., 1978; Loretto, 1984; Feldman and Mayer, 1988].

3.3.2. *Examination of the growth surfaces and cross-sections*

SEM was used throughout this study to image the oxide growth surface, fracture cross sections, and polished taper sections. To prepare polished taper sections, the oxide was covered with a conductive gold film by sputtering and then electrolytically coated with Ni. After mounting in cold setting resin and mechanical polishing, some oxides were etched electrolytically in a solution containing hydrochloric acid, glacial acetic acid, and water with a ratio of 1:1:4.

A detailed analysis of the oxide topography was conducted using a Digital Instruments Nanoscope III atomic force microscope (AFM). The microscope was operated in contact mode using a 0.12 Nm^{-1} Si_3N_4 cantilever and in tapping mode with a pure Si probe. Data files of 512x512 points were collected from the scan area, usually smaller than 12.5x12.5 μm, depending on magnification. For topographical measurements, the scanning parameters were set to collect the data without filtering or smoothing.

3.3.3. *Thin foil examinations in electron microscopes*

The majority of microstructural observations were performed on planar view thin foils using a transmission electron microscope (TEM), a Philips CM12 equipped with a Gatan 607 EELS (electron energy-loss spectrometer). During TEM observations the foil thickness was calculated from the EEL spectrum by the relation [Leapman et al., 1984]:

$$t = \lambda \ln (I_t / I_o) \qquad (3.1)$$

where λ is the mean free path for inelastic scattering, and I_t and I_o are, respectively, the total number of electrons in the EEL spectrum and the number of electrons having lost no energy. The value for λ = 110 nm was taken from measurements by Malis et al., [1988]. Values of I_t and I_o were found by a computer integration of EEL spectrum. Images were also analyzed by selected area electron diffraction (SAD) and convergent beam electron diffraction (CBDP).

Microdistribution of the reactive element in the oxide was measured on thin foils by a field emission gun, scanning transmission electron microscopy (STEM), a Vacuum Generator Microscopes Ltd. HB5 with a 3.5 nm electron probe and a windowless Link detector (EDX).

To prepare the planar thin foils covering the total oxide thickness, the oxide films were stripped from the substrate in a saturated solution of iodine in methanol. Because of the small size of oxide pieces, special grids were used. To prepare the planar thin foils located at a specific depth, discs with diameters of 3 mm were made by cutting the oxidized samples with an ultrasonic drill and then grinding them from the opposite side. After preliminary thinning of the nickel substrate by the electrolytic method, the discs were epoxied between two metal apertures. The apertures were then masked with lacquer and the remaining Ni was totally dissolved. In order to prepare cross sectional thin foils, the samples were glued together along the oxide/gas interface. After mechanical dimpling with boron nitride paste using Gatan dimpler, the foil was Ar ion milled to a final thickness. Specimens for examining the oxide structure at different depths were made by ion milling in a Gatan 600 duomill with an Ar beam at 4-4.5 keV.

3.3.4. *X-ray measurements*

An x-ray technique was used to examine: i) the phase composition of oxides, ii) the grain size of nano-sized CeO_2 particles, and iii) the crystallographic texture of both the polycrystalline substrates and oxides. The phase composition of oxides was examined by x-ray diffraction at room temperature after cooling, and "in situ" at high temperatures using a hot stage attached to a rotating anode, Rigaku diffractometer with $Cu_{K\alpha}$ radiation.

The diffraction line broadening method was used to estimate the crystallite size in nanometre range. Assuming the absence of lattice strains, the mean crystallite size (*L*) was calculated according to the Scherrer's equation [Klug and Alexander, 1974]:

$$L = 0.9\lambda/\beta\cos\theta \qquad (3.2)$$

where λ, β, and θ are the wavelength of x-rays, corrected diffraction peak broadening at its half maximum intensity, and the diffraction angle, respectively. In order to calculate the correction for instrumental broadening, Warren's formula was used [Klug and Alexander, 1974]:

$$\beta^2 = \beta_m^2 - \beta_s^2 \qquad (3.3)$$

where β_m and β_s are diffraction peak broadenings for analyzed sample and standard, respectively. The sample after annealing at 2000 K served as a standard. The values of β_m and β_s were determined by computer after correcting for background noise and fitting the Gaussian curves to the experimental points.

The texture of oxides and substrates was analyzed by a Siemens D-500 diffractometer, equipped with a texture goniometer. Pole figures were measured using the reflection technique, up to a maximum tilt in the specimen of 80° in 5° intervals. The results were corrected for absorption and defocussing using a standard specimen of random NiO. The pole figures were normalized within the available interval of distribution of the crystallographic planes, and the intensity was shown using multiples of intensities from the random specimen.

Fig. 3.1. Optical micrograph of Ni (99.9% purity) annealed at 1173 K for 1 h and preoxidized at 673 K for 2 h in 760 torr oxygen. Weight gain of 7.7 μg/cm^2 which corresponds to average NiO thickness of 54 nm.

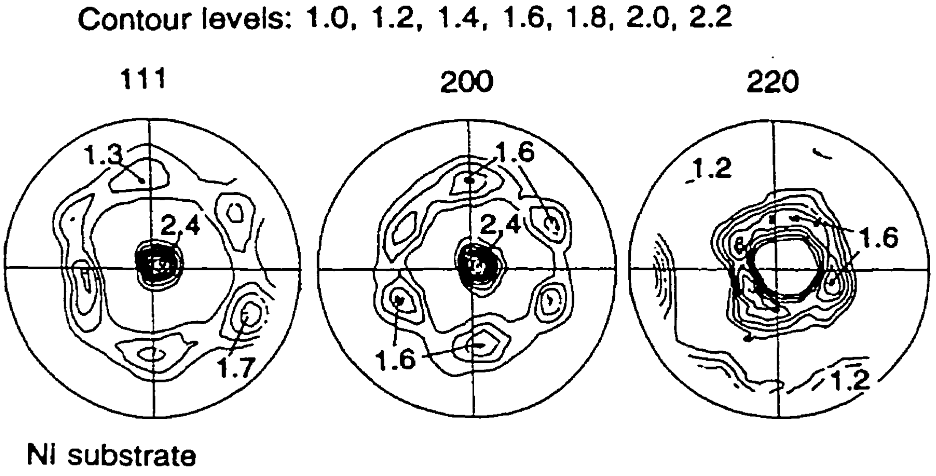

Fig. 3.2. Pole figures of annealed Ni (99.9% purity) used as substrates for oxide growth.

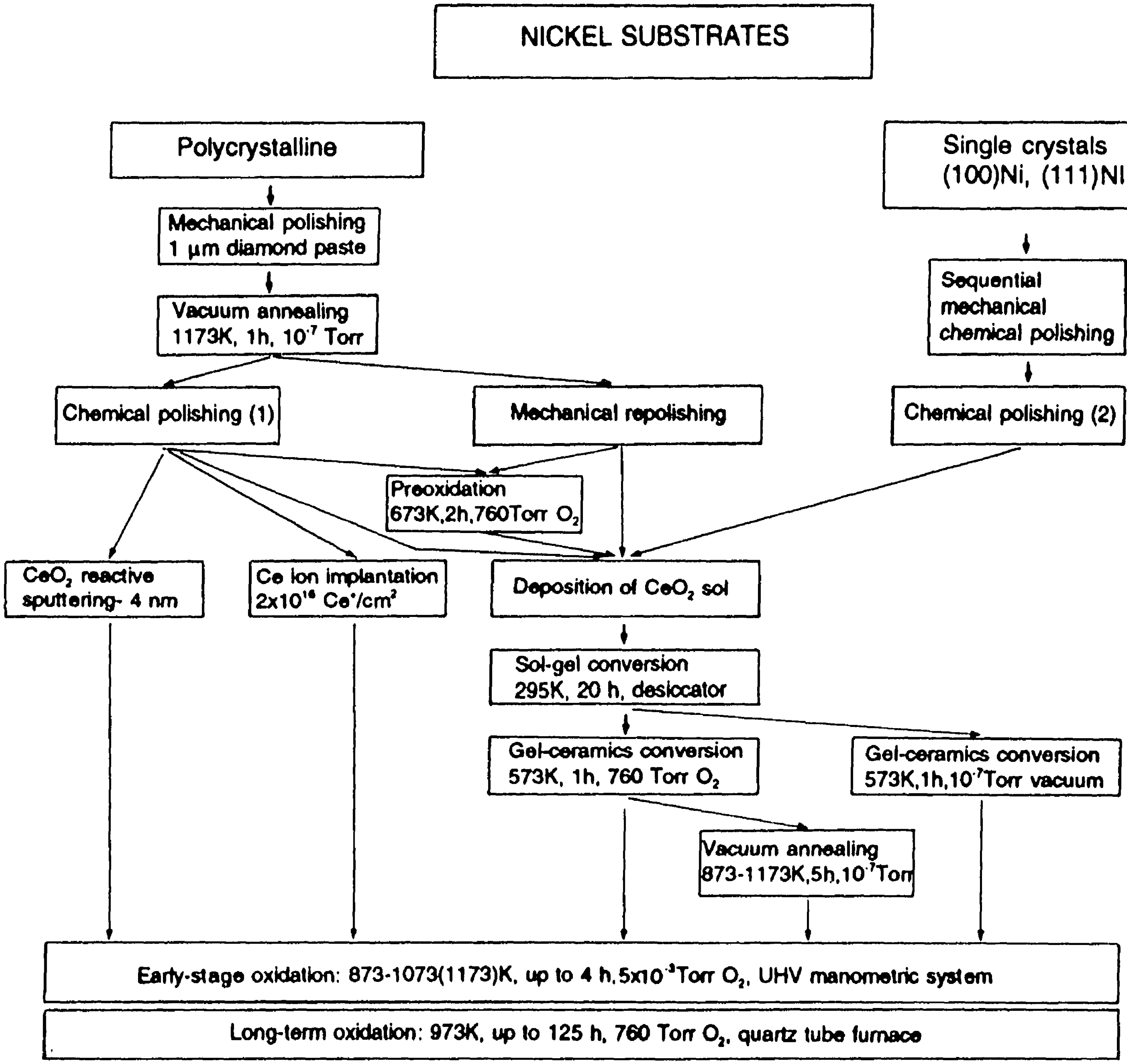

Fig. 3.3. Schematic diagram of preparation of the Ni substrates for oxidation experiments.

CHAPTER 4. CHARACTERIZATION OF CeO_2 CERAMICS DERIVED FROM SOL-GEL

4.1. Introduction

The sol-gel process is a major technique of Ni-substrate modification with the reactive element explored in this study. Our preliminary results showed that the protective properties of sol-gel coatings depend on their microstructure, which is sensitive to high temperatures during thermal processing. Therefore, to design the coating technology and to select the appropriate thermal process for gel-ceramics conversion, a knowledge of the evolution of the coating microstructure which accompanies heat treatment, is required. In this Chapter, the thermal decomposition of CeO_2 gel is assessed by monitoring the changes of coating weight (TGA) and chemistry (FTIR) of both the removed gases and the remaining coating. Moreover, the grain growth in bulk material and in nanocrystalline coatings deposited on substrates with essentially different oxidation resistance, such as Pt, Si and Ni, are analyzed *"in situ"* as a function of the annealing temperature up to 1173 K. The measurements allowed us to estimate how the rate of CeO_2 incorporation into growing native oxide affects the CeO_2 grain coarsening. As a result, the optimum conditions for the processing of coatings will be selected.

4.2. Thermal decomposition of CeO_2 gel

The weight changes of CeO_2 gel during the continuous heating of bulk specimens up to 1273 K at a rate of 5 K/min, are depicted in Fig. 4.1a. The plot of derivative of weight loss versus temperature (Fig. 4.1a, inset) revealed that the calcination curve exhibited three essential stages with different rates of weight loss. The highest evaporation rate was observed during the first stage below 450 K. In the second stage, three different ranges may be distinguished: 450-570 K, 570-650 K, and 650-750 K. The changes in weight loss rate suggest that different species were removed. At approximately 750 K, the thermal decomposition was completed with a total weight loss of 17.5 %, as compared to the sample weight after drying. A further heating up to 1273 K led to the sintering only.

The gravimetric analysis of the thermal decomposition of coatings deposited on Pt substrate is shown in Fig. 4.1b. As was found by a high-sensitivity microbalance, the coating weight after drying at 293 K for 20 h was between 15 and 220 $\mu g/cm^2$. After calcination, the same coatings weighed between 5 and 190 $\mu g/cm^2$. The line fitted to the experimental points is marked as "1". Line "2" in Fig. 4.1b shows the dependence between the coating weight after drying and after calcination, calculated from TGA analysis of bulk ceria. The thermal cycle during TGA analysis of the bulk CeO_2 was the same as that used during calcination of coatings. Both lines are located quite close to each other, especially for thicker coatings. Thus both methods can be used to estimate the necessary amount of sol-gel to be deposited for a required coating thickness.

The loss of weight of the sol-gel coatings during heating was caused by the evaporation of some coating components. To assess the evolution of chemical composition, IR spectroscopy analyses were performed on 200-250 nm thick CeO_2 coatings deposited on Pt substrate as well as on gases evolved from coating during annealing. Some exemplary IR reflectance spectra in the wave number range of 4000-500 cm^{-1} from coating after drying and annealing, are shown in Fig. 4.2a. After drying, the coating showed peaks at 3600 cm^{-1} and in the region of 1600-1650 cm^{-1} corresponding to the water of hydration. The addition of nonionic surfactant Triton X-100 produced a peak at 1050 cm^{-1}. The bands at 2320 cm^{-1} are attributed to CO_2 from the atmosphere. As proven below, the weak peak at about 725 cm^{-1} was produced by CeO_2. The spectrum after annealing at 573 K showed a marked decrease of water and surfactant peaks, suggesting removal of those components. After annealing at 873 K, only the peaks of CeO_2 and CO_2 remained. In order to prove the location of the CeO_2 peak, the powder specimens of a larger volume were prepared from CeO_2 annealed at 973 K. The spectrum obtained (Fig. 4.2b) gives the peak location at about 700-720 cm^{-1}. Fig. 4.2c shows a typical absorbance spectrum obtained from gas collected during annealing below 500 K, with clear peaks for water and CO_2.

The comparison of TGA and IR spectroscopy data does not distinguish the essential differences of the kinds of species removed at various annealing temperatures. The slightly higher weight loss below 450 K was caused probably by a higher intensity of water removal.

4.3. Evolution of CeO_2 microstructure during annealing

The direct imaging of the wet gel by TEM was not possible; therefore, to prepare thin foils, the coatings were first calcined at 573 K for 1 h and then stripped from the substrate. According to x-ray measurements presented below, this procedure did not cause a coarsening of CeO_2 particles. The TEM bright field image of coating after calcination is shown in Fig. 4.3. The selected area electron diffraction (SAD) pattern in Fig. 4.3a was composed of continuous rings for CeO_2 and indicated that the coating is characterized by random distribution of the grain orientations. Some additional rings were present in SAD pattern, which are marked by arrows and were formed by thin NiO film supporting the brittle CeO_2 coating during TEM examination. The spots for Ni were produced by an incompletely dissolved metallic substrate. The average size of CeO_2 grain, estimated from the TEM image, was approximately 5 nm.

The CeO_2 coatings with thicknesses below 50 nm were continuous and relatively uniform. On the contrary, the coatings thicker than 100-150 nm contained numerous microcracks. As seen in Fig. 4.3b, in the case of 200 nm thick coating, the network of microcracks was present on a whole area of thin foil. However, detailed observations revealed that the microcracks did not often penetrate through the total coating thickness and did not expose the substrate surface to the environment. Some amount of CeO_2 still remained in those places, providing protection.

The major microstructural change which accompanied the gel-ceramics conversion, as well as further densification of the ceramics, was a coarsening of CeO_2 grains. The AFM image of 50 nm thick coatings deposited on (100)Si shows the uniform grains with an average diameter of 20-25 nm. According to AFM roughness analysis (Fig. 4.4a), the coating uniformly covered the substrate. Although the area of the image contained some features with a height of up to 26.7 nm, the mean roughness was as low as 2.8 nm. The roughness parameters measured on the part of the image in Fig. 4.4a, limited by the frame, exhibited even smaller values. The comparison of vertical roughness and grain size on the planar surface, indicates that the initially spherical CeO_2 particles, after annealing, formed a coating with a flat outer surface. This finding is of importance for the continuous covering of the substrate during annealing by nanometre-thick coatings.

An example of the morphology of bulk ceramics after annealing at 1173 K for 50 h is shown in Fig. 4.4b. The fracture cross section revealed that material did not contain pores and had an average grain size of about 100 nm. After annealing at 2000 K for 5 h, the average grain size of CeO_2 was increased up to 50 μm, which is four orders of magnitude larger than the initial size after coating deposition (Fig. 4.4c). The powder prepared from this sample was later used as a standard for grain size determination by x-ray technique.

4.4. X-ray examination of grain size growth during annealing

The structural evolution of CeO_2 gel during annealing is affected by gel substrate interactions. For example, the existence of the solid-state epitaxy in nano-composite xerogel powders and in sol-gel coatings has been reported by Roy [1987] and Selvaray et al. [1992]. Therefore, to verify the role of the substrate, in addition to bulk CeO_2, the coatings deposited on various materials were examined.

The deposit after drying at room temperature for 20 h already displayed all the major reflections of crystalline CeO_2, which has a fluorite type structure (Fig. 4.5). The main change which accompanied the increase in the annealing temperature was the decrease of the diffraction line width. In situ x-ray analysis of the annealing behaviour of CeO_2 deposited on (100) face of Si single crystal is shown in Fig. 4.6. The purpose of using this substrate, which has a very flat and well-defined surface, and does not produce a thick oxide, was to reveal an epitaxial relationship between the substrate and the coating. In general, however, the changes of diffraction spectra for CeO_2 films on (100)Si were similar to those observed above for bulk CeO_2. Peak intensities were roughly in agreement with the JCPDS card, suggesting a random distribution of grain orientations. The diffraction peaks from the silicon oxide formed are not seen and are probably at the noise level of the diffraction pattern. Also, the annealing of CeO_2 deposited on the polycrystalline Pt substrate did not result in the formation of any evident texture and, similarly as for Si, the essential change in the x-ray pattern was a decrease of the diffraction line width.

According to the diffraction patterns in Fig. 4.7, the annealing of CeO_2 coating on the Ni substrate was accompanied by substrate oxidation. The peaks for NiO were clearly seen after heating to 973 K. At the same time, an increase in temperature caused the decrease of the width of the diffraction peaks for CeO_2. For the system studied, no mutual compounds between Ce, Ni and O were detected.

The x-ray diffraction spectra were analyzed to measure the evolution of CeO_2 grain size in the nanometre range. Assuming the absence of lattice strains, the mean grain size was calculated from diffraction line broadening according to Scherrer's equation [Klug and Alexander, 1974]. The sample after annealing at 2000 K for 0.5 h served as a standard. The values of diffraction peak broadening were determined by computer after correcting for background noise and fitting the Gaussian curve to the experimental points.

The values of grain size, calculated for the various substrates and temperatures are given in Fig. 4.8. It is seen that the initial grain size obtained from diffraction line broadening is the same as that observed directly with TEM (Fig. 4.3a). The calcination at 573 K did not change the grain size in both the bulk material and in the coatings. Minor changes were also detected below 680 K. However, annealing at higher temperatures resulted in rapid grain growth. Some differences between grain growth rates for individual samples were present. The largest coarsening of CeO_2 grains was detected in coatings deposited on the substrate with the highest oxidation resistance, namely Pt. Against this, the grain growth of CeO_2 deposited on a substrate forming relatively thick, protective oxide, such as Ni, was shifted about 100-150 K towards the higher temperatures.

According to the literature data, the grain growth in thin metallic foils is faster than that observed in bulk specimens of identical material [Kramer, 1992]. Thus, the evolution of grain size shown in Fig. 4.8 should be attributed to the coating-substrate interaction which results in the inhibition of grain growth. The occurrence of such an interaction has been proven by the process of texture formation during the crystallization of ceramics from a sol-gel derived amorphous phase [Roy, 1987; Selvaray et al., 1992]. The essential difference between the substrates used in this study was the oxidation resistance. As has been shown by SEM observations, the CeO_2 particles during annealing were incorporated into growing native oxide films, which prevented their coalescence. Prevention of the coarsening of CeO_2 is caused by separation of individual particles by NiO film and the complete lack of solubility of Ce in the NiO lattice [Moon and Bennett, 1989]. In regions where the coating had an excessive thickness, CeO_2 remained on the outer oxide surface, contributing in part to the sharp diffraction peaks for CeO_2 in Fig. 4.7, suggesting the large size of grains. At the same time, according to the microstructural observations, the size of CeO_2 particles incorporated into the oxide remained almost unchanged. It is obvious that the higher oxidation rate of the substrate leads to the faster incorporation of CeO_2 into native oxide. Therefore, the rate of the formation of native oxide affects the grain coarsening process in CeO_2 coatings.

4.5. Summary

The CeO_2 coatings after drying at room temperature are composed of crystallites of the size of 5 nm. On all the substrates used, including Pt, (100)Si, and Ni, the coatings are characterized by the random distribution of grain orientations. The thermal decomposition of CeO_2 gel during annealing is accompanied by processes of ceramics densification and grain growth, without the formation of any evident crystallographic texture. For bulk CeO_2 specimens, the critical temperature of rapid grain coarsening is found to be about 680 K. In the case of coatings, this temperature depends on the substrate nature and mainly its oxidation resistance. In general, the higher the oxidation rate of the substrate, the higher the temperature of rapid grain growth. In the case of 100-200 nm thick coatings deposited on Ni, this temperature is about 100-150 K higher than that found for Pt substrate.

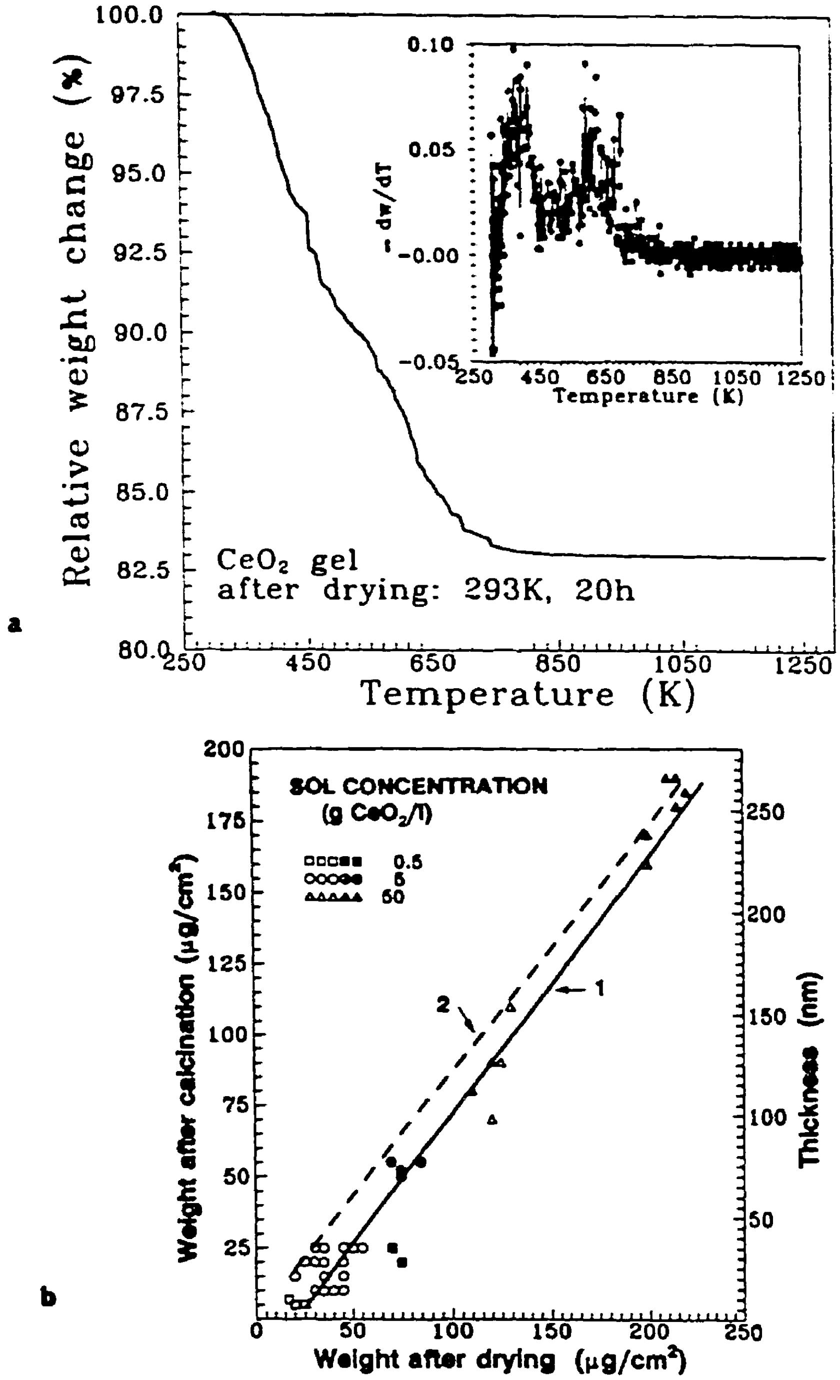

Fig. 4.1. Gravimetric analysis of thermal decomposition of CeO_2 gel: (a) TGA results of weight loss for bulk CeO_2 dried at 293 K for 20 h during continuous heating to 1273 K at a rate of 5 deg/min in argon atmosphere; plot of derivative dw/dT (w - relative weight loss, T - temperature) is shown in the inset; (b) correlation between weight after drying (293 K, 20 h) and after calcination (573 K, 1 h) for coatings with different thicknesses deposited on Pt substrates; line 1 - obtained from fitting to measurements on coatings, line 2 - calculated from TGA analysis of bulk specimens; full symbols indicate two-fold dipping; thickness estimated for coatings after calcination.

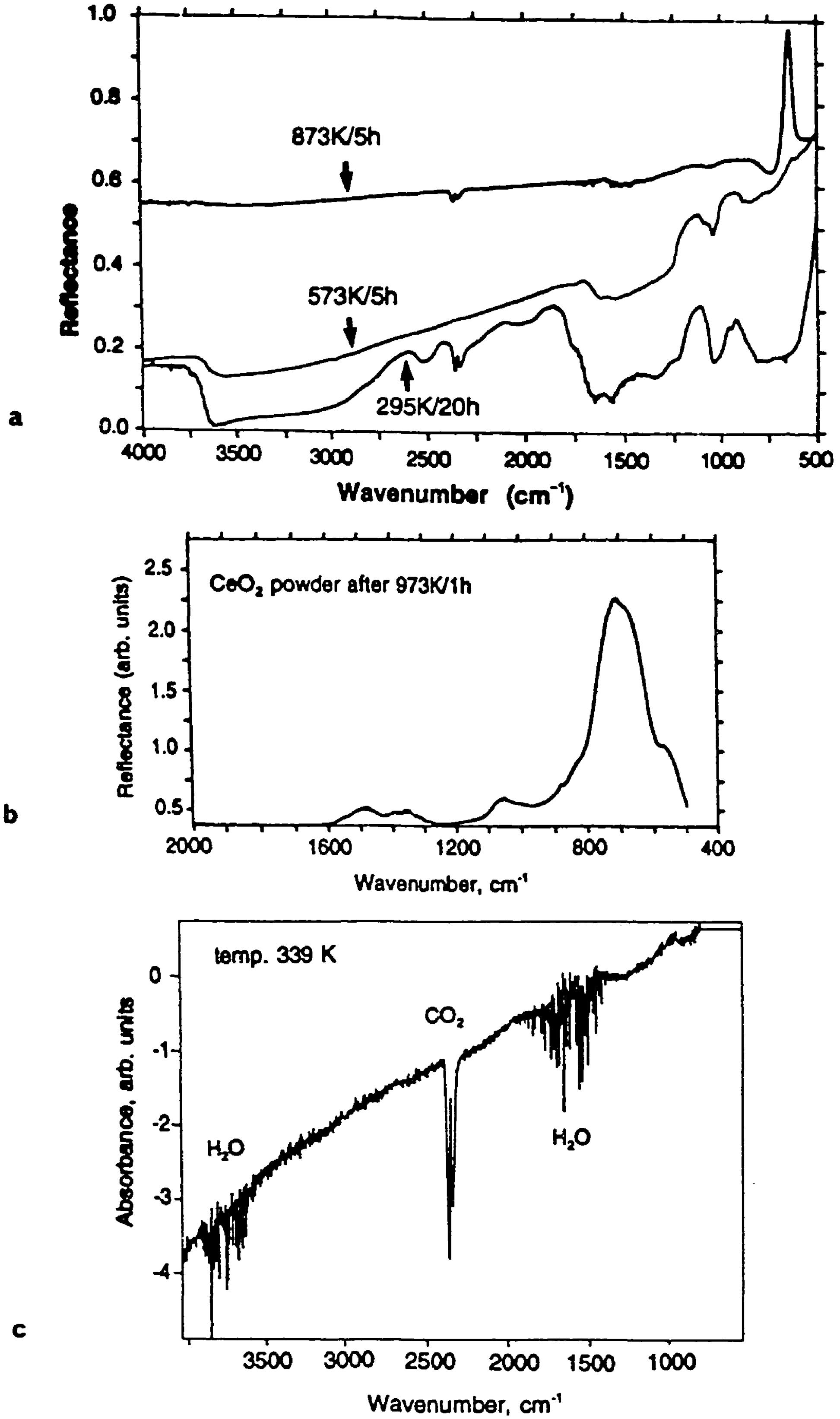

Fig. 4.2. IR spectroscopy analysis of thermal decomposition of CeO$_2$ gel: (a) IR reflectance spectra of CeO$_2$ deposited on Pt substrate after annealing at temperatures indicated; (b) IR reflectance spectrum of CeO$_2$ powder specimen after annealing at 973 K for 1 h; (c) IR absorbance spectrum of gas evolved during coating annealing at 339 K.

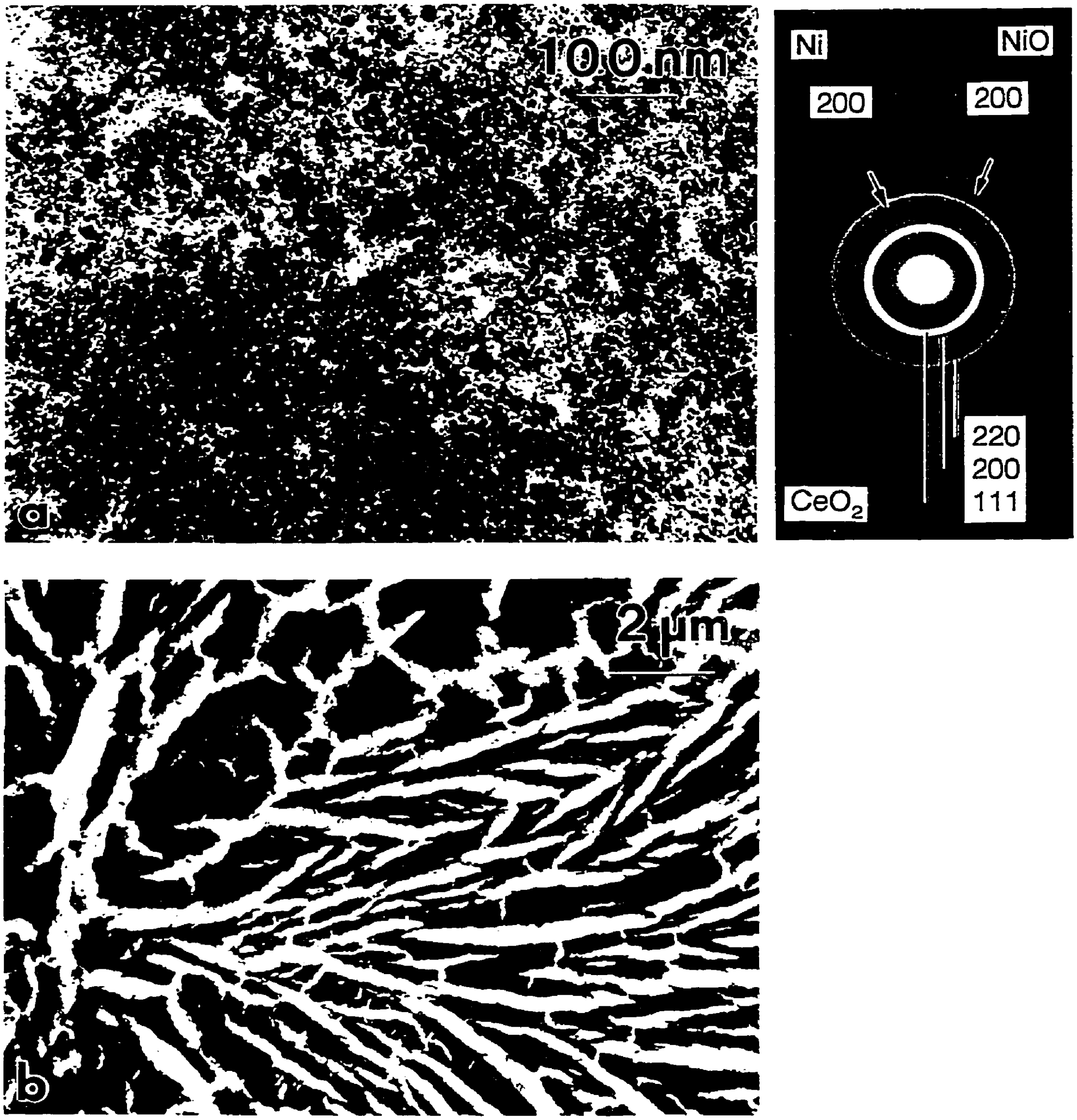

Fig. 4.3. TEM bright field images and SAD pattern of CeO$_2$ coatings stripped from Ni substrate after calcination at 573 K for 1 h (traces of Ni are from the substrate, not completely dissolved during coating stripping): (a) coating thickness of about 20 nm; (b) coating thickness of about 150-200 nm.

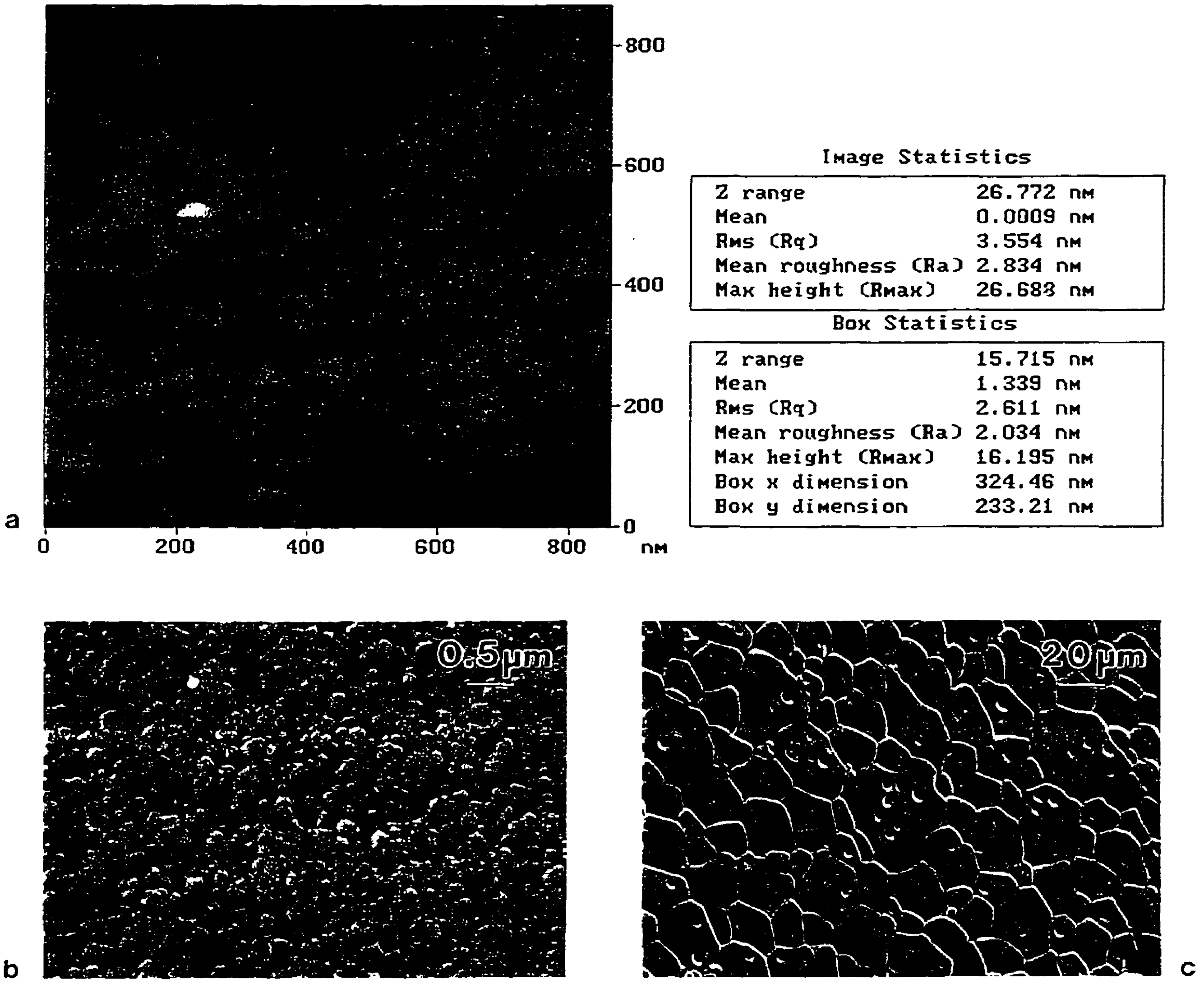

Image Statistics

Z range	26.772 nm
Mean	0.0009 nm
Rms (Rq)	3.554 nm
Mean roughness (Ra)	2.834 nm
Max height (Rmax)	26.683 nm

Box Statistics

Z range	15.715 nm
Mean	1.339 nm
Rms (Rq)	2.611 nm
Mean roughness (Ra)	2.034 nm
Max height (Rmax)	16.195 nm
Box x dimension	324.46 nm
Box y dimension	233.21 nm

Fig. 4.4. The morphology of CeO_2 after annealing: (a) 973 K, 1h - AFM surface morphology of 50 nm thick coating on (100)Si substrate; (b) 1173 K, 50 h - SEM fracture cross section of bulk specimen; (c) 2000 K for 5 h - SEM morphology of outer surface of bulk specimen.

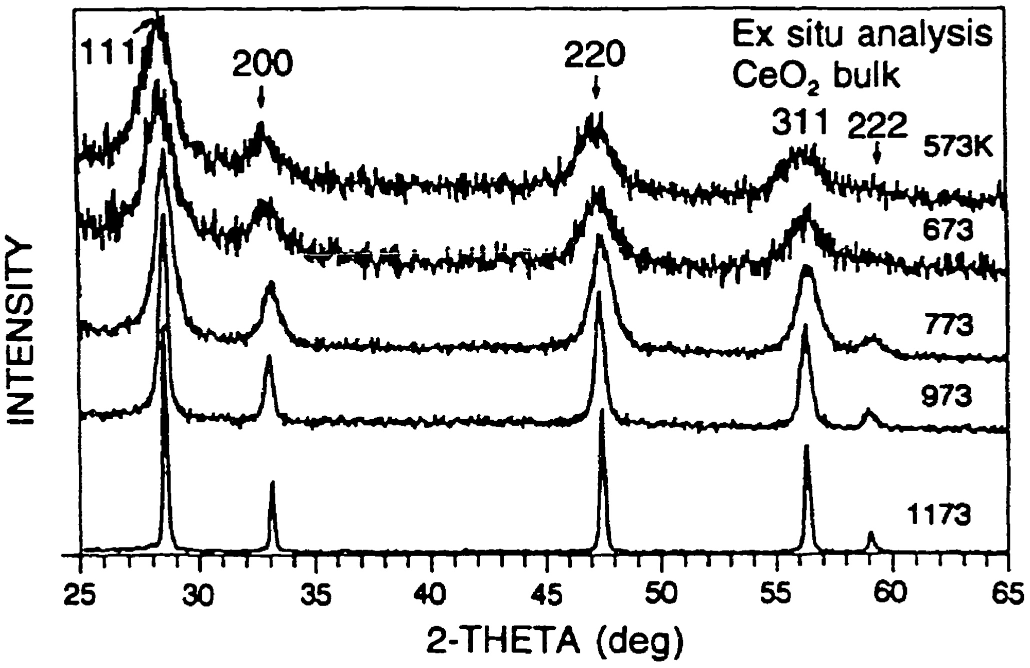

Fig. 4.5. X-ray diffraction patterns of bulk CeO_2 samples, annealed at temperatures indicated. Analysis "ex situ" at room temperature after cooling.

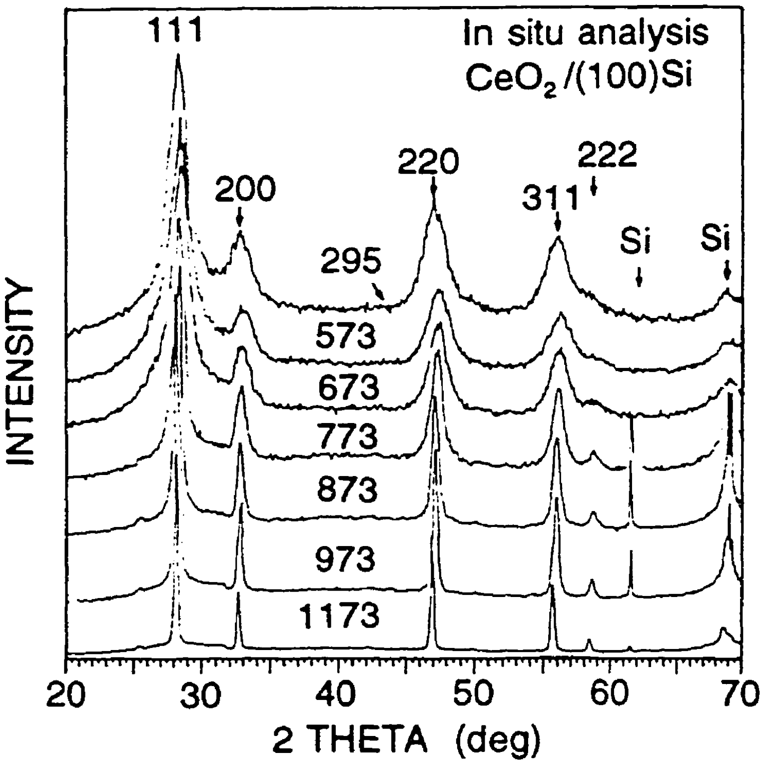

Fig. 4.6. X-ray diffraction patterns of 100-200 nm thick CeO_2 coatings deposited on (100)Si substrate and annealed at temperatures indicated. Analysis "in situ" at reaction temperature.

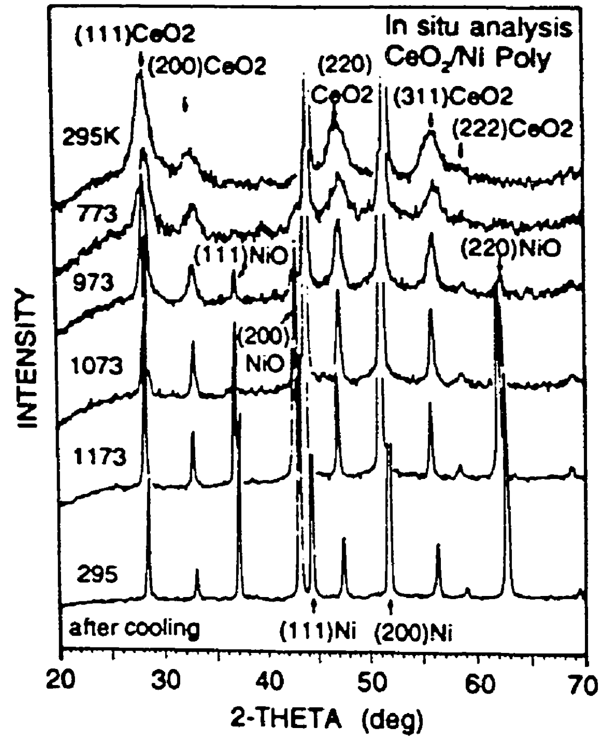

Fig. 4.7. X-ray diffraction patterns of 100-200 nm thick CeO_2 coatings deposited on polycrystalline Ni substrate and annealed at temperatures indicated. Analysis "in situ" at reaction temperature.

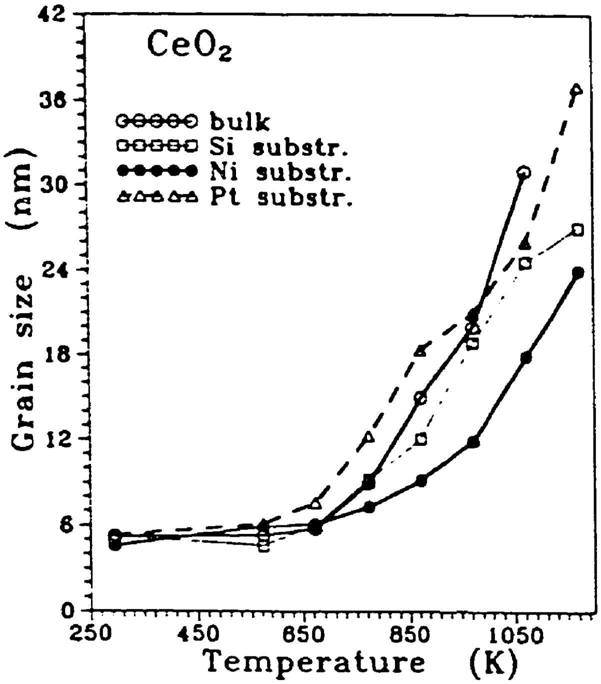

Fig. 4.8. The growth of grain size of bulk CeO_2 and of 100-200 nm thick coatings deposited on Pt, (100)Si and Ni substrates during annealing for 0.5 h at temperatures indicated. Grain size calculated from x-ray diffraction measurements at room temperature.

CHAPTER 5. EARLY-STAGE OXIDATION KINETICS OF POLY-CRYSTALLINE Ni COATED WITH CeO_2 SOL-GEL

5.1. Introduction

Since NiO films have a relatively good adherence to the Ni substrate, the major influence of the reactive element addition is expressed by the decreasing Ni oxidation rate. Thus, the change of oxidation kinetics and the reduction in oxide thickness are the main indicators of the effectiveness of the reactive element coatings deposited on Ni. In this Chapter, detailed measurements of the oxidation kinetics during the early-stages of NiO formation on pure and on CeO_2 coated polycrystalline Ni will be conducted. In order to identify a number of factors which may influence the effectiveness of CeO_2 coatings, the polycrystalline Ni substrates will be additionally modified both before and after coating deposition.

5.2. Effect of substrate surface finishing and coating thickness

The surface of Ni specimens was finished by two major techniques: mechanical and chemical polishing. The purpose of chemical polishing was to remove the thin film of oxide formed during vacuum-annealing and to reveal a clean surface with the arrangement of atoms, specific for the crystallographic orientation of each Ni grain. Conversely, to suppress the influence of crystallographic orientation of the individual Ni grains, the surface of Ni was mechanically polished lightly using a 1 μm diamond paste. This treatment produced a uniformly deformed metallic film on the Ni surface. Subsequent exposure of such surfaces to oxygen resulted in different oxidation rates. Oxide on the mechanically polished surface grew much faster than that formed after chemical polishing. After coating with CeO_2 sol, despite the reduction in oxidation rates, significant differences still existed (Figs. 5.1a and 5.1b).

The coating is the only reservoir of the reactive element on the substrate surface. Thus, according to the conventional approach, a greater coating thickness should lengthen its lifetime. However, the experimental data indicates that this is not the case for CeO_2 sol-gel coatings. As seen in Figs. 5.1a and 5.1b, a relatively small amount of the reactive element is required to significantly suppress Ni oxidation. This amount is of 5-10 μg CeO_2/cm^2, which corresponds to a coating thickness of 7-14 nm. The thicker coatings were less effective in oxidation reduction of both the chemically and mechanically polished Ni.

5.3. Effect of substrate preoxidation before coating deposition

A typical problem in the industrial application of sol-gel coatings is the uniform coverage of surfaces with complex geometry and large size. Therefore, to improve the surface wetting, the coatings are often deposited onto preformed thin oxide films. The influence of 54 and 124 nm NiO films formed at 673 K on chemically and mechanically polished substrates, respectively, is shown in Figs. 5.2a and 5.2b. Here the kinetic data are represented by the parabolic form, as a square of oxygen uptake versus time. Some runs in Fig. 5.2 were carried out in duplicate to determine the reproducibility of measurements. A difference of the order of a few percent supports the excellent reproducibility of the oxygen uptake data. The major effect of preoxidation, which is possible to estimate from Fig. 5.2, is the reduction of the oxygen uptake after longer oxidation times. It is expected, however, that preformed NiO will exert more significant influence during very initial periods of reaction.

The oxidation kinetics during the first 25 min of reaction are shown in Fig. 5.3. It is clear that CeO_2 particles affected the nucleation of NiO and that this effect depended on substrate preoxidation. To facilitate analysis of the oxidation kinetics during the initial periods of exposure, the instantaneous parabolic rate constants k_{pi} were calculated from oxidation data. The value of k_{pi} was calculated as $2w \cdot dw/dt$, where w is oxygen uptake and t is time of oxidation. The calculations were performed numerically for time intervals dt = 1 min. Plots of k_{pi} versus time for chemically polished Ni oxidized at 973 K are shown in Fig. 5.4. It is clear that preoxidation decreased the oxidation rate of uncoated Ni. For Ni with CeO_2 coatings without preoxidation, the values of k_{pi} after reaching by a specimen temperature of 973 K were very high, although still lower than for uncoated Ni. The coated Ni, in fact, oxidized at higher rate than the uncoated one during heating up to 973 K (Fig. 5.3). The largest decrease of k_{pi} from its initial maximum of 2.7×10^{-13} $g^2cm^{-4}s^{-1}$ was observed during the first 20 min of oxidation. Further exposure, especially for times longer than 1 h, was accompanied by relatively small changes in k_{pi}. The time dependence of k_{pi} for preoxidized coated Ni has the same character as for unpreoxidized coated Ni. However, the initial maximum value of k_{pi}, i.e 3×10^{-14} $g^2cm^{-4}s^{-1}$, is one order of magnitude lower than that obtained for coated Ni which had not been preoxidized. Hence, the plots of k_{pi} show that a substantial decrease of the oxidation rate due to presence of the CeO_2 coating takes place during the initial stages of oxidation.

5.4. Effect of oxidation temperature

In order to examine the effect of oxidation temperature on the inhibition of nickel oxidation by CeO_2 sol coatings, experiments were carried out in the temperature range from 873 to 1073 K. Results obtained for both mechanically and chemically polished substrates are shown in Figs 5.5a and 5.5b. At temperatures 973 and 1073 K, the reduction in oxidation rate compared to the uncoated samples was similar. Surprisingly, at 873 K, the reduction in oxidation rate was smaller and, in this case, the oxidation product was characterized by discrete plates of CeO_2 which remained on the sample surface. To avoid this, the coating should be quickly incorporated into a native oxide by oxidation at a higher temperature. An example of such a two-fold experiment is shown by the marked curve in Fig. 5.5a. First, the coated Ni was exposed to oxygen at 973 K for 40 min with a measured oxygen uptake of 7.32 $\mu g/cm^2$, which corresponds to about 50 nm of NiO. Subsequent oxidation at 873 K for 4 h resulted in an oxygen uptake as low as 1.9 $\mu g/cm^2$.

At all temperatures in the range 873-1073 K oxidation of both uncoated and CeO_2 coated Ni followed a near parabolic relation, as is illustrated for the reaction at 973 K by the plots in Fig.5.2 approaching straight lines. However, before the onset of parabolic kinetics, the reaction kinetics exhibited a transient stage. Oxygen uptakes during this transient period are shown in Table 5.1.

Oxidation kinetic data are summarized as Arrhenius plots in Fig. 5.6, which includes data from additional runs at 1173 K on coated Ni. Since the oxide formed during preoxidation at 673 K for 2 h reached from 10 up to 100% oxide thickness formed during subsequent reoxidation, the parabolic rate constants were calculated from weight gain data after 4 h as average values by applying the following equation [Harris et al., 1990]:

TABLE 5.1. Oxygen uptake before onset of the parabolic kinetics for preoxidized uncoated and CeO_2-coated Ni ($\mu g/cm^2$).

Oxidation temperature	Chemically polished		Mechanically polished	
	uncoated	coated	uncoated	coated
873 K	8	5	27	30
973 K	17	6	43	33
1073 K	23	14	80	43

$$k_p = (2w_o + \delta w)\ \delta w/\delta t \qquad (5.1)$$

where w_o is the initial value of the oxygen uptake obtained during preoxidation, δw and δt are changes of the oxygen uptake and time, respectively, during reoxidation. Equation 5.1 was derived assuming that average oxygen uptake is the mean of the values at the start and finish of re-oxidation.

The activation energies evaluated from the slopes of the least squares linear fits are also given in Fig. 5.6. For comparison, the values of k_p for the lattice diffusion of Ni in NiO are included, which were calculated utilizing the value of the tracer diffusion coefficient of Ni in NiO [Atkinson and Taylor, 1979] and the dependence of the k_p on oxygen pressure (Chapter 2).

5.5. Effect of CeO_2 particle size in coating

As shown in Chapter 4, the CeO_2 sol-gel coatings deposited on Ni were polycrystalline with a random distribution of grain orientations. In such a microstructure, the most evident component which can be changed by thermal treatment is the size of CeO_2 particles. In order to assess the effect of this parameter on subsequent coating performance, the CeO_2 grain size was modified by the annealing of coated Ni prior to oxidation under a vacuum of 10^{-7} torr. The oxidation kinetics of uncoated and coated substrates are shown in Fig. 5.7a. Thus, the vacuum annealing increased the oxidation rate to values even larger than that measured for uncoated Ni. In Fig. 5.7b the oxygen uptakes after 4 h exposure were plotted as a function of CeO_2 particle size, evaluated from x-ray measurement (Chapter 4). It is clear that the CeO_2 particles with size of 5 nm substantially decreased the oxidation rate. However, in the case of particles larger than about 10 nm, the coating did not protect the substrate and caused a higher oxygen uptake than that measured for uncoated Ni. The last finding is of importance for the analysis of the mechanism of oxidation inhibition by CeO_2 coatings.

5.6. Summary

After conversion to the form of ceramic coating, superficially applied CeO_2 sol-gel significantly improves the oxidation resistance of Ni at temperatures in the range of 873-1073 K. The extent of the effect depends on coating thickness, size of CeO_2 particles, substrate surface finishing, and substrate preoxidation before coating deposition. For both techniques of substrate finishing, mechanical and chemical polishing, the thinner coatings were more effective. The size of CeO_2 particles in the coating is a decisive factor affecting their protective properties. While coatings containing CeO_2 particles with a size of 5 nm reduced the Ni oxidation rate, the coatings with particles larger than 10 nm were ineffective, and even caused the opposite effect.

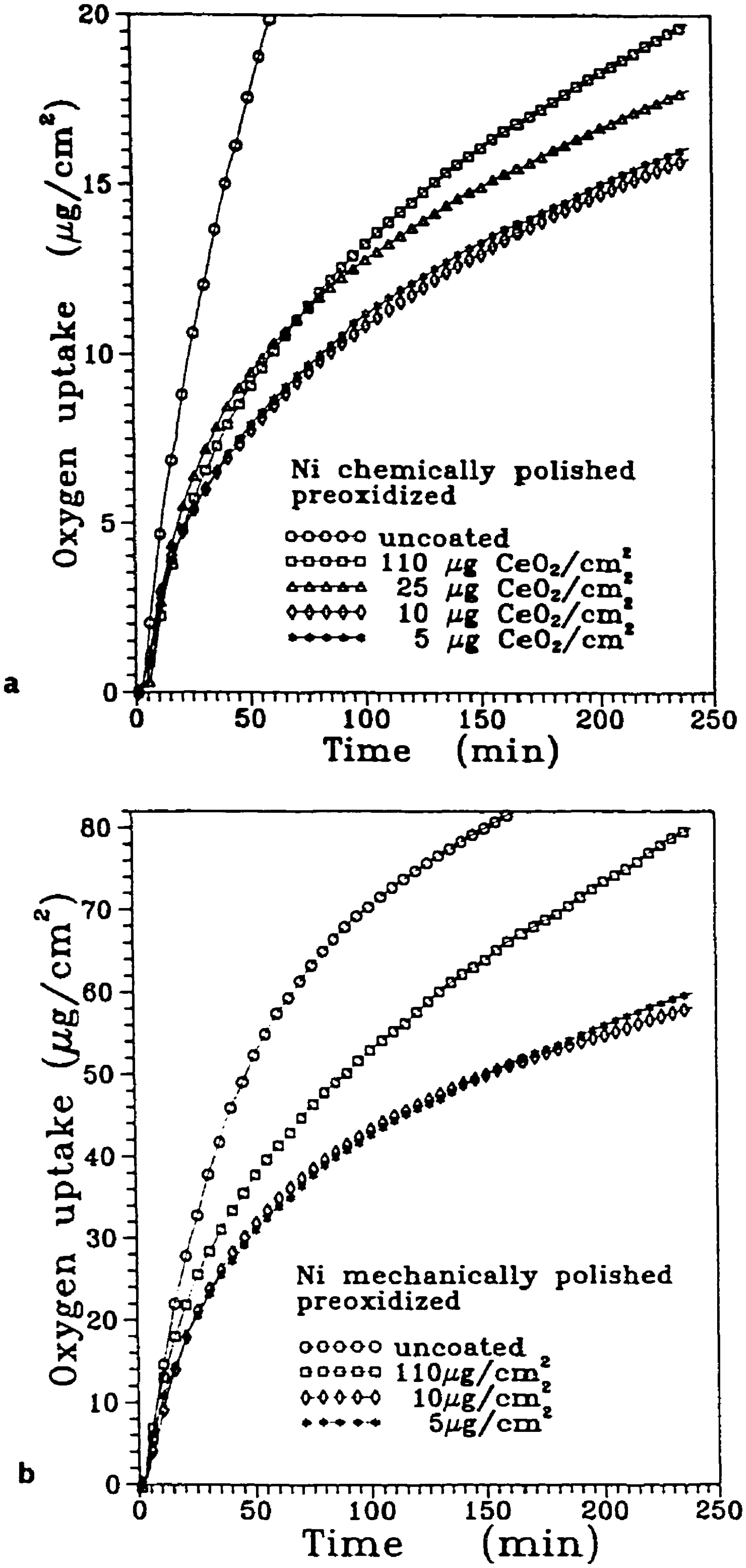

Fig. 5.1. Effect of CeO_2 coating thickness on oxidation kinetics at 973 K of (a) chemically polished and (b) mechanically polished nickel. Total oxygen uptakes after 4 h for uncoated substrates are 112.4 and 43.8 μg/cm² for mechanical and chemical polishing, respectively.

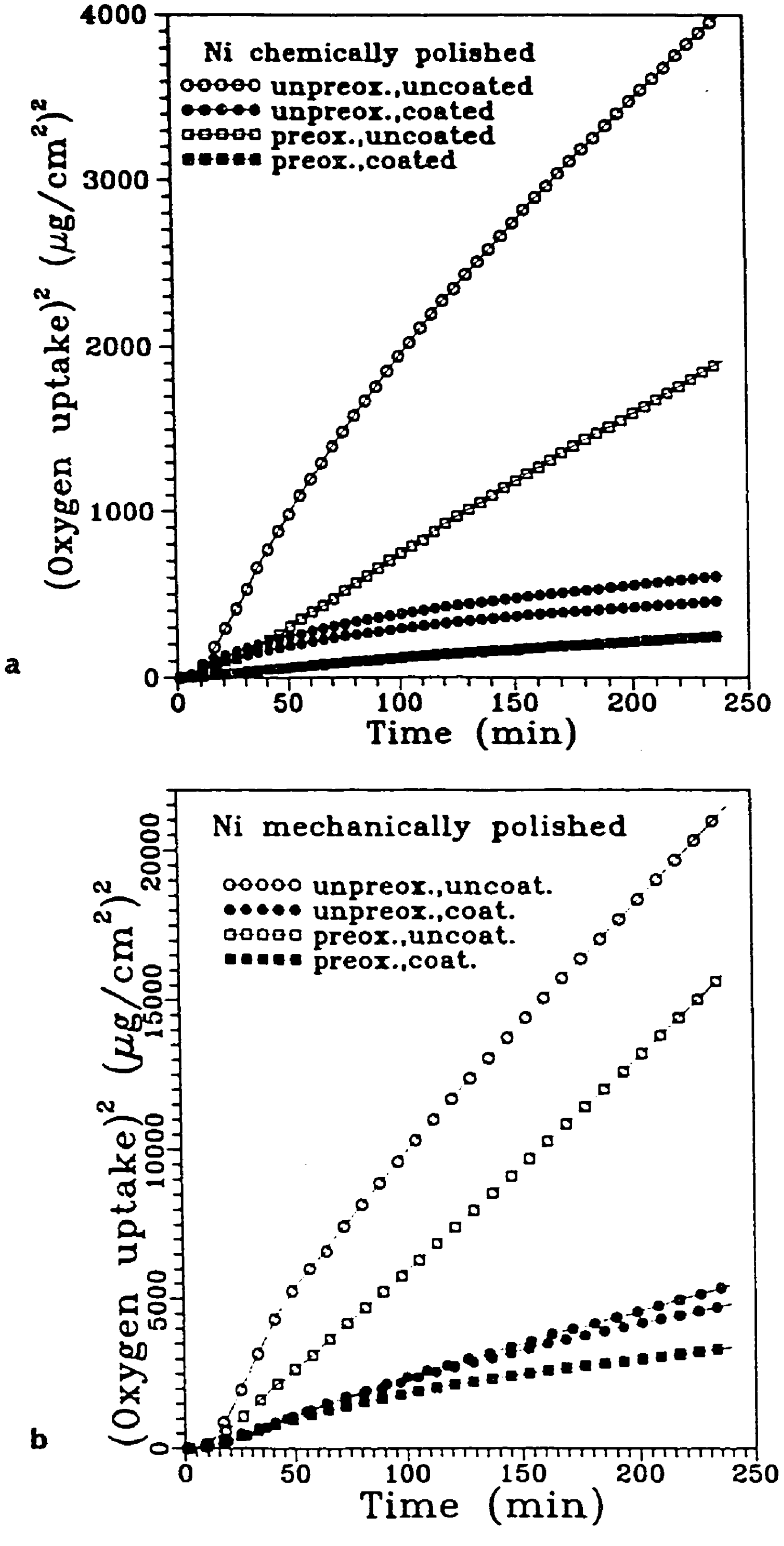

Fig. 5.2. Effect of preoxidation and CeO_2 coatings with thickness of 14 nm on the oxidation kinetics of (a) chemically and (b) mechanically polished nickel.

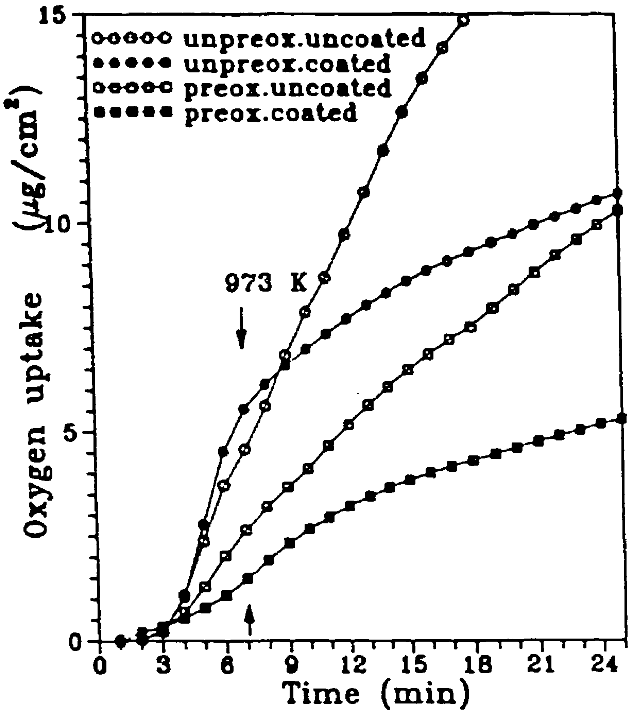

Fig. 5.3. Oxidation kinetics for chemically polished nickel during initial periods of exposure. Heating to oxidation temperature at a rate of 100 K/min in oxygen. Arrows show time when the temperature of 973 K was attained. Coating thickness of 14 nm.

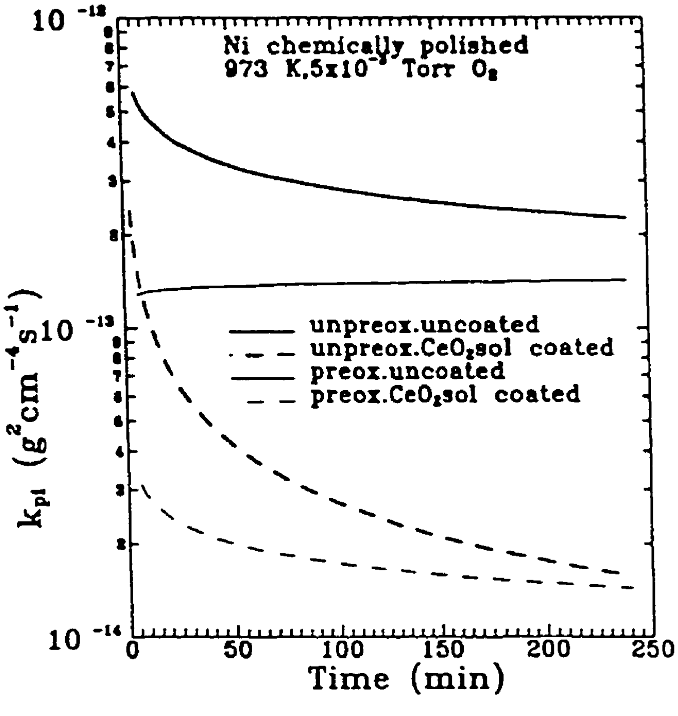

Fig. 5.4. Instantaneous parabolic rate constants 2*w* · *dw/dt* (*w* - weight gain, *t* - oxidation time) as a function of time for uncoated and CeO$_2$ coated nickel (14 nm thick coatings). Plots start when the oxidation temperature was attained.

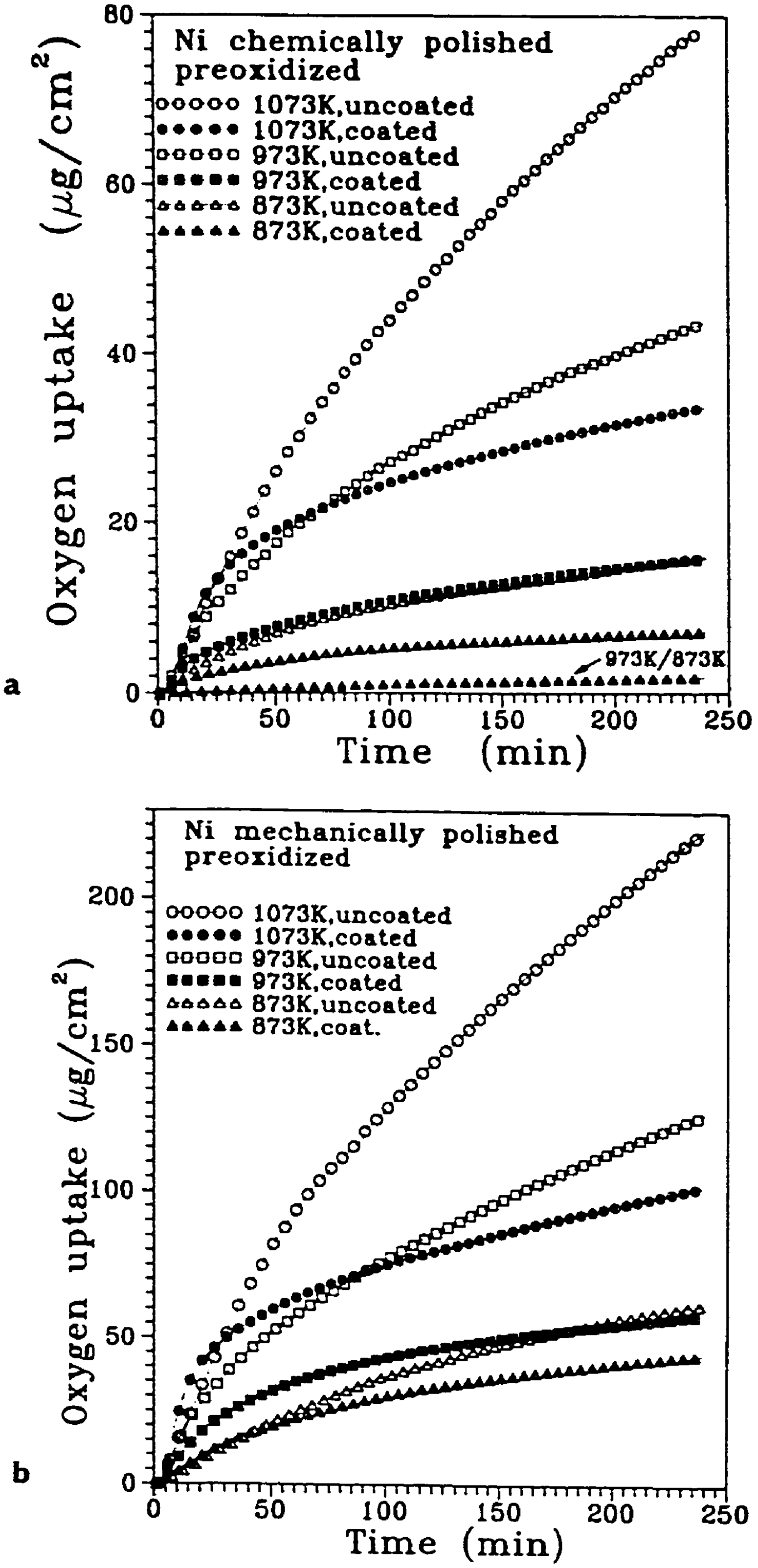

Fig. 5.5. Effect of temperature and CeO_2 coatings with thickness of 14 nm on the oxidation kinetics of (a) chemically, and (b) mechanically polished nickel.

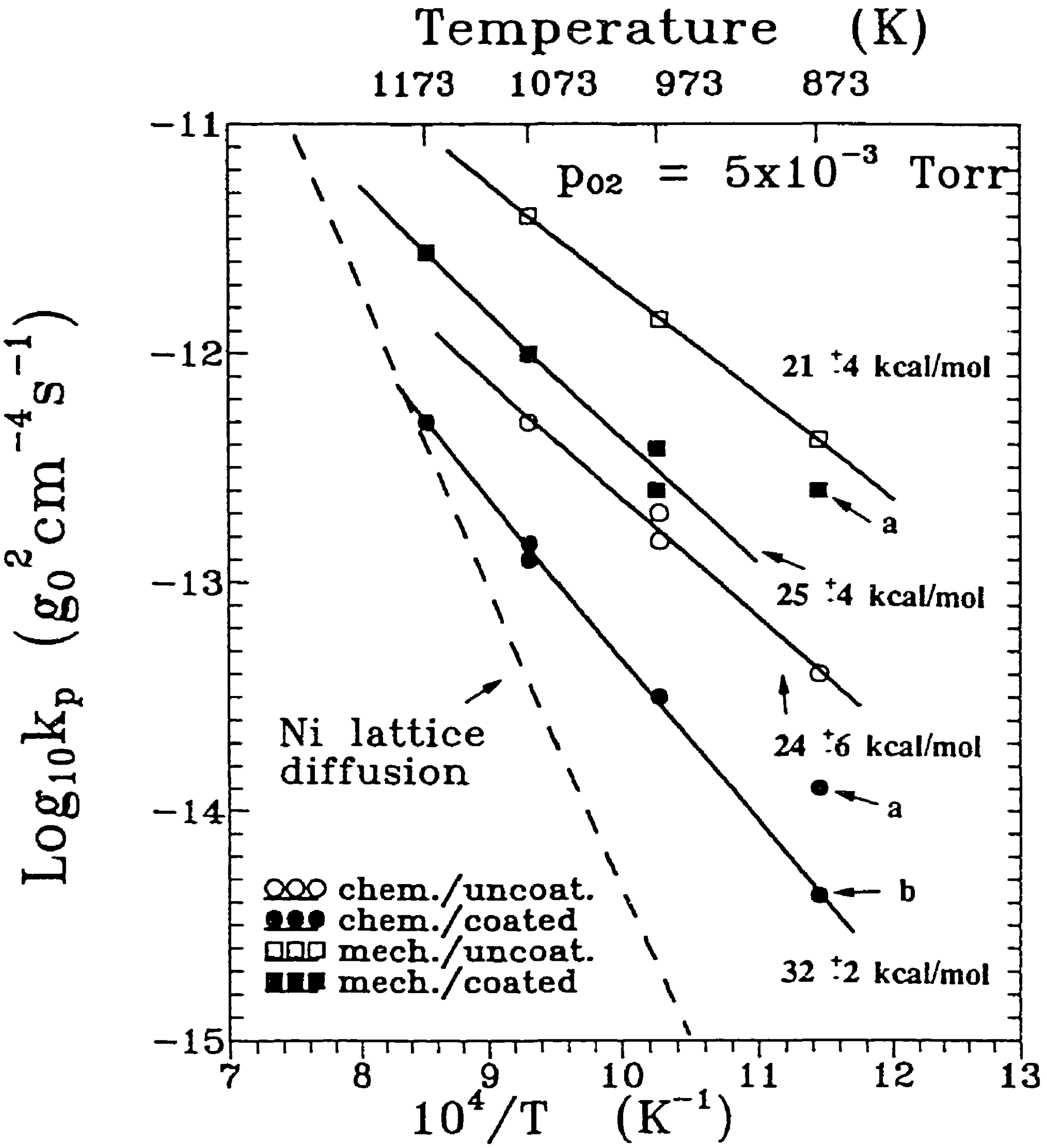

Fig. 5.6. Summary of oxidation kinetics data of chemically and mechanically polished uncoated and CeO_2 treated nickel as a function of temperature. Data points indicated by the arrows are: (a) data omitted in the least squares linear fits because after oxidation at this temperature discrete plates of coating remained on the specimen surface; (b) after additional pre-oxidation of the coated samples at 973 K for 40 min.

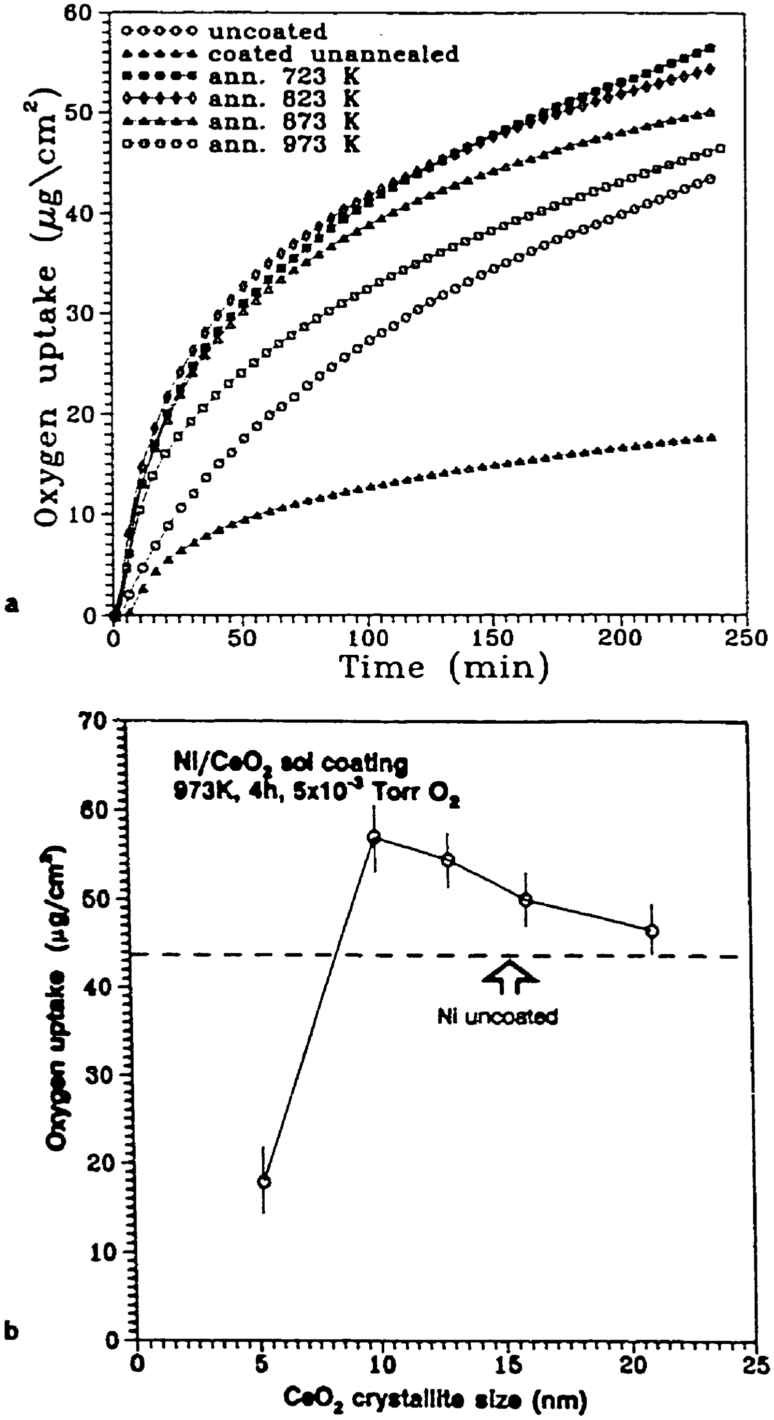

Fig. 5.7. (a) Oxidation kinetics at 973 K of nickel coated with 14 nm CeO_2, without and after vacuum annealing at temperatures in the range of 723-923 K for 5 h prior to the exposure to oxygen. (b) Oxygen uptake after 4 h exposure according to Fig. 5.7a plotted as a function of CeO_2 crystallite size in vacuum annealed coatings. Crystallite size measured by x-ray diffraction line broadening.

CHAPTER 6. MICROSTRUCTURAL CHARACTERIZATION OF THIN OXIDE FILMS FORMED ON Ni COATED WITH CeO_2 SOL-GEL

6.1. Introduction

The protective properties of oxide films formed on metals at high temperatures depend on the transport of reactants through the film and its structure. Thus the transport properties and structure of the oxide are inter-related. While in pure NiO this relationship is relatively straightforward, in Ce-doped NiO it is extremely complicated. Complex factors include a multilayered structure, dislocations, grain boundaries, interfaces, and segregation of the reactive element. Therefore, understanding the transport properties of the oxides requires their detailed microstructural characterization. In this Chapter, the oxide films with growth kinetics tested previously, will be characterized in terms of their microstructure and microchemistry.

6.2. Analysis of oxide growth surfaces

6.2.1. *Factors affecting oxide surface morphology*

The surface morphology of CeO_2 coatings after calcination at 573 K is shown in Fig. 6.1a,b. Coatings with a weight of 5-10 $\mu g/cm^2$ uniformly covered the substrate surface (Fig. 6.1a). Deposits with a higher weight were nonuniform with thicker regions having a tendency to crack during calcination. In coatings of about 100 $\mu g/cm^2$ a network of microcracks was present on the whole area of the specimen (Fig. 6.1b). During the very initial stages of exposure to oxygen (about 3 min), small grains of NiO nucleate on the coating surface (Fig. 6.1c). Longer exposure resulted in the increase in the number and size of individual NiO grains; however, after approximately 40 min, these changes were relatively small, suggesting that the subsequent growth process took place mainly under the coating.

The beneficial effect of thin coatings, found by kinetic measurements in Chapter 5, was supported by SEM observations of specimen surfaces after 4 h oxidation (Fig. 6.2). Thin coatings were incorporated into the growing NiO film (Fig. 6.2a), whereas the thicker CeO_2 layers looked flake-like and tended to spall from the substrate surface (Figs. 6.2b and 6.2.c). Similar surface morphologies were observed after the oxidation of mechanically polished Ni. Also flakes of CeO_2 remained on the surface while NiO was formed beneath the coating (Fig. 6.2d).

Pure NiO grown on polycrystalline substrates with surfaces finished by mechanical polishing exhibited faceted morphology, with pyramidal grains limited by certain types of crystallographic planes (Fig. 6.3a). When the atomic structure of the Ni surface was revealed by chemical polishing, NiO growth was highly anisotropic (Fig. 6.3b). Although differences in the thicknesses and the morphologies of oxides grown on individual Ni grains were quite substantial, in general, the oxide surfaces exhibited a similar crystallographic and faceted appearance. The morphology of NiO modified with CeO_2 was dependent on the method of substrate surface finishing before coating. The CeO_2 coatings deposited onto mechanically polished substrates developed an oxide which was uniform in thickness. An additional feature of this oxide was a tendency to form large conglomerates, each composed of numerous fine oxide grains (Fig. 6.3c). However, a different morphology was observed in the oxide grown on chemically polished substrates coated with CeO_2 particles (Fig. 6.3.d). In this case, very small NiO grains which were spherical in shape uniformly covered the majority of Ni grains. We believe that such a surface was formed during the very initial stages of growth as a result of the nucleation of small NiO grains on nano-sized CeO_2 dispersions. It is interesting to note that this morphology did not change significantly with oxidation time.

6.2.2. *AFM measurement of surface roughness evolution during oxide growth*

In addition to the differences in the morphological features described above, there were also essential differences in the surface roughness of NiO films and in the kinetics of roughening during oxide thickening. In this Section, the AFM technique is used to analyze the evolution of surface morphology during the growth of thin NiO films at high temperatures. Typical AFM images of pure and CeO_2 modified NiO films are shown in Fig. 6.4. On the basis of preliminary measurements, the oxidation parameters were adjusted to produce oxide films with thicknesses in the range of 100-950 nm for all the substrates. The quantitative description of the oxide/gas interface using roughness parameters was applied to verify the relationship between the evolution of surface topography and the mechanism of oxide growth analyzed in Chapter 10.

Two parameters were selected to characterize the oxide surface: standard deviation *rms* and maximum height R_p. The value of *rms* was calculated according to the formula [Bennett and Mattsson, 1989]: $rms = [\Sigma\ (Z_i - Z_{ave})^2 /N]^{1/2}$; where Z_{ave} is the average of the height values within the given area, Z_i is the current height value, and N is a number of 262144 points analyzed for each image. This value was not corrected for tilt in the plane of the data. R_p was calculated as the difference in height between the highest and lowest points on the surface relative to the mean plane, which is defined as a flat plane about which the image data has a minimum variance [AFM operating manual, 1993]. An example of the cross-sectional profiles of of pure NiO and NiO modified with CeO_2 are shown in Figs. 6.5a and 6.5b. The *rms* and R_p values were averaged for at least five regions with a size of 12.5x12.5 μm. The results of *rms* plotted as a function of film thickness and oxidation temperature are shown in Fig. 6.6. In these plots, experimental points exhibit two kinds of behaviour. For all oxides formed on pure substrates, the *rms* values substantially increased during oxide growth. The same tendency was observed for CeO_2 coated mechanically polished Ni (Fig. 6.6a). Conversely, the *rms* of the oxide formed after coating with CeO_2 particles of chemically polished Ni, only slightly increased for oxide thicknesses studied up to 950 nm (Fig. 6.6b).

Fig. 6.7 shows the evolution of the second roughness parameter, R_p, which characterizes the presence of growth features with excessive height. To plot the changes on a two-dimensional graph, the R_p values were averaged over oxidation temperatures of 873-1073 K. Although the R_p values were markedly larger than *rms*, the tendency of their changes during oxide growth was very similar to that observed for *rms*. While R_p

significantly increased during oxide growth for pure Ni substrates finished using both polishing techniques and for CeO_2 coated mechanically polished Ni, R_p exhibited only a small increase over the same range of oxide thicknesses for CeO_2 coated chemically polished Ni.

An important factor characterizing the surface of thin oxide film is the ratio of the roughness parameters to the film thickness. The values of roughness/thickness ratio, calculated for both *rms* and R_a , are plotted in Fig. 6.8 as a function of the oxide thickness. To show the results on a two-dimensional plot, as above for the R_p graph, the roughness data were averaged over the temperature range of 873-1073 K. It is seen that for oxides grown on all the substrates, *rms* was initially close to 0.2 of the average film thickness estimated from the oxygen uptake. The influence of substrate surface finish and CeO_2 coating was seen during further growth. While for oxides exhibiting a large increase of surface roughness, the *rms*/thickness ratio only slightly decreased up to a thickness of 950 nm, for oxides with a stable roughness, this ratio decreased to 0.07. At the same time, individual growth features were present on the surfaces of all the oxides with a thickness of 100 nm for which the height exceeded three times the average oxide thickness. This finding is represented by the R_p/thickness plot in Fig. 6.8. Although a marked reduction in the R_p/thickness ratio with increasing oxide thickness occurred, for 950 nm thick oxides it was still of the same order of magnitude as the oxide thickness. For substrates of chemically polished Ni coated with CeO_2 the topography of 950 nm thick oxides was quite uniform and the R_p/thickness ratio was about 0.3.

6.3. Oxide depth composition

During oxidation the reactive element is redistributed within the oxide film. To find the depth composition of the oxide, two techniques such as RBS and AES were used. Essentially different surface area of oxides from which the information is collected by RBS and AES allowed us the characterization of oxides having very non-uniform surface morphology. The depth-composition profiles were subsequently compared with the description of surface morphology.

Before oxidation, the sol-gel coatings deposited onto both chemically and mechanically polished nickel covered the substrate uniformly to a thickness of 14 nm, as determined by gravimetric measurements. As can be seen from RBS analysis (Fig. 6.9a), the substrate surface finish prior to the coating deposition, was a critical factor in the Ce distribution after 4 h oxidation at 973 K. The RBS spectra of oxide formed after coating chemically polished surfaces, exhibited a distinct Ce peak. For the case of oxide grown on a mechanically polished surface, the reduced height of the nickel peak indicated that a thicker, more uniform oxide had formed, and the absence of a clear Ce peak indicated that cerium was not present near the surface in large concentrations. The Ce concentration profiles derived from the above spectra (Fig. 6.9b) indicate that in oxide grown on a chemically polished surface to a thickness of 165 nm (as calculated from oxygen uptake data), the Ce maximum concentration is approximately 15 nm beneath the gas/oxide interface, i.e. one to two detector resolutions below the outer surface of the oxide. The Ce profile derived after tilting the sample through 45° with respect to the analysis beam was within the experimental uncertainty of the spectrum for a sample tilt of zero degrees; the apparent slight shift to a greater depth is probably due to the surface roughness of about 30 nm.

Fig. 6.9b shows that the RBS analysis did not detect much Ce at all in oxide grown for 4 h on mechanically polished, coated nickel. In order to find the reason for this behaviour, additional samples were prepared for shorter oxidation times. The AES spectrum in Fig. 6.10a shows that after an initial 6 minute oxidation at 973 K the Ce is clearly located in the near surface region of the oxide. Extended oxidation resulted in the gradual disappearance of the Ce peak. AES analysis of oxide formed after 4 h oxidation at 973 K showed no Ce; the profile for this element was characteristic of background noise for the whole oxide thickness of 486 nm (Fig. 6.10b). In this sample, very sensitive SIMS analysis revealed a Ce peak with a very low concentration, less than 1 percent, well below the surface. The rest of the Ce was distributed throughout the oxide volume (Fig. 6.10c).

The oxide grown on mechanically polished substrates generally had a thickness of about three times that grown on chemically polished substrates. To determine whether this factor was the reason for the differences in the Ce depth distribution, longer oxidations were conducted to produce thicker oxides on chemically polished, coated nickel substrates. The RBS analyses of such scales, obtained after up to 75 h oxidation at 973 K in 760 torr O_2 are presented in Chapter 9. For both films there are distinct Ce peaks in the RBS spectra which indicate the relocation of Ce during oxidation: increasing oxidation time resulted in a broader Ce profile with a lower peak concentration and peak depth. Although the oxides were much thicker than those previously analyzed for a mechanically polished substrate, the Ce peaks were easily detected. Hence, the oxide thickness cannot be the main reason for the difference in the Ce distributions among coated nickel samples polished mechanically or chemically.

6.4. The microstructure of thin NiO films

The surface analysis of oxides by AFM was extended by examinations of internal structure using analytical electron microscopy.

6.4.1. *General observations*

The effect of the surface finish on the microstructure of oxide formed on unmodified nickel is illustrated in Fig. 6.11. Oxide grown on a mechanically polished surface is polycrystalline and the SAD pattern indicates the presence of texture (Fig. 6.11a). This oxide film contains high angle grain boundaries which are easy diffusion paths. The microstructure of oxide on chemically polished substrates depends on nickel grain orientation, but the structure generally seems to approach that of a single crystal with added low angle boundaries or lattice defects. An example for one Ni grain is seen in Fig. 6.11b. The same essential difference existed in the structure of oxides formed at 673 K prior to coating deposition. Thus, in the previously described experiments, the CeO_2 coatings were deposited onto preformed oxide films with very different microstructure, due to the different polishing techniques used.

To analyze the mechanism of the incorporation of CeO_2 particles derived from sol-gel into the growing oxide, thin foils for TEM were prepared from oxides formed during short periods of exposure to oxygen, i.e. the early transient stage. TEM observations indicate that the oxide formed on CeO_2 coated nickel during initial stages had the same microstructure for both methods of substrate surface finish. Since the same oxide structure was also formed for polycrystalline Ni and Ni single crystals, the typical TEM image is presented later (Chapter 7, Fig. 7.6b). The microstructure of the film (approximately 60 nm thick) is composed of a mixture of ultra-fine grains of NiO and CeO_2. In the SAD pattern there are only continuous diffraction rings for both phases. After further oxidation distinct spots were also visible in the SAD pattern (Fig. 6.12a). It has been shown in experiments with CeO_2 coated Ni single crystals (Chapter 7) that these spots are due to the crystallographic orientation relationship of the inner portion of the oxide with the nickel grains in the substrate. This indicates that NiO grains initially nucleate randomly on top of CeO_2 particles. During prolonged oxygen exposure a Ce modified NiO layer is formed which offers resistance to oxide growth during the subsequent stage of oxidation. When the entire oxide film thickness is imaged by TEM, it is possible to see the effect of surface roughness on the image contrast (Fig. 6.12a). The darker areas with sharp contours correspond to NiO grains extended above the specimen surface. Although the highest magnification possible while imaging the total oxide thickness was too low for detailed observations of CeO_2 particles, the image contrast produced by their presence can also be seen in Fig. 6.12a.

A bright-field TEM image of NiO formed on ceria-coated Ni annealed at 973 K for 5 h before oxidation is shown in Fig. 6.12b. According to previous measurements, this treatment increased the CeO_2 particle size (Fig.4.8) and the oxidation rate of Ni (Fig. 5.7). The SAD pattern indicates the presence of randomly oriented NiO and CeO_2 phases. A lack of distinct NiO diffraction spots suggests that oxide does not contain NiO sublayer which grows with the crystallographic orientation relationship with the Ni substrate, as observed in Fig. 6.12a.

6.4.2. *High-magnification analysis of Ce-rich part of the CeO_2 modified NiO films*

The high magnification TEM image of the near-surface region of oxide films, covering the Ce-rich part, is shown in Fig. 6.13a. The structure is composed of NiO grains and small CeO_2 particles distributed randomly, at grain boundaries and within grains. SAD pattern indicates that both phases in this sublayerare oriented randomly. The NiO grain boundaries in this region were examined by an energy dispersive x-ray analyzer in STEM to detect the distribution of the reactive element. Typical results shown in Fig. 6.13b demonstrate the segregation of Ce in NiO grain boundaries.

In order to describe quantitatively the microstructure of the Ce-rich part, images for stereological analysis in the Leco 2001 analyzer were prepared manually from TEM micrographs. Fig. 6.14a gives an example of the microstructure created on the basis of the bright-field image. The CeO_2 particles seen as a black phase, are superimposed on the network of NiO grain boundary. A simple visual assessment of this microstructure supports the random distribution of CeO_2 particles. The distribution of the size of NiO grains is shown in Fig. 6.14c. NiO grains in this region are characterized by an average size of 29.1 nm with a higher fraction at 24 and 36 nm. Under the simplified assumption of a one phase structure it gives a value of 13.7×10^5 cm^{-1} of the surface area of grain boundaries per unit volume of specimen. The average diameter of CeO_2 particles was measured to be 5.5 nm, however, a high percentage of the particles had a diameter of about 4 nm (Fig. 6.14b). The volume fraction of CeO_2 found as a ratio of the surface covered by this phase on a two-dimensional image is approximating to 17.3%. The average spacing between particles of 12.4 nm is smaller than the average NiO grain size.

6.5. Summary

At high temperatures, superficially applied CeO_2 sol-gel coatings on Ni are incorporated into growing NiO films affecting the oxide surface morphology and internal microstructure. A correlation was found between the evolution of the topography of the oxide/gas interface, depth location of the reactive element, internal microstructure of the oxide and reduction in the oxidation rate caused by the presence of the CeO_2 coating. After oxidation, Ce was present as CeO_2 particles located inside the NiO film. For chemically polished Ni, the Ce-rich part is located, in general, near the oxide/gas interface and is composed of CeO_2 particles located randomly between and inside NiO grains. Moreover, Ce segregation was detected in NiO grain boundaries in this region. However, this location changes from grain to grain of the Ni substrate. Experiments on a polycrystalline substrate indicate the important role of Ni grain orientation in oxidation inhibition by CeO_2 coatings.

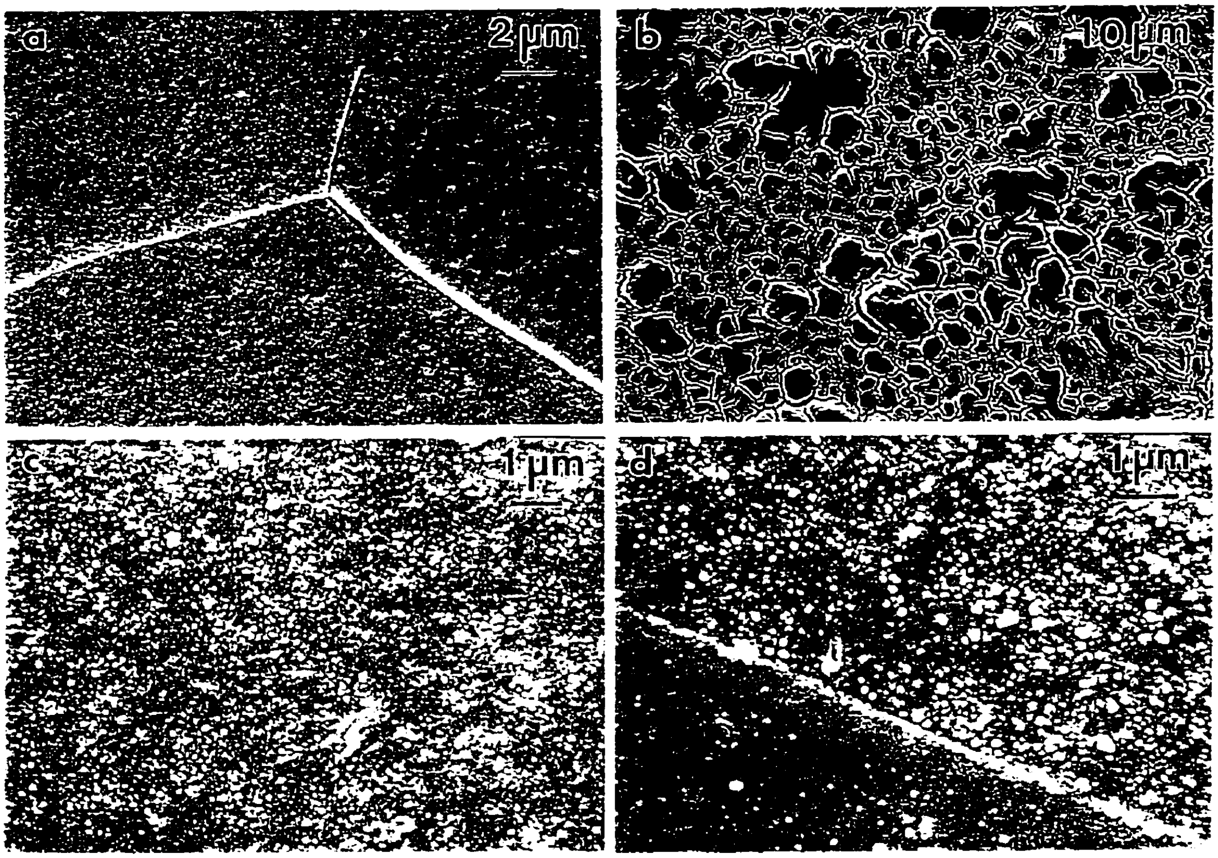

Fig. 6.1. Surface morphology of CeO_2 sol coatings with thickness of 14 nm (a) and 154 nm (b), deposited on chemically polished nickel after calcination at 573 K for 1 h in 760 torr oxygen. Coating with thickness of 14 nm after oxidation at 973 K for 3 min (c) and for 30 min (d).

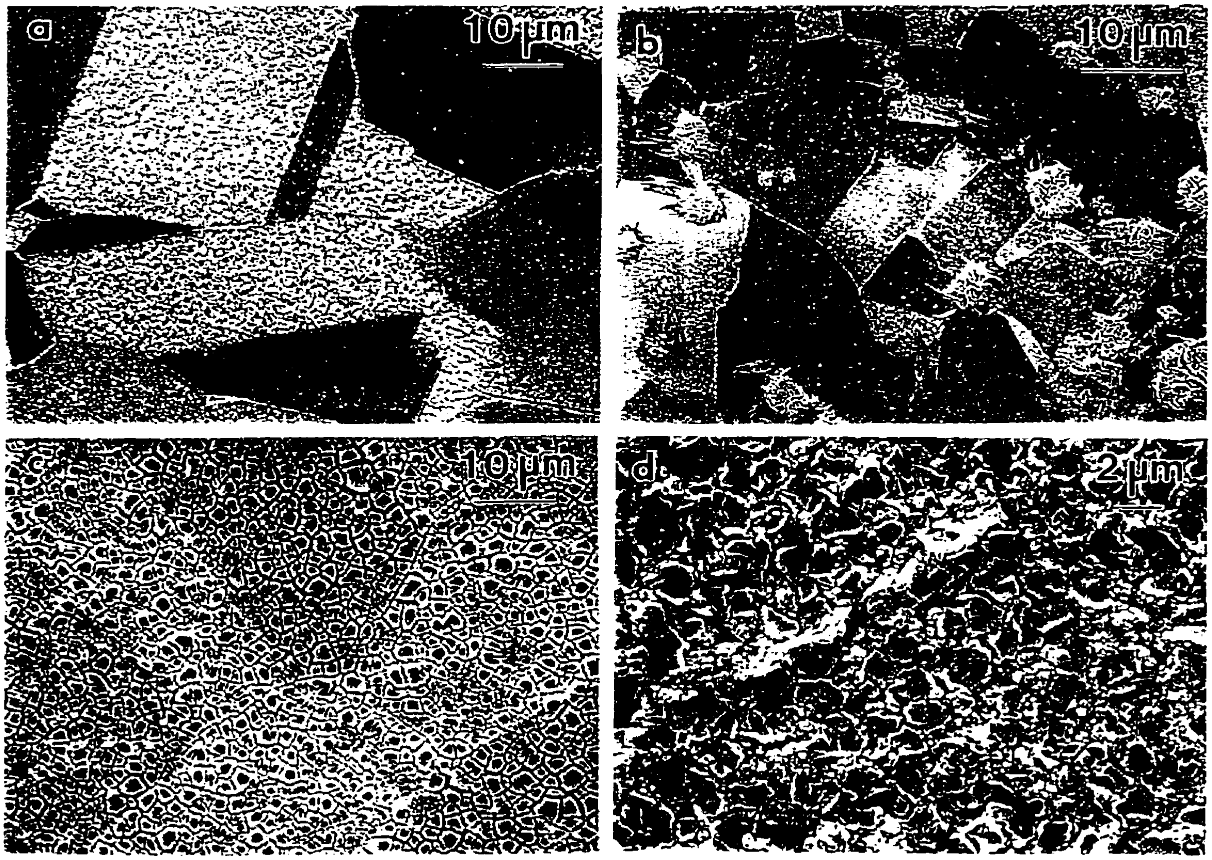

Fig. 6.2. Effect of CeO_2 sol coating thickness on oxide surface morphology after 4 h exposure at 973 K. Chemically polished preoxidized substrate: (a) 7 nm CeO_2, (b) 35 nm CeO_2, (c) 154 nm CeO_2. Mechanically polished preoxidized substrate: (d) 154 nm CeO_2.

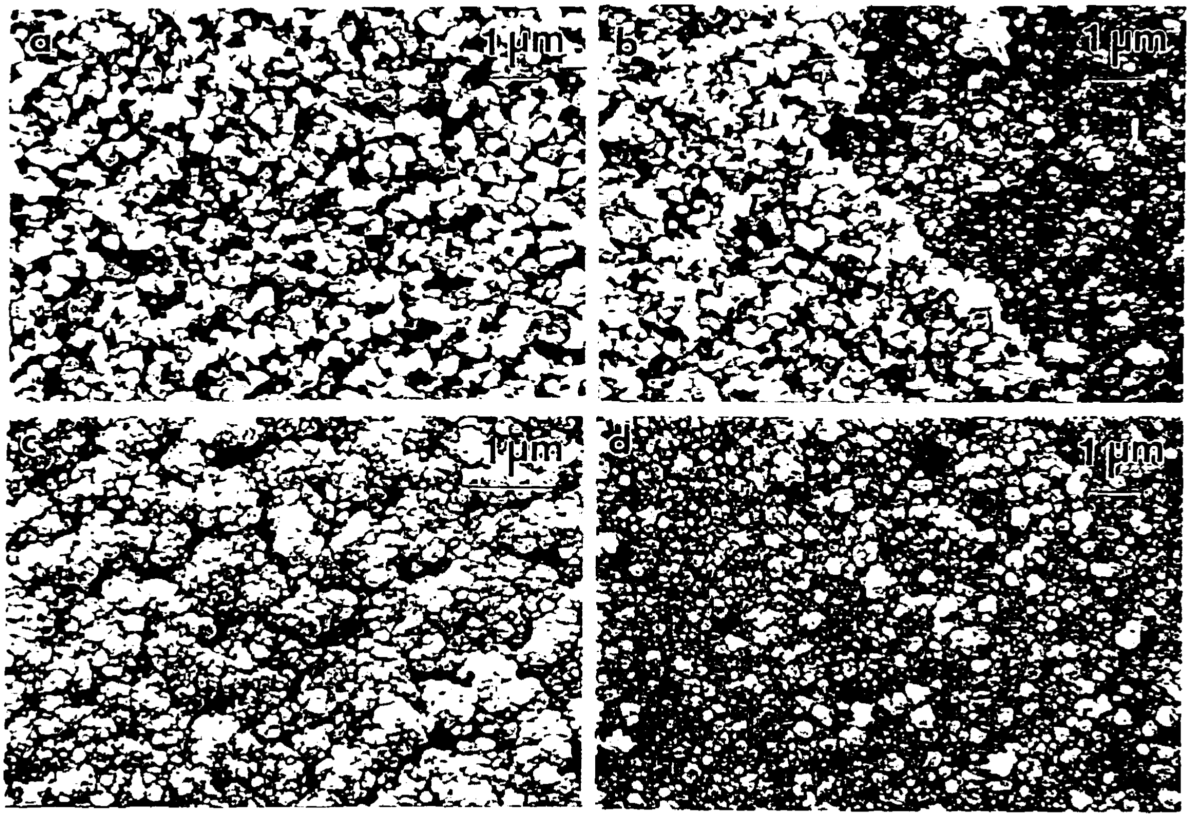

Fig. 6.3. SEM surface morphology of nickel after oxidation at 973 K for 4 h: (a) mechanically polished uncoated; (b) chemically polished uncoated;(c) mechanically polished coated; (d) chemically polished coated. CeO_2 coating thickness of 14 nm.

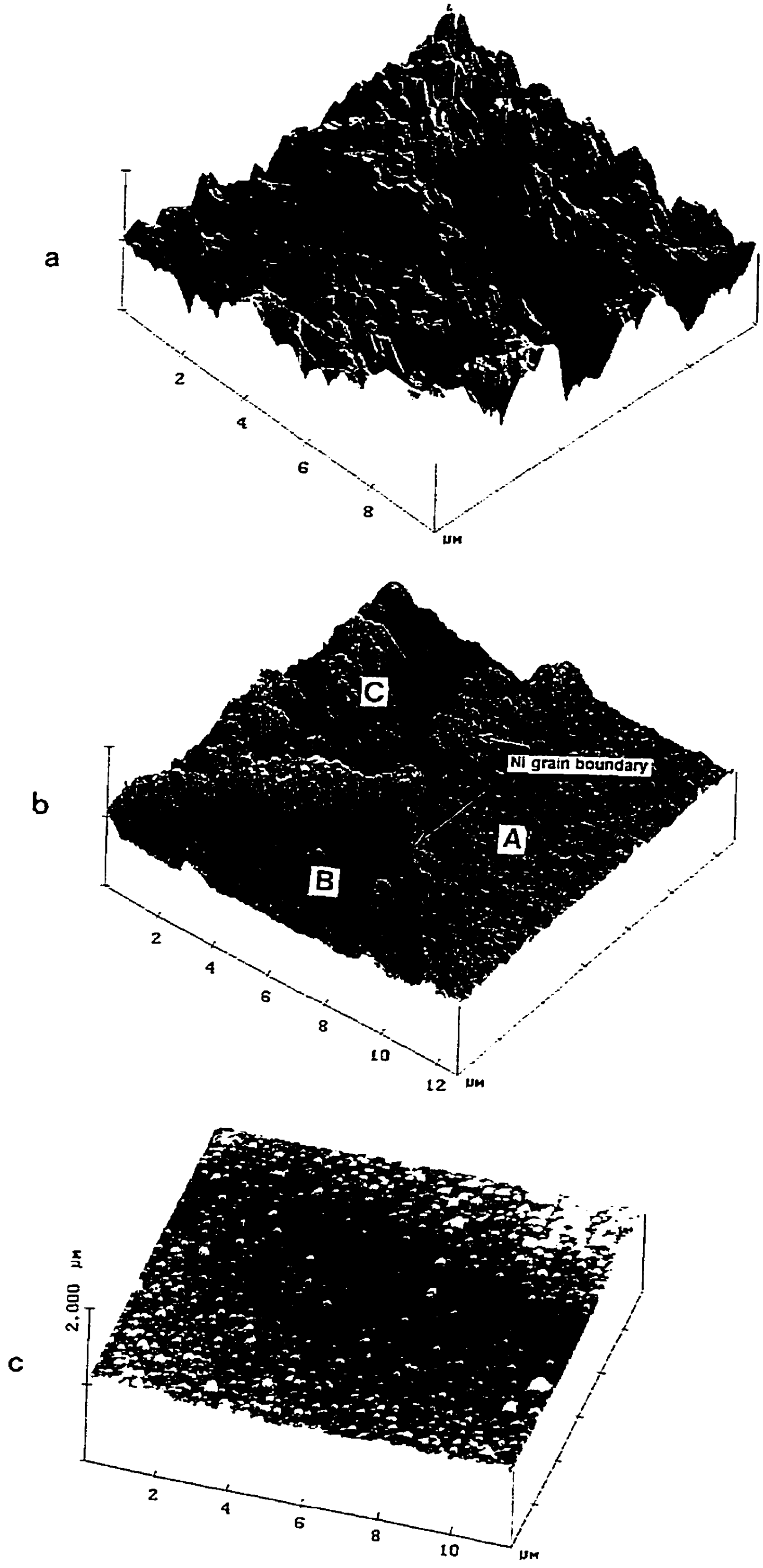

Fig. 6.4. AFM surface morphology of oxide grown at 973 K for 4 h on Ni substrate: (a) uncoated surface finished by mechanical polishing, average oxide thickness of 630 nm; (b) uncoated surface finished by chemical polishing, average oxide thickness of 280 nm (grains of Ni substrate beneath the oxide are indicated as A,B and C; (c) 14 nm CeO_2 coated finished by chemical polishing, average oxide thickness of 102 nm.

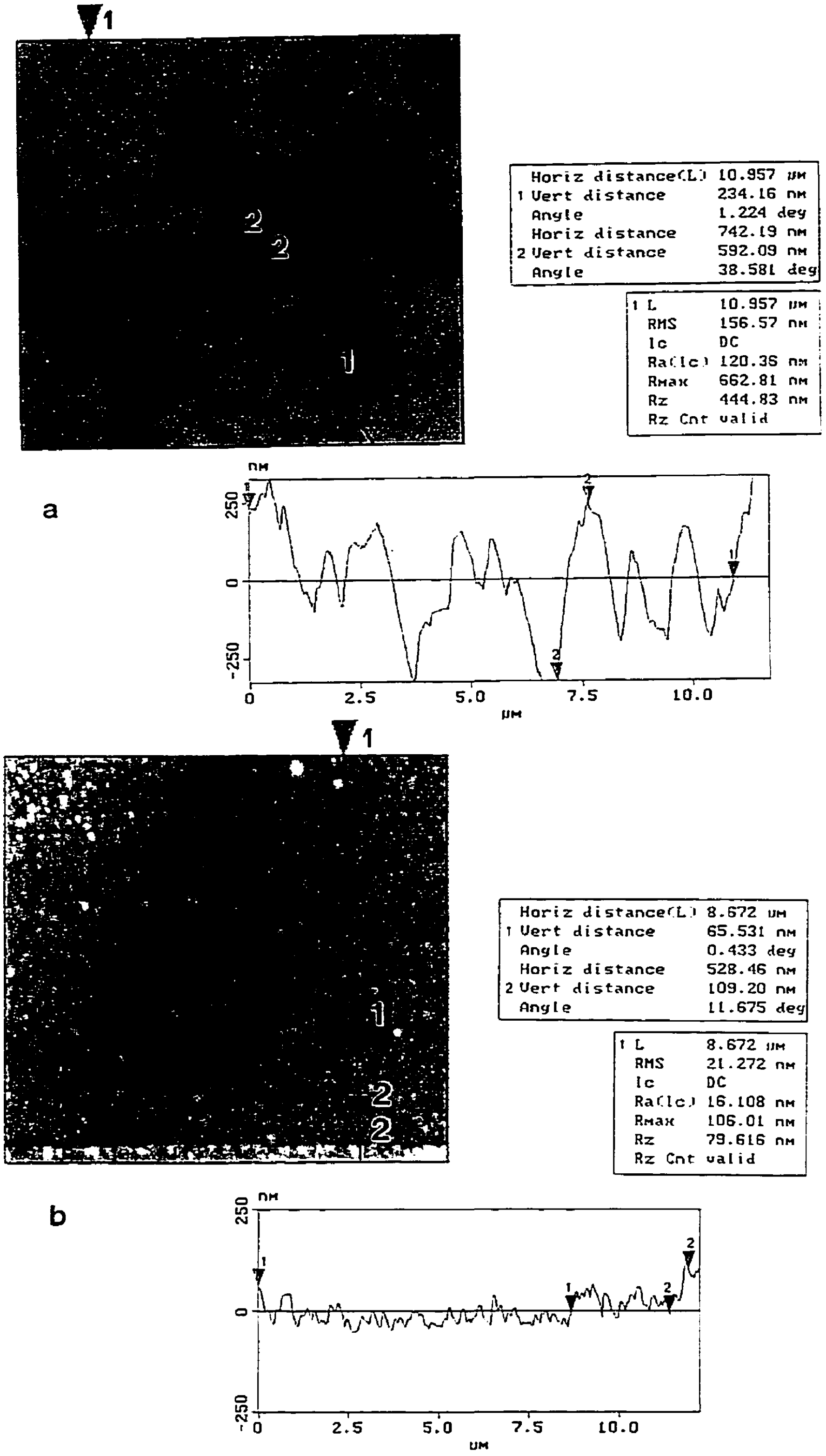

	Horiz distance(L)	10.957 µm
1	Vert distance	234.16 nm
	Angle	1.224 deg
	Horiz distance	742.19 nm
2	Vert distance	592.09 nm
	Angle	38.581 deg

1	L	10.957 µm
	RMS	156.57 nm
	Ic	DC
	Ra(Ic)	120.36 nm
	Rmax	662.81 nm
	Rz	444.83 nm
	Rz Cnt	valid

	Horiz distance(L)	8.672 um
1	Vert distance	65.531 nm
	Angle	0.433 deg
	Horiz distance	528.46 nm
2	Vert distance	109.20 nm
	Angle	11.675 deg

1	L	8.672 µm
	RMS	21.272 nm
	Ic	DC
	Ra(Ic)	16.108 nm
	Rmax	106.01 nm
	Rz	79.616 nm
	Rz Cnt	valid

Fig. 6.5. AFM cross-sectional analysis of oxide grown at 973 K for 4 h on: (a) uncoated Ni finished by mechanical polishing, thickness 630 nm and (b) 14 nm CeO_2 coated Ni finished by chemical polishing, thickness of 102 nm. The are shown: planar view image, cross-sectional profile along line shown on the image, distances between markers and roughness parameters.

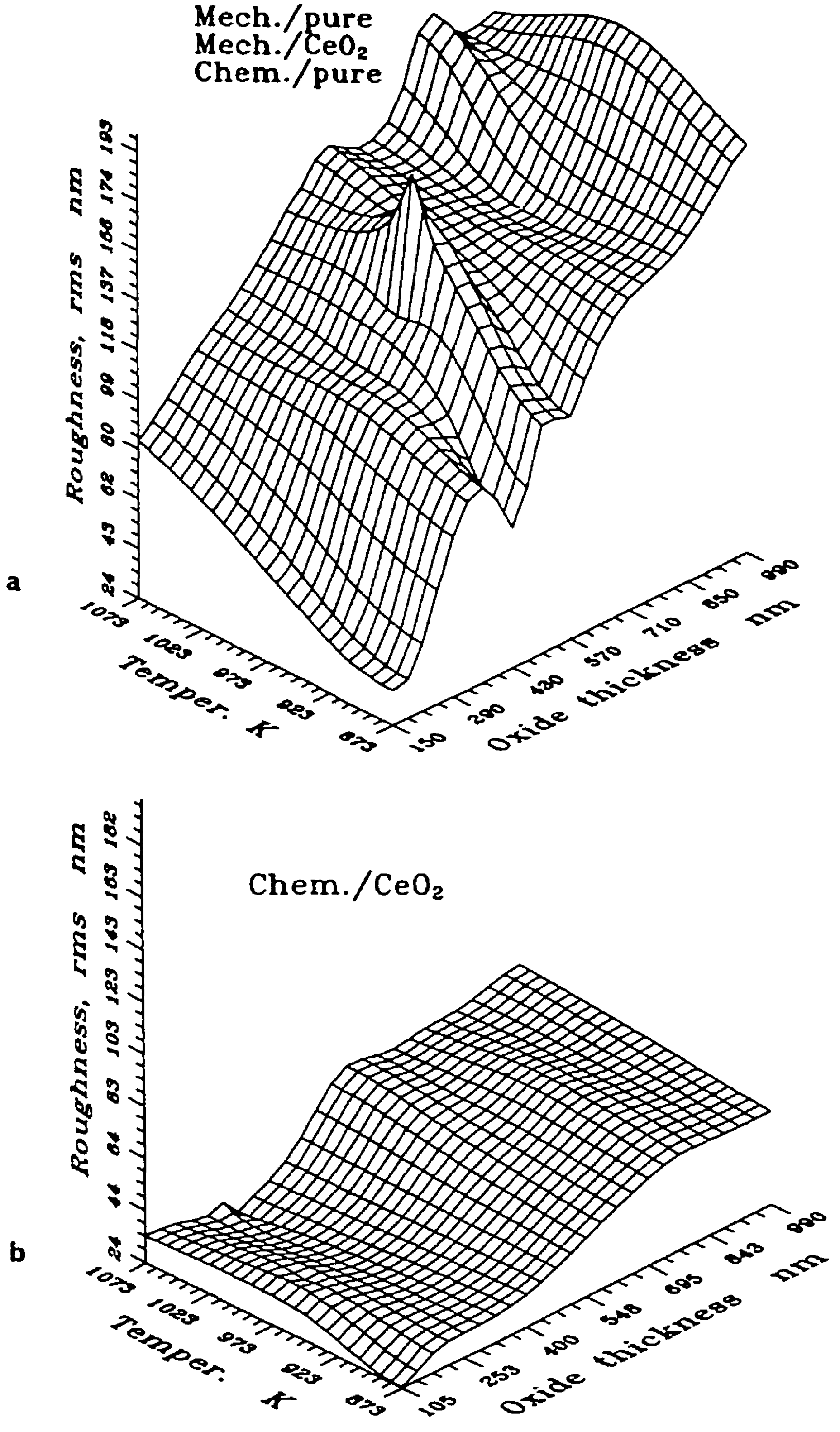

Fig. 6.6. Surface roughness expressed by standard deviation *rms* as a function of oxide thickness and oxidation temperature: (a) uncoated Ni finished by mechanical and chemical polishing, and CeO_2 coated Ni finished by mechanical polishing; (b) CeO_2 coated Ni finished by chemical polishing.

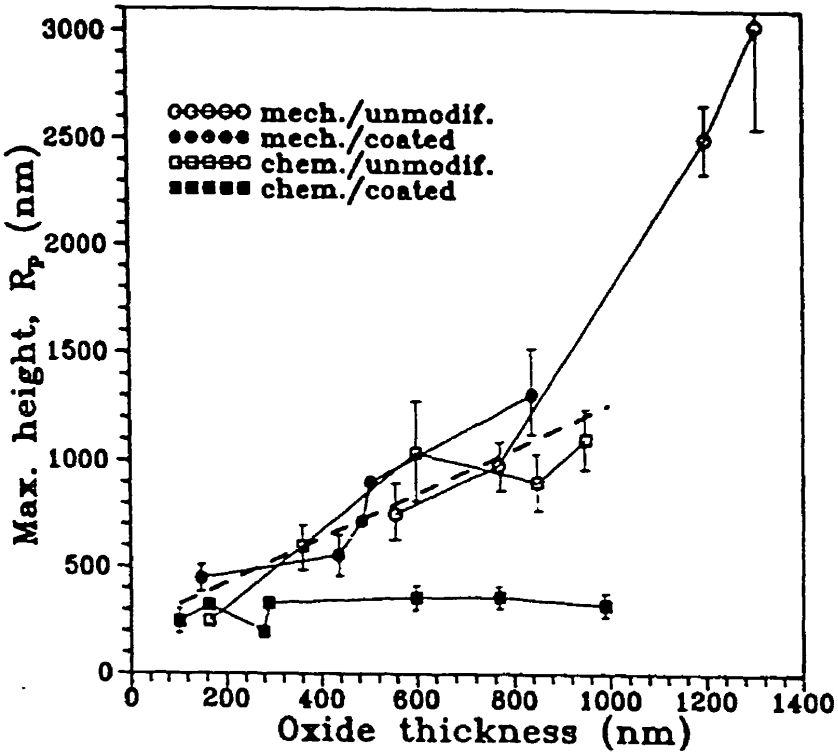

Fig. 6.7. The maximum height R_p plotted as a function of oxide thickness. R_p values were averaged over a temperature range 873-1073 K.

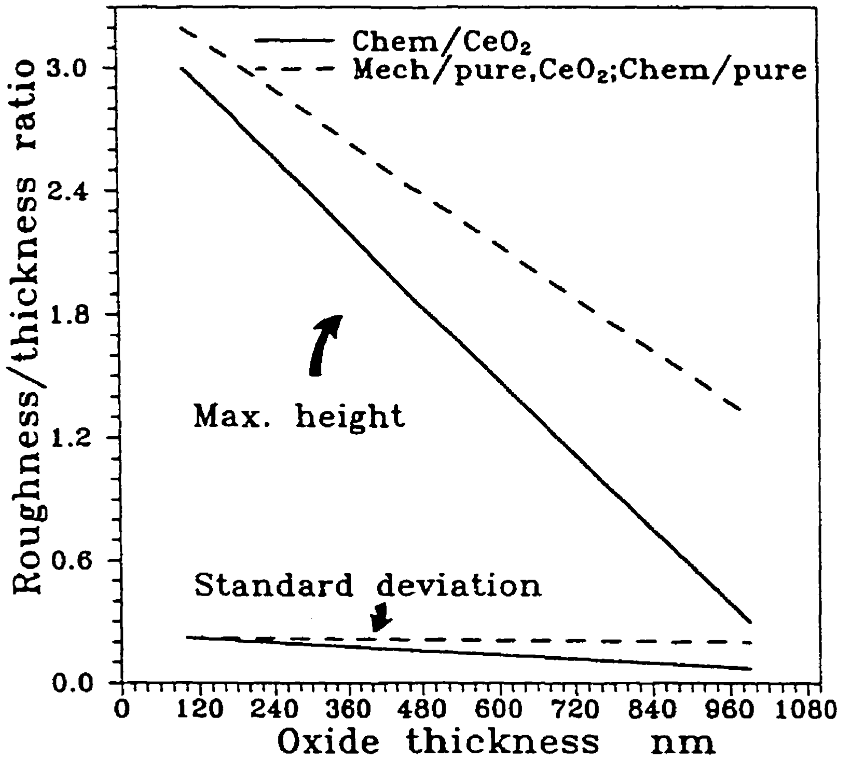

Fig. 6.8. The ratio of roughness parameters: standard deviation *rms* and maximum height R_p to oxide thickness plotted as a function of oxide thickness.

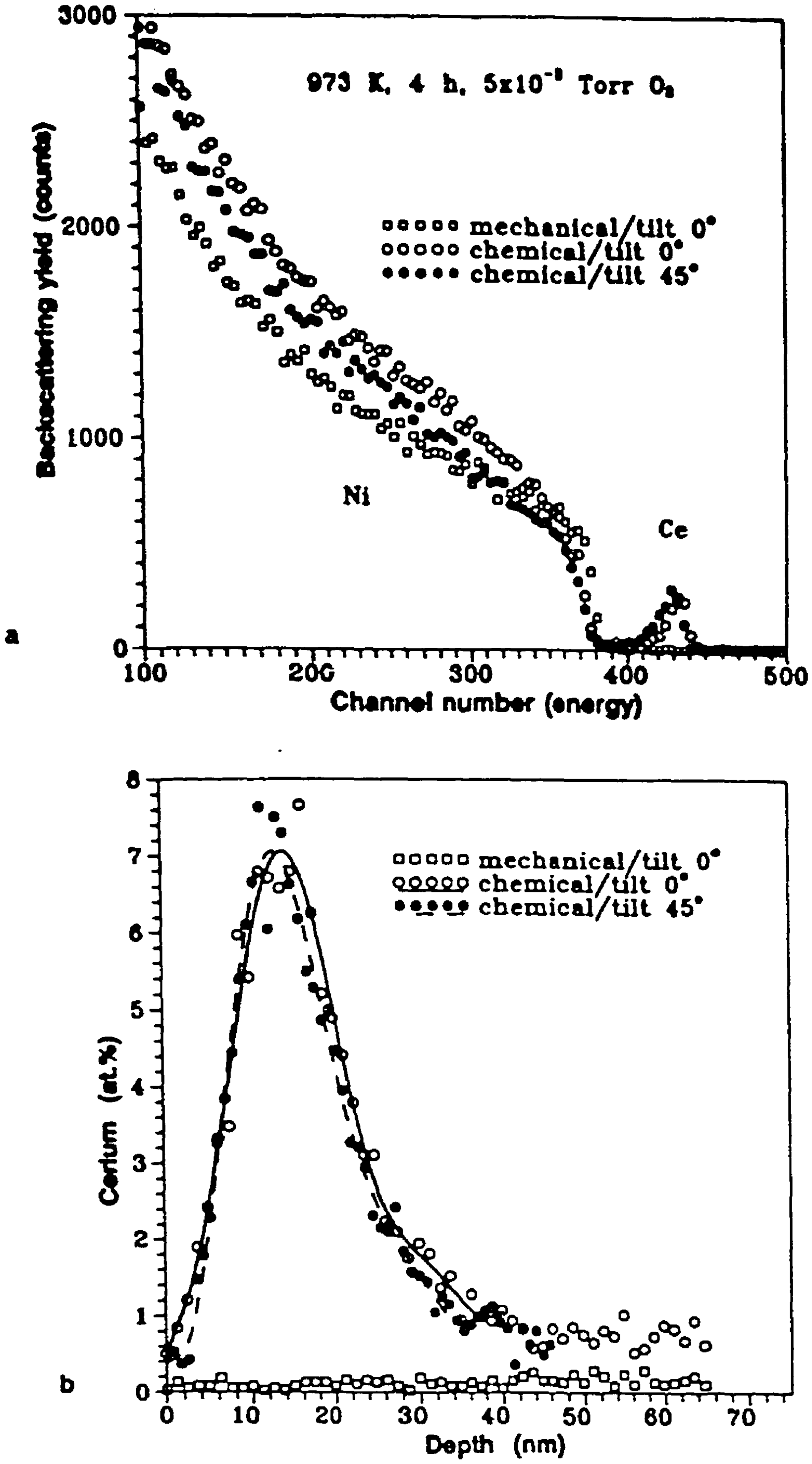

Fig. 6.9. RBS analysis of oxide films formed on CeO_2 coated chemically and mechanically polished nickel: (a) energy spectra of 1 MeV $^4He^+$ ions backscattered from oxide surface; (b) Ce concentration versus depth profiles, as derived from spectra shown in (a); estimated depth resolution is 12.2 nm at 0 deg tilt and 9.3 nm at 45 deg tilt.

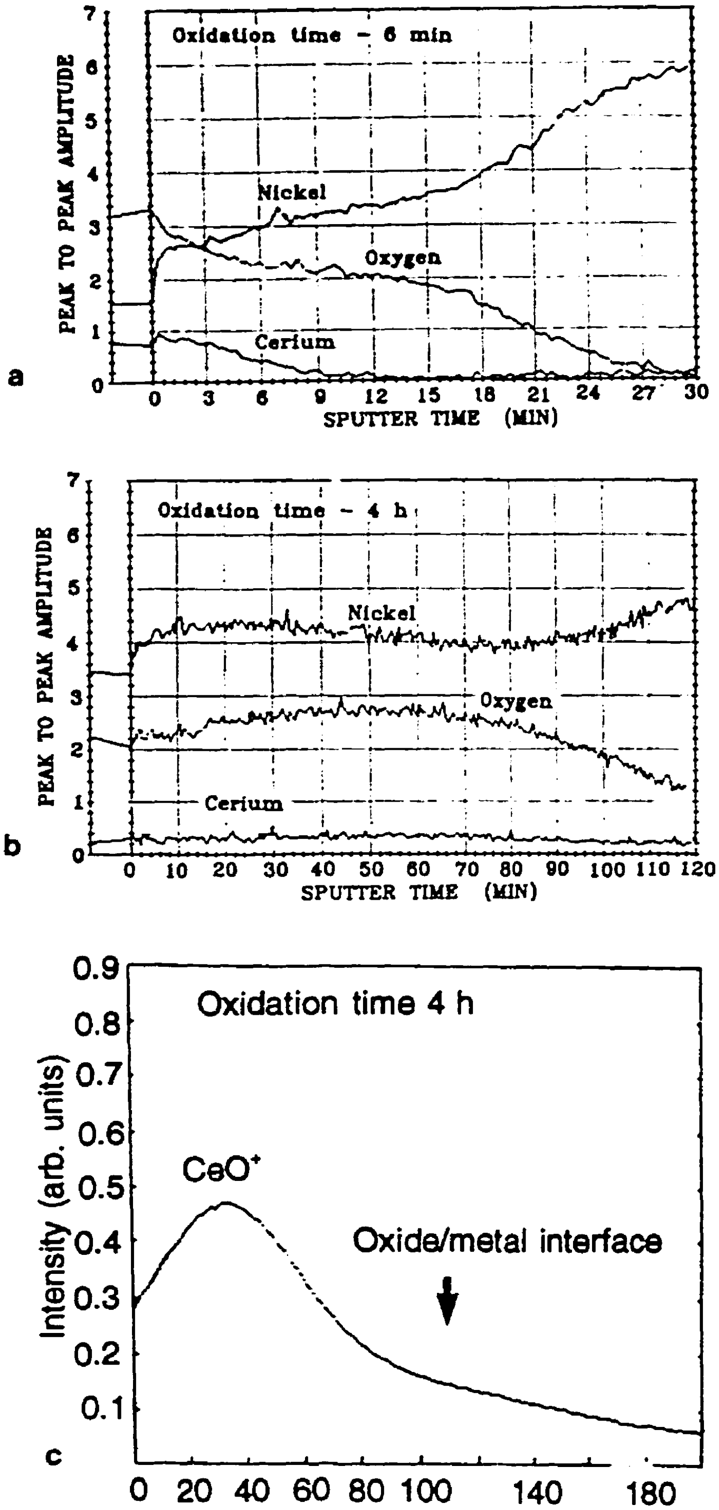

Fig.6.10. Composition analysis of oxide films formed on mechanically polished, CeO_2 coated nickel: (a) AES composition-depth profiles for 150 nm thick oxide formed after 6 min oxidation, oxide/metal interface is estimated to be at a sputter time of 23 min; (b) AES composition-depth profile for 486 nm thick oxide formed after 4 h oxidation, oxide/metal interface at a sputter time of about 100 min; (c) SIMS composition-depth profile for oxide analyzed in (b).

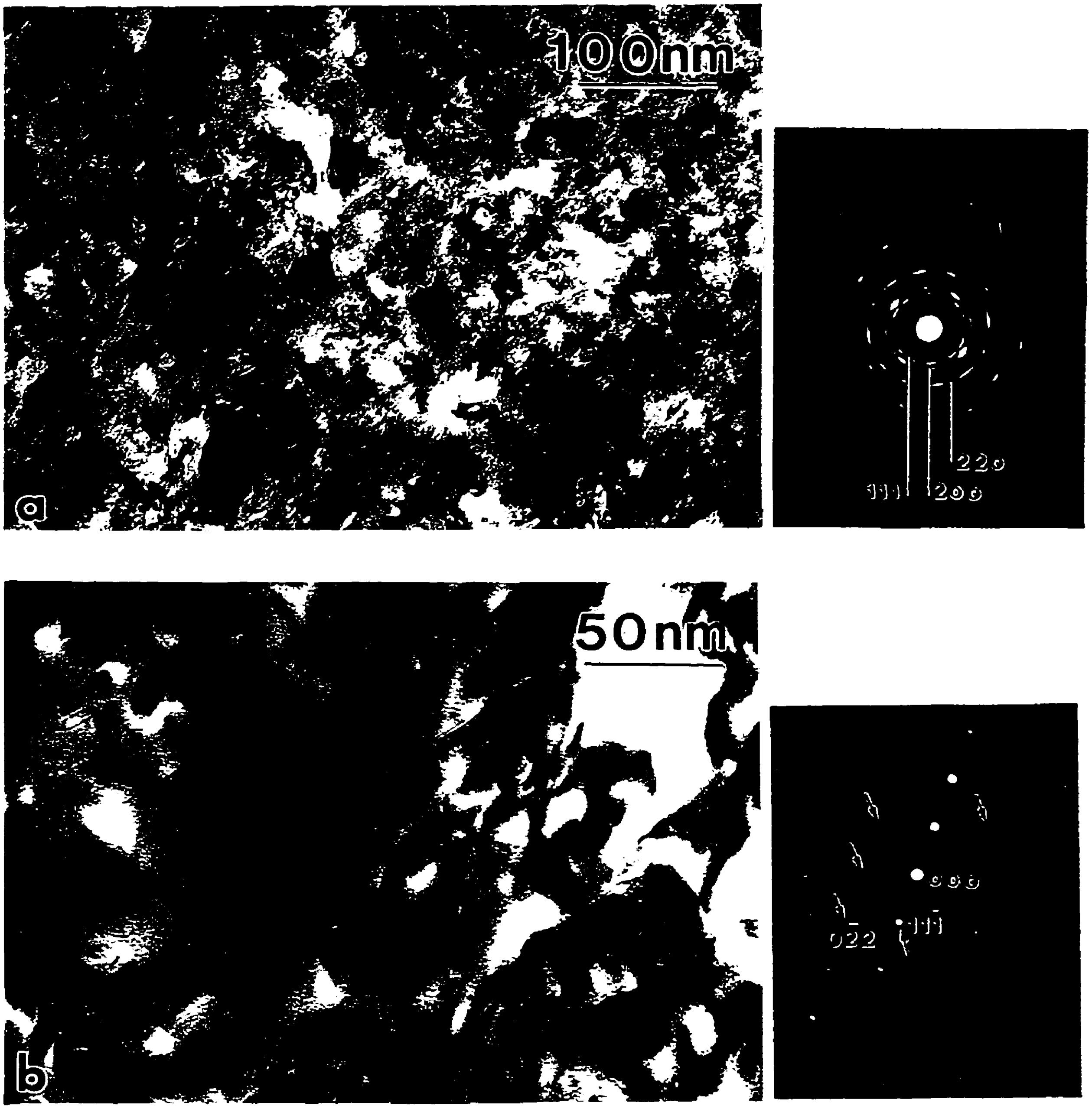

Fig. 6.11. TEM images and SAD patterns illustrating the effect of substrate finish on the microstructure of pure NiO grown during first minutes oxidation at 973 K: a) mechanical polishing; b) chemical polishing.

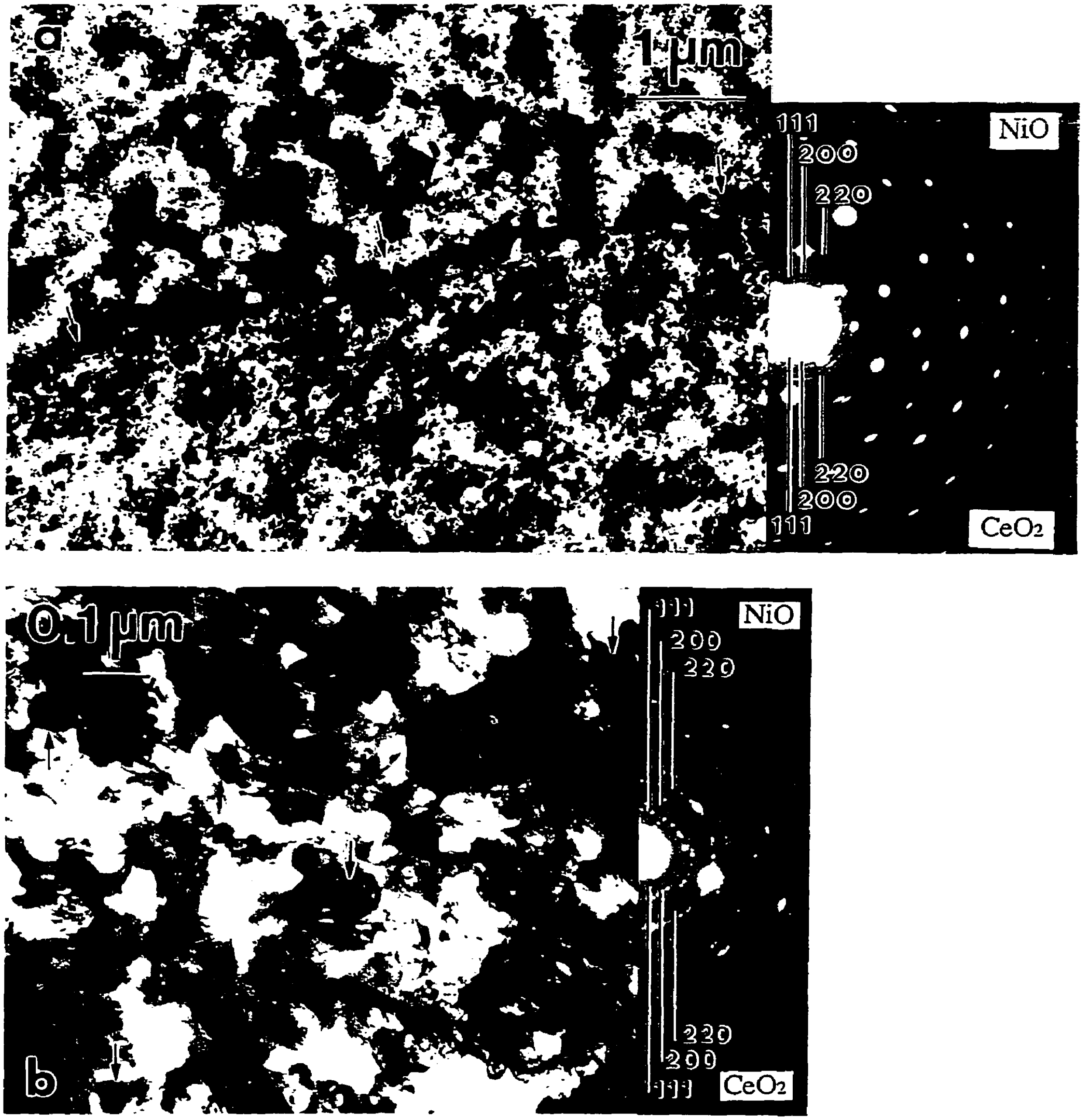

Fig. 6.12. TEM micrograph and SAD patterns of NiO formed on CeO_2 coated Ni: (a) Ni directly oxidized at 973 K for 4 h after coating; (b) oxidation followed vacuum annealing at 973 K for 5 h, some of the coarse CeO_2 particles are indicated by arrows.

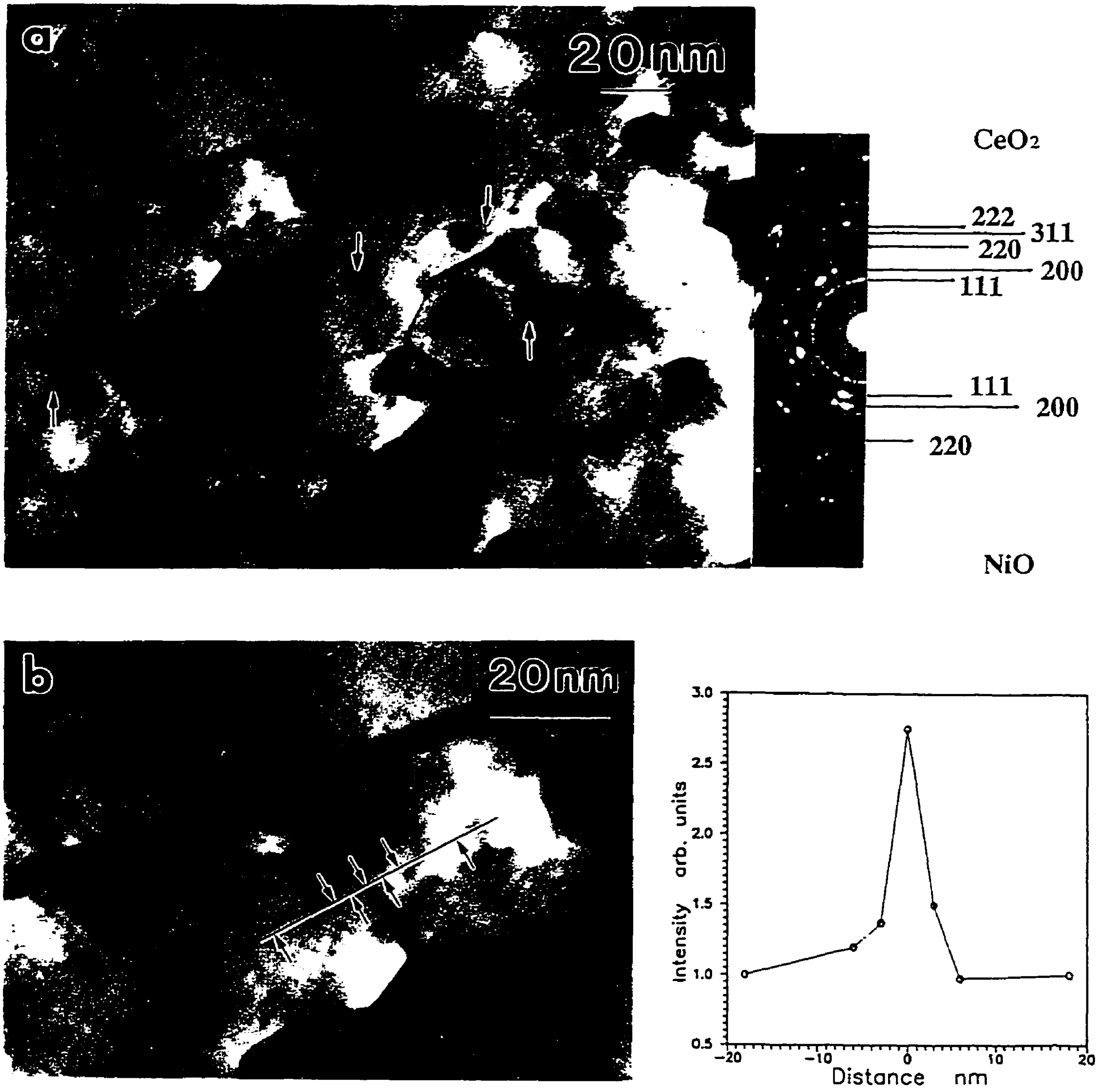

Fig. 6.13. (a) High magnification TEM bright field image and SAD pattern of a surface region of oxide formed during 4 h at 973 K on CeO_2 coated nickel; (b) TEM bright-field image and corresponding STEM/EDX analysis of Ce segregation in NiO grain boundary.

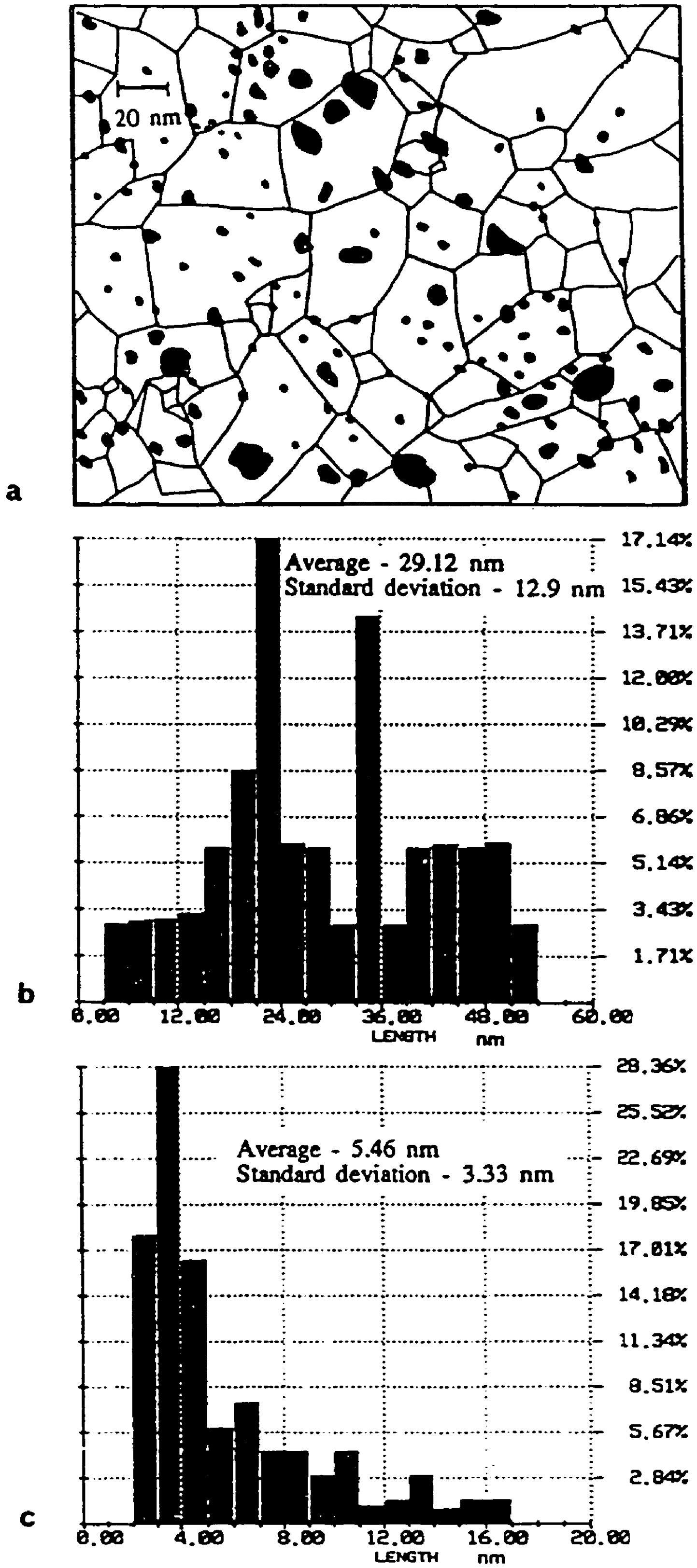

Fig. 6.14. Results of stereological quantitative analysis of Ce rich portion of oxide shown in Fig. 6.13: (a) microstructure with elements analyzed: NiO grain boundary network and CeO_2 particles as black phase, (b) distribution of NiO grain diameters, (c) distribution of CeO_2 particle diameters.

CHAPTER 7. THE INFLUENCE OF THE CRYSTALLOGRAPHIC ORIENTATION OF THE NICKEL SURFACE ON OXIDATION INHIBITION BY CeO_2 SOL COATINGS

7.1. Introduction

Experiments with the oxidation of polycrystalline Ni demonstrated that the effectiveness of a surface-applied reactive element depends essentially on the nature of the substrate surface. For pure NiO, an especially crucial role was played by the Ni grain orientation, leading to the anisotropy of oxidation. Surprisingly, oxide growth anisotropy is also present after the surface modification with CeO_2 coatings deposited by both sol-gel technology and reactive sputtering. Therefore, in order to analyze the role of the crystallographic orientation of the Ni substrate in oxidation inhibition caused by a superficially applied reactive element, experiments on single crystals will be conducted. For this purpose, two crystal faces, (111)Ni and (100)Ni, known for their large differences in oxidation resistance, have been chosen. The experimental data obtained from many analytical techniques reveal the essential differences in the growth kinetics and structure of oxides formed on both Ni faces coated with CeO_2, and give new insights into the technologically important problem of increasing the lifetime of reactive element coatings at high temperatures.

7.2. Oxidation kinetics and the reactive element effect

The growth of oxide on pure and CeO_2 coated crystal faces of Ni was studied by the continuous monitoring of oxygen uptake in a manometric system. Some exemplary oxidation curves for 873 and 973 K are shown in Fig. 7.1. The oxygen uptake after 4 h reaction was then used to calculate the average values of the parabolic rate constants k_p.

Results are summarized in the Arrhenius plot (Fig. 7.2), which indicates the essential differences in oxidation behaviour of both crystal faces before and after CeO_2 coating. The growth rate of oxide on uncoated (100)Ni was slightly lower than that found for polycrystalline Ni with a surface plastically deformed by mechanical polishing. Although the presence of CeO_2 on this face decreased the oxide growth rate by about one order of magnitude, the values of k_p were still higher than that obtained for uncoated (111)Ni.

The influence of the CeO_2 coating on the oxidation rate of (111)Ni depended upon the temperature. The highest improvement was achieved at 1073 K. For a reaction at this temperature, the rate constant k_p was very low and practically the same as that calculated from literature data, assuming the lattice diffusion of Ni in NiO [Atkinson and Taylor, 1982]. The low effectiveness of CeO_2 coatings on (111)Ni at 873 and 973 K was caused by a relatively low incorporation rate of CeO_2 particles into growing oxide on this face. Experiments on polycrystalline substrates revealed that the reactive element coating must be quickly incorporated into the native oxide to avoid the coarsening of CeO_2 particles. However, this is not the case during the oxidation experiment at 873 K, because after 4 h of exposure the coating still remained on the substrate surface. In order to increase coating effectiveness at 873 K, the CeO_2 coating should be first incorporated into NiO by exposure at a higher temperature, as shown in Chapter 5.

7.3. Redistribution of the reactive element within the oxide

Before oxidation, both Ni faces were uniformly covered with a 14 nm thick and dense CeO_2 film. During the exposure to oxygen, the coating was incorporated into growing NiO, and this resulted in the redistribution of the reactive element within the oxide film. After 4 h oxidation at 973 K, the essential differences in Ce depth-concentration in oxide formed on both Ni faces were detected. In oxide grown on coated (111)Ni, the distinct Ce peak was located close to the outer surface (Fig. 7.3a). However, in the oxide formed during the same time on coated (100)Ni, the AES did not detect Ce at all; the profile for this element was characteristic of background noise for the whole oxide thickness of 437 nm (Fig. 7.3b). To detect the Ce location in the oxide formed on this Ni face, we used a technique with higher sensitivity. Analysis using polyatomic

SIMS, detected the Ce peak ($^{140}Ce^{16}O^+$ - mass 156) of low intensity located inside the oxide film (Fig. 7.3c). The $^{58}Ni^{16}O_2^-$ - (mass 90) species were monitored as an indicator of the oxide/metal interface. Since the lattice solubility of Ce in NiO is negligible, as it was determined by both the theoretical calculations and the measurements [Moon and Bennett, 1989], the CeO_2 particles play the role of inert markers and their depth location indicates the oxide growth mechanism. Thus, the difference in depth-location of the reactive element detected by AES and SIMS suggests a different oxide growth mechanism on both crystal faces of Ni modified with CeO_2.

7.4. The evolution of oxide surface morphology

During the growth of oxide at high temperatures, growth kinetics control the surface morphology. Therefore, important information about the growth mechanism can be obtained from an analysis of the oxide/gas interface. AFM, with its high depth resolution, allows precise observations of ceramic oxide surfaces. Some examples of AFM imaging of the growth surface of pure and Ce-modified NiO are shown in Fig. 7.4. The surface morphology of the oxide formed on both uncoated Ni faces had a highly crystallographic character (Fig. 7.4a,b). Pyramidal grains exhibited some specific types of surface planes. Observations at high magnification detected the nucleation of new faceted oxide grains at the boundaries between pyramids, which in pure NiO act as diffusion paths for the transport of Ni ions from the substrate to the outer surface (Fig. 7.4c).

After coating with CeO_2, the oxide morphology depended upon the Ni face orientation. Oxide grown on coated (100)Ni developed a "cauliflower-like" structure. The conglomerates with sizes of up to 1 μm were composed of many small oxide grains. In general, the individual grains had a faceted morphology which was similar to that observed on uncoated substrates. A markedly different surface was observed on CeO_2 coated (111)Ni. In this case, very small and spherical grains of oxide uniformly covered the Ni substrate (Fig. 7.4d). It is believed that such morphology has been formed as a result of the nucleation of small oxide grains on the nano-sized CeO_2 particles.

A quantitative analysis of the oxide growth morphology involves the estimation of the vertical roughness of the oxide surface. Some examples of AFM measurements are given in Table 7.1. For oxide grown on (100)Ni, the mean roughness R_a was up to 0.25 of the average oxide thickness calculated from the oxygen uptake. Moreover, on the oxide surface, the individual oxide grains were present, the heights of which, represented by R_{max} parameter, exceeded the average oxide thickness. For (100)Ni after coating, the ratio of roughness R_a to the average oxide thickness was essentially the same as that observed in oxide formed on the pure face. Oxide grown on (111)Ni was more uniform, especially after coating with CeO_2, and the ratio of R_a to oxide thickness was about 0.04. Estimation of the vertical roughness of the oxide growth surface is important for a correct interpretation of AES and SIMS depth composition profiles. In addition, as will be shown later, the evolution of the surface roughness during oxidation may be used as an indicator of the type of the oxide growth mechanism.

7.5. NiO grain size and calculated oxidation rate

The major influence of the reactive element on the oxide growth morphology, frequently reported in the literature [Moon and Bennett, 1989], is the refinement of oxide grains. For our system, this can be clearly seen in Figs 7.4a, 7.4d, and in Table 7.1. Microscopical observations show that the smaller grain size was caused both by increasing densities of oxide nuclei and by restricting grain growth. It is obvious that the higher density of grain boundaries, accompanied by a lower oxidation rate, suggests that the reactive element inhibits the diffusivity of oxide grain boundaries. In order to verify this finding, experimental grain size data were used to calculate the parabolic rate constants k_{pc}, assuming growth was controlled by grain boundary diffusion. For this calculation, the equation determined by Atkinson et al. [1979, 1981,1982]] was used:

$$k_{pc}(1\ atm\ O_2) = 6.4\ \{\ D_l + 2(D_{gb}\delta)\ /g\ \} \qquad (cm^2/s) \qquad (7.1)$$

where D_l is the lattice diffusion coefficient expressed by:

$$D_l\ = 0.022\ exp\ \{-2.56\ (eV)\ /kT\} \qquad (cm^2/s) \qquad (7.2)$$

and $D_{gb}\delta$ is the product of the grain boundary diffusion coefficient and grain boundary width described by the equation:

$$D_{gb}\delta = 3.0x10^{-8} \exp\{ -1.78 \, (eV) /kT\} \qquad (cm^3/s) \qquad (7.3)$$

In equation (7.1), g is the oxide grain size. In order to transform the values of k_{pc} to the oxygen pressure in our experiment, i.e. $5x10^{-3}$ torr, the dependence $k_p = k_p^{\circ} \, (p_{O2})^{1/6}$ [Graham and Cohen, 1972] was used. Results of the calculations are shown in Table 7.1, together with experimental values of average (k_p) and instantaneous (k_{pi}) rate constants obtained from oxidation kinetics.

7.6. Epitaxy and texture formation in oxide films

7.6.1. Early stage of oxide growth

The influence of CeO_2 coatings on the microstructure of the oxide formed during the early stages of oxidation, was analyzed by TEM on planar thin foils. The initial oxide, which developed on both uncoated Ni faces, was epitaxially oriented with the substrate (Fig. 7.5). The major orientation relationships were (100)Ni // (100)NiO and (111)Ni // (111)NiO. Although in both cases the NiO films approach single crystals, there are essential differences in the size of mosaic regions and the density of lattice defects. A simple visual assessment of the microstructure in Figs. 7.5a and 7.5b indicates that the density of structural defects in oxide grown on (100)Ni is significantly higher.

The TEM microstructure of the oxide grown on (111)Ni revealed a contrast of well-defined triangular features up to 100 nm in size (Fig. 7.5b). When the larger area of the oxide is imaged, two sets of triangular features twisted 180 deg with respect to each other may be distinguished (Fig. 7.5c). The crystallographic analysis of NiO nucleation on (111)Ni, shows that the first orientation may be one in which oxide and metal lattices are parallel to one another. The second orientation may be obtained by a 180 deg rotation of the oxide lattice about its surface normal to produce the so-called anti-parallel orientation. According to Cathcart et al. [1969], such a nucleation leads to twinning in NiO. In our case, the SAD pattern did not support twins occurrence in such a thin oxide.

TABLE 7.1. The parameters of the surface morphology and growth kinetics for selected oxides formed on both Ni faces after 4 h exposure at 973 K.

Ni crystal face	Thickness nm	Roughness R_a,nm	Roughness, R_{max}, nm	Grain size g, nm	k_p $g^2cm^{-4}s^{-1}$	k_{pi} $g^2cm^{-4}s^{-1}$	k_{pc} $g^2cm^{-4}s^{-1}$
(100)/pure	982	106.5	1110(137)	420	$1.4x10^{-12}$	$8.2x10^{-13}$	$1.4x10^{-12}$
(100)/CeO_2	437	90.8	864.9(90)	150	$2.8x10^{-13}$	$8.3x10^{-13}$	$4.2x10^{-12}$
(111)/pure	263	22.8	117.6(17)	120	$9.8x10^{-14}$	$1.4x10^{-13}$	$5.2x10^{-12}$
(111)/CeO_2	178	8.2	108.6(10)	67	$4.5x10^{-14}$	$3.9x10^{-14}$	$9.4x10^{-12}$

(Fig. 7.5b). To detect the twins, the sample was tilted during observation to avoid <111> beam direction ({111} is the twinning plane in NiO). The twin relationship was detected in thicker oxides on (111)Ni by an x-ray diffraction technique, which is described in the next section of this thesis.

After applying CeO_2, both Ni faces were initially covered with fine-grained polycrystalline oxide characterized by a random distribution of grain orientation. This random orientation is seen on the SAD pattern of the film stripped from the substrate after a few minutes of exposure to oxygen which is composed exclusively of the continuous rings for NiO and CeO_2 (Fig. 7.6a). The SEM observation of the surface morphology at this stage of growth clearly shows that small oxide grains nucleate on the top of the CeO_2 coating (Fig. 7.6b). However, the structure of the oxide developed during further oxidation depended upon substrate orientation. Such conclusions can be drawn from the SAD pattern, which exhibits the distinct spots for NiO superimposed on the continuous rings (Fig. 7.6c). The comparison of this pattern with the SAD pattern of NiO formed on the uncoated face (Fig. 7.5a), indicates that this sublayer has an epitaxial relationship with the Ni substrate which is essentially the same as that observed without coating.

7.6.2. Steady stage of oxide growth

The structure of NiO layers developed during steady stages of oxidation is influenced by the substrate nature, the growth process, and the reactive element additions. Our study, however, revealed the crucial role of substrate orientation in the microstructural evolution of the oxide.

The x-ray data obtained for NiO formed after 15 h oxidation at 1073 K of uncoated (100)Ni are shown in Fig. 7.7. Since the oxide layer was totally penetrated by x-rays, the peaks from the Ni substrate were also detected (Fig. 7.7a). The diffraction pattern indicates that after 15 h exposure the oxide is polycrystalline. The clear separation of peaks for both the oxide and the substrate, allowed the measurement of pole figures from all the major oxide reflections (Fig. 7.7b). It is seen that two major texture components are present: a {100} component formed by oxide grains, misoriented by about 10-15 deg, developed from initially epitaxial crystals, and a <111> rough fibre component. The pole figures of the oxide after coating are shown in Fig. 7.8. It is surprising that although the CeO_2 coating led at the beginning to the nucleation of a randomly oriented NiO (Fig. 7.6a) and at a steady stage introduced the complex depth structure, the NiO texture revealed by x-ray was very similar to that observed on uncoated (100)Ni.

X-ray data show that NiO developed on (111)Ni after 15 h exposure at 1073 K was polycrystalline, and strongly textured (Fig. 7.9a). Pole figures indicate that the {111} texture was formed by two sets of twinned grains Fig. 7.9b). At this point, it is not clear whether laminar or columnar twinning occurred, although the surface morphology seems to support the latter possibility. In such a case, according to the model proposed by Cathcart et al. [1969], incoherent twin boundaries with high diffusivity should be oriented perpendicularly to the surface. NiO with such grain boundaries should exhibit a high growth rate, which was not supported by the oxidation kinetics measurements (Figs 7.1 and 7.2). Instead, a low growth rate might suggest either coherent twin boundaries connecting the substrate and the oxide/gas interface or the existence of laminar twinning.

The other texture component, i.e. {100}, with an intensity of 2.1 times random, is relatively weak in comparison to the main {111} texture. The x-ray diffraction pattern of the oxide formed after coating is shown in Fig. 7.10a. Despite a small quantity of CeO_2 introduced by 14 nm thick coating, its presence was detected by x-rays. Because the (200)NiO peak had a low intensity and was located close to the strong (111) peak of the Ni substrate, measurement of (200) pole figure for oxide was impossible. In this case, the coating inhibited the formation of the twin relationship between oxide grains (Fig. 7.10b). Moreover, the <110> texture component with an intensity of 5.9 times random was formed. The major oxide texture, however, {111} which developed as a result of the influence of (111)Ni substrate, was still present.

7.7. Summary

Inhibition of NiO growth on CeO_2 coated Ni depends essentially on the crystallographic orientation of the substrate. CeO_2 coatings deposited on (100)Ni markedly improve the oxidation resistance; however, the NiO growth rate on this coated face is still higher than that measured for uncoated (111)Ni. CeO_2 coatings on (111)Ni, when incorporated into growing NiO without the coarsening of CeO_2 particles, decreased the oxidation rate to the values predicted from lattice diffusion only. Moreover, the beneficial effect of CeO_2 on (111)Ni is stable over the exposure time up to 4 h. The structure of NiO developed on both the pure and CeO_2-coated Ni crystal faces is mainly influenced by the crystallographic orientation of the substrate. For (111)Ni, the initial epitaxially oriented NiO film with a low dislocation density is transformed to polycrystalline with a strong {111} texture. For (100)Ni, the initially epitaxial {100} film with a high dislocation density is transformed to polycrystalline with two major texture components: <111> and {100}. For the temperatures and times of this experiment, the presence of CeO_2 introduced a complex depth structure of NiO. The structure of the main NiO sublayer, however, was essentially the same as that observed without the coating.

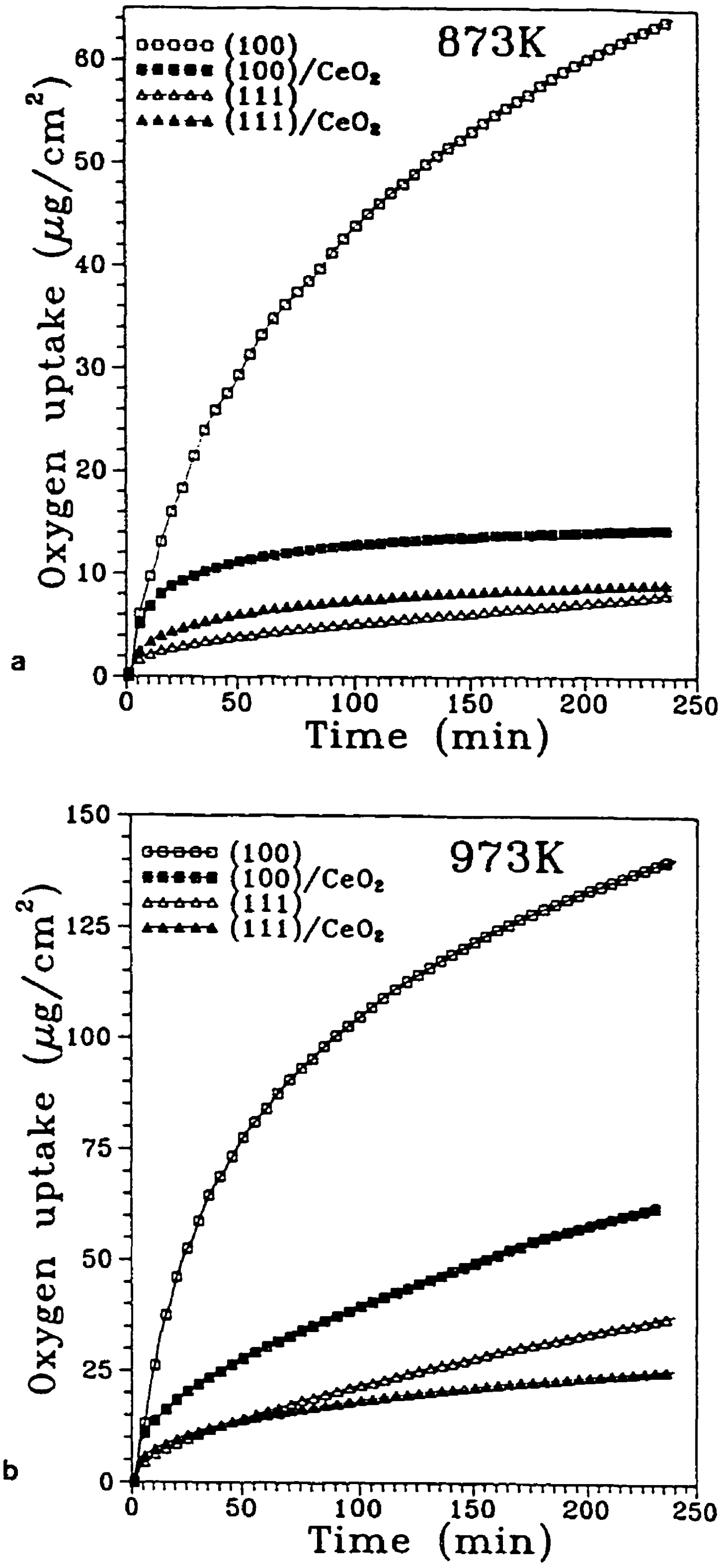

Fig. 7.1. Oxidation kinetics at 873 K (a) and 973 K (b) of pure and CeO_2 coated Ni crystal faces.

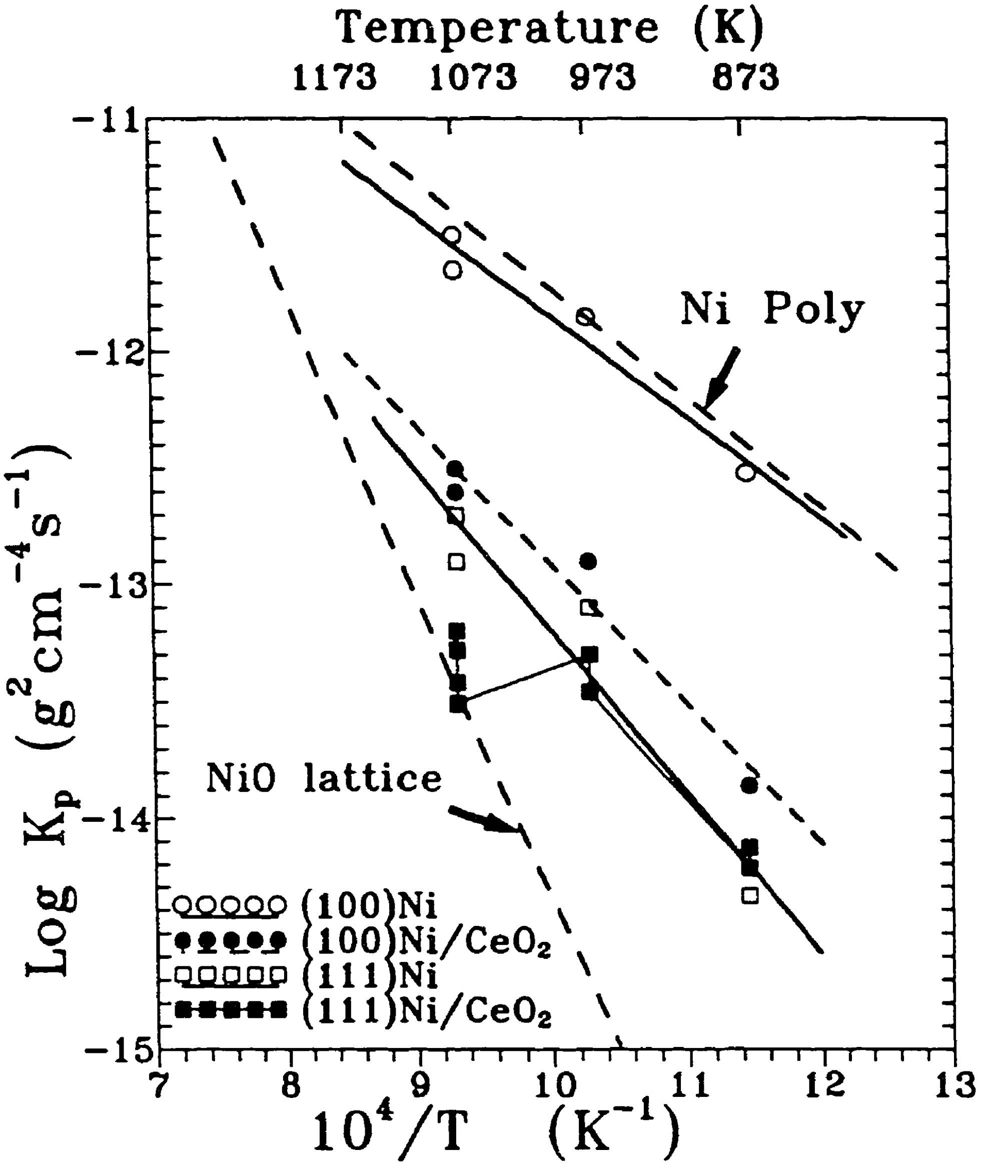

Fig. 7.2. Arrhenius plot of the parabolic rate constants for oxide growth on pure and CeO_2-coated Ni crystal faces. Oxygen pressure of 0.005 torr. Values of k_p calculated as w^2/t, where w and t are the oxygen uptake and oxidation time, respectively. Data for polycrystalline Ni are from Chapter 5.

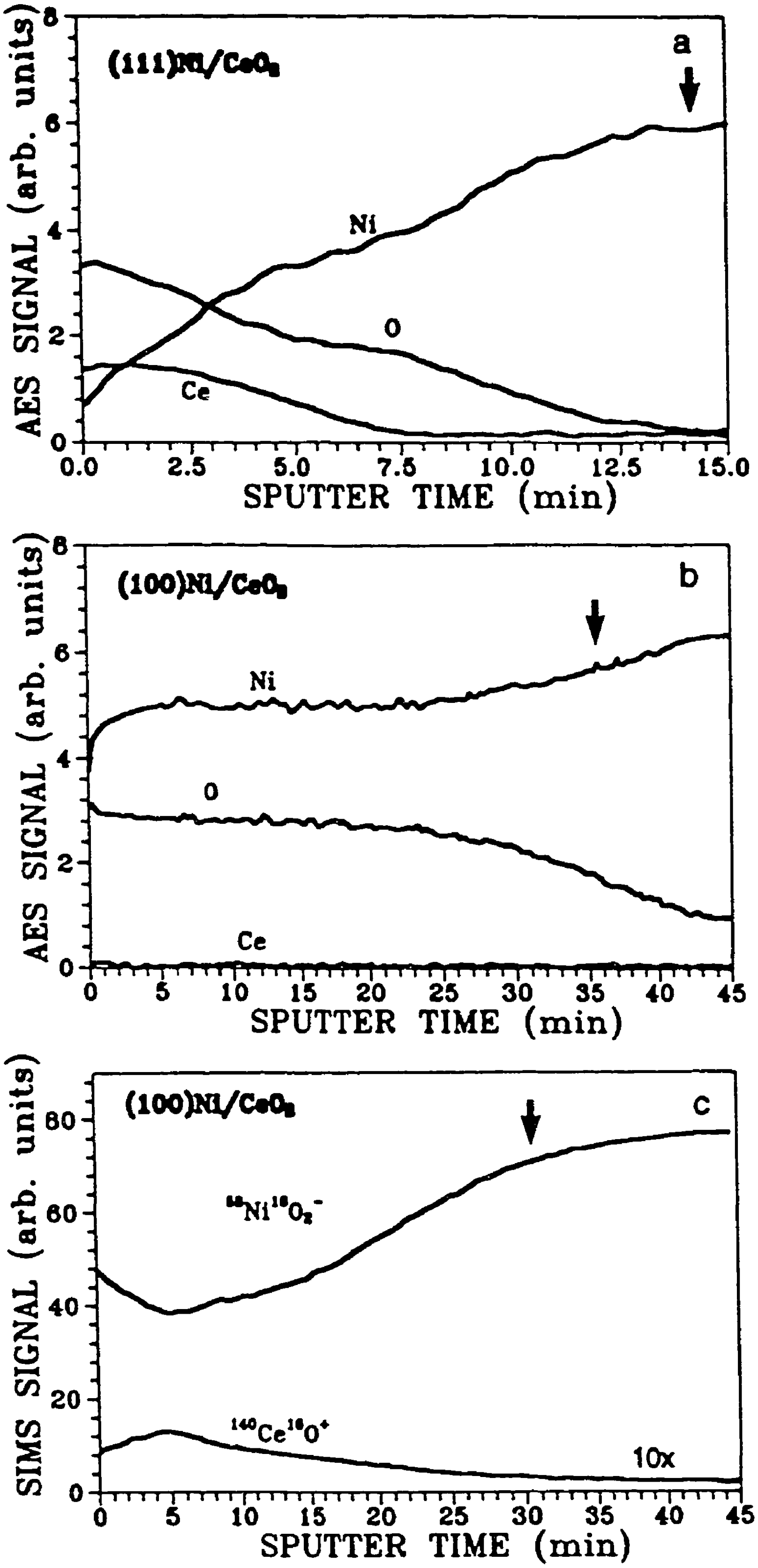

Fig. 7.3. Depth composition analysis of oxides formed after 4 h oxidation at 973 K on CeO_2-coated Ni: (a) AES - (111)Ni; (b) AES - (100)Ni; (c) SIMS - (100)Ni; arrows indicate the estimated oxide/metal interface.

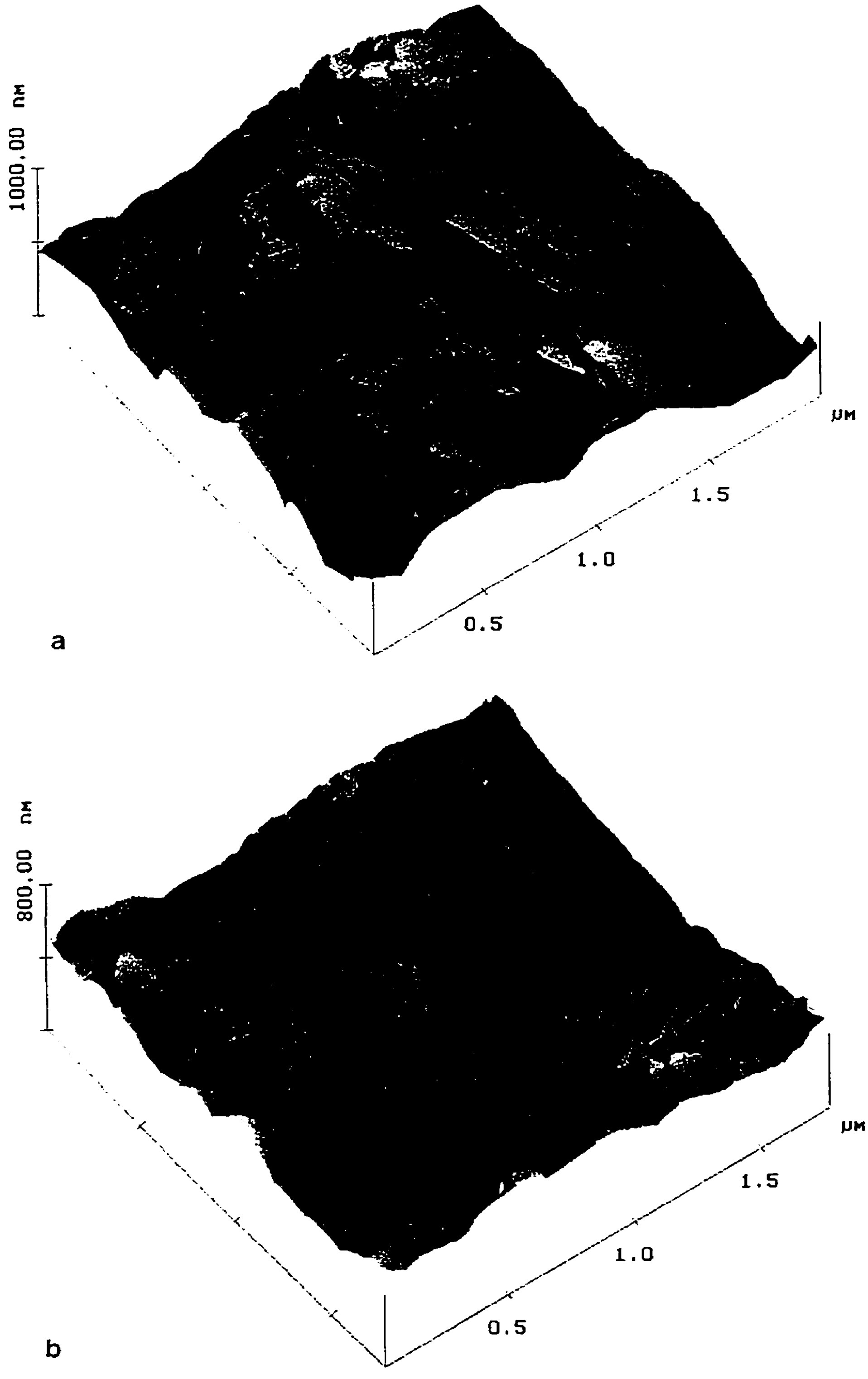

Fig. 7.4. AFM morphology of growth surface of oxides formed on pure and CeO_2-coated Ni crystal faces (1073 K, 15 h): (a) (111)Ni - uncoated; (b) (100)Ni - uncoated; (c) (100)Ni - uncoated - showing the nucleation of new oxide grains at oxide/gas interface; (d) (111)Ni - CeO_2-coated.

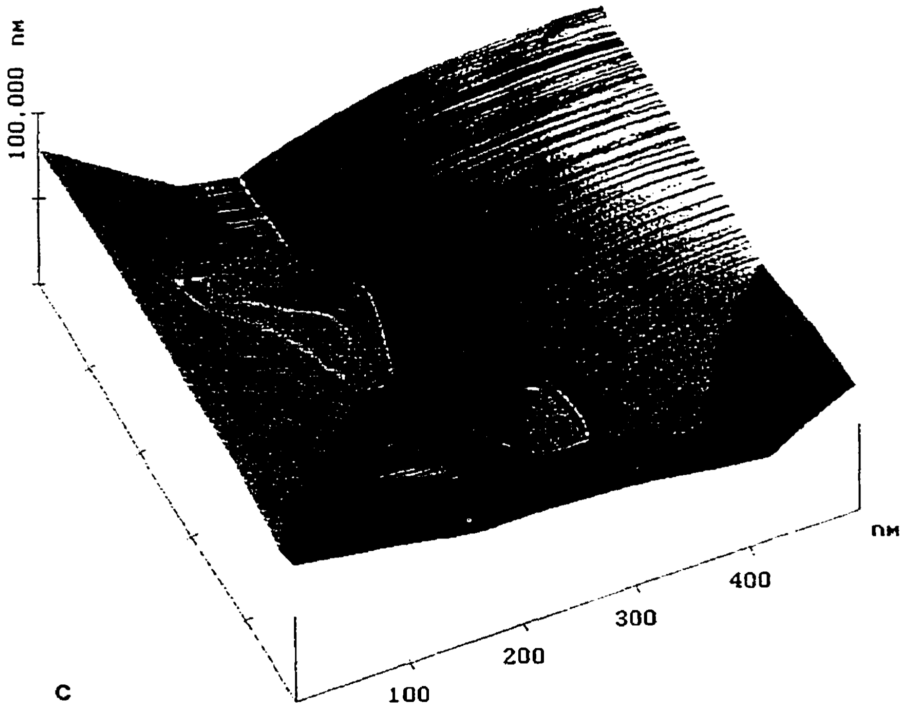

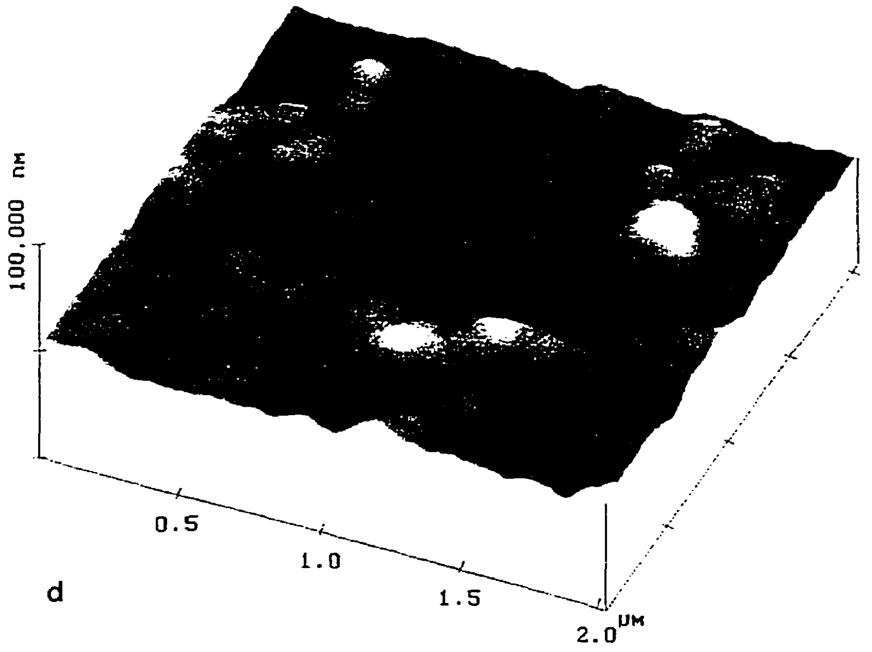

Fig. 7.4. - continued.

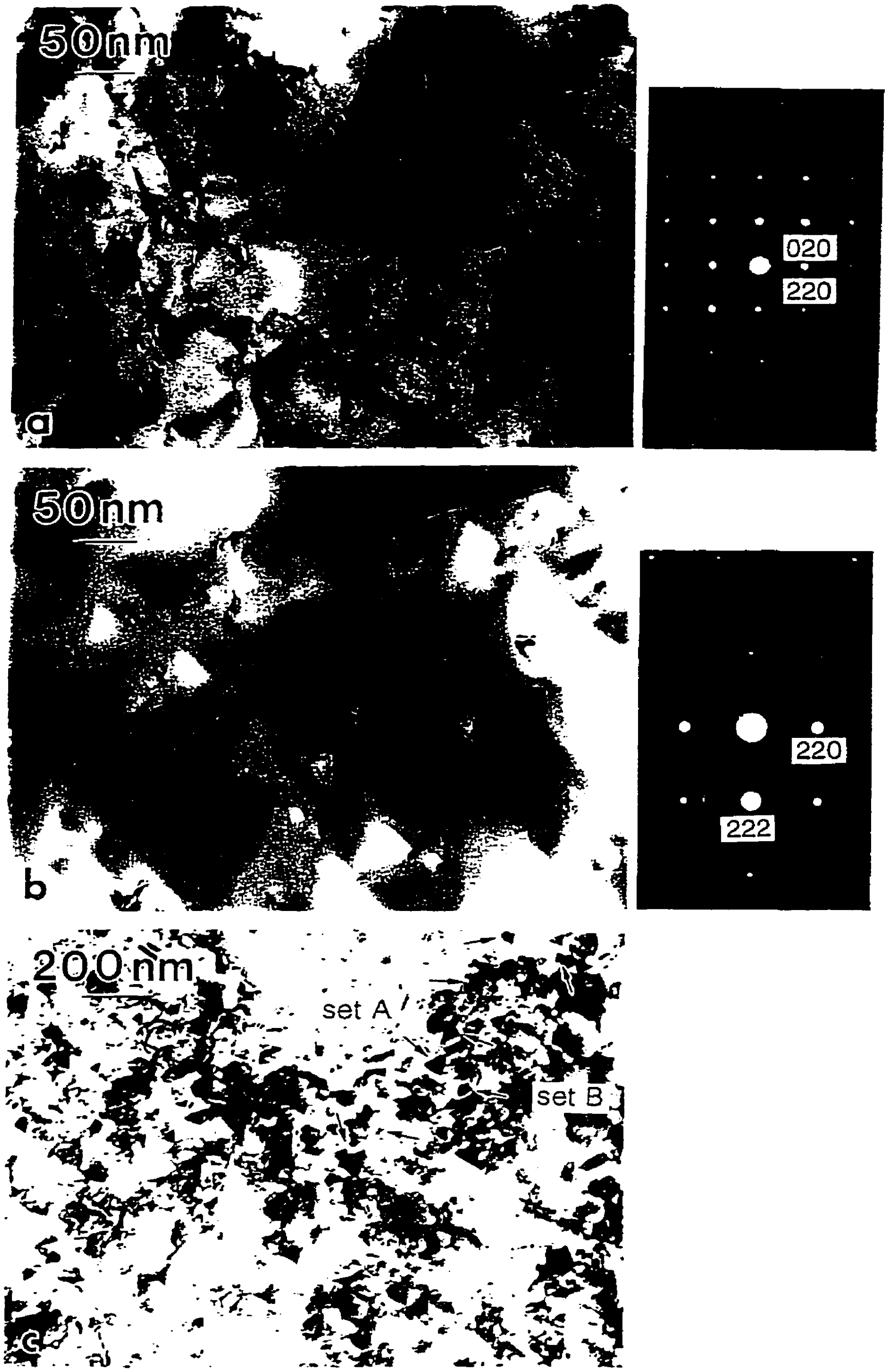

Fig. 7.5. TEM microstructure and SAD pattern for NiO grown at 973 K on pure Ni faces: (a) (100)Ni, beam direction B = [001]; (b) (111)Ni beam direction B = [112], (sample tilted during observation), (c) (111)Ni - two sets of triangular blocks twisted 180 deg with respect to each other are indicated as A and B.

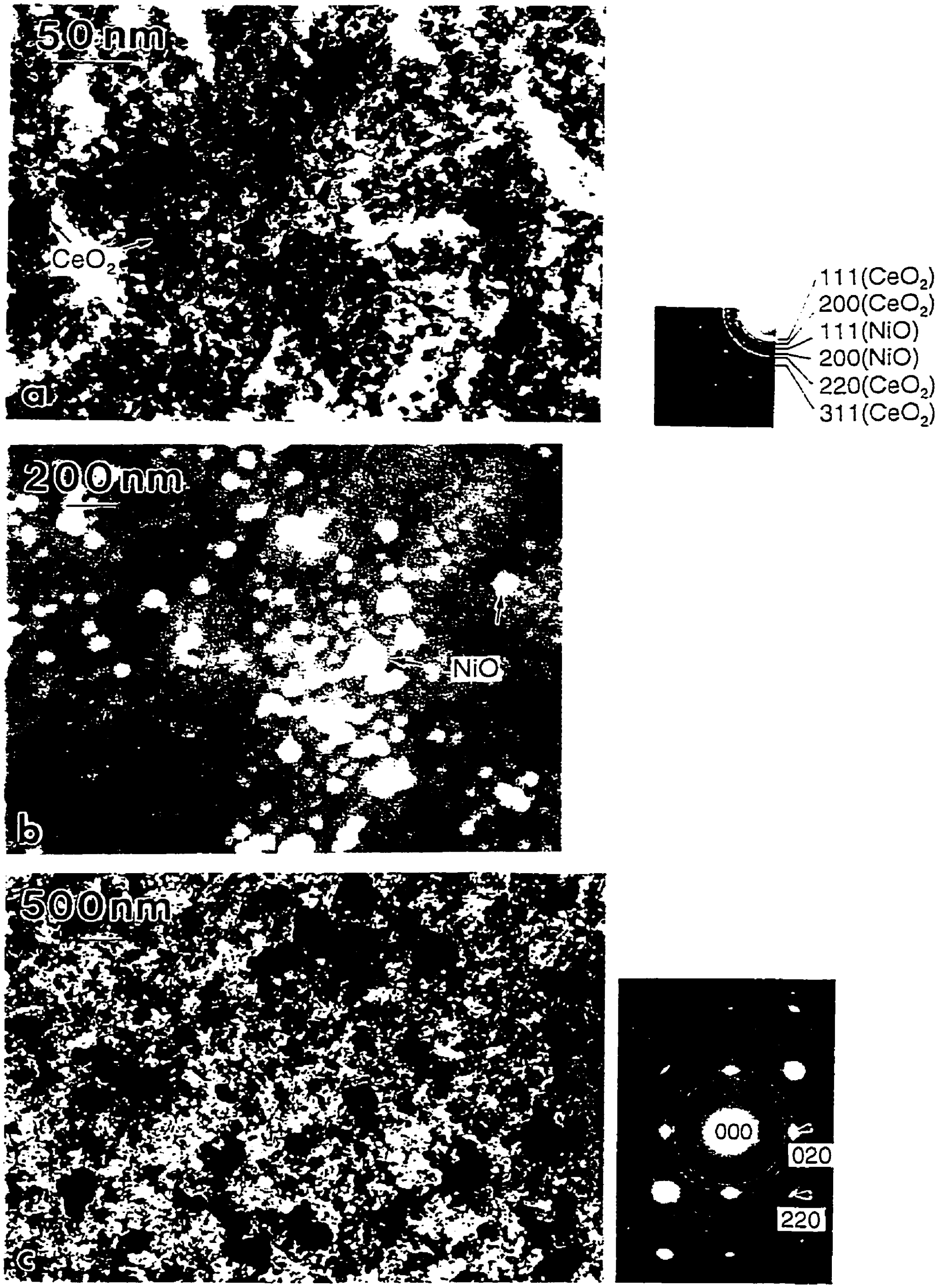

Fig. 7.6. Evolution of microstructure of the oxide grown at 973 K on CeO$_2$ coated (100)Ni: (a) TEM image and SAD pattern of oxide during initial stage of exposure to oxygen (5 min); (b) SEM image of NiO nucleation on the top of CeO$_2$ coating; (c) TEM image and SAD pattern of oxide at steady stage of growth.

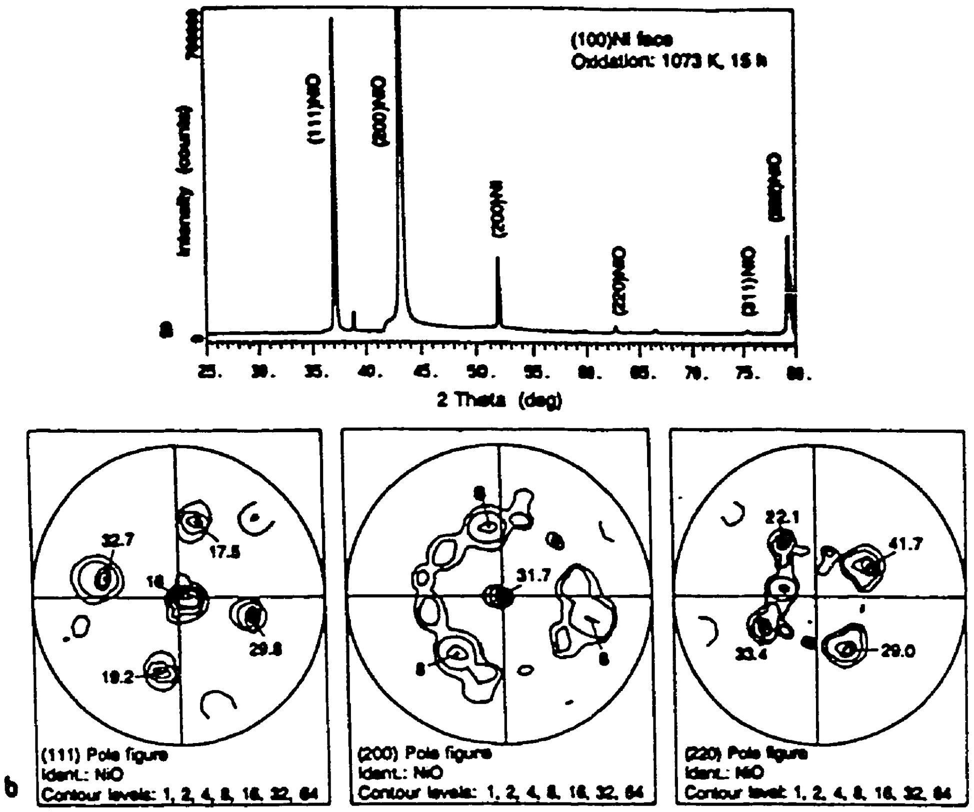

Fig. 7.7. X-ray diffraction pattern (a) and pole figures (b) for oxide formed after 15 h at 1073 K on uncoated (100)Ni.

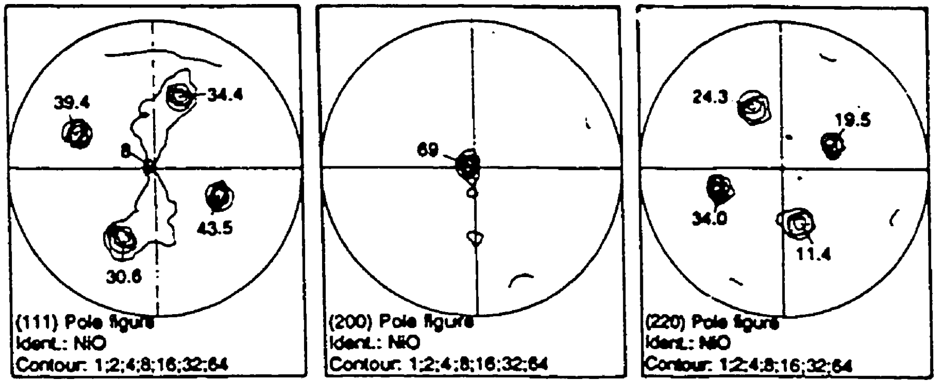

Fig. 7.8. Pole figures for oxide formed after 15 h at 1073 K on (100)Ni - CeO_2-coated.

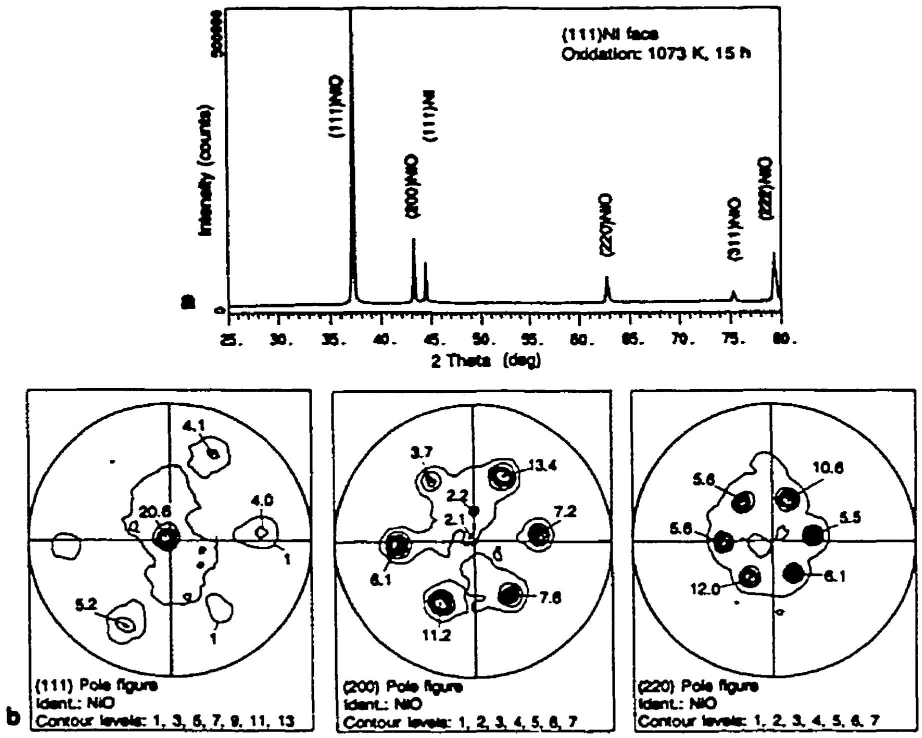

Fig. 7.9. X-ray diffraction pattern (a) and pole figures (b) for oxide formed after 15 h at 1073 K on uncoated (111)Ni.

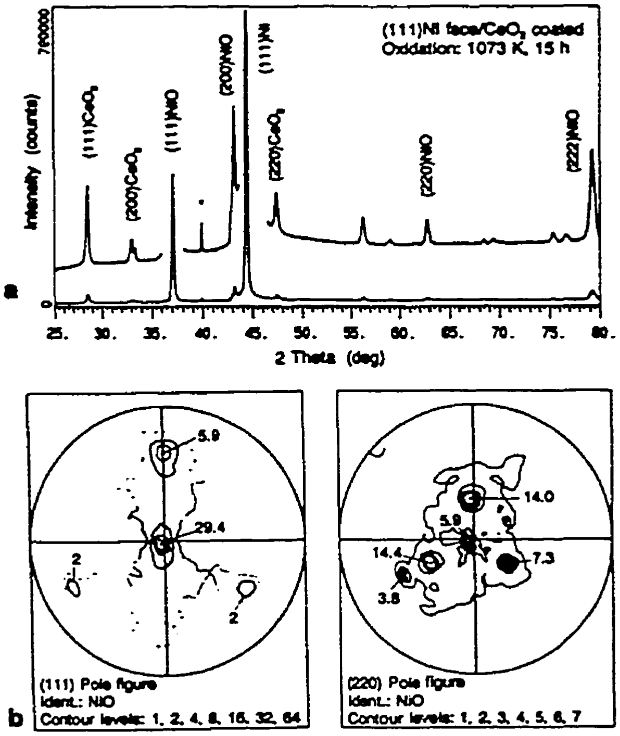

Fig. 7.10. X-ray diffraction pattern (a) and pole figures (b) for oxide formed after 15 h at 1073 K on (111)Ni - CeO$_2$-coated.

CHAPTER 8. THE GROWTH AND STRUCTURE OF THIN OXIDE FILMS ON CERIUM ION-IMPLANTED NICKEL

8.1. Introduction

Ion-implantation was selected as a second technique of surface modification with a reactive element. In this Chapter we investigate the early stages of oxide formation on Ce-implanted Ni, using a number of analytical techniques in order to identify the oxide microstructure and location of the reactive element. The comparison of these results with the previously reported characterization of oxide growth on Ni with surfaces modified by CeO_2 sol coating, gives important insights into the mechanism by which Ce reduces the NiO growth rate.

8.2 Oxide growth kinetics

The decrease in oxygen pressure in the manometric system was converted into the oxygen uptake to calculate the oxidation kinetics. As can be seen in Fig. 8.1, during the very initial stages of exposure to oxygen, particularly during the process of heating-up to 973 K, the Ce implants enhanced the nucleation of oxide and the oxygen uptake was slightly higher than that measured for pure substrate. Shortly after the temperature of 973 K was attained (10 min of exposure), the growth rate of the Ce modified oxide started to decrease rapidly. At this stage of growth, the oxide films had a thickness of about 60 nm, as estimated from the oxygen uptake. After 4 h exposure, the oxide on the implanted substrate with an average thickness of 175 nm, was almost 2.5 times thinner than that grown on pure Ni. Vacuum annealing of implanted substrates at 1073 K before oxidation, decreased the beneficial effect of Ce.

Plots of the log of oxygen uptake versus the log of time revealed that for all the substrates, the oxide growth exhibited an early transient stage followed by a steady-stage reaction. For pure Ni the transient stage lasted about 60 min. After that, the oxidation followed roughly parabolic law with the exponent around 2.2±0.1 The Ce implants shortened markedly the duration of the transient stage: for both implanted substrates, this period was found to last only 12-15 min. There is, however, a difference in the deviations from the parabolic law displayed by the implanted substrates. Whereas the oxidation curve for substrate annealed after implantation exhibited an exponent similar to that for pure Ni, the exponent found for the substrate directly oxidized after implantation was even larger than 2.2±0.1. Other researchers have also observed deviations from the parabolic law after the implantation of reactive elements. Hampikian et al. [1989] even suggest the paralinear equation for oxidation of Ni implanted with Y. Our analysis indicates, however, that the extent of deviation observed in our experiment is still within the margin of experimental error for parabolic relations. Thus, we believe that oxide growth on all the substrates follows roughly the parabolic law after the early transient stage.

Oxidation curves were also analyzed numerically to evaluate the instantaneous rate constants for oxide growth. The values obtained at the beginning and end of the oxidation cycles are shown in Table 8.1. The decrease of the rate constant by a factor of 2, observed in pure Ni, is interpreted in terms of the oxide grain growth [Smeltzer, 1988]. Rapid decrease that is, by more than one order of magnitude measured for implanted Ni, cannot be explained solely by the development of grain size but, as is shown later, can be attributed to the chemical role of Ce implants. Experimental values of oxidation rate constants will be used later during an analysis of the growth mechanism of the oxide.

8.3. The surface morphology of oxide films

Since growth kinetics control oxide surface morphology, the analysis of the oxide/gas interface gives valuable information about the oxidation mechanism. To characterize oxide morphology, two techniques were employed: SEM and AFM. As is shown in Fig. 8.2a, Ce implantation strongly affected the outer surface of the oxide. It is characteristic that after substrate finishing by chemical polishing, which revealed the crystallographic structure of metal grains, large differences in oxide thickness at different grains were observed. Thus, oxide surface morphology depends on the orientation of Ni grain and on the type of Ni grain boundary. Ce implants inhibited the anisotropy of oxidation much more strongly than the reactive element oxide coating (Chapter 6), probably because of radiation damage to the surface layer of Ni during ion bombardment. Simple visual assessment of the growth surface (Fig. 8.2b) indicates a high refinement of oxide grains caused by Ce implants. Because the transport of Ni^{2+} cations along grain boundaries is thought to control the NiO growth at this temperature [Smeltzer, 1988], the finer-grained structure which is accompanied by a lower growth rate, is the important piece of evidence which supports the inhibition of grain boundary diffusion by reactive element implants. Post-implantation annealing caused essential changes of the oxide surface, which was covered with nodules of pure NiO (Fig. 8.2c,d). Such morphology, not observed during the oxidation of pure Ni, suggests the presence in some areas of oxide film, a very fast path for Ni ion transport towards the surface.

An important factor characterizing the surface morphology of thin oxide films is the roughness of the surface. AFM measurements of surface roughness parameters and oxide grain size for pure and modified oxides are given in Table 8.2, together with average thicknesses of oxide films calculated from the oxygen uptake while assuming a flat surface. The oxide grown on the implanted Ni had a surface with the lowest mean roughness R_a (Fig. 8.3). The NiO nodules present on implanted and annealed substrate contributed to the high values of R_a, which were even higher than that measured for pure NiO. For all the oxide films, the values of maximum height R_z exceeded the average oxide thickness. In the case of NiO formed on the implanted and annealed substrate, R_z was more than 4 times larger than the average thickness calculated from the oxygen uptake. For oxides in the thin film range, the knowledge of surface roughness is important during the analysis of depth-composition profiles obtained by RBS, AES and SIMS. Moreover, there is a correlation between surface roughness and the reduction of NiO growth caused by Ce additions (Chapter 6) i.e. the less rough and more stable with time the growth surface is, the higher the reduction of the NiO growth rate caused by Ce. The comparison of kinetic data (Fig. 8.1 and Table 8.1) and the surface morphology description (Table 8.2), seems to support this correlation. The lower the rate of NiO growth, the lower the surface roughness.

TABLE 8.1. Oxygen uptakes and instantaneous values of oxidation rate constants [a)] for the growth of NiO on unimplanted and Ce-implanted Ni (973 K, $p_{O2} = 5\times10^{-3}$ torr).

Ni substrate	Oxidation time 10 min		Oxidation time 240 min	
	$\mu g\ O_2/cm^2$	k_{pi} $(g^2cm^{-4}s^{-1})$	$\mu g\ O_2/cm^2$	k_{pi} $(g^2cm^{-4}s^{-1})$
unimplanted	7.9	4.1×10^{-13}	63.3	2.2×10^{-13}
Ce implanted	8.7	3.3×10^{-13}	25.0	3.0×10^{-14}
Ce impl./anneal	8.6	4.2×10^{-13}	33.3	7.9×10^{-14}

[a)] k_{pi} obtained from numerical analysis of oxidation curves as $2w(dw/dt)$, where w is the oxygen uptake and t is the time of oxidation.

8.4. Cerium depth distribution

Oxidation results in the redistribution of Ce implants within the oxide. In order to determine the location of Ce in NiO, RBS and AES techniques were used.

The RBS spectra of all the implanted and oxidized nickel exhibited a distinct Ce peak (Fig. 8.4a). For oxidized samples, the height of the Ni peak was reduced due to the presence of NiO. Depth profiles derived from those spectra are shown in Fig. 8.4b. The implantation with 2×10^{16} Ce^+/cm^2 resulted in an enrichment of the approximately 50 nm-thick surface region of the Ni substrate, with Ce up to a maximum concentration of 8 at.%. A computer simulation using a Monte Carlo TRIM 91 code [Ziegler and Biersack, 1985] predicted a mean ion range of 24 nm with a half width HM of 12 nm, which is in close agreement with the results of the experiment. After oxidation, the Ce peak was slightly shifted towards the oxide surface, but the maximum Ce concentration remained the same. AES analysis essentially supported the RBS measurements (Fig. 8.5a). Ce was detected in a surface region of the oxide corresponding to 10 min sputtering, whereas the oxide/metal interface corresponded to a sputtering time of 45 min.

Post-implantation annealing affected the distribution of Ce in both Ni and NiO. After 1 h annealing at 1073 K, Ce had moved towards the outer surface of Ni. According to the RBS profile (Fig. 8.4b), after this treatment Ce was located in a 10 nm thick surface region of Ni, with a maximum concentration of 20 at.%Ce. RBS shows again that, after oxidation, the Ce peak was slightly shifted towards the oxide surface. To interpret correctly the RBS/AES data, the roughness of the oxide surface should be taken into account. An analysis indicates that Ce is present in the outer part of the compact part of the oxide which is covered with NiO nodules having a height up to 1035 nm (Table 8.2). Such a distribution is essentially different from that observed in NiO formed directly after implantation.

TABLE 8.2. AFM analysis of surface morphology of oxides formed on unimplanted and Ce-implanted Ni (973 K, 4 h, 5×10^{-3} torr oxygen).

Ni	Average thickness	Mean rough. (nm)		Max. height (nm)		Grain size b) (nm)	
substrate	a) (nm)	R_a	σ	R_z	σ	g	σ
unimplan.	443	140	21	1103	167	1000	55
implanted	175	33	6	220	76	40	7
impl./ann.	233	151	16	1035	183	320	37

a) - thickness calculated assuming negligible surface roughness and NiO density-6.67g/cm^3

b) measured by AFM software as an average of 500 grains

The extremely high affinity of Ce to oxygen caused the formation of CeO_2 during annealing, despite the ultra high vacuum of 10^{-9} torr applied. This conclusion can be drawn from the AES spectrum in Fig. 8.5b, which shows a correlation between concentration profiles for oxygen and cerium. Thus, two kinds of substrates modified by ion-implantation were used for oxidation. The unannealed Ni substrates contained Ce implants and surfaces damaged by ion bombardment. Conversely, the vacuum-annealed substrates contained CeO_2 and the surface recrystallized from radiation damage.

8.5. X-ray diffraction analysis of phase composition

X-ray analysis shows that oxides formed on both implanted substrates are polycrystalline (Fig. 8.6a,b). It is characteristic that CeO_2 was only detected in oxide grown on a pre-annealed substrate. Since all the substrates were simultaneously implanted with the same doses of Ce, the only difference between them is the size of the CeO_2 particles (this will be seen later during TEM observations). It is possible that the ultra-fine CeO_2 particles, present in oxide grown on Ni directly oxidized after implantation, were also partially dissolved in oxide grain boundaries. Thus, the remaining amount was unable to produce peaks of intensity higher than the noise level. An additional difference in the diffraction patterns shown in Figs 8.6a and 8.6b, can be seen in the NiO peak intensities. The comparison with the JCPDS standard suggests the presence of {111} texture in oxide formed on an annealed substrate. However, during such a comparison, slight differences in the intensities of Ni peaks must be taken into account. Because of very thin oxide films, our attempt at a direct measurement of the oxide texture, using a conventional texture goniometer, was unsuccessful.

8.6. Analytical electron microscopy of the oxide microstructure

8.6.1. Oxide formed on Ni directly oxidized after implantation

The nonuniform concentration of elements versus oxide thickness, as found by RBS and AES, suggests the complex depth structure of the oxides. Therefore, thin foils were prepared to expose the three main layers of the oxide structure: i) the region close to the oxide/gas interface, ii) the middle part, and iii) the zone close to the oxide/metal interface. In these sublayers an essentially different microstructure was found by TEM. To specify the sublayer location inside the oxide film, the thin foil thickness was calculated from the EEL spectrum by the relation 3.1 [Leapman et al., 1984].

The thin foils for examining the outer region of the oxide were prepared by ion sputtering from the metal side. In this sublayer, the TEM revealed the nanocrystalline structure composed of CeO_2 and NiO phases (Fig. 8.7a). The film thickness, calculated from the EEL spectrum in Fig. 8.7b, was found to be 35 nm. The Ce concentration, estimated from the high energy-loss part of the EEL spectrum (Fig. 8.7b, inset), is the highest of all the other sections in this oxide.

In order to examine the oxide structure beneath the outer part, the sample was first separated from the substrate. After, it was thinned by sputtering using Ar ions from the oxide/metal side for time intervals two times longer than form gas/oxide side. A typical TEM microstructure of this region is shown in Fig. 8.8a. The essential difference between this microstructure and that in the outer sublayer is the larger NiO grain size. It is seen that CeO_2 particles are distributed randomly inside the oxide grains and at the oxide grain boundaries. The SAD and convergent beam diffraction pattern (CBDP), obtained with a beam size of 20 nm, confirmed the NiO and CeO_2 phases (Fig. 8.8b). Unfortunately, the reflections on CBDP from the CeO_2 are so weak that only {111} spots are visible. The weakness of the other CeO_2 diffraction spots makes it difficult to identify the zone axis and to find the orientation relationship between phases. As estimated from the EELS spectrum in Fig. 8.8c, using the equation 3.1, is 66 nm. This means that approximately 40 and 80 nm-thick layers were removed during sputtering from the gas/oxide and metal/oxide sides, respectively. As is seen in the high energy-loss part of the spectrum (Fig. 8.8c, inset), the Ce concentration in this region is lower than that detected above in the outer part. To assess the size of CeO_2 particles, the TEM micrographs were quantitatively examined by an image analyzer. It was found that an average size of CeO_2 particles is 3.14 nm and the particle size has a distribution as illustrated in Fig. 8.8d. The volume fraction of the CeO_2 phase, estimated from surface analysis, is 4.2%.

Because of the small size of NiO and CeO_2 phases, a microchemical analysis was performed by STEM, with a beam spot size of 3.5 nm. The images of the region selected for analysis, obtained by TEM and STEM, are shown in Fig. 8.9a and 8.9b, respectively. Typical EDX spectra from CeO_2 particles and from the NiO matrix are shown in Fig. 8.9c. The key factor of the microchemical analysis was the detection of Ce segregation in NiO grain boundary. Since the presence of the CeO_2 particle in the NiO grain boundary would affect the segregation measurement, the region for analysis was selected where STEM imaging under the highest available magnification did not detect the presence of CeO_2 particles (Fig. 8.9d). The EDX analysis across the grain boundary proved the existence of Ce segregation (Fig. 8.9e). Since the beam spot size used (3.5 nm) was larger than the grain boundary width, the real Ce concentration may have been higher than values shown in Fig. 8.9e. The comparison of RBS/AES depth profiles and EELS analysis indicates that the two sublayers described above cover the Ce-rich part of the oxide.

To examine the region near the metal/oxide interface, the oxide was ion-milled from the gas side only. As is seen in Fig. 8.10, this part of the oxide consisted almost entirely of pure NiO grains with sizes of up to 1 μm. In general, the NiO grains near the substrate/oxide interface were randomly oriented.

8.6.2. Oxide formed on the Ni substrate annealed after implantation

A different structure of the oxide was observed after annealing of the implanted Ni. The NiO nodules with a maximum height up to 1035 nm (Table 8.2) were removed during specimen preparation and thin foils covered the compact part of the oxide. A typical TEM image of the outer part obtained by sputtering from the oxide/metal side only is shown in Figs. 8.11a and 8.11b. In this oxide, the ultra fine-grained layer of NiO and CeO_2, which had been observed previously (Fig. 8.7), was absent. The characteristic feature was a markedly larger size of CeO_2 particles. In addition to particles having a size in the range of 8-10 nm, a larger fraction of particles with a size up to 40 nm was also present (Fig. 8.11c). The large CeO_2 particles were probably formed by the coalescence of small particles during vacuum annealing, as was observed for the CeO_2 coating (Chapter 6). The TEM foil obtained by thinning the oxide from the gas/oxide interface, consisted essentially of randomly oriented NiO grains with sizes of 1-2 μm.

8.7 Summary

The Ce implant dose of 2×10^{16} ion/cm^2 caused a significant decrease in the oxidation rate of polycrystalline nickel at 973 K. Radiation damage introduced by ion bombardment caused a slight increase in the NiO growth rate during the initial stage.

However, the essential improvement in oxidation resistance was derived entirely from the chemical role of the implants. The beneficial effect of Ce was reduced when the implanted substrate was vacuum-annealed at 1073 K prior to oxidation. The NiO films formed on Ni directly oxidized after implantation, have a uniform surface morphology and are composed of three distinct sublayers, each with an essentially different microstructure and Ce concentration. The Ce implants are present near the oxide surface in the form of CeO_2 particles which have an average size of 3 nm and are randomly distributed within NiO grains and at NiO grain boundaries. In the oxide sublayer, where CeO_2 particles are present, the Ce ion segregation at NiO grain boundaries has been detected. When the oxidation takes place after vacuum annealing at 1073 K, the oxide growth surface is nonuniform and is covered with NiO nodules. In this case, CeO_2 particles have an average size of 8.4 nm and are present in that part of the oxide film which grew beneath the NiO nodules.

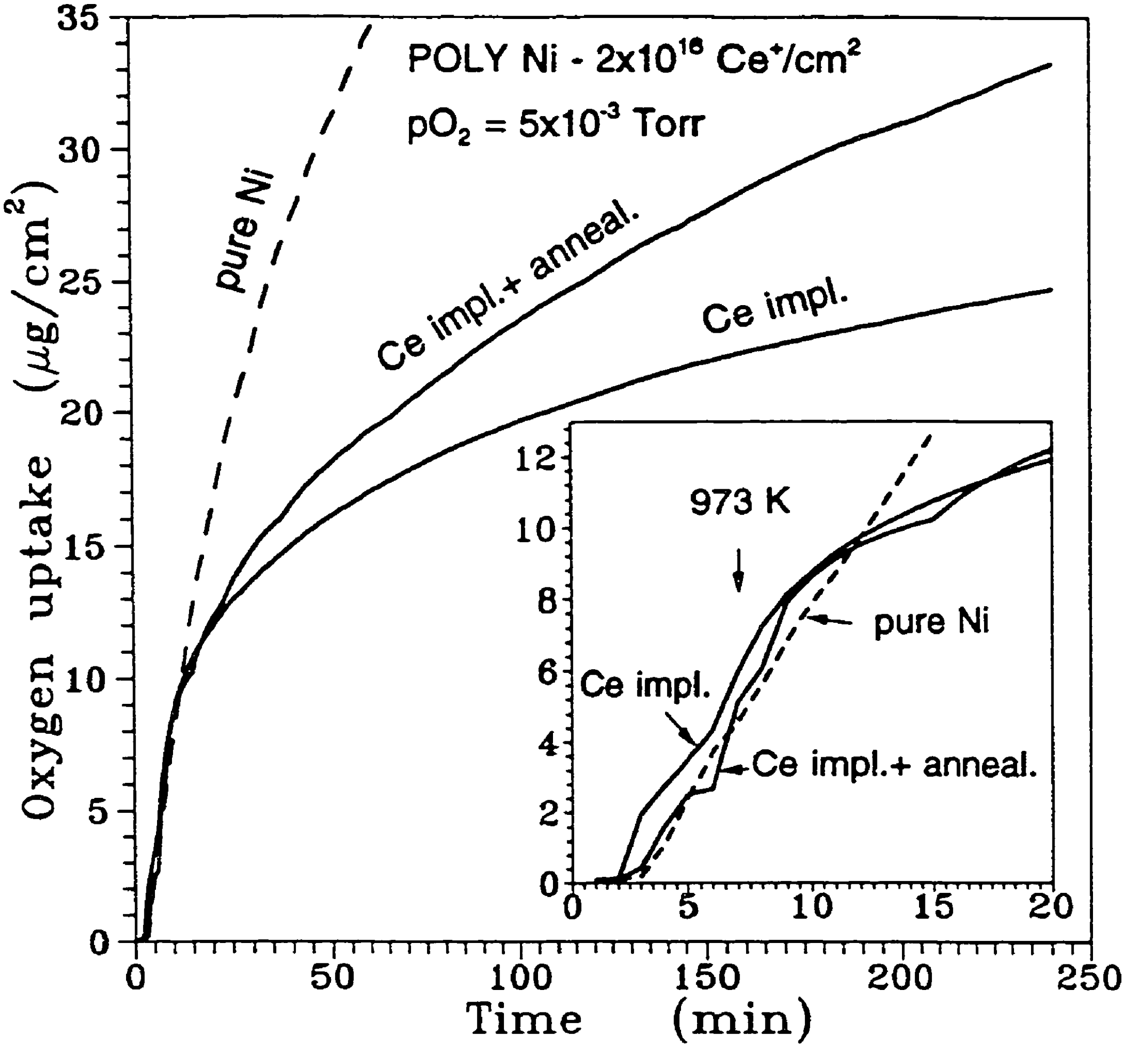

Fig. 8.1. Oxidation kinetics at 973 K of pure and Ce-implanted nickel. Initial stage of oxidation is shown in the inset. Time when the temperature of 973 K was attained is indicated by the arrow.

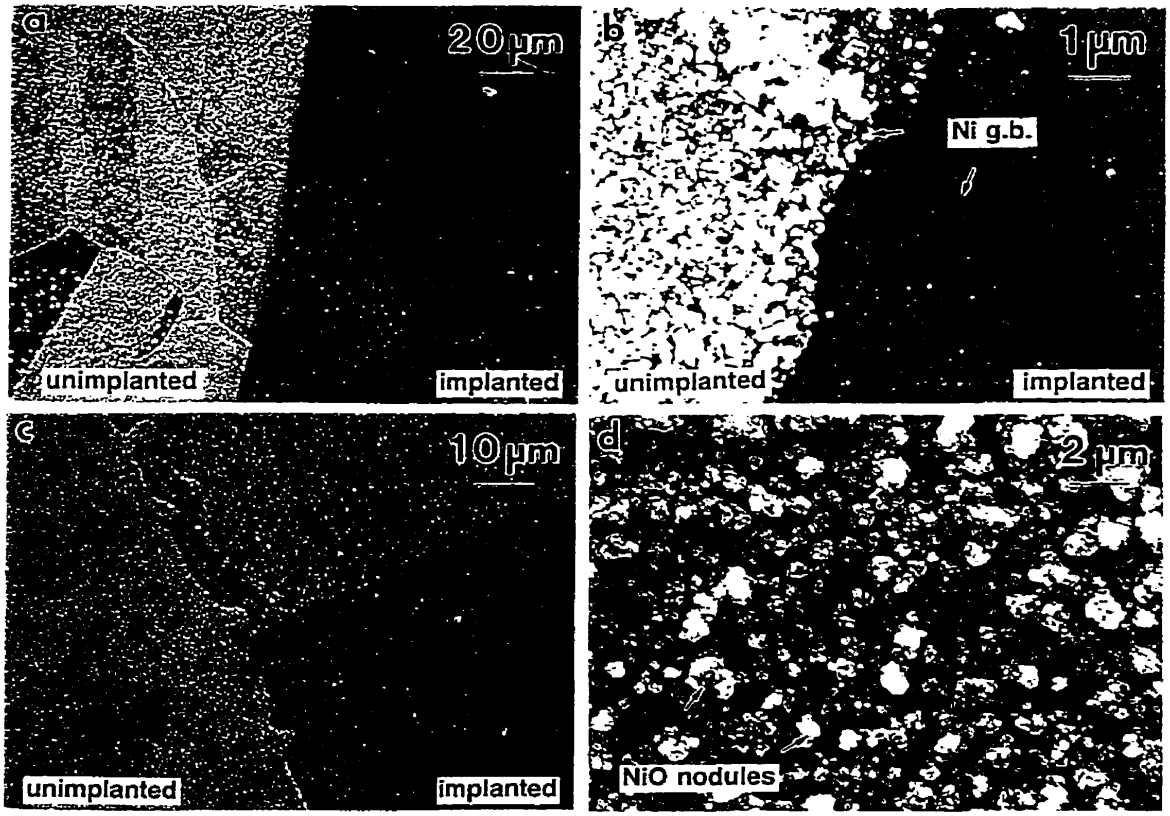

Fig. 8.2. SEM surface morphology of oxide films grown at 973 K for 4 h on Ni directly oxidized after implantation with Ce (a,b), and oxidized at 973 K for 4 h after post implantation vacuum annealing at 1073 K for 1 h (c). Nodules from implanted part of sample (c) are shown in (d).

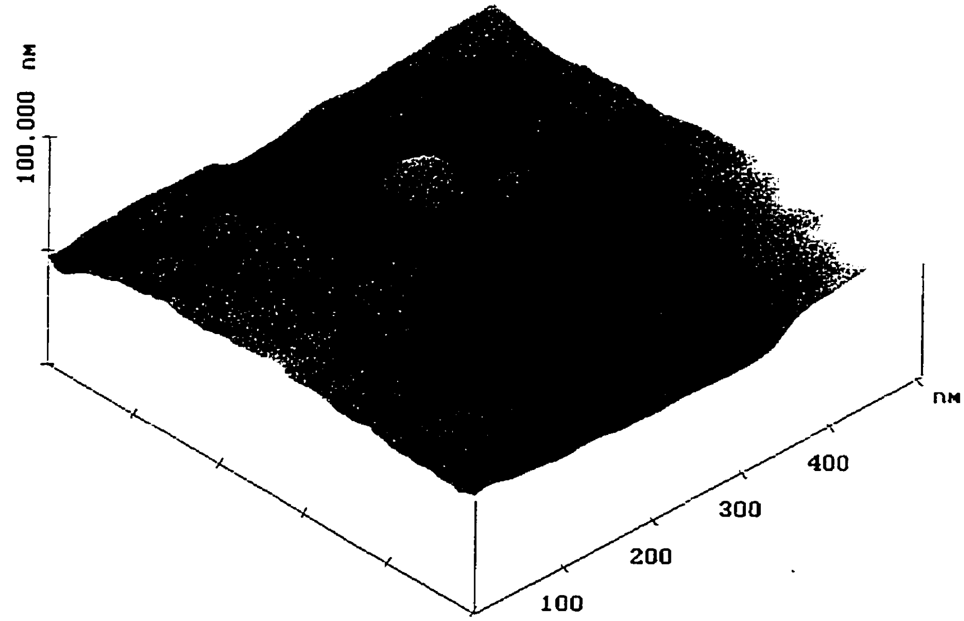

Fig. 8.3. AFM surface morphology of oxide film formed at 973 K for 4 h on Ni directly oxidized after implantation with Ce.

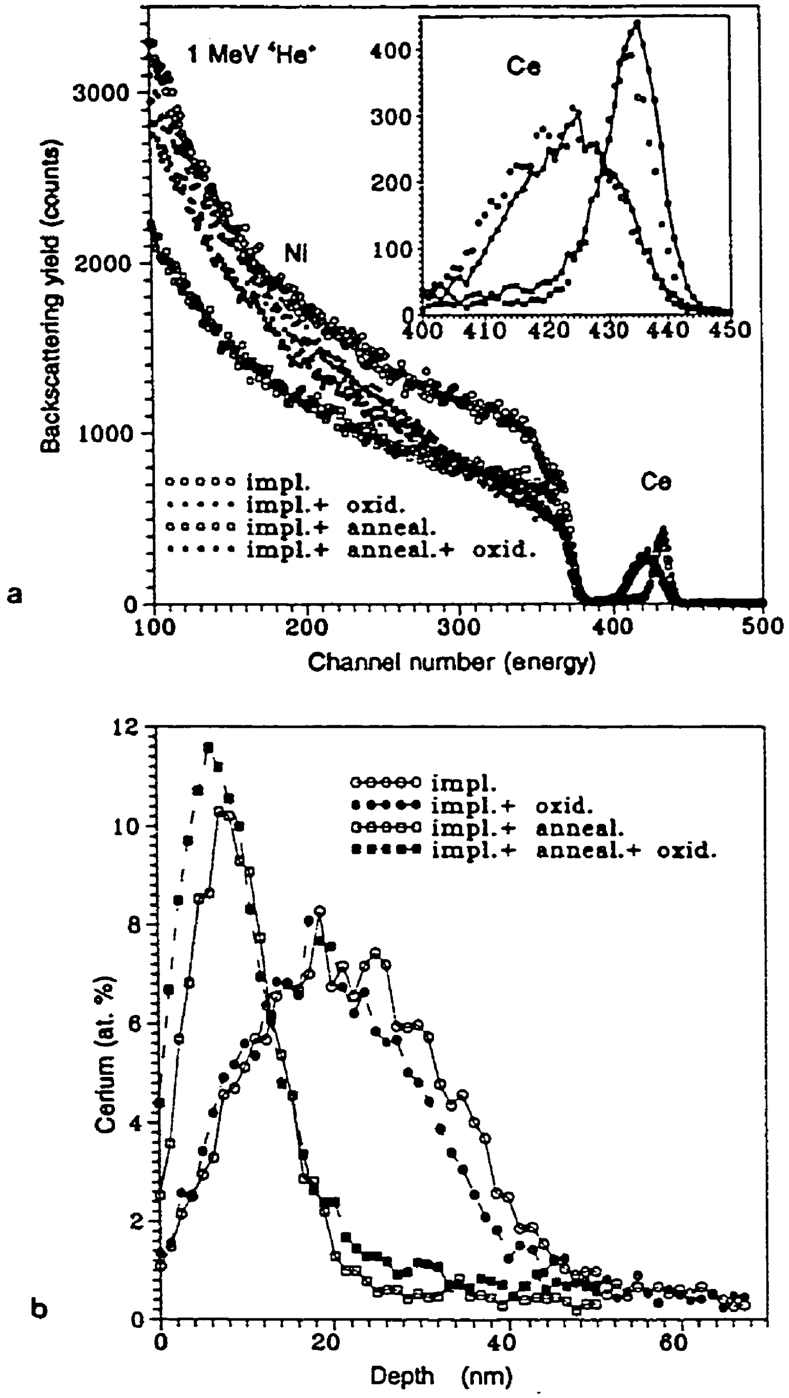

Fig. 8.4. RBS measurements of Ce distribution in Ni and in NiO: (a) energy spectra of backscattered 1MeV $^4He^+$ ions; (b) Ce concentration- depth profiles derived from spectra shown in (a); estimated resolution is 11.5 nm for as-implanted samples (Ni) and 12.2 nm for oxidized samples (NiO).

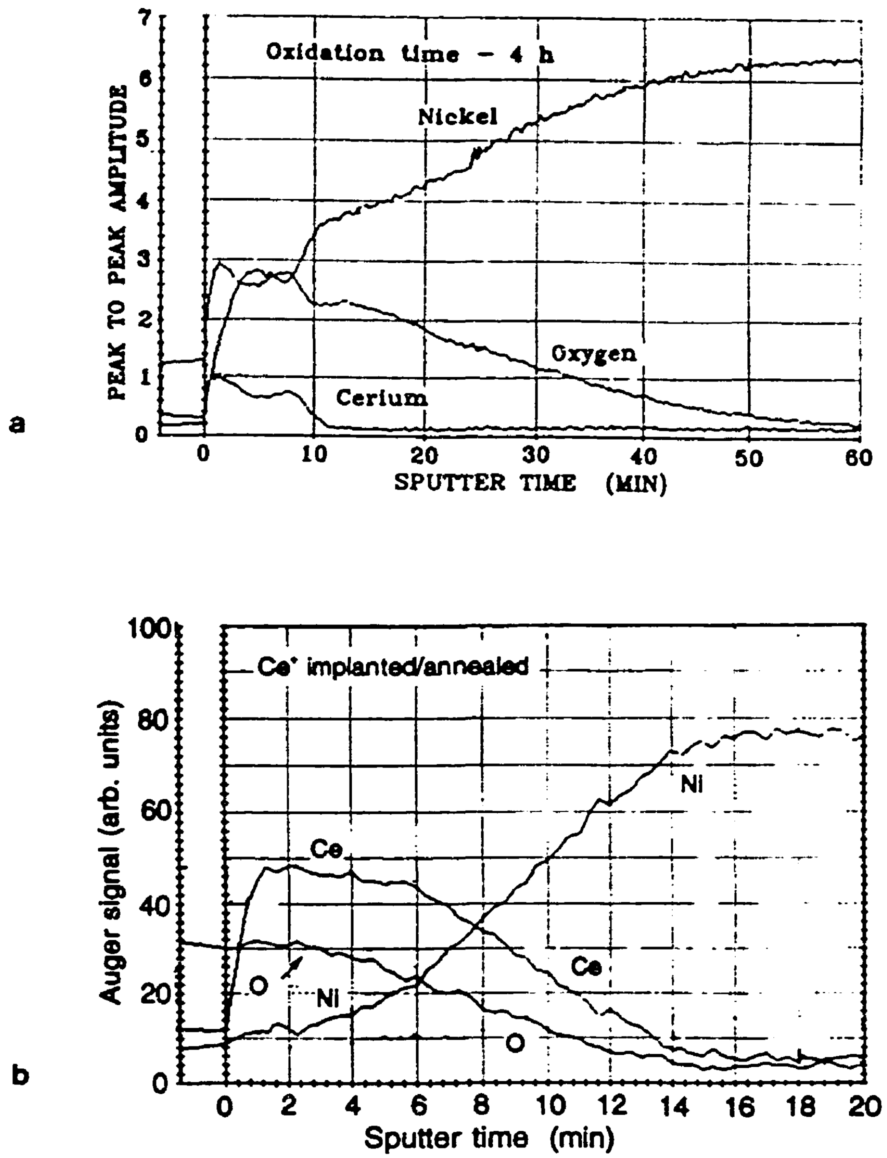

Fig. 8.5. AES analysis of Ce distribution in NiO formed for 4h at 973 K on Ni directly oxidized after implantation (a) and in Ni after implantation and vacuum annealing at 1073 K for 1 h (b).

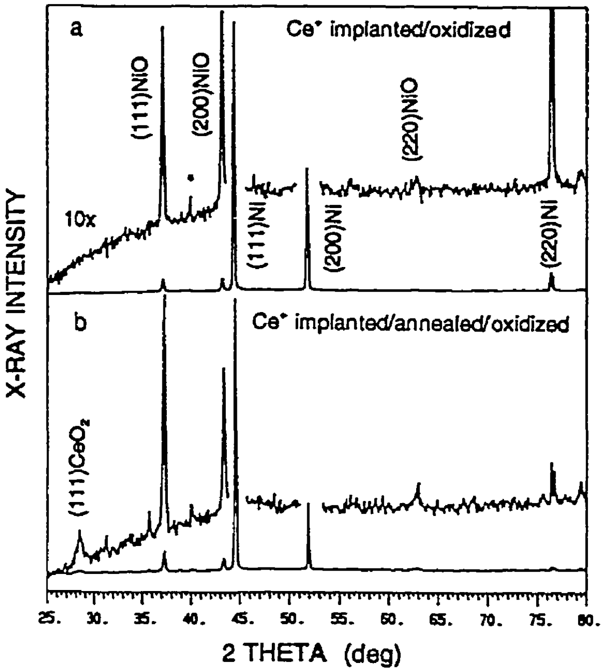

Fig. 8.6. X-ray diffraction patterns of oxides formed on Ni directly oxidized after implantation (a) and oxidized after post implantation vacuum annealing at 1073 K (b), *) diffraction peak of Pt from a thermocouple spot-welded to the specimen.

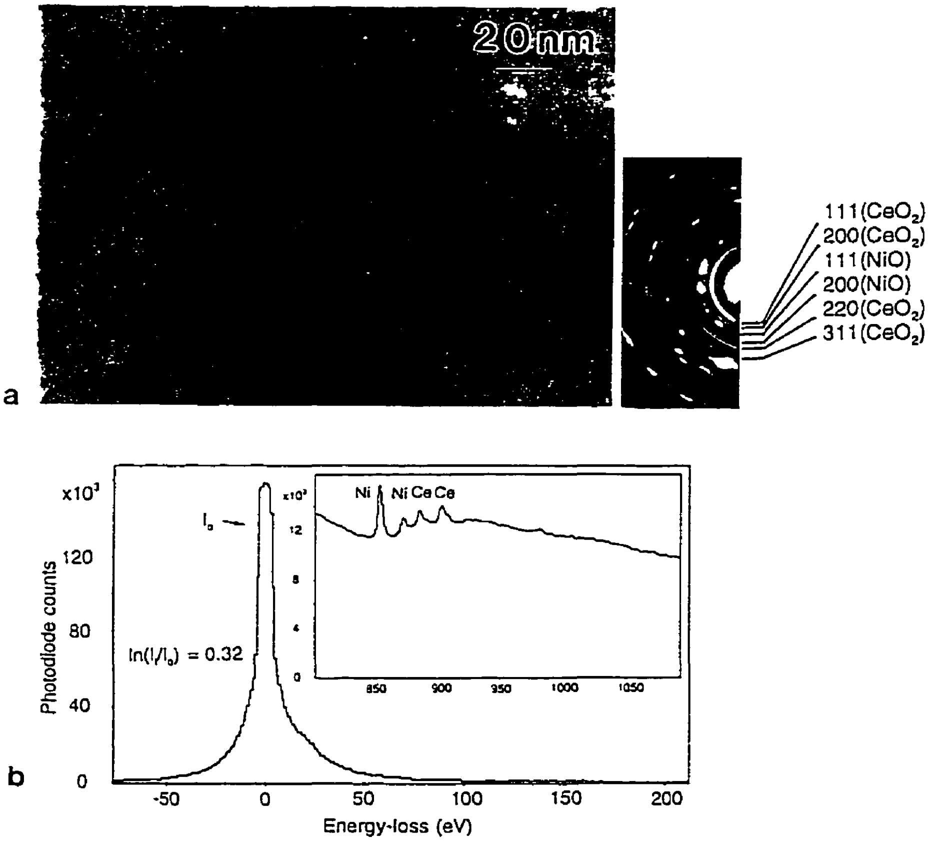

Fig. 8.7. TEM microstructure of outer part of the oxide formed on Ce implanted Ni: (a) bright field image and SAD pattern; (b) EELS spectrum from region shown in (a), high loss-energy part is shown in the inset.

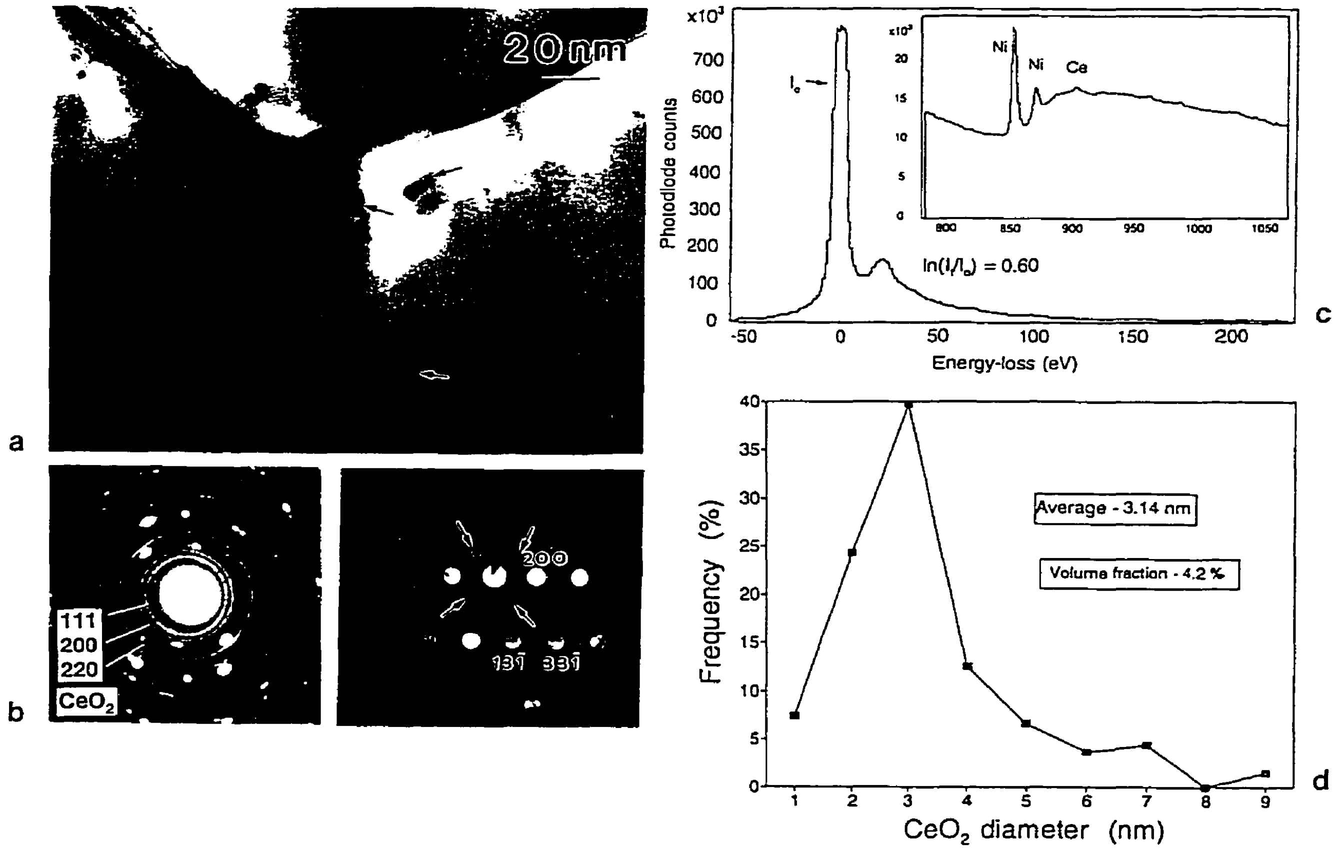

Fig. 8.8. TEM microstructure of the middle part of the oxide, foil thickness 66 nm: (a) bright field image of the triple point in the oxide, CeO_2 particles are indicated by arrows; (b) SAD pattern from area shown in (a) and CBDP from a CeO_2 particle, where [013] NiO zone axis are labelled by indices and {111} spots for CeO_2 are indicated by arrows; (c) EELS spectrum, high loss-energy part is shown in the inset; (d) distribution of CeO_2 particle size.

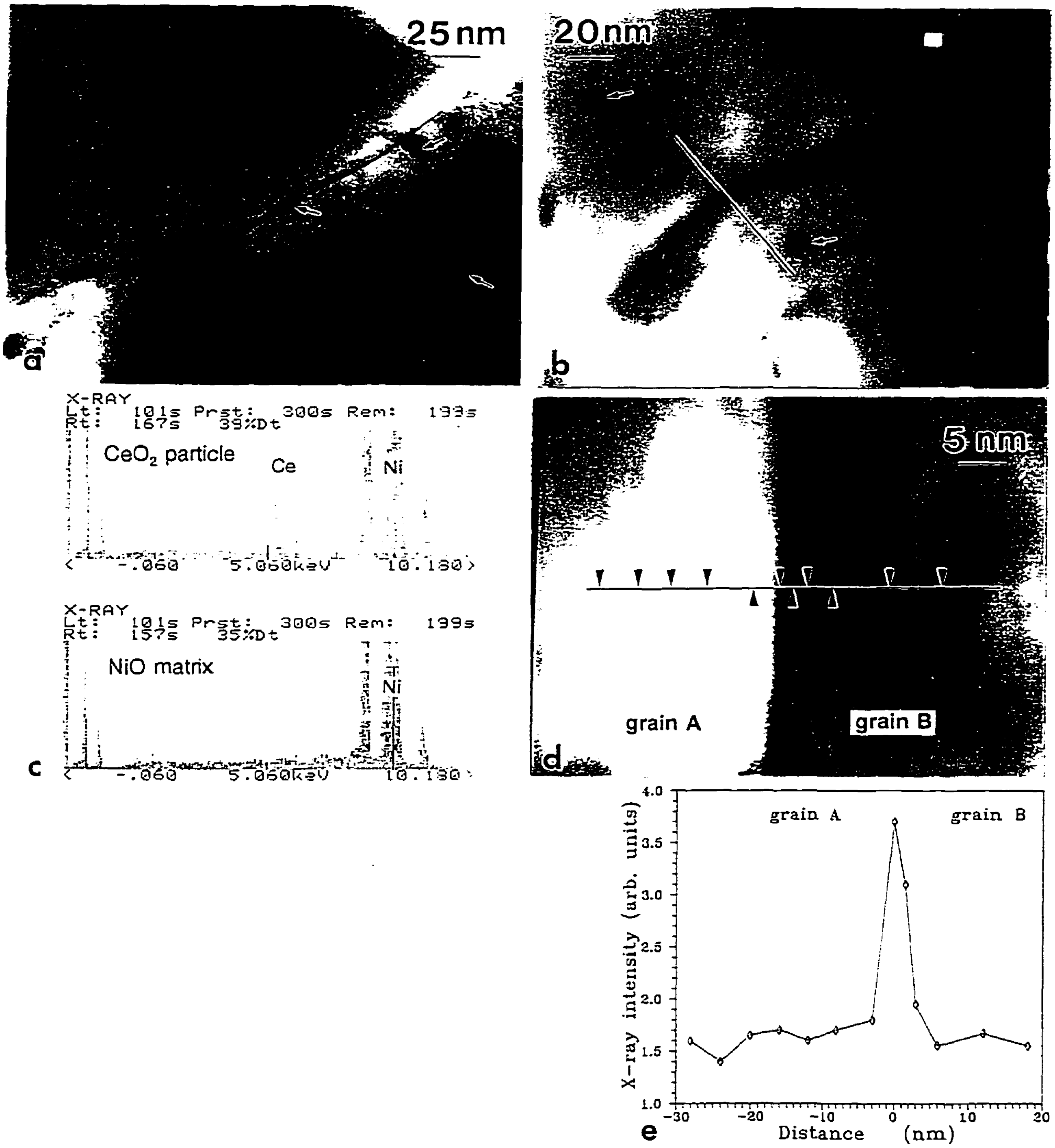

Fig. 8.9. Microchemical analysis of the oxide: (a) TEM image showing CeO_2 particles at NiO grain boundary and inside grains, some of them are indicated by arrows; (b) STEM image of area shown in (a); (c) STEM/EDX spectra from CeO_2 particles and NiO matrix; (d) STEM image of grain boundary region; (e) EDX analysis of Ce concentration along line shown in (b,d).

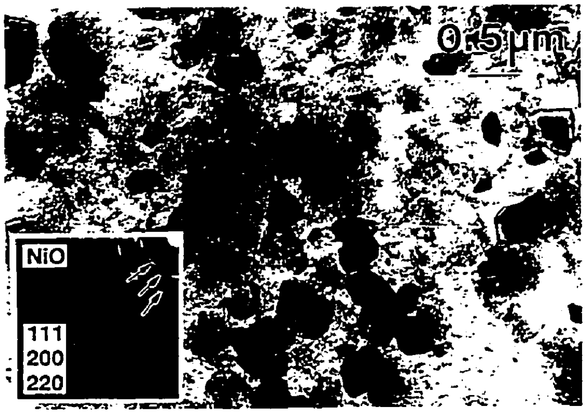

Fig. 8.10. TEM image and SAD pattern of near substrate region of NiO grown on Ni directly oxidized after implantation.

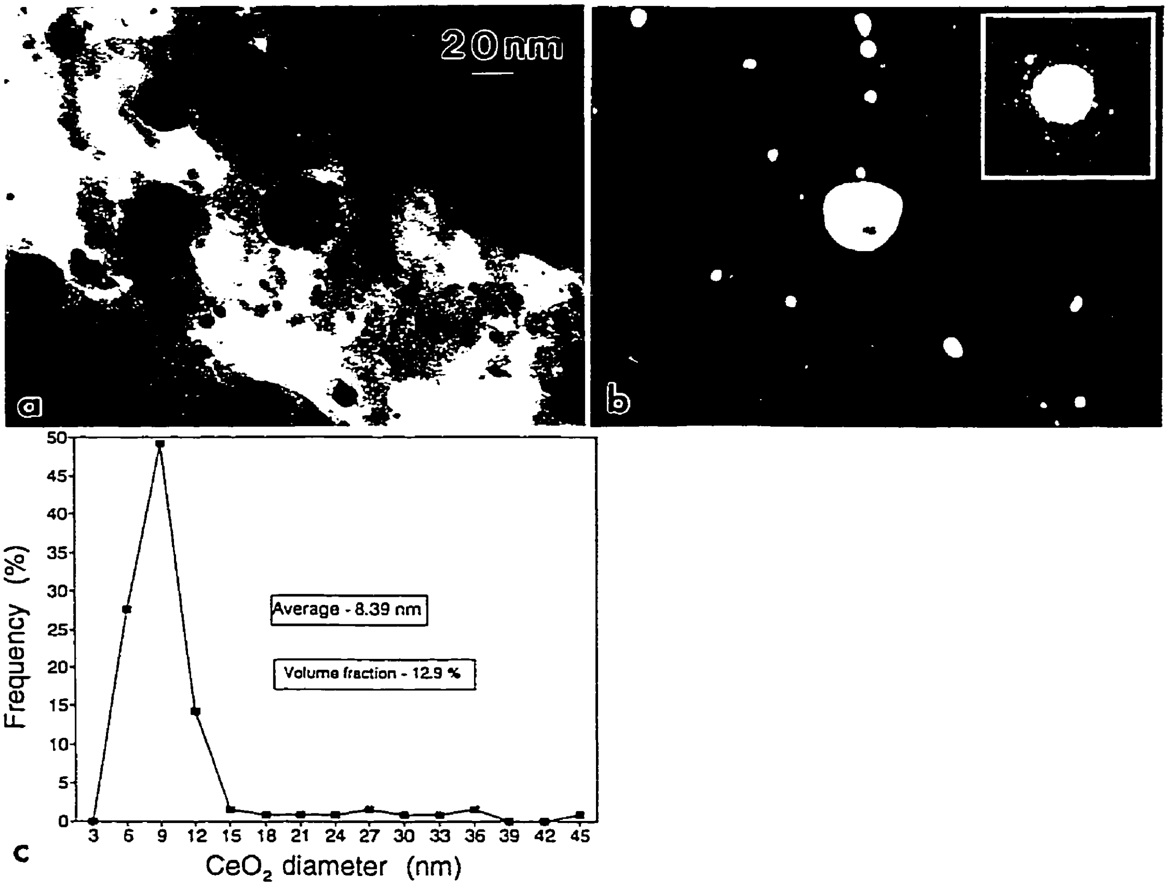

Fig. 8.11. CeO_2 particles in outer part of oxide grown on Ce implanted Ni, annealed after implantation at 1073 K: (a) bright field image; (b) dark field image of the same area in the illumination of (200) of CeO_2; (c) distribution of CeO_2 particle size.

CHAPTER 9. STEADY-STAGE GROWTH OF NICKEL OXIDE ON CeO_2 SOL-COATED POLYCRYSTALLINE NICKEL

9.1. Introduction

The experiments reported in previous Chapters showed that the superficially applied Ce/CeO_2 caused a significant improvement in Ni oxidation resistance during early-stages of exposure to oxygen. Thus, the important technological question arises: how long can such a trace amount of the reactive element provide the protection against high-temperature oxidation. In order to answer this question, the long-term oxidation behaviour of the $Ni-NiO-CeO_2$ system is examined in this Chapter. The comparison of early-stage and long-term experiments will allow us to assess the factors which control the lifetime of protection by the surface applied reactive element.

9.2. Oxide growth kinetics

In order to assess the influence of CeO_2 sol-gel coatings on NiO formation, the oxidation kinetics for uncoated and coated Ni substrates were measured. The gravimetric data, plotted as the weight gain versus time, are shown in Fig. 9.1. For coated specimens the results were divided into two groups: one for coatings with a weight of 10-20 $\mu g/cm^2$ and the second for coatings of 25-30 $\mu g/cm^2$. Assuming fully dense CeO_2, a 10 $\mu g/cm^2$ corresponds to the thickness of 14 nm [Nelson et al., 1981]; i.e. the coatings used had thicknesses in the range of 14-42 nm. It is found that CeO_2 significantly decreased the Ni oxidation rate and that the oxidation of both uncoated and coated Ni during the steady stage roughly obeyed the parabolic law. However, a larger deviation from parabolic law was observed for thicker coatings of 25-30 $\mu g/cm^2$.

The values of the parabolic rate constants, calculated from gravimetric measurements after 5 and 125 h exposures, are shown in Table 9.1. A comparison shows that the reduction in the rate constant caused by CeO_2 after 125 h is in the range of 20-45 times, which is greater than the 12-14 times reduction achieved after 5 h exposure, or 3-6 times reduction reported previously for much thinner oxides grown for 4 h at low oxygen pressure (Chapters 5 and 6). It should be noted that an increase in the above ratios was caused almost entirely by the decrease in the rate constant of CeO_2 modified NiO (Table 9.1). Only slight changes in the growth rate constant of pure NiO were detected. In order to compare in detail the kinetic data for NiO, which were reported in Chapter 5 and obtained at oxygen pressure of 5×10^{-3} torr and the present data, the conversion of rate constants to the same oxygen pressure is necessary. Such a conversion allows us to make a general conclusion from the kinetic measurements that for a time period of 125 h, the effectiveness of Ce in inhibiting Ni ion diffusion through NiO, was significantly increased.

TABLE 9.1. Parabolic rate constants k_p ($g^2cm^{-4}s^{-1}$) for oxide growth on pure and CeO_2 coated Ni at 973 K and 760 torr O_2.

Oxidation time	Uncoated Ni	Ni coated with 10-20 $\mu gCeO_2/cm^2$	Ni coated with 25-30 $\mu gCeO_2/cm^2$
125 h	1.20×10^{-12}	2.70×10^{-14}	5.80×10^{-14}
5 h	9.68×10^{-13}	6.81×10^{-14}	8.15×10^{-14}

9.3. Depth location of the reactive element in the oxide

The RBS technique was used to measure the oxide depth composition. Since the RBS system used an analyzed oxide area which corresponds to approximately 100 grains of Ni, the results can be considered as an average for the polycrystalline Ni substrate.

For all the specimens analyzed, the RBS spectra exhibited a distinct Ce peak (Fig.

9.2, inset), which was shifted to lower energies (channel numbers) with increasing oxidation time. The reduced height of the Ni peak indicates the formation of NiO. The Ce-concentration profiles derived from the above spectra, assuming NiO matrix and following the procedure described by Chu et al. [1978], show that after a longer oxidation time the Ce is shifted towards the oxide/metal interface (Fig. 9.2). However, a comparison of the Ce profiles and the average oxide thicknesses estimated from weight gain data (Fig. 9.1) indicates that for all specimens, Ce was still located close to the outer surface of the oxide. For example, after 75 h exposure, the Ce peak was detected at a depth of 55 nm, whereas the average oxide thickness was about 950 nm.

9.4. Surface morphology

Differently-oriented grains of uncoated Ni oxidized at a rate dependent on their crystallographic orientation. This is illustrated on the optical micrograph of the oxide surface after 38 h exposure (Fig. 9.3a). A pattern of a different contrast on this micrograph is caused by interference colours and the darker areas correspond to the thicker oxide scale. It should be mentioned that the interference colours were used in earlier studies by Young et al. [1956] as a means of determining the thickness of the oxide films grown on Cu single crystals. The SEM observations of the same semiconductor NiO were done without the application of an additional conductive layer which is often deposited to improve conductivity. The thicker areas in SEM micrographs, therefore, gathered more electrons than thin areas and appeared brighter (Fig. 9.3b). The SEM image revealed also that oxide thickness depends on the type of the grain boundary in the Ni substrate (9c,d).

The presence of CeO_2 coatings partly inhibited the anisotropy of NiO growth. However, the oxide growth surface in Fig. 9.4a shows that the influence of the substrate grain orientation was still strong. Also the type of the substrate grain boundary still affected the thickness of NiO. An example of the morphology of NiO formed on differently oriented Ni grains is shown in Fig. 9.4b. While the oxide grown on grain A has a faceted morphology (Fig. 9.4c), the oxide present on grain B has a nodular appearance (Fig. 9.4d). Conversely, the oxide grown on grain C has a typical globular morphology (9.4e). SEM/EDX analyses from the well-developed nodule and the surrounding region are depicted in Fig. 9.4f. The markedly weaker relative intensity of Ce signal obtained from the nodule as compared to that from surrounding region, suggests that the nodule is composed of pure NiO.

9.5. Oxide microstructure

An anisotropy of the thickness of NiO grown on the polycrystalline substrate was also examined on polished taper-sections. To increase an effective scale thickness for observation, the oxide growth surface was tilted during mounting in resin. A geometrical relationship indicates that by using a tilt angle of 12° , the effective scale thickness was increased by 500%.

The taper-section image of pure NiO after 110 h exposure with an average thickness of 5.1 μm, as estimated gravimetrically, is shown in Fig. 9.5. The observed differences in thicknesses of the oxide grown on various Ni grains exceed one order of magnitude (Fig. 9.5a,b). In general, the oxide/metal interface is rough, and excluding some fine features, in most cases represents a mirror image of the outer oxide surface. Electrolytical etching reveals a relatively uniform morphology across the entire oxide thickness (Fig. 9.5c). A nonuniform oxide thickness was also observed on CeO_2-coated specimens (Fig. 9.6a,b). In this case the NiO thicknesses on various Ni grains were between 1 and 7 in relative units. In contrast with pure NiO, NiO formed on CeO_2-coated Ni had a two layer structure after electrolytic etching (Fig. 9.6c). Since there was no essential variation in the chemical composition between the outer and the inner part of the oxide, the observed difference in etched morphology may be caused by other structural features, such as the grain size, porosity or texture. According to the TEM images presented below, the Ce-rich film should be located between the differently etched sublayers.

Additional information regarding oxide structure was obtained from fractured cross sections which show that in NiO formed on pure Ni, the grain size increases with increasing scale thickness (Fig. 9.7a). However, the oxidation at 973 K did not produce a well-developed columnar structure, typical at higher temperatures [Kofstad, 1988]. This means that the nucleation of the new grains took place during oxide growth. Since the NiO grain boundaries act as diffusion paths, one would expect the nucleation process at the intersections of grain boundaries and gas/oxide interface. In fact, such a phenomenon was observed previously during detailed investigation of NiO growth surface using the AFM technique (Fig. 7.4c). An additional feature of the NiO microstructure are micropores, indicated by arrows in Fig. 9.7a, and distributed through the entire scale thickness. A fractured cross section of oxide formed on CeO_2-coated Ni shows the lower scale thickness and smaller grain size (Fig. 9.7b).

To locate the Ce-rich sublayer within the oxide an attempt was made to prepare cross-sectional thin foils for TEM. Although the foils were not thin enough over the entire oxide thickness to perform detailed structural observations, they allowed us to measure the depth location of the Ce-rich sublayer within the oxide. For the oxide grown for 125 h with the total thickness of 716 nm, the Ce-rich sublayer was 10-15 nm thick and was located at a depth of 50 nm (Fig. 9.8a). The thicknesses of the outer and inner sublayers, as evaluated from thin foil prepared from the oxide produced after 100 h exposure, were 100 and 550 nm, respectively.

For planar TEM imaging of the Ce-rich sublayer, the scale was thinned by ion milling predominantly from the oxide/metal interface. The TEM image of the scale portion which was transmittable for 100-120 kV electrons is shown in Fig. 9.8b. Similarly as was observed during the early-stages (Chapter 6), the Ce-rich sublayer formed at the steady-stage of oxidation shows a two-phase structure composed of NiO and CeO_2. NiO grains have diameters of between 50 and 100 nm, the CeO_2 particles have diameters between 10 and 100 nm. Some of the CeO_2 particles are seen in the dark field TEM image in Fig. 9.8c. The selected area electron diffraction pattern (SAD), shown in Fig. 9.8c (inset), indicates that both phases in this sublayer are randomly oriented. The high-magnification TEM image reveals that in addition to the relatively large CeO_2 particles observed above, very small particles with a size of up to 5 nm are also present (Fig. 9.8d). On the convergent beam electron diffraction pattern (CBDP) obtained with a beam spot of 20 nm, the diffraction spots for a $[\bar{2}33]$NiO zone axis are clearly seen. For the CeO_2 phase, however, only two spots of {200} are visible, which makes it impossible for us to establish the crystallographic relationship between the two phases. EDX analysis from dark contrast regions in Fig. 9.8d (arrowed), performed with a beam spot size of 3.5 nm in the scanning transmission electron microscope (STEM), clearly shows that the dark areas correspond to the Ce-rich phase, i.e. CeO_2.

9.6. Summary

Surface applied CeO_2 films with a thickness of 14-42 nm decreased the oxidation rate of polycrystalline Ni at 973 K after 125 h by a factor of up to 45. As was observed for the early stages of oxidation, thinner coatings of CeO_2 (14-28 nm) were more favourable in oxidation inhibition than thicker ones (35-42 nm). The thickness of NiO showed a clear dependence on the crystallographic orientation of the Ni substrate. For pure NiO, the differences in thickness were up to 10 times, depending on the orientation of Ni grains. The presence of CeO_2 slightly increased the scale uniformity; however, after 75 h exposure, oxides still differed in thickness by a factor of 7. The NiO scales developed at the steady stage on CeO_2 coated Ni were composed of three distinct sublayers. Ce was present in the intermediate layer composed of small NiO grains (60-90 nm) and CeO_2 particles (5-50 nm). This layer was generally located close to the outer surface, however, with increasing oxidation time it gradually shifted deeper into the oxide. A comparison of the morphology of oxide formed on polycrystalline Ni presented in this experiment and on Ni single crystals reported in Chapter 7 suggests the variation in depth location of the Ce-rich layer from grain to grain of the Ni substrate.

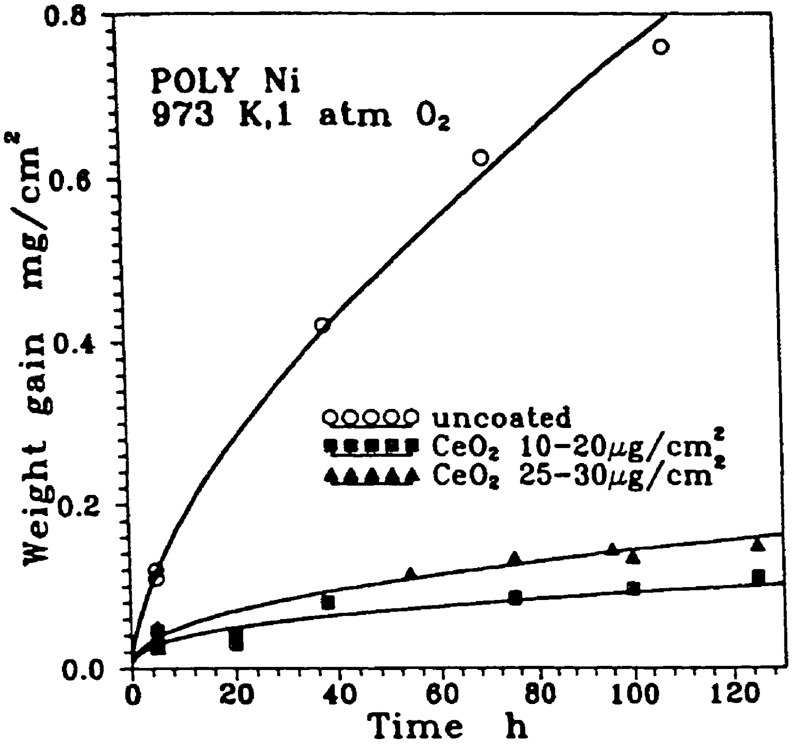

Fig. 9.1. Oxidation kinetics of bare (uncoated) and CeO_2 coated polycrystalline Ni at 973 K. Each data point represents the individual sample. Weight gain of 1 mg/cm^2 corresponds to 7 μm NiO.

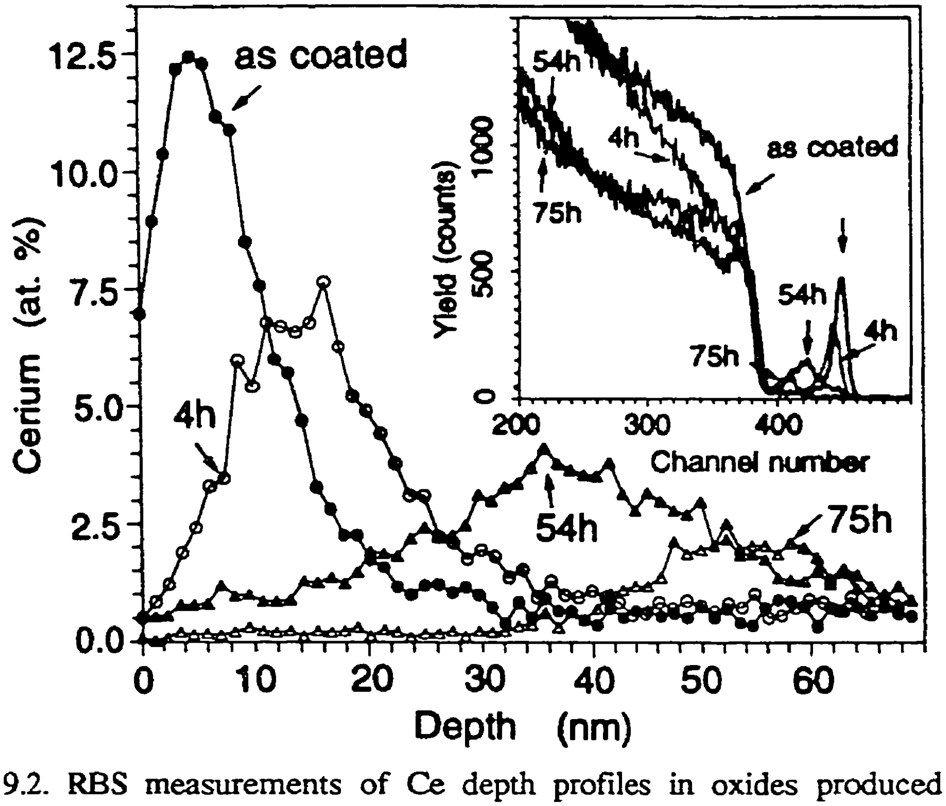

Fig. 9.2. RBS measurements of Ce depth profiles in oxides produced after various exposure times at 973 K. The inset illustrates the energy spectrum of backscattered 1-MeV $^4He^+$ions. The estimated depth resolution is about 12 nm.

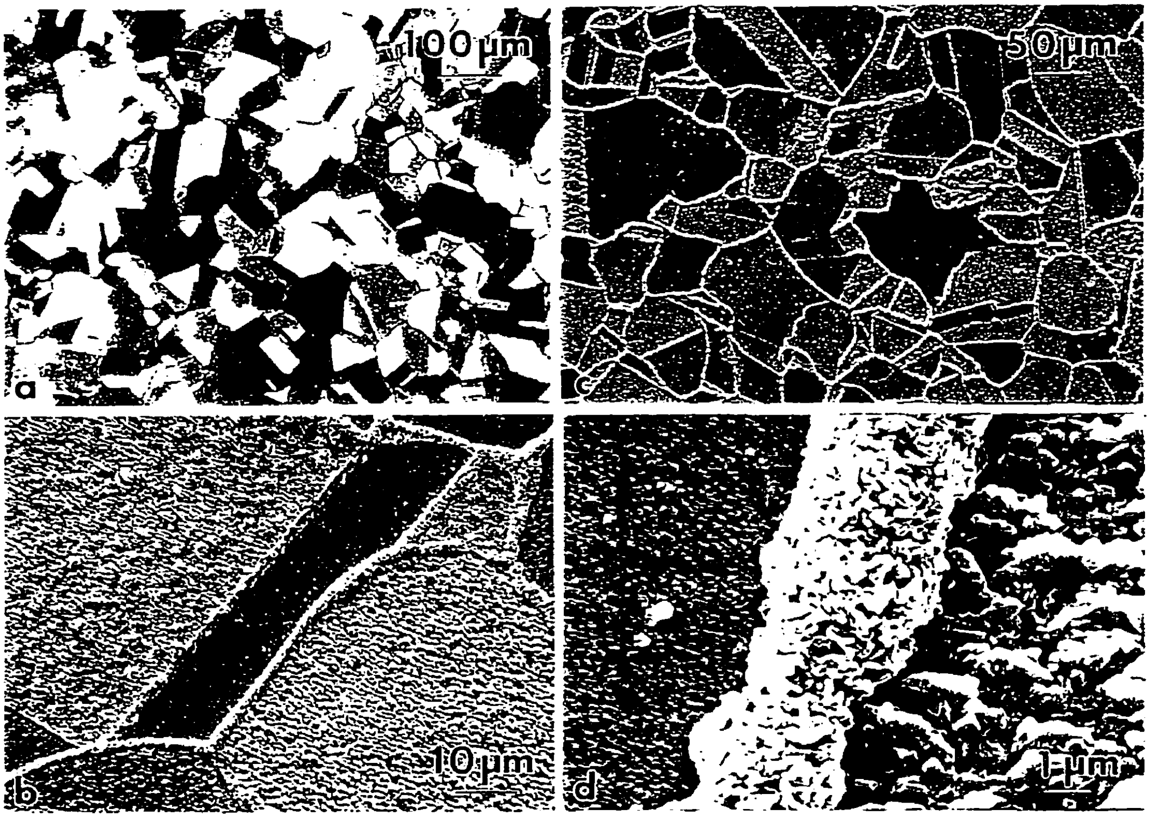

Fig. 9.3. Surface morphology of oxide grown on uncoated Ni: (a) after 38 h exposure at 973 K, optical micrograph showing a pattern caused by colour interference; (b) SEM image of a portion of the oxide shown in (a); (c) SEM image of NiO surface after 125 h exposure at 973 K; (d) fragment of morphology shown in (a).

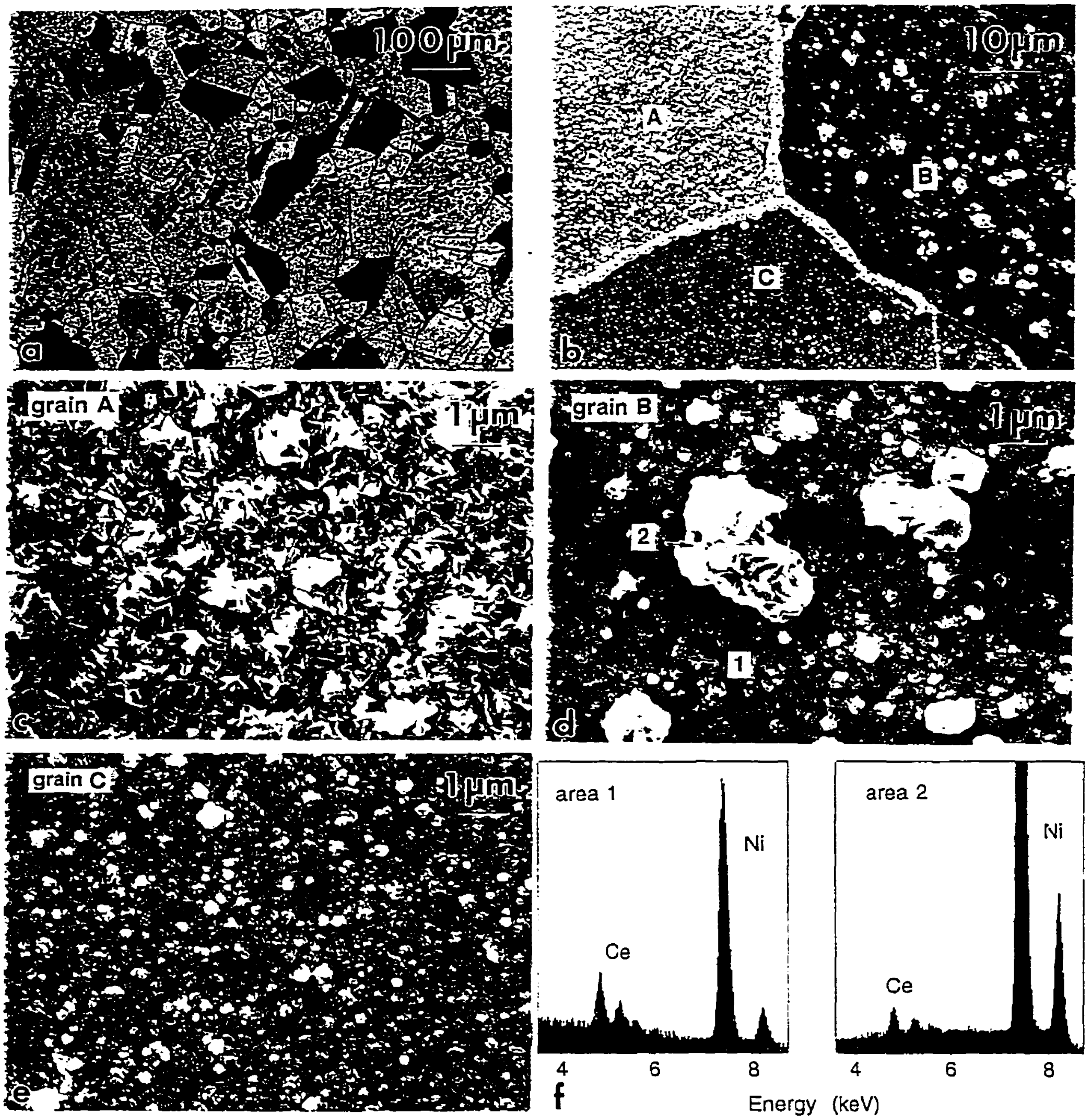

Fig. 9.4. Surface morphology of oxide grown at 973 K on Ni coated with 15 μg CeO_2 /cm^2: (a) optical micrograph of oxide formed after 38 h exposure at 973 K; (b) SEM image of oxide grown after 70 h exposure; (c) faceted morphology of oxide formed on grain A; (d) nodular morphology developed on grain B; (e) globular morphology of oxide formed on grain C; (f) SEM/EDX spectra from regions marked in (b).

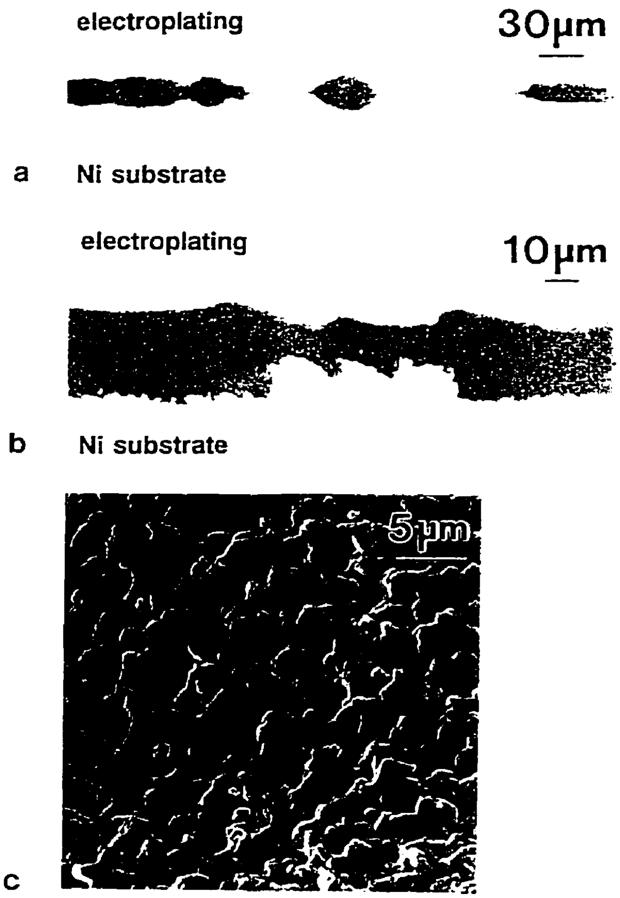

Fig. 9.5.

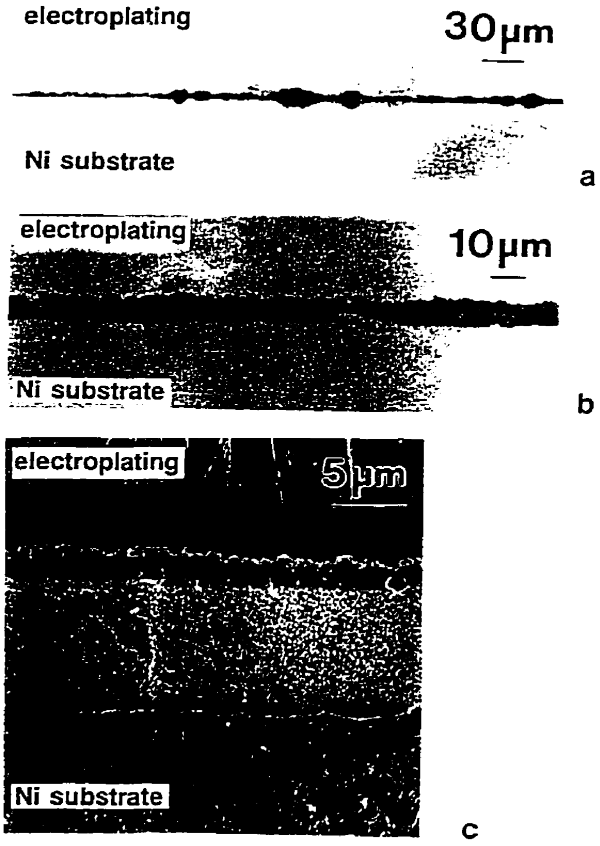

Fig. 9.6.

Fig. 9.5. Taper sections of oxide formed on pure Ni after 110 h exposure at 973 K (weight gain of 0.760 mg/cm^2): (a) nonuniform thickness of the oxide grown on various substrate grains; (b) magnified part of oxide shown in (a); c) SEM image of a part of oxide shown in (a,b) after electrolytical etching. Tilt angle 12°.

Fig. 9.6. Taper sections of oxide formed on Ni coated with 15 μg CeO_2 /cm^2 after 75 h exposure at 973 K (weight gain of 0.085 mg/cm^2): (a) non-uniformity of oxide grown on various substrate grains; (b) magnified part of the oxide shown in (a); (c) microstructure of a part of oxide shown in (a,b) after etching, revealing two sublayers. Tilt angle 12°.

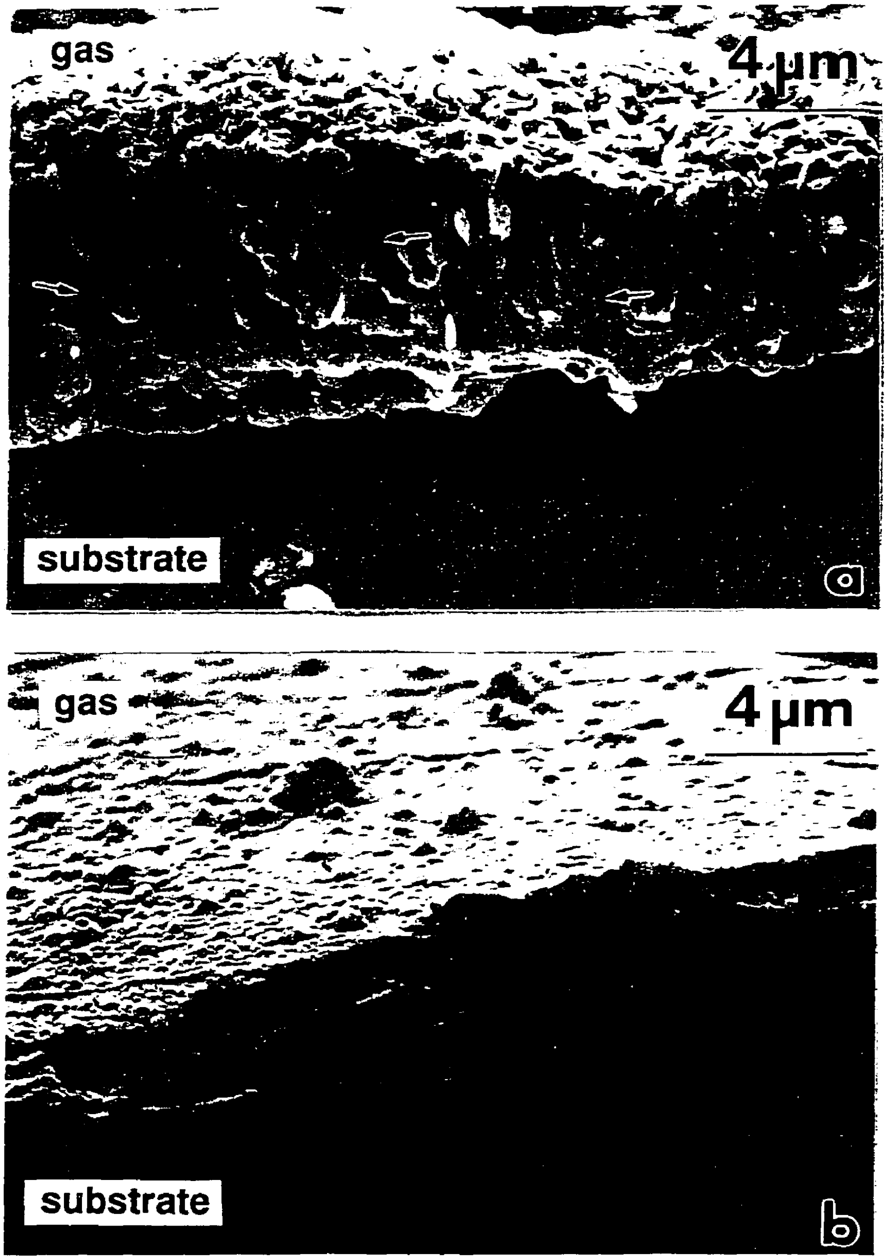

Fig. 9.7. SEM image of fracture cross-sections of oxide formed after 70 h on pure Ni (weight gain of 0.625 mg/cm^2) (a), and on Ni coated with 30 μg CeO_2 /cm^2 after 54 h exposure (weight gain of 0.115 mg/cm^2) (b). Arrows indicate some porosity in oxide.

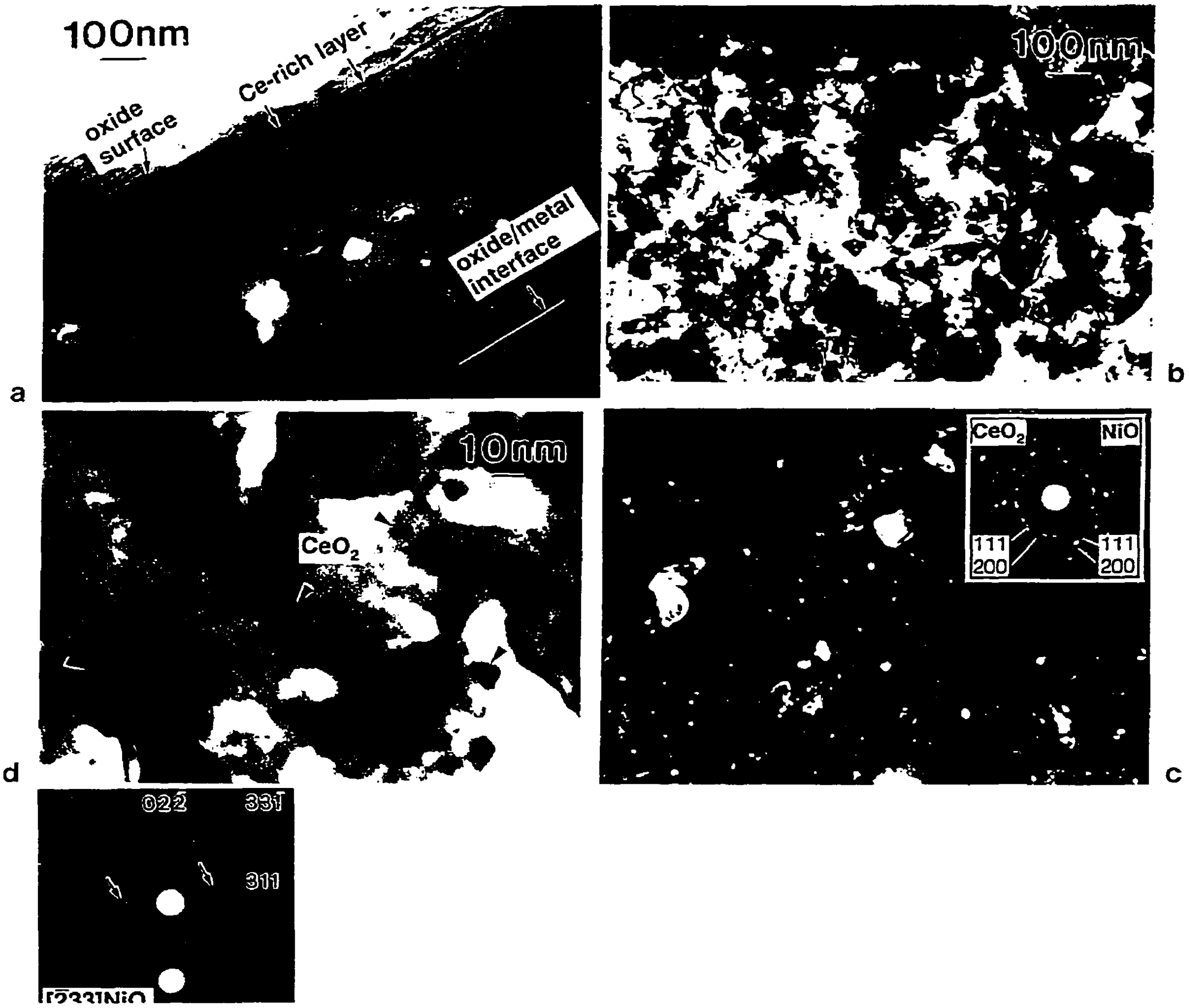

Fig. 9.8. TEM analysis of oxide grown at 973 K on Ni coated with 14 nm CeO_2: (a) cross-sectional view of oxide formed after 125 h; (b) bright field image of Ce-rich sublayer inside the oxide after 30 h exposure; (c) dark field image of the region shown in (b) in the illumination of a part of $\{111\}$ ring of CeO_2, and corresponding SAD pattern (inset); (d) high magnification image showing NiO and CeO_2 phases and CBDP pattern from CeO_2 particle in the NiO matrix (a $[\bar{2}33]$ zone axis for NiO is labelled by indices, arrows indicate two $\{200\}$ spots for CeO_2).

CHAPTER 10. ANALYSIS OF THE MECHANISM OF OXIDE GROWTH USING OXYGEN ISOTOPES

10.1. Introduction

Assuming that the reactive element oxide particles may be considered as an inert marker, the reactive element effect on Ni oxidation is interpreted in the literature in terms of slowing down the outward diffusion of Ni^{2+} [Moon and Bennett, 1989; Smeggil et al., 1988]. This is in contrast to chromia formers where the change of the oxidation mechanism from primarily outward Cr transport to predominant inward O^{2-} diffusion is well documented [Cotell et al., 1987; Przybylski and Yurek, 1989]. Experiments described in previous Chapters and conducted on nickel with various techniques of the reactive element applying and substrate surface pretreatment, revealed the new factors affecting the NiO growth inhibition by the reactive element. These results suggest that in the case of Ni the reactive element addition may also result in scale growth by predominant inward oxygen diffusion Hence, the two stage oxidation using the $^{18}O_2$-tracer has been undertaken to provide a direct evidence of the transport mechanism in NiO modified by the reactive element.

10.2. Sequential oxidation in $^{16}O_2/^{18}O_2$

The oxidation was performed in an ultrahigh vacuum manometric apparatus at 973 and 1073 K, oxygen pressure of 5×10^{-3} torr and for exposure times up to 6 h. The cold insertion to oxygen and furnace raise technique with a heating rate of 200 deg/min was used. The surface modified samples were sequentially oxidized in $^{16}O_2$ first and then in $^{18}O_2$. To avoid the formation of cracks in the oxide films, the two-stage experiment was carried out isothermically. Namely, the evacuation of a system up to 10^{-8} torr of vacuum after oxidation in $^{16}O_2$ and subsequent admission of $^{18}O_2$, was carried out at the oxidation temperature. The oxygen isotope used during the second stage, according to the supplier certificate (ICON Services Inc., N.J.), contained of 96 at.% $^{18}O_2$. Details regarding two stage oxidation are shown in Fig. 10.1 and listed in Table 10.1.

TABLE 10.1. Oxidation data for the two-stage experiment $^{16}O_2/^{18}O_2$, (oxygen pressure - 5×10^{-3} torr, 1 µgO/cm² = 7 nm NiO).

Ni sample characterization	Oxidation temperat. (K)	$^{16}O_2$		$^{18}O_2$	
		time (min)	O_2 upt. µg/cm²	time (min)	O_2 upt. µg/cm²
Polycrystalline,mech. polished, CeO_2 sol	973	125	50.6	125	22.5
Polycrystalline,chem. polished, Ce^+ impl.	973	240	24.7	120	3.2
Polycrystalline,chem. polished, CeO_2 sputt.	973	240	18.9	120	3.4
(100) face, CeO_2 sol coating	1073	120	44.4	120	14.7
(111) face, CeO_2 sol coating	1073	192	21.7	192	7.6

For samples sequentially oxidized in $^{16}O_2/^{18}O_2$, the SIMS polyatomic analyses were performed. The principal species analysed in depth profiling were: $^{58}Ni^{16}O_2^-$ (mass 90), $^{58}Ni^{18}O_2^-$ (mass 94), $^{58}Ni^{16}O^{18}O^-$(mass 92), $^{140}Ce^{16}O^+$ (mass 156) and $^{140}Ce^{18}O^+$ (mass 158). The data were corrected for mass interferences and elemental sensitivities, and are presented as atomic concentration versus sputter time. On some samples the depth-composition was also measured by RBS and AES.

10.3. Oxygen isotope distribution in oxides

In order to gain information regarding the purity of the oxygen isotope $^{18}O_2$ used and proper interpretation of the results of sequential oxidation, the first experiment was conducted with the use of $^{18}O_2$ only. The SIMS analysis of 461 nm thick oxide grown after 4 h exposure at 973 K on polycrystalline mechanically repolished and CeO_2 sol-coated nickel, is shown in Fig. 10.2. The ^{18}O level ($Ni^{18}O_2^-$) is above 90% whereas ^{16}O level ($Ni^{16}O_2^-$) is less than 10%. Thus, such a level of ^{18}O should be anticipated during further analysis. Cerium ($^{140}Ce^{18}O^+$) is generally present close to the oxide/gas interface, but tails in throughout the oxide. The oxide/metal interface in the SIMS profile is relatively broad. As observed by SEM, such a composition profile was accompanied by quite a rough surface at this depth.

10.3.1. *Polycrystalline nickel*

The sample of polycrystalline nickel CeO_2 sol coated, with surface finished identically as those analysed above, was sequentially oxidized at 973 K first in $^{16}O_2$ for 125 min (oxygen uptake of 50.6 μg/cm^2) and then for the same period of time in $^{18}O_2$ (oxygen uptake of 22.5 μg/cm^2). The SIMS analysis of a 511 nm thick oxide film is shown in Fig. 10.3. The $Ni^{18}O_2^-$ and $Ni^{16}O_2^-$ profiles indicate a high concentration of ^{18}O in the outer portion of oxide. This suggests that in this region the new oxide was formed (the level of the mixed polyatomic species $Ni^{16}O^{18}O^-$ was found to be practically constant). As seen also in Fig. 10.3, the Ce peaks ($Ce^{16}O^+$ and $Ce^{18}O^+$) with the higher fraction of Ce associated with ^{16}O than with ^{18}O, are within the oxide, at the interface between the $Ni^{16}O$ and $Ni^{18}O$ oxides. Thus, during the diffusion through the oxide film, some of the ^{18}O isotope has exchanged with ^{16}O in the CeO_2 phase.

The sequential oxidation of Ce implanted Ni was conducted at 973 K by exposure first in $^{16}O_2$ for 240 min and subsequently for 120 min in $^{18}O_2$. Depth distribution of polyatomic species in 195 nm thick oxide is illustrated in Fig. 10.4. Since the ^{18}O uptake was relatively low, a small amount of ^{18}O containing species was detected. The Ce containing species ($Ce^{16}O^+$ and $Ce^{18}O^+$) are present in the outer part of the oxide. The

$Ni^{18}O_2^-$ level is higher in the outer part but tails in through the oxide.

In the case of chemically polished nickel sputter coated with 4 nm CeO_2, the oxidation strongly depended on substrate grain orientation. Since the grain size of the Ni substrate was about 100 μm, the SIMS results did not give the average distribution over oxide grown on many different orientations. To obtain the average depth concentration, an analysis was performed using RBS. In this technique a signal was produced from an area of about (700 μm)^2 which corresponds to surface of about 100 Ni grains. The energy spectra of 1 MeV $^4He^+$ ions backscattered from the sample surface before and after oxidation at 973 K, are shown in Fig. 10.5a. The Ce concentration-depth profiles derived from these spectra (Fig. 10.5b) indicate that in the 195 nm thick oxide (average thickness for entire sample as estimated from oxygen uptake), Ce was concentrated in a 20-30 nm thick surface region of the oxide. Since the nonuniform morphology of the oxide surface (Chapter 6) suggested the differences in Ce distribution exists, the measurements of Ce depth location in the oxide that was grown on individual Ni grains were performed by AES. In this technique the signal was generated from an area of about (45 μm)^2, which is much less than area of one Ni grain. It was observed that the depth location of Ce in the oxide changes from grain to grain of the Ni substrate. An example of the analysis from the oxide formed on one Ni grain is shown in Fig. 10.5c. This oxide, as estimated from SEM surface observations, was thinner than oxides on the surrounding Ni grains. Conversely, the Ce peak obtained from the thicker oxide had a lower intensity and was shifted towards the oxide/metal interface. The SIMS analysis of oxide grown on this substrate, including also ^{18}O containing species, is shown in Fig. 10.5d. The $Ce^{16}O^+$ and $Ce^{18}O^+$ peaks coincide and are located inside the oxide layer, between $Ni^{16}O$ and $Ni^{18}O$ oxides. Moreover, the $Ce^{16}O^+$ peak is much higher than $Ce^{18}O^+$. The presence of $Ni^{18}O_2^-$ close to the oxide/gas interface indicates the growth mechanism by the outward Ni^{+2} diffusion.

10.3.2. *Ni single crystals*

In the $^{16}O/^{18}O$ experiment a CeO_2 sol coated (100)Ni face was oxidized at 1073 K for 120 min in $^{16}O_2$ and then also for 120 min in $^{18}O_2$. The partitioning of the ^{16}O and

^{18}O containing species in a 414 nm thick oxide is shown in Fig. 10.6. The $Ce^{16}O^+$ and $Ce^{18}O^+$ peaks coincide and are located inside the oxide but still rather close to the outer surface. In this film, the $Ce^{18}O^+$ peak is higher than $Ce^{16}O^+$ indicating a strong exchange of oxygen isotopes in the CeO_2 phase. The $Ni^{18}O_2^-$ peak is located inside the oxide, at a depth just below the Ce peaks. Such distribution suggests that, in this sample the new oxide is formed beneath the Ce-rich portion of the scale.

The sequential oxidation of CeO_2 sol coated (111)Ni conducted at 1073 K for 192 min in $^{16}O_2$ and for 192 min in $^{18}O_2$, resulted in the distribution of polyatomic species shown in Fig. 10.7. The oxygen uptake during the second stage ($^{18}O_2$) was of 7,6 μg/cm^2 and allowed the obtaining of very clear SIMS profiles for ^{18}O containing species in the oxide. The Ce containing species are present on the outer surface of the oxide with the level of the $Ce^{16}O^+$ slightly higher than $Ce^{18}O^+$. In this film, the $Ni^{18}O_2^-$ signal is lower than the $Ni^{16}O_2^-$ in the outer region of the oxide. Moreover, the $Ni^{18}O_2^-$ profile tails in the oxide, which indicates the formation of new oxide beneath the Ce-rich region.

10.4. Summary

The sequential oxidation using $^{16}O_2/^{18}O_2$ isotopes provided evidence regarding the influence of the surface applied reactive element on the oxidation mechanism of Ni. In particular, it shows that the oxidation mechanism of Ni modified with Ce/CeO_2 depends on the substrate surface pre-treatment before the reactive element application. For polycrystalline Ni a decisive factor is the surface finishing. CeO_2 sol-gel coatings deposited onto a mechanically polished surface significantly decrease outward Ni^{2+} diffusion, but the outward Ni^{2+} transport is still predominant for NiO growth. Higher inward diffusion of oxygen is observed for chemically polished Ni, both for the ion-implanted and CeO_2 sputter-coated. The mechanism of oxide growth on CeO_2 sol-coated Ni single crystals depends on crystallographic orientation. Of two Ni orientations studied (100) and (111), the higher contribution of inward O^{2-} diffusion is observed for the (111)Ni face.

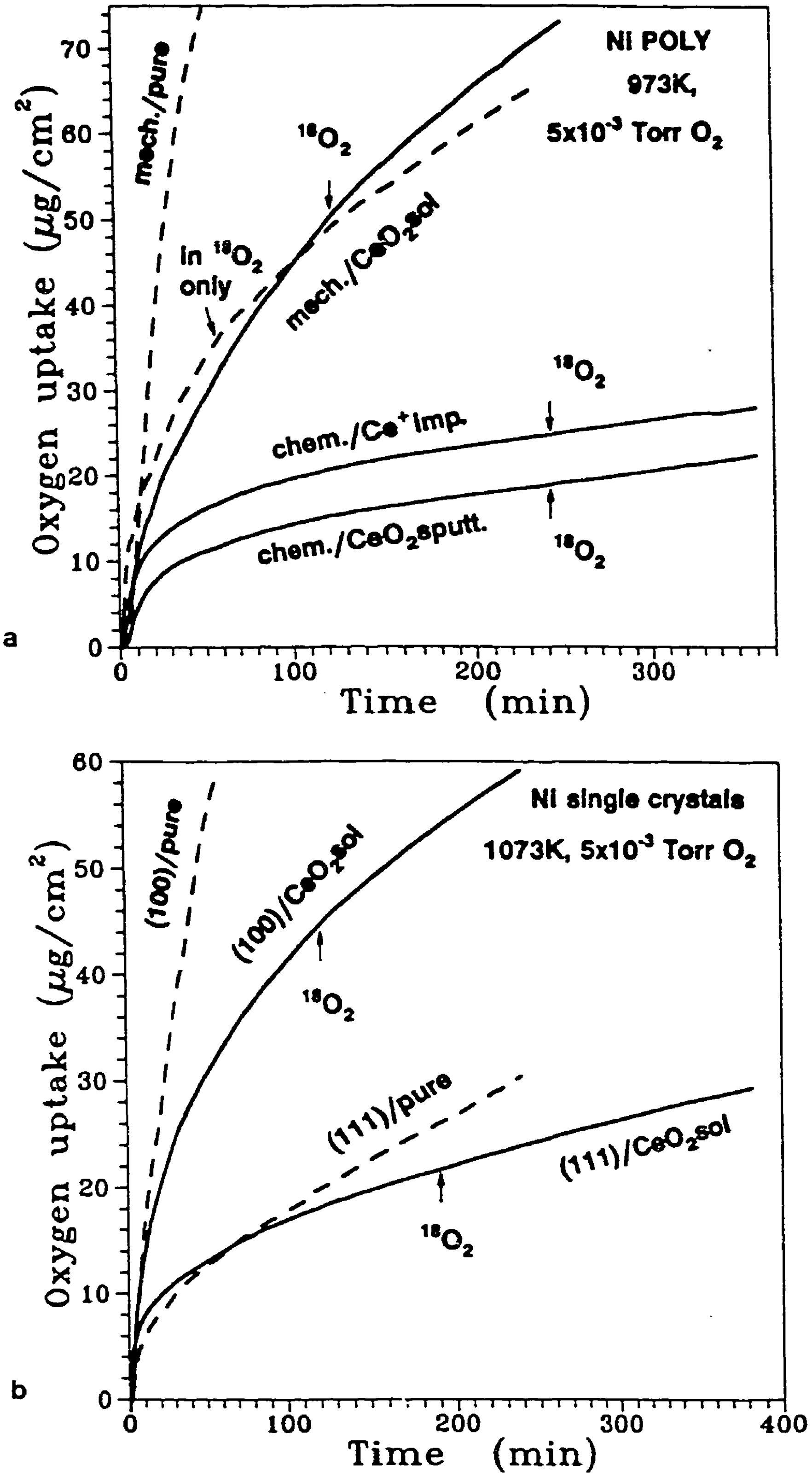

Fig. 10.1. Oxidation kinetics of pure and Ce/CeO$_2$ modified polycrystalline Ni (a) and Ni crystal faces (b). Continuous lines - sequential oxidation in $^{16}O_2/^{18}O_2$ (time of $^{18}O_2$ admission to the manometric system is indicated by arrow).

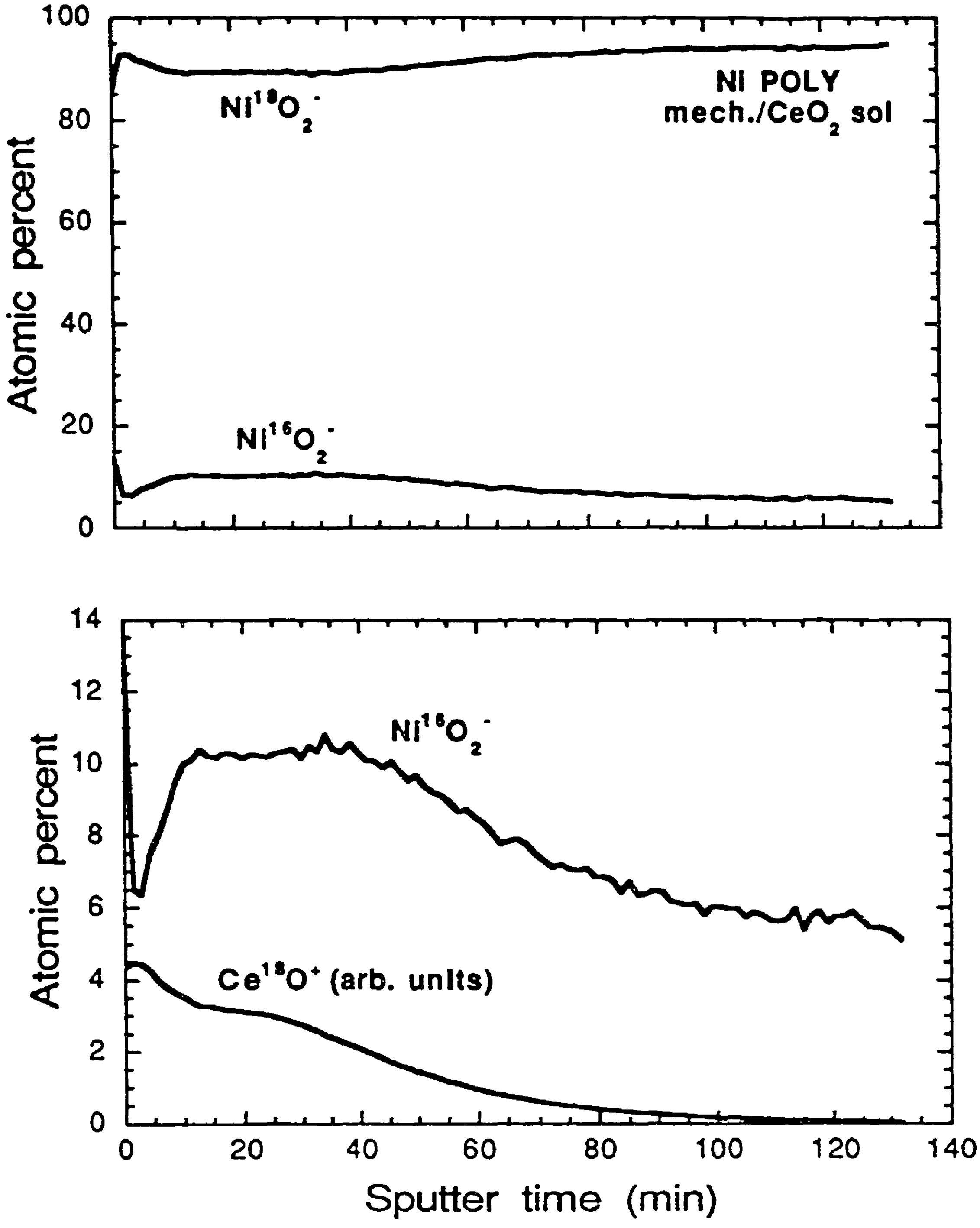

Fig. 10.2. SIMS composition-depth profiles for a 461 nm thick oxide formed at 973 K after 4 h on polycrystalline mechanically polished nickel, sol coated with 14 nm CeO$_2$. Oxidation in ^{18}O$_2$ only.

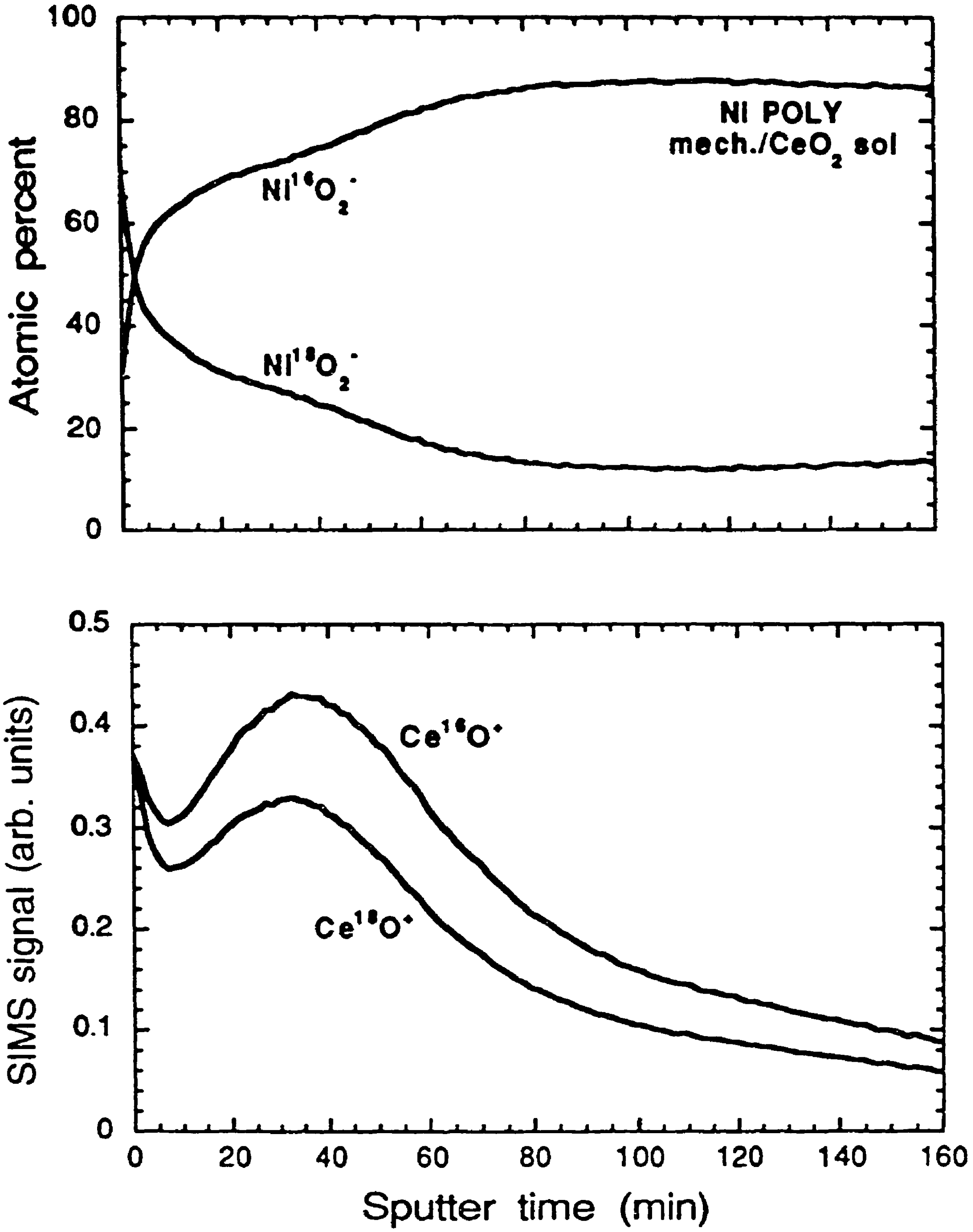

Fig. 10.3. SIMS composition-depth profiles of a 512 nm thick oxide film formed on mechanically repolished nickel sol coated with 14 nm CeO_2 after oxidation at 973 K in: i) $^{16}O_2$ for 125 min, ii) subsequent oxidation in $^{18}O_2$ for 125 min; oxide thicknesses were 354 and 158 nm respectively.

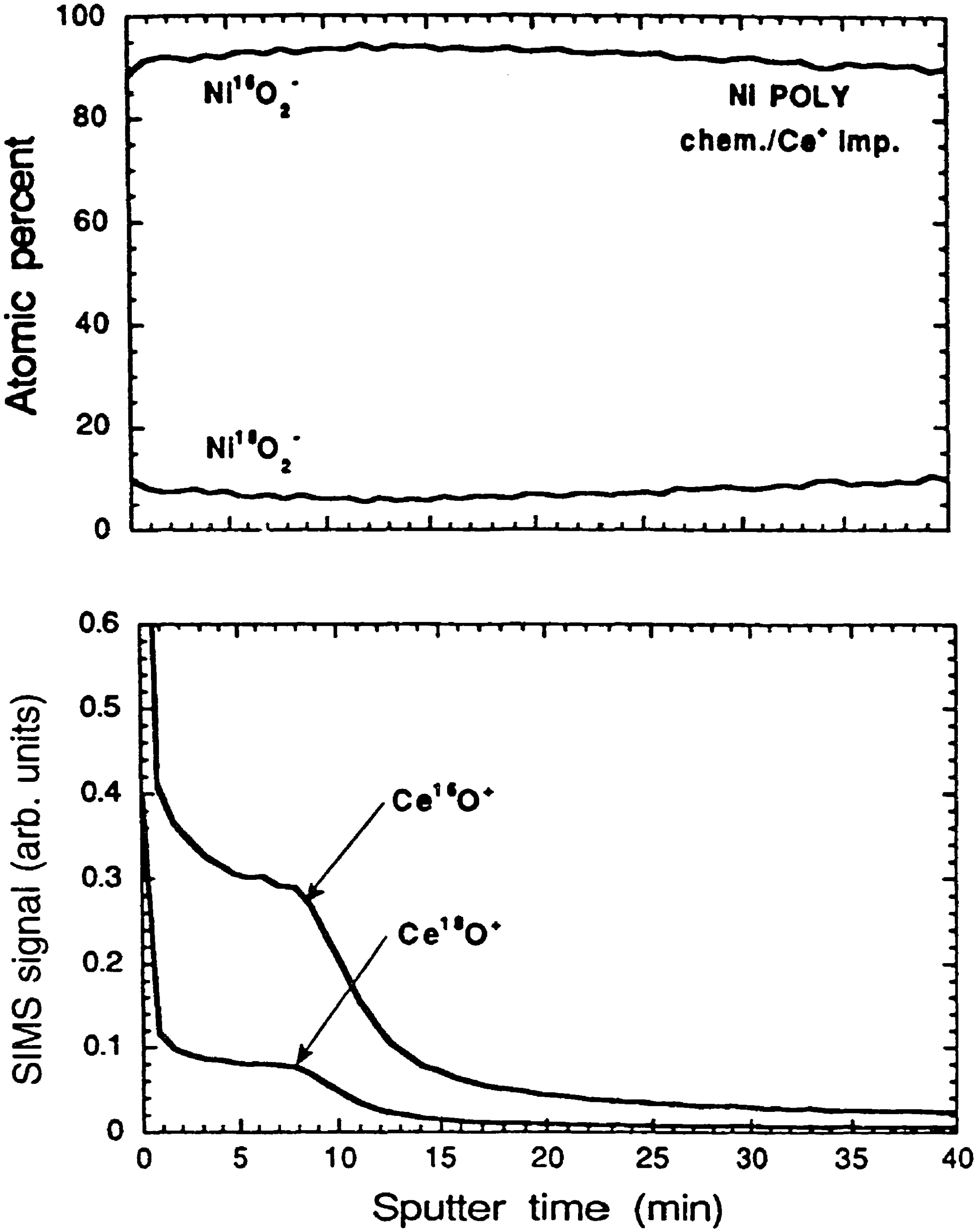

Fig. 10.4. SIMS composition-depth profile of a 195 nm thick oxide film formed on chemically polished nickel implanted with 2×10^{16} Ce$^+$/cm^2. Oxidation at 973 K first in $^{16}O_2$ for 240 min and then in $^{18}O_2$ for 120 min; oxide thicknesses were 173 and 22 nm respectively.

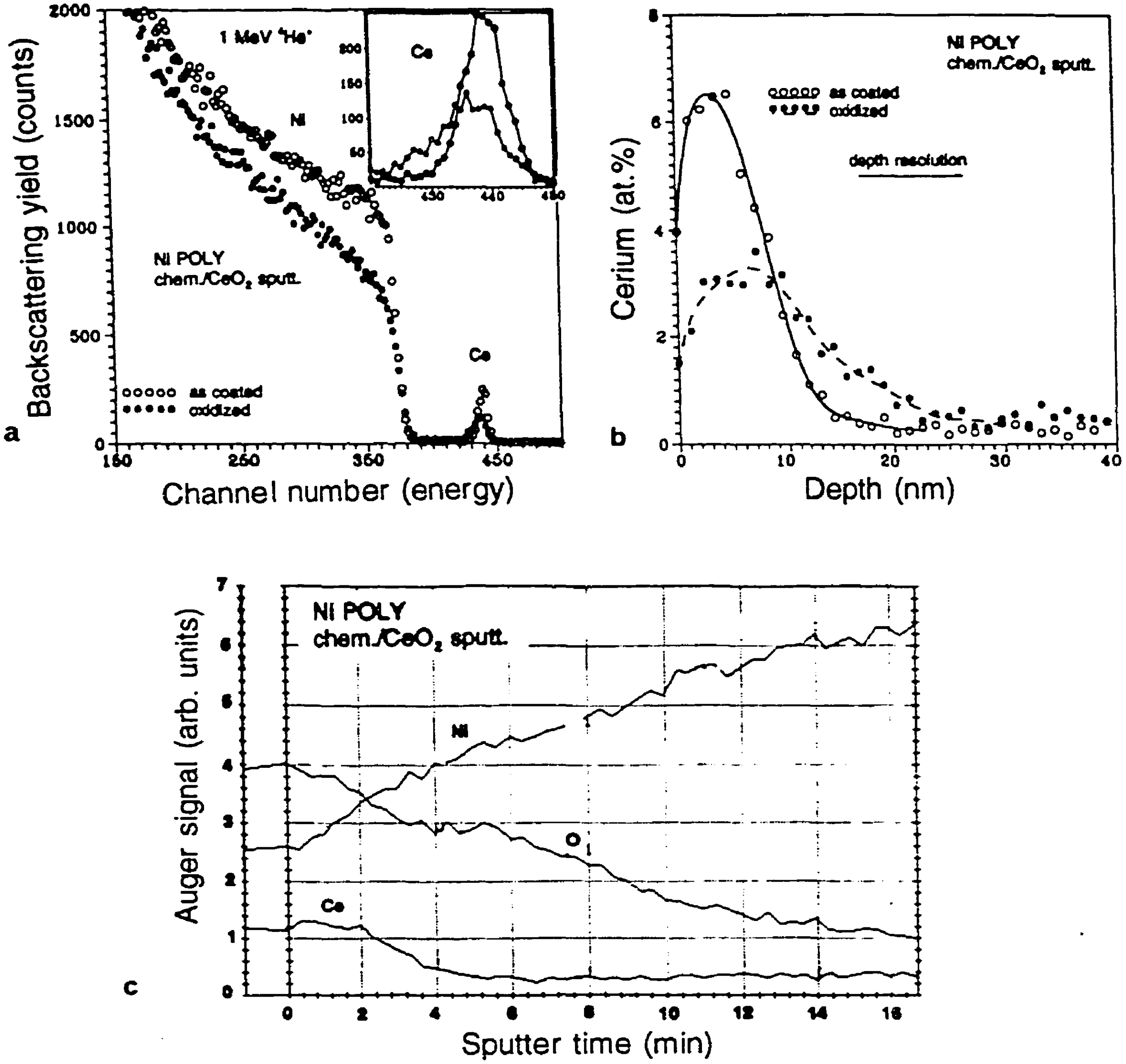

Fig. 10.5. Composition-depth analyses of oxide film formed on chemically polished nickel, sputter coated with 4 nm CeO_2 after oxidation at 973 K (average thickness of 156 nm):

(a) RBS energy spectra of 1MeV $^4He^+$ ions backscattered from surface equal to 100 Ni grains before and after oxidation, and Ce concentration vs depth profile derived from these spectra (b);

(c) AES sputter-depth profile of oxide formed on one Ni grain (oxide on this grain was thiner in comparison to that formed on surrounding Ni grains);

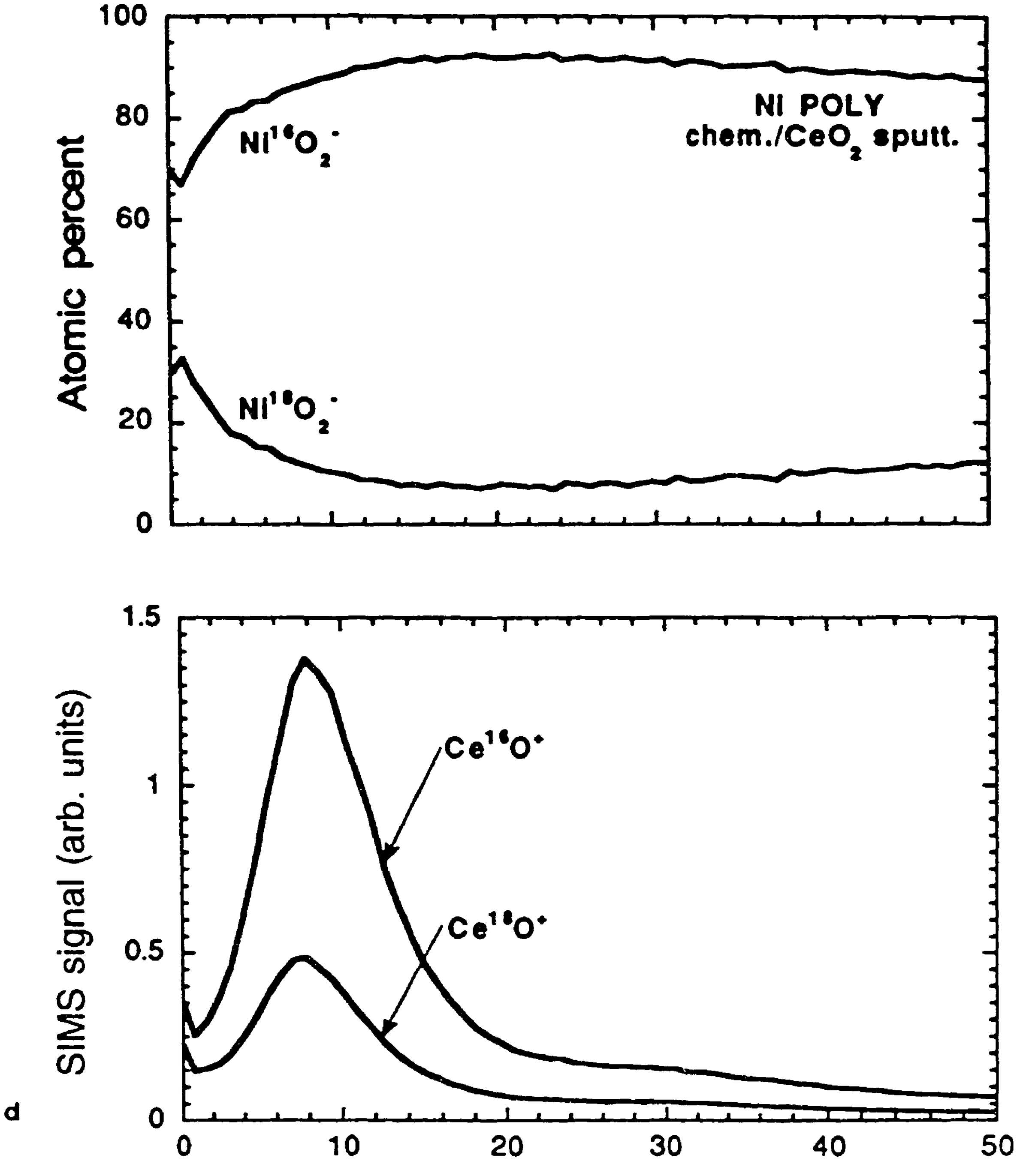

Fig. 10.5. (d) SIMS profiles after two-stage exposure, first in $^{16}O_2$ for 240 min and then in $^{18}O_2$ for 120 min; oxide thicknesses were 132 and 24 nm respectively.

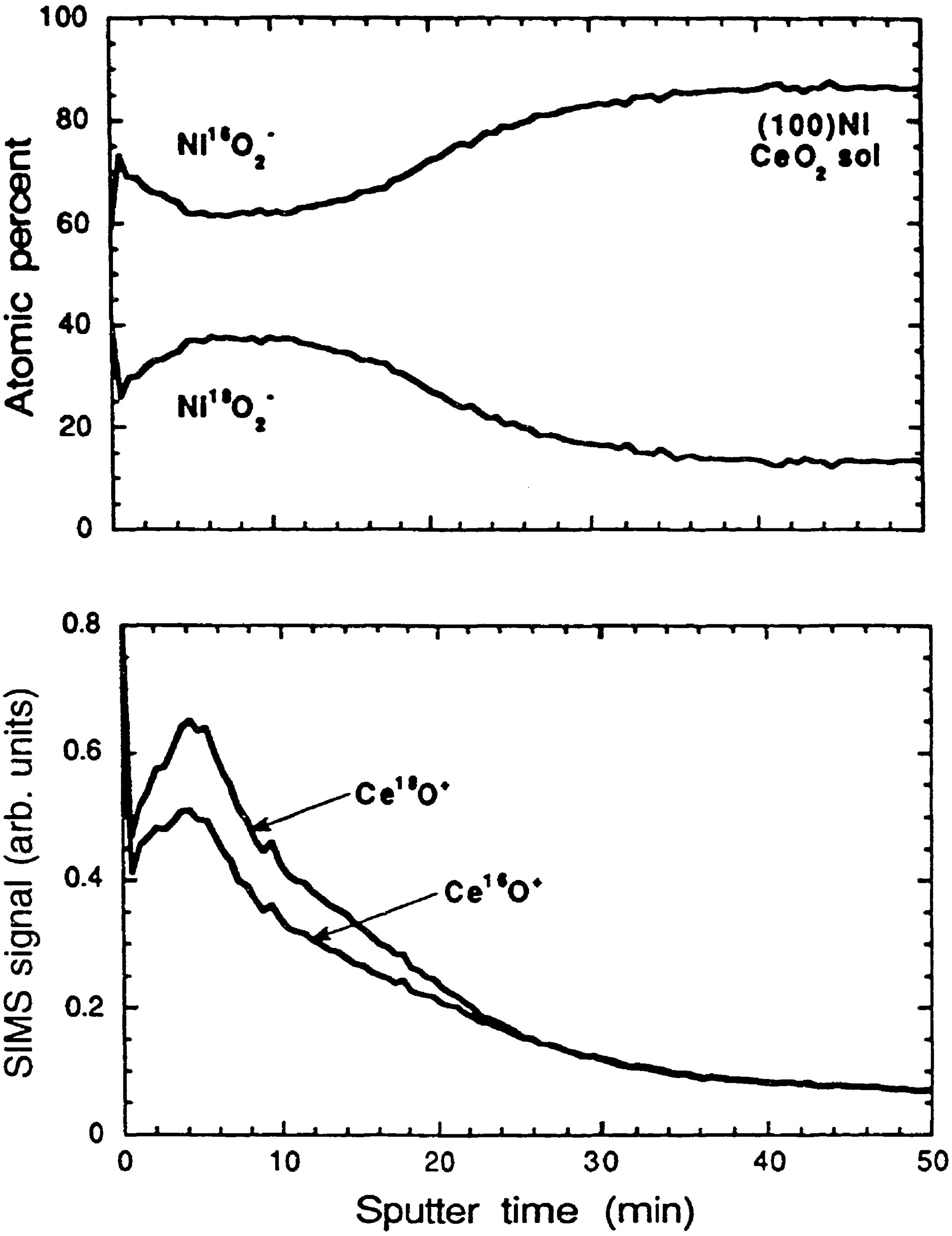

Fig. 10.6. SIMS composition- depth profile of a 414 nm thick oxide film formed on (100)Ni sol coated with 14 nm CeO_2 after oxidation at 1073 K first in $^{16}O_2$ for 120 min and then in $^{18}O_2$ for 120 min; oxide thicknesses were 311 and 103 nm respectively.

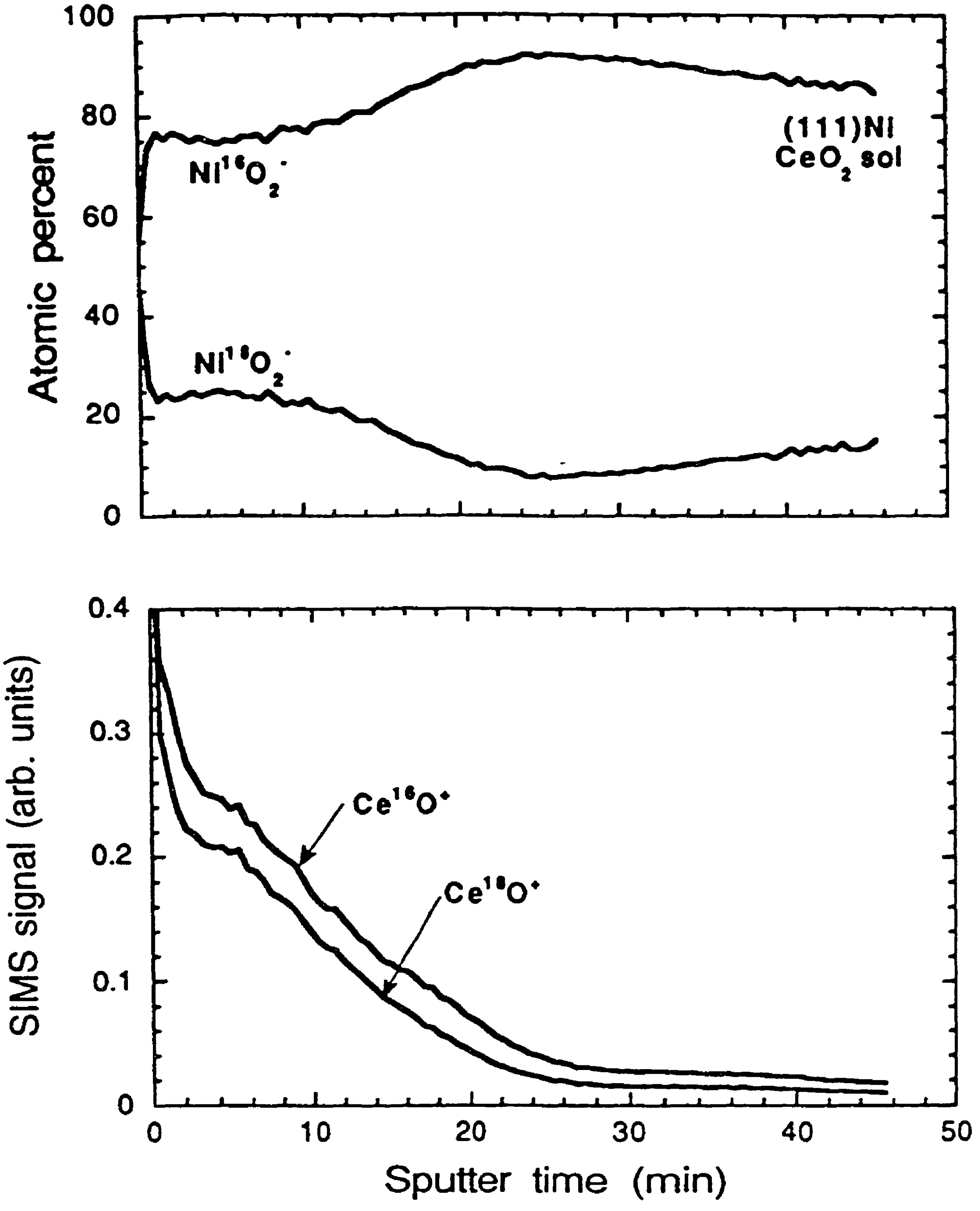

Fig. 10.7. SIMS composition-depth profile of a 205 nm thick oxide film formed on (111)Ni sol coated with 14 nm CeO_2 after oxidation at 1073 K first in $^{16}O_2$ for 192 min and then in $^{18}O_2$ for 192 min; oxide thicknesses were 152 and 53 nm respectively.

CHAPTER 11. TEXTURE AND GRAIN BOUNDARY CHARACTER DISTRIBUTION IN NiO MODIFIED WITH THE REACTIVE ELEMENT

11.1. Introduction

The grain boundaries in protective oxides act as so called "short-circuit paths" for diffusion and have an essential influence on the oxidation resistance of many materials. This implies that fine-grained oxide structures should result in high growth rates. Surprisingly, a low growth rate of oxides doped with the reactive-element is accompanied by small grain size (Chapters 6 and 8). Such a finding suggests a lower diffusivity of oxide grain boundaries which, according to the one of many hypotheses, is caused by reactive element ion segregants [Przybylski et al. 1988; Cotell et al. 1990]. However, suppressing diffusion may also result from changes in the structure of the grain boundaries. It is known, that grain boundary diffusivity is related to the grain boundary structure and energy: a low activation energy for diffusion is usually associated with high interfacial energy. Although no theoretical model for oxide grain growth and texture formation during oxidation is currently available, from a comparison with metals one can suspect that a small amount of ultra-fine reactive element oxide particles may influence the grain boundary structure, with consequences for grain boundary transport [Gleiter and Chalmers, 1972].

In this Chapter, we analyze the texture of pure and CeO_2-modified NiO scales in order to verify the role of the reactive element in affecting the grain boundary character distribution in oxides grown at high temperatures.

11.2. Phase composition and the texture of oxides grown on Ni

11.2.1. *Characterization of the polycrystalline Ni substrate*

The polycrystalline cold-rolled nickel sheet (99.5% purity), after annealing at 1173 K for 1 h, had an average grain size of 100 μm. According to x-ray measurements, the substrate had a {100}<023> texture with a maximum intensity of 4.1 times random (Fig. 11.1a). The surface of Ni specimens was prepared by two techniques: mechanical or chemical polishing. Then, the CeO_2 sol-gel coatings were applied onto surfaces finished by both techniques.

11.2.2. *Phase analysis of the oxides*

A single NiO phase was grown on pure Ni. On the CeO_2 coated substrate, in addition to the NiO phase, some traces of CeO_2 were found. No mixed compounds, however, between Ni, O and Ce were formed. Exemplary x-ray diffraction patterns are presented in Chapter 7. It should be noted that all the oxides were totally penetrated by x-rays during diffraction experiments, which is evident from the presence of the substrate peaks on the diffraction patterns. The results obtained represent therefore the through-thickness average over some complex depth-structures present in CeO_2 modified oxides. Thus, all individual sublayers contributed to the measured pole figures. Moreover, the x-ray diffraction patterns show that all the major peaks of NiO i.e.: (111), (200), and (220) are clearly separated from the other peaks for Ni or CeO_2. As a result, no error is expected from overlapping diffraction peaks during texture measurement.

11.2.3. *The texture of NiO grown on chemically polished substrates*

The texture of NiO formed on chemically polished Ni is represented by three basic pole figures in Fig. 11.1b. In this figure, the rolling and transverse directions of Ni substrates are indicated. Analysis of the pole figures shows that NiO exhibits a {100}<013> texture, very similar to that which is present in the Ni substrate (Fig. 11.1a). Thus, the comparison of pole location on pole figures of Ni and NiO and the crystallographic relationships between the Ni and NiO lattice, observed previously for single crystalline Ni substrates (Chapter 7), suggest the epitaxial character of the oxide grown after 15 h exposure. The shape of contour lines on pole figures, however, seems to suggest the diminishing contribution of the epitaxy for longer exposures. The maximum intensity on (200) NiO pole figures increased from 3.1 to 3.8 times random and remained at that level up to a period of 75 h of oxidation.

It is surprising that the application of the CeO_2 coating did not essentially change the NiO texture. As seen in Fig. 11.1c, the clear contour lines on pole figures suggest an even stronger influence of the substrate than that observed in the absence of coating. In addition, the maximum intensities of 3.6 and 4.3 are higher than previous ones and practically meet those measured for Ni.

11.2.4. *The texture of NiO grown on mechanically polished substrates*

In NiO grown on mechanically polished Ni no similarity between the substrate and oxide textures, indicating an epitaxy, was found (Fig. 11.1d). The NiO grown on pure Ni has a fibre texture with the major component of <110> oriented along the growth direction, and an intensity of 3.5 times random. This intensity decreased to 2.6, and further to 2.5, after 35 and 75 h exposure, respectively. The changes observed on (111) and (200) pole figures with oxidation time show the strength of the <100> fibre component for thicker scales increases.

The presence of the reactive element coating changed the NiO texture. After 15 h of growth, the pole figures show that the <100> fibre dominates the texture. The shape of contour lines, suggests some weak influence of the substrate. The substrate effect should probably be attributed to the changes of the substrate surface during deposition of the CeO_2 coating. One suspects that the plastically deformed surface layer obtained as a result of mechanical polishing was partly removed due to etching by nitric acid which is a component of the sol and the subsequent thermal treatment at 573 K for 1 h. A further exposure produced a clear <100> fibre, and the maximum intensity of (100) poles increased continuously up to 3.7 times random after 75 h oxidation (Fig. 11.1e)

The texture of NiO formed on pure and CeO_2 coated Ni is represented by the ODF calculated from pole figures measured by x-ray diffraction. According to Bunge [1982] notation, the standard coordinates (Φ, ϕ_1, ϕ_2) are used in ϕ_2 projection. The evolution of oxide texture as a function of oxidation time up to 75 h at 1073 K is shown in Fig. 11.2. For clarity, only one part of the ODF cross section for $\phi_2 = 0$ deg is used. One can conclude that the oxidation time does not significantly affect the texture in both the pure and CeO_2 -modified NiO. There were only some changes in intensities of the fibre texture component.

11.3. Grain boundary character distribution

Various representations are used to describe grain boundary statistics in polycrystalline materials [Sutton and Baluffi, 1995]. The distribution of grain boundaries as a function of misorientation represented by an axis-angle pair is called the grain boundary misorientation distribution [Field and Adams, 1992]. Special grain boundaries are described by the parameter Σ, which is the reciprocal density of common sites in the coincidence site lattice (CSL) model [Grimmer et al., 1974]. A boundary is usually classified as belonging to a certain Σ value if the deviation from an exact CSL misorientation is specified by Brandon criteria [1966]. It is known that the frequency of the occurrence of CSL boundaries in polycrystalline materials is affected by texture, correlation between orientations of neighbouring grains, inhomogeneities, and grain size. The computer program used in this study [Morawiec et al., 1993] allows us to calculate the probability of special misorientations from the texture data under the assumption of the absence of spatial correlations between grain orientations (Chapter 4).

The pure and CeO_2 modified NiO grown during 15 h were analyzed and the misorientation angle and frequency of CSL boundaries are shown in Fig. 11.3 and 11.4, respectively. In general, the reactive element did not change substantially the misorientation angle between grains. The major change in GBCD is a slightly lower frequency of $\Sigma 1$ and $\Sigma 3$ boundaries in the modified NiO (Fig. 11.4). The results of the numerical analysis of ODF performed for several oxides are shown in Table 11.1. In this table, the CSL boundaries were divided into three groups: i) low-angle grain boundaries ($\Sigma = 1$); ii) twin boundaries ($\Sigma = 3$), and iii) the remaining CSL boundaries with Σ values between 5 and 51. It is observed that in pure NiO after 15 h oxidation, about 20% of overall grain boundaries can be classified as special boundaries. Since there was no essential change in texture as a function of oxidation time, it is obvious that grain boundary statistics after 35 and 75 h did not change. It is however surprising that despite differences in texture, a very similar grain boundary character distribution was obtained for CeO_2-modified NiO. This finding is of essential importance for analysis of the mechanism of oxidation inhibition of Ni by CeO_2.

TABLE 11.1. The grain boundary character distribution evaluated by numerical analysis of experimental texture data for NiO pure and modified with CeO_2 additions. Oxidation temperature 1073 K. Frequency of occurrence in %.

	G.B. type	15 h	35 h	75 h
NiO pure	LAGB*)	3.05	2.75	3.10
	Σ3	1.99	2.09	2.16
	Σ5-51	14.31	14.42	14.08
	Random	80.64	80.74	80.66
NiO/CeO_2	LAGB	2.54	3.06	3.20
	Σ3	1.83	1.62	1.71
	Σ3-51	14.32	13.78	14.43
	Random	81.31	81.54	80.66

*) LAGB - low angle grain boundaries

11.4. Summary

The surface finishing of polycrystalline nickel affected the texture of both pure and CeO_2 -modified NiO grown at 1073 K in 760 torr O_2. The oxidation of uncoated, chemically-polished Ni with a {100}<023> texture led to oriented nucleation and the epitaxial growth of NiO with a final {100}<013> texture. The presence of CeO_2 coatings on the chemically polished substrate caused a random nucleation of NiO during the initial stages of growth, though it did not substantially change the texture of thick NiO layers formed at a steady stage of reaction. Plastic deformation of the Ni surface by mechanical polishing, in the absence of CeO_2, resulted in the random nucleation of NiO and development of <110> fibre growth texture. The deposition of CeO_2 coatings on a plastically deformed Ni surface also led to the nucleation of randomly oriented NiO at the beginning of oxidation. The CeO_2 coating did, however, change the growth texture of thicker NiO scales on this substrate to a <100> fibre. Numerical analysis of the orientation distribution function of oxide grains shows that NiO formed on pure Ni contains 3% of low-angle grain boundaries, 2% of twins and 14.3% of the other CSL boundaries with Σ value up to 51. The presence of a reactive element did not change substantially the grain boundary character distribution. Thus the suppression of the diffusion of ionic species within the oxide caused by the reactive element is not accompanied by the creation of a larger quantity of special grain boundaries with a low diffusivity.

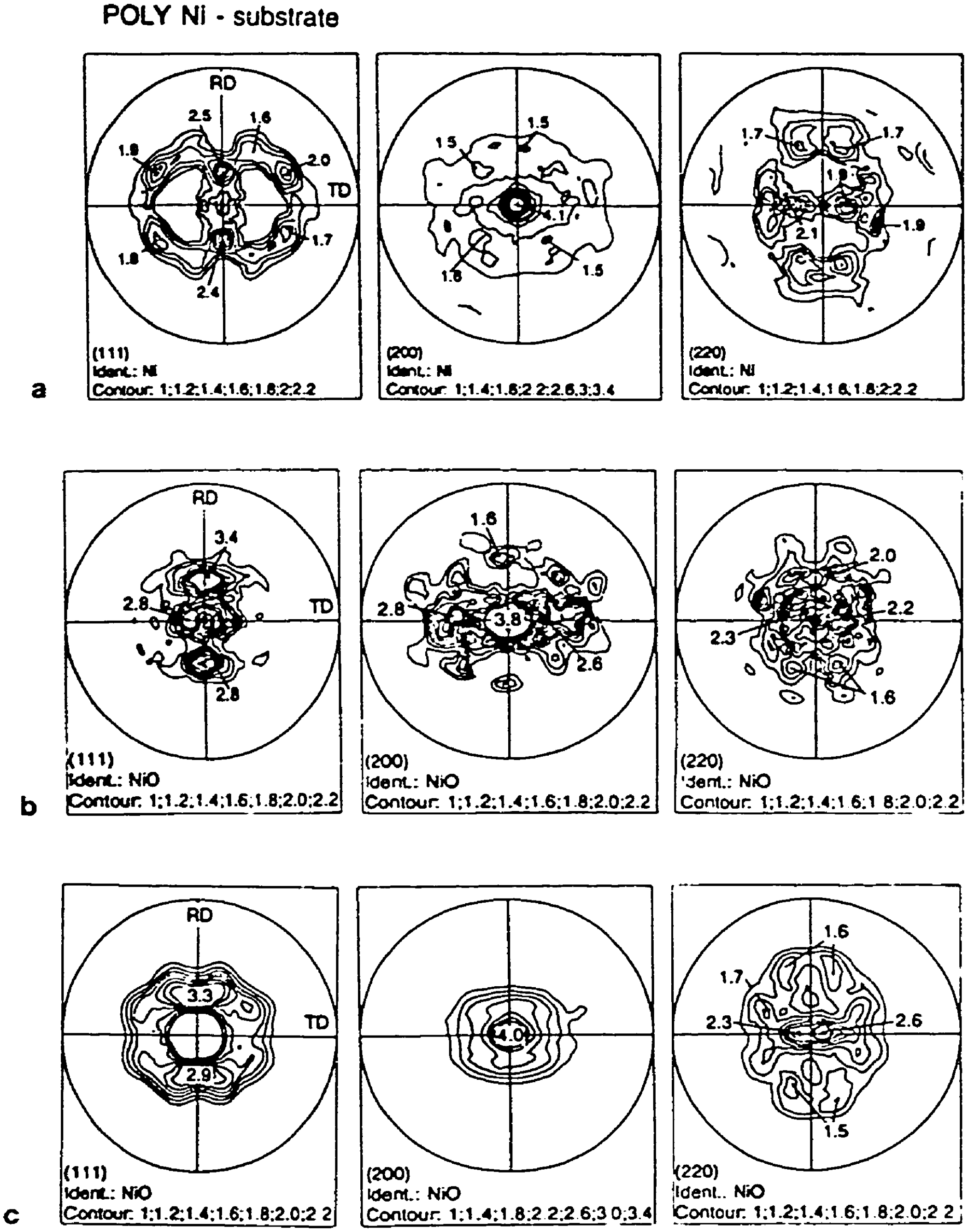

Fig. 11.1. Influence of substrate surface finishing and CeO_2 coating on texture of NiO grown at 1073 K for 75 h (760 torr O_2): (a) Ni substrate; (b) chemical polishing, no coating; (c) chemical polishing, CeO_2-coated;

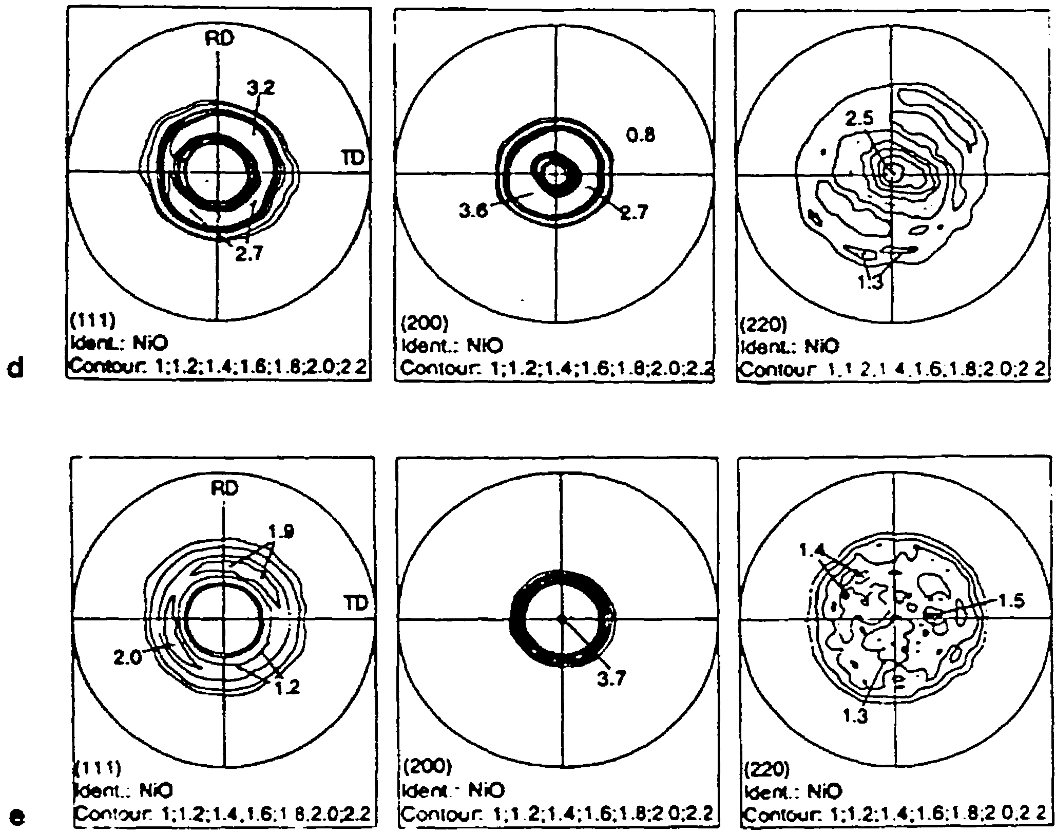

Fig. 11.1. - continued: (d) mechanical polishing, no coating; (e) mechanical polishing, CeO_2-coated.

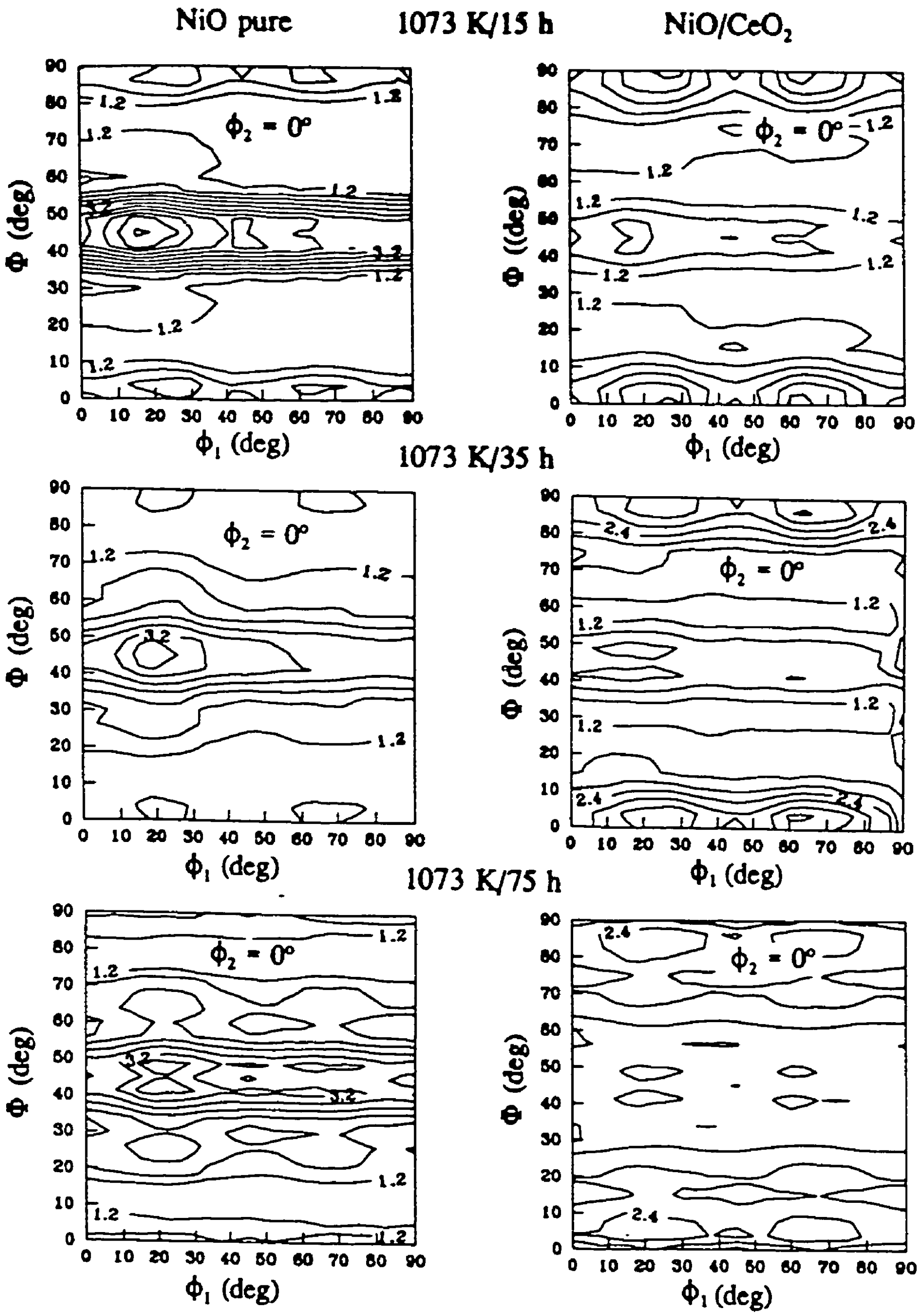

Fig. 11.2. Influence of oxidation time at 1073 K on texture evolution in pure and CeO$_2$ modified NiO. Results shown as a part of orientation distribution functions for $\phi_2 = 0°$. Contour levels for all graphs: minimum - 1.2, step - 0.4.

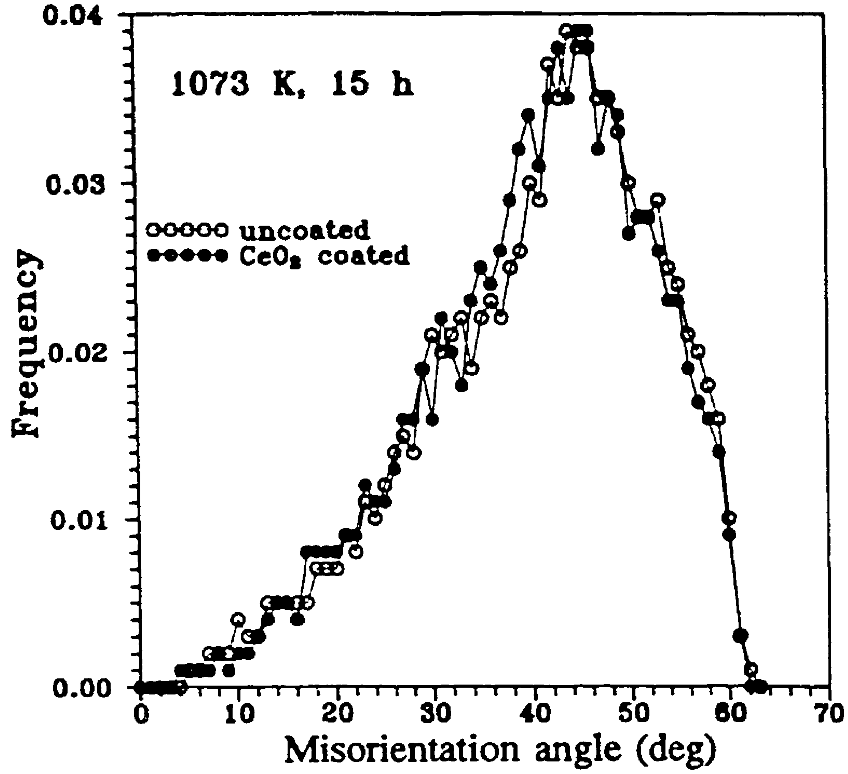

Fig. 11.3. Misorientation angle distributions for pure and CeO_2 modified NiO grown for 15 h at 1073 K.

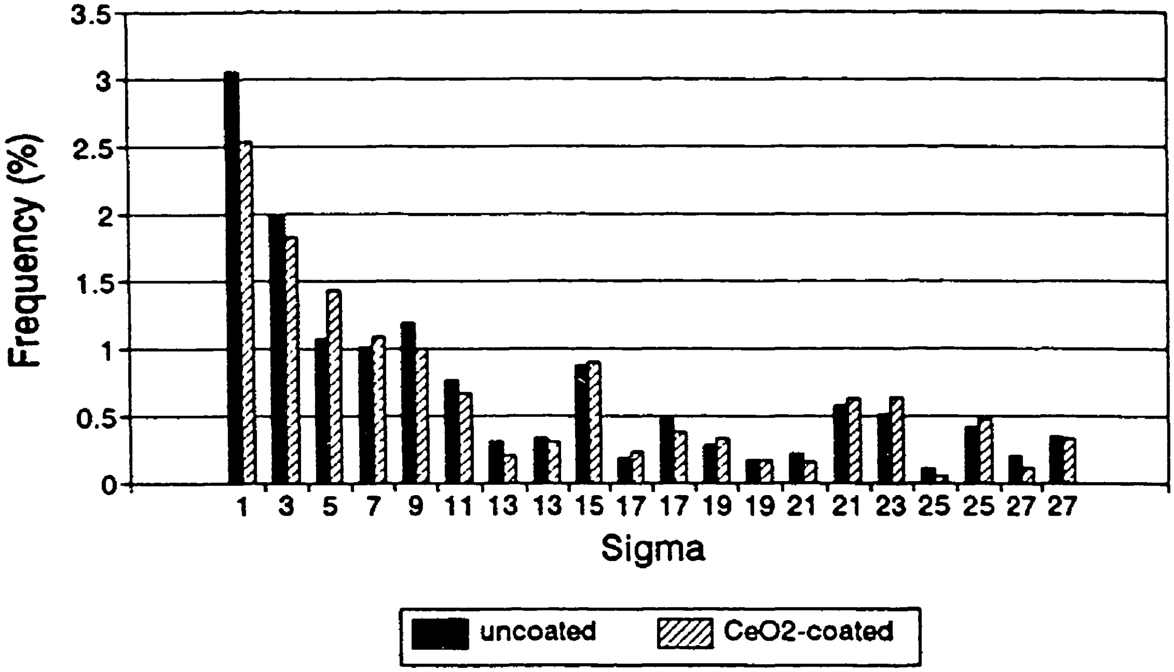

Fig. 11.4. Histogram of grain boundary character distributions for Σ up to 27 for pure and CeO_2 modified NiO grown at 1073 K for 15 h. Σ's: 13, 17, 19, 21, 25, and 27 are *a* and *b* type.

CHAPTER 12. DISCUSSION OF RESULTS

In the previous Chapters, the experimental results were presented and some specific problems were briefly discussed. This Chapter contains the discussion of general research findings, based on the data from several Chapters.

12.1. Analysis of factors controlling the protective properties of CeO_2 sol coatings

The thermo-manometric and thermo-gravimetric measurements demonstrate that CeO_2 sol-gel coatings significantly reduce the oxidation rate of nickel at temperatures where the grain boundary diffusion controls the NiO growth. The measurements established the major factors affecting the protective properties of CeO_2 coatings at high temperatures, as is summarized in Fig. 12.1.

The role of the coating nature in oxidation inhibition is considered in terms of the coating thickness and CeO_2 particle size. Since the coating is the only reservoir of the reactive element particles inside the growing oxide, therefore, according to the conventional approach, a greater coating thickness should extend its lifetime. However, the experimental data indicates that this is not the case for CeO_2 sol-gel coatings. As seen in Fig. 5.1, a relatively small amount of the reactive element is sufficient to markedly suppress the oxidation rate. This amount is 5-10 μg CeO_2/cm^2 for Ni substrate, which corresponds to a coating thickness of 7-14 nm. The literature data show a wide range of thicknesses for the effective reactive element coatings. For example, Moon [1989] observed that CeO_2 sol coatings with weights between 2 and 80 $\mu g/cm^2$ induced a similar reduction in NiO growth rate at 1173 K. On the other hand, for 800H steel substrate, Haanappel et al. [1991] found that the optimum CeO_2 coating thickness is 500 nm. Based on the above data, it is clear that a minimum coating thickness is required to improve oxidation resistance. However, the same results show that with increasing the coating thickness above the optimum value, there is a tendency to decrease the effectiveness of the coating (Fig. 5.1). The observation of oxide growth morphology and distribution of the reactive element inside the oxide film explain the role of coating thickness. While a thin coating is easily incorporated into the growing oxide (Fig. 6.2a), a thick one remains for a longer time on the substrate surface, which leads to coarsening of CeO_2 particles due to sintering (Fig. 4.8). When the coating is extremely thick, it cannot be incorporated at all into growing oxide. As a result, oxidation takes place beneath it, whereas the ineffective coating remains attached to the outer oxide surface (Fig. 6.2c,d).

According to measurements of oxidation kinetics, only the CeO_2 particles with a size of approximately 5 nm substantially decreased the oxidation rate. In the case of particles larger than about 10 nm, the coating did not protect the substrate, and even increased the oxygen uptake in comparison to uncoated Ni (Fig. 5.7). The role of CeO_2 particle size can be explained if its influence on grain boundary transport is considered. The small particles can dissolve more easily and therefore may act as a source of the reactive element ion segregants in NiO grain boundaries. On the other hand, the CeO_2 particles, being the heterogeneous nucleation sites, may stimulate the refinement of NiO grain size. If the increase in the density of oxide grain boundaries is not compensated by reduction in their diffusivity, the resultant oxidation rate must be higher than the rate observed without coating.

Among other factors related to the substrate nature, chemical composition plays an important role. While for NiO [Moon, 1989] and Cr_2O_3 [Roure et al., 1994] formers, the beneficial effect of reactive element coatings is well documented, and the results published on nitrate converted reactive element oxides indicate that there is no beneficial effect for Al_2O_3 formers [Hou et al., 1992]. According to our tests, the substrate surface finishing prior to the coating deposition is also important (Figs. 5.5 and 5.6). The higher growth rate on both pure and CeO_2 coated mechanically polished Ni than on chemically polished is explained by the influence of substrate finishing on the NiO structure. Thus, the fine and randomly oriented grains of NiO formed on the surface plastically deformed by mechanical polishing lead to a higher growth rate caused by a higher density of grain boundaries (Fig. 6.11). After the CeO_2 coating is deposited on mechanically polished Ni it is more difficult to obtain a high Ce ion concentration at NiO grain boundaries.

Assuming that the reactive element additions block grain boundary transport, one should expect their beneficial effect at temperatures where the grain boundary diffusion controls the growth. The oxidation kinetic measurements confirm the above predictions. CeO_2 coated Ni shows in general a reduction in the growth rate between 873 and 1073 K (Fig. 5.6). Excluding the temperature of 873 K, the extent of the reduction is similar; approximately one order of magnitude. Microscopy observations show that at 873 K the coating remains on the substrate surface for a longer time, which results in the coarsening of CeO_2 particles. To avoid this, the initial oxidation conditions have to be modified to incorporate quickly all of the CeO_2 particles into growing NiO. The evident benefit of such a two-fold experiment is documented in Fig. 5.5. Some other factors controlling coating behaviour, including substrate crystallographic orientation and oxidation time will be discussed in greater detail later.

The sol-gel technique is one of many methods used to apply reactive elements to the substrate surface. In Fig. 12.2, the comparison of the reduction in the oxidation rate by sol-gel coatings and two other more costly techniques of surface modification, the reactive sputtering and ion implantation, is presented. The plots of the instantaneous values of the oxidation rate constants, calculated using weight-gain data (Figs. 5.2,8.1, and 10.1) indicate that the factors specific for the individual modification technique affect only a very initial stage of the oxidation. In particular, the high initial oxidation rate of Ni implanted with $2x10^{16}$ Ce ions/cm^2 is caused by radiation damage of the surface layer. Conversely, the low initial oxidation rate was observed for a 4 nm thick CeO_2 coating obtained by reactive sputtering. This may be caused by a higher uniformity of the coating, accompanied by a slower formation of the first oxide layer, than is the case for sol-gel coating. However, after a very short, initial period of exposure, the reduction in the oxidation rate caused by the reactive element Ce is quite similar for all three techniques used. Based on the above comparison, we may conclude that CeO_2 sol-gel coatings, offering comparable protection, have advantages in simplicity of deposition and significantly lower costs.

12.2. The role of the crystallographic orientation of the Ni surface in microstructural evolution of NiO modified with CeO_2

The differences in oxidation rates of individual crystal faces of uncoated Ni observed in this study are in qualitative agreement with results reported previously [Cathcart et al., 1969; Graham and Cohen, 1972; Atkinson and Taylor, 1981]. Although some discrepancies concerning the oxidation rate of various crystallographic planes of Ni still exist, there is agreement that (100)Ni oxidizes at a higher rate than (111)Ni. Since the growth of pure NiO at temperatures lower than 1300 K is controlled by Ni ion diffusion through the network of so called "easy-diffusion paths" [Harris and Atkinson, 1990], the oxidation kinetic data (Figs. 7.1 and 7.2) imply that there are differences in the type and density of the structural defects in the oxide grown on differently oriented crystals. The films formed during the initial stages of oxidation on both Ni crystal faces are epitaxially oriented. In such epitaxial structures, the dislocations are the main paths of fast ion transport. Thus, a density of dislocation in the oxide grown on (100)Ni must be higher than on (111)Ni (Fig. 7.5a-c), and is responsible for a higher oxidation rate of (100)Ni. During growth, the epitaxial films are transformed into polycrystalline structures, probably by recrystallization at high temperatures.

In thicker oxides, the grain boundaries dominate as paths of easy diffusion. Therefore, an assessment of the structure of the grain boundaries in oxides formed on both Ni faces is essential. The microstructural and diffraction data obtained for NiO grown on (111)Ni (Figs. 7.5 and 7.9) suggest that a low angle and coherent twin boundaries, are dominant in this structure. In fact, comparison of the rate constants measured experimentally and calculated by using available diffusion constants for random boundaries shows that the values calculated are smaller by almost two orders of magnitude (Table 7.1), proving that in this oxide, the grain boundaries have low diffusivity. On the other hand, in NiO formed on (100)Ni, the mixture of <111> and {100} textures (Figs. 7.7 and 7.8) is accompanied by high angle random grain boundaries. Indeed, for this oxide, the calculated and measured values of rate constants are in good agreement (Table 7.1). Our most significant finding is that after coating with CeO_2, the same differences in grain boundary structure exist and affect the oxidation behaviour of both Ni faces, as explained later, by modifying Ce distribution.

The oxidation kinetic data for NiO grown on Ni crystal faces show the two aspects of the influence of surface applied CeO_2 on inhibition of oxide growth. Namely, in addition to the reduction of the average oxidation rate expressed in Arrhenius' plot (Fig. 7.2), the time dependence of this influence, expressed by the instantaneous rate constants, must be taken into account. The comparison of k_{pi} values in Table 7.1 shows that for (100)Ni, despite high reduction in total oxygen uptake, the rate constants k_{pi} at 240 min of exposure to oxygen for pure and modified oxide are practically the same. Such a comparison for (111)Ni demonstrates that, at the same time, the rate constant k_{pi} for a coated (111)Ni is one order of magnitude lower. Thus, the analysis of changes in rate constants with time suggests that on (100)Ni the efficiency of the CeO_2 coating is decreasing with time, whereas on (111)Ni during the same time, this effect is relatively stable.

All the microstructural and kinetic data obtained allowed us to formulate the model of oxide growth on polycrystalline Ni and on Ni crystal faces after coating with CeO_2. The schematic diagram is presented in Fig. 12.3. Before oxidation, the Ni substrate was covered with a uniform, 14 nm thick layer of CeO_2 (Fig. 12.3a). After exposure to oxygen, the NiO nucleates initially on the top of CeO_2 layer. Thus, at the beginning of the exposure, the CeO_2 nanocrystals play the role of substrates, enhancing the NiO nucleation. This is macroscopically expressed by the higher oxygen uptake on coated Ni during initial periods, in comparison to the uptake for pure Ni (Figs. 5.3 and 7.1). Since the CeO_2 crystallites in the coating are randomly oriented (Fig. 4.3), the initially formed NiO does not exhibit any preferred orientation (Fig. 7.6a). The thickness of this NiO film, estimated from the oxygen uptake, is approximately the same on polycrystalline Ni and on both Ni crystal faces, i.e. of 50-60 nm (Table 5.1).

As soon as the CeO_2 particles are incorporated into NiO (Fig. 12.3b), the oxidation rate starts to decrease and the mechanism of NiO growth changes from outward metal ion diffusion to inward oxygen ion diffusion. Such a conclusion is supported by the depth location of CeO_2 which acts as inert marker (Figs. 6.10,7.3 and 8.5). However, the detailed study using oxygen isotopes $^{16}O_2/^{18}O_2$ (Fig. 10.5) revealed that oxygen does not diffuse to the metal/oxide interface, but only to the region beneath the Ce rich zone, as indicated by the arrow in Fig 12.3c. This means that the inner sublayer of oxide is developed during the steady stage of oxidation by outward Ni^{2+} diffusion from the metal/oxide interface. It is thus clear that the oxygen transport through the Ce-rich part to the reaction front, being a slower of these two processes, controls the growth rate.

The experiments on Ni single crystals reveal that the structure of NiO formed at the initial stage on CeO_2 coated Ni is directly influenced by crystallographic orientation of the substrate surface, as in the case of uncoated Ni (Figs. 7.5 and 7.6). It is believed that the growth of the inner sublayer of NiO on CeO_2 coated Ni takes place by copying the structure of already existing very thin epitaxial NiO film. This film may be formed during the stage of coating calcination at 573 K, or even during exposure of the Ni surface to oxygen at room temperature. This explanation is supported by the fact that the plastic deformation of a very thin surface layer of Ni, e.g. by mechanical polishing, suppressed the influence of substrate surface crystallography on the oxide structure (Figs. 6.3 and 6.11). As is discussed below, the structure of the inner sublayer of NiO leads to differences in the further oxide growth mechanism by affecting the diffusion of reactive element ions from the layer where CeO_2 is dispersed.

During the steady stage of oxide growth, two reaction fronts are present: the first at the oxide/gas interface, and the second at the interface between the CeO_2 containing, middle sublayer, and the inner sublayer of NiO (Fig. 12.3c). In the case of oxide formed on CeO_2 coated (111)Ni, only one front located inside the oxide is active. In the oxide grown on CeO_2 coated (100)Ni, the reaction takes place simultaneously on both interfaces; with extended oxidation time, however, the reaction at oxide/gas interface becomes predominant. For polycrystalline Ni substrate the location of reaction fronts depends on the surface finishing before coating. While for mechanically polished Ni it is similar to the (100)Ni single crystal, for chemically polished Ni it changes from grain to grain of the Ni substrate.

12.3. Analysis of NiO growth on Ce-implanted Ni

Ion implantation causes two major changes to the surface region of the Ni substrate: the chemical composition is modified and the radiation damage is introduced. The radiation damage represents a major difference between modification by ion implantation and by the CeO_2 coatings. Although the literature data often neglects the effect of radiation damage on the oxidation process [George et al., 1989], there are also published results indicating that radiation damage is important [Srnivasan et al., 1986]. To verify the role of physical damage, some ion-implanted samples were vacuum-annealed prior to oxidation.

The ultra-high vacuum of 10^{-9} torr applied during post-implantation annealing, prevented the formation of NiO. Unfortunately, because of the extremely high affinity to oxygen, the Ce implants oxidized, forming CeO_2 (Fig. 8.5b). At 1073 K, the Ce diffusion towards the outer surface continued until all the implants were moved into the surface region with a thickness of 10 nm (Fig. 8.4). The diffusion of the reactive element towards the outer surface, observed also for yttrium implants in Ni [Hampikian et al., 1989], is caused by the high affinity of the reactive element to oxygen. This compensates for the tendency of implants to move towards the substrate, because of radiation enhanced diffusion, as reported for Al implanted Ni [Potter and McCormick, 1979; Hampikian and Potter, 1992]. Since for Ni the movement of vacancies begins at temperatures near 573 K [Schumacher et al., 1962], annealing at 1073 K for 1 h leads to complete repair of the damaged structure. In order to investigate this problem, two sets of substrates characterized by differences in the distribution and the chemical state of Ce, and the radiation damage of the surface layer, were oxidized.

The development of the oxide microstructure on Ce-implanted Ni is similar to that shown in Fig. 12.3 for CeO_2 coatings. Some growth aspects, specific for implanted Ni are discussed here. During the very initial stages of exposure to oxygen (Fig. 12.3a), Ce is oxidized to CeO_2. Then, CeO_2 particles are incorporated into growing NiO with the reaction taking place at the oxide/gas interface by an outward Ni ion transport (Fig. 12.3b). Moreover, at the beginning, the oxidation is accompanied by recrystallization of the region damaged by ion bombardment. The latter process is completed very quickly. For example, at 873 K about 2 min were necessary to recrystallize the radiation damaged Ni [Ahmed and Potter, 1987]. It is believed that the heavily damaged, or even amorphous thin surface layer, as observed for similar fluence of yttrium implants in Ni [Hampikian and Potter, 1992], leads to nucleation of extremely fine grained NiO, having a structure shown in Fig. 8.7. When oxidation follows vacuum annealing, the CeO_2 particles present already on the Ni surface are directly incorporated into the growing NiO.

Oxidation kinetic data presented in Fig. 8.1 do not support the strong influence of radiation damage on oxide growth rates during the initial stages. The substrate which was unannealed exhibits a slightly higher, but above the experimental error and reproducible, oxygen uptake during the first minutes of the reaction (Fig. 8.1, inset). This uptake, in fact, is caused partly by the oxidation of the Ce implants itself. To oxidize all the Ce implants to CeO_2, an amount of 1.03 μg O_2/cm^2 is necessary. As can be estimated from the depth location of Ce implants (Fig. 8.4), this oxygen consumption is superimposed on the oxygen uptake caused by oxidation of Ni, and takes place continuously up to roughly 7-8 min of exposure, which corresponds to the formation of about 50 nm thick oxide film. The kinetic curves indicate that Ce implants after oxidation to CeO_2 enhanced the nucleation and growth of NiO, in the same way as was reported for CeO_2 coatings (Figs. 5.3 and 7.1). After approximately 10 min of reaction and the formation of oxide with a thickness of 60 nm, as estimated from the oxygen uptake, the oxidation rate starts to decrease. As we will discuss later, we believe that at this time Ce segregates in NiO grain boundaries and blocks the ion transport.

A schematic representation of a cross-sectional view of oxide obtained from the imaging of a planar TEM section is similar to that described for the CeO_2 coated substrate (Fig 12.3c). However, conversely as during oxidation of the CeO_2 coated Ni, after implantation, no influence of the Ni grain boundary and Ni grain orientation on the preferential formation of the oxide was detected (Figs. 6.3, 9.3 and 9.4). When there is no physical damage of the substrate, the oxidation mechanism leads to the evolution of the oxide structure influenced by the substrate. Experiments with CeO_2-coated Ni showed that the structure of the inner oxide layer (Fig. 12.3c) is affected by the crystallographic orientation of the Ni grains resulting in the characteristic growth anisotropy (Fig. 6.2). For implanted Ni, the NiO growth anisotropy is almost totally suppressed (Fig. 8.2). Moreover, the inner oxide sublayer is characterized by a random distribution of grain orientations (Fig. 8.10). We suggest that such structure is caused by radiation damage extending far below the implanted region, as is documented by Ahmed and Potter [1987]. Recrystallization of the region damaged by radiation leads to a formation of polycrystalline fine-grained Ni, which in turn results in the growth of polycrystalline oxide with grains randomly oriented (Fig. 8.10). This information will be important to further discussion.

12.4. Analysis of long-term oxidation behaviour of Ni coated with CeO_2

The inhibition in the NiO rate by a factor of 50 achieved in long-term experiments (Table 9.1) is significantly higher than the approximately ten-fold reduction observed previously during early stages of oxidation (Fig. 5.6). The typical improvement in rate constant, cited in the literature for the NiO/CeO_2 system at temperatures below 1200 K, is up to 10 times [Moon and Bennett, 1989]. For the NiO/CaO system the rate constant reduction at 1123 K by a factor of 20 was recently reported [Strawbridge and Rapp, 1994]. The simple visual assessment of the oxide growth surface (Figs. 9.3, 9.4) shows that the reactive element effect during long-term exposure depends strongly on the substrate surface orientation. The observed differences in thicknesses of the oxide formed on various Ni grains (Figs. 9.5 and 9.6) exceed the values measured for (111) and (100) Ni single crystals (Figs. 7.1 and 7.2).

Both the oxide growth morphology (Fig. 9.4) and the cross-sectional images (Fig. 9.6) show that the oxidation rate anisotropy after long-term exposure also exists after Ni modification with CeO_2. It is obvious that CeO_2 coatings do not act as barrier layers to the diffusional scale growth, since thicker coatings were less favourable than thinner ones (Fig. 9.1). SEM images of the oxide growth surface in Fig. 9.4 support the notion that a CeO_2 coating does not remain on the sample surface but is incorporated into the growing oxide.

Data on oxidation kinetics obtained after applying CeO_2 indicate that there is a change in the NiO grain boundary diffusion. The rate constant for pure NiO with a grain size of 600 nm as measured in Fig. 9.7 for pure NiO, calculated using diffusion data from the literature [Atkinson and Taylor, 1981; Atkinson et al., 1982] is $7.8\text{x}10^{-12}$ $g^2cm^{-4}s^{-1}$, which is quite close to the rate constant measured experimentally (Table 9.1). The presence of CeO_2, however, decreases the oxide grain size. For the grain size of 60 nm, as found from the TEM image of the Ce-rich part (Fig. 9.8), the calculated rate constant is 1.3×10^{-10} $g^2cm^{-4}s^{-1}$, which is almost four orders of magnitude larger than the experimental rates in Table 9.1. Thus, we believe that the reactive element ions detected at the NiO grain boundaries change their diffusivity. It is also possible that the saturation of NiO grain boundaries with Ce^{+4} ions after long-term exposure is higher than that used at early stages, and this is responsible for a higher reduction of the NiO growth rate.

12.5. Texture and grain boundary character in NiO modified with CeO_2

12.5.1. *Texture development in NiO modified with CeO_2*

The x-ray measurements presented in Chapter 11 revealed the essential differences in the textures of oxides grown on polycrystalline Ni substrates. These differences are accompanied by changes in oxidation kinetics, depth location of the reactive element, and the evolution of surface topography. In order to correctly interpret the texture data, they should be compared with the corresponding depth microstructure of the oxides.

Of all the substrates studied, the simplest oxide microstructure was developed on mechanically polished Ni. When CeO_2 is absent, at the beginning, the fine and randomly oriented oxide grains nucleate on the deformed surface of Ni. After a few minutes' exposure, however, there are signs of the formation of the preferred orientation, as shown by TEM electron diffraction (Fig. 6.11). The pole figures of oxides formed during longer exposures exhibit evident growth texture, apparently unrelated to the substrate texture (Fig. 11.1). The major texture component observed here, a <110> fibre, was also detected by Chadwick and Taylor [1985] in thick NiO scales formed at 1373 K. Although some possibilities to develop the duplex structures exist for thick NiO scales and are believed to be caused by the inward transport of molecular oxygen [Atkinson and Smart, 1988], according to SEM imaging of fracture cross-section, for temperature and time range of this study, the single NiO layer existed and contributed to the x-ray diffraction signal.

The presence of CeO_2 coatings on mechanically polished Ni leads to the more complex depth structure of the oxide (Fig. 12.3c). Thus, the x-ray signal was diffracted from all three sublayers. While the texture of the middle layer is apparently random (Fig. 6.13a), both the inner and outer layers are characterized by specific preferred orientations. After the oxidation of mechanically polished and coated Ni, the CeO_2 -containing part is located deep inside the oxide (Fig. 6.10). In such a structure, the outer layer, being thicker, has a higher contribution to the x-ray signal diffracted. It can be concluded therefore that the outer layer is characterized by a <100> fibre texture with strength increasing with oxidation time (Fig. 11.1).

In order to follow the formation of the three-layer structure of oxide shown in Fig. 12.3c, one should remember that the CeO_2 particles in the coating are randomly oriented, as is the first layer of NiO nucleated on top of the coating (Fig. 7.6a). At a steady stage of oxidation, two growth fronts are active: at the oxide/gas interface and beneath the CeO_2 rich part. According to the oxygen isotope experiment, however, the predominant reaction front is at the oxide/gas interface, with the growth dominated by the outward diffusion of Ni cations (Fig. 10.4). The oxide texture measured on this substrate was, therefore, developed during growth from a randomly nucleated NiO film on top of the CeO_2 coating.

The literature suggests that during outward growth, the oxide grains do not change their orientation and that the texture must result rather from the growth selection. According to Khoi et al. [1975], the preferential absorption of oxygen at the oxide surface could be a decisive factor in that mechanism. An alternative hypothesis, suggested by Chadwick and Taylor [1985], is based on the lower surface energy of (100) planes, as NiO has a preferred cubic habit. The results of this study show that CeO_2 affected the development of NiO-growth texture on mechanically polished Ni (Fig. 11.1). Since no CeO_2 particles are present inside the outer layer, one may suspect that Ce ions diffusing along NiO grain boundaries could contribute to the changes observed. In fact, the presence of some ion segregants in the outer layer of NiO formed on mechanically polished Ni was detected by some authors [Chadwick and Taylor, 1985; Moon, 1989].

The texture of pure NiO grown on chemically polished Ni should be considered a sum of textures developed on individual Ni grains. In general, oxide texture depends on Ni substrate orientation, and a number of specific epitaxial relationships is given in the literature [Khoi et al, 1975]. According to x-ray measurements presented in Chapter

7, oxidation of (111)Ni face leads to the growth of NiO characterized by a single component (111) texture (Fig. 7.9). In NiO grown on (100)Ni, there is present a <111> fibre in addition to (100) epitaxial component (Fig. 7.7). The comparison of pole figures of the Ni substrate and NiO layers (Fig. 11.1) shows that oriented nucleation and epitaxial growth dominate the oxide texture development on chemically polished Ni.

The development of NiO texture on chemically polished and CeO_2 coated Ni starts in the same way as for mechanically polished Ni. Namely, the presence of CeO_2 leads to random nucleation of NiO on top of the coating at the beginning of oxidation, as was shown by TEM electron diffraction (Fig. 7.6a). As soon as the CeO_2 -modified NiO layer is formed, the growth mechanism of oxide changes from outward Ni to inward oxygen ion diffusion. As a result, the dominant reaction front moves underneath the CeO_2 -containing layer, and Ni orientation again plays an important role in NiO growth, the same when the CeO_2 coating was absent. Although the NiO growth depends on the Ni grain orientation, in general, the inner NiO layer increases predominantly its thickness (Chapter 10) and finally contributes to the textures measured. This explains, why the textures of the NiO layers grown on chemically polished Ni, both pure and CeO_2 coated, do not exhibit substantial differences.

12.5.2. *Analysis of GBCD in NiO modified with CeO_2*

A lower oxidation rate of CeO_2-coated Ni accompanied by smaller grain size, i.e. higher density of grain boundaries in CeO_2 modified NiO, directly indicates the suppression of grain boundary diffusivity by CeO_2 or Ce. Such a suppression of diffusivity may result from changes in the grain boundary structure. This idea was explored by Chadwick and Taylor [1985] using electron diffraction and TEM technique. Because of experimental difficulties with small grain size, these authors were not able to conduct a reliable representative analysis. The x-ray diffraction technique used in this study, provides information about a large population of grain boundaries from all the regions between oxide/gas and the oxide/metal interface.

The GBCD in pure NiO grown for 15 h on polycrystalline mechanically polished Ni is characterized by higher contribution of $\Sigma 1$ and $\Sigma 3$ boundaries as compared to those types of boundaries calculated from a random distribution of grain orientations [Garbacz and Grabski, 1989; Morawiec et al. 1993]]. The differences, however, are small - for example, with randomly oriented grains, the frequency of $\Sigma 1$ is 2.32% as compared to 3% found for textured NiO (Table 11.1). A very strong oxide texture is necessary to dramatically change GBCD. Such a texture is present in NiO grown on single-crystalline substrates (Figs. 7.7-7.10).

According to the numerical analysis presented here, the changes of NiO texture caused by CeO_2 are not accompanied by significant changes in GBCD. As shown in Fig. 11.4, the only differences are in frequencies of $\Sigma 1$, $\Sigma 3$, and $\Sigma 5$. It is clear that those changes are small and cannot be responsible for the reduction of the oxide growth rate. Thus, the GBCD in pure and CeO_2-modified NiO films seem to indicate indirectly a beneficial role of Ce in inhibiting grain boundary transport in NiO, by the segregation mechanism which is discussed below.

12.6. Influence of the reactive element on the diffusion processes in NiO and analysis of the dynamic segregation mechanism

At present, two possible explanations of reactive element effect seem to satisfy most of the existing experimental evidence: (i) blocking of diffusion paths along oxide grain boundaries by reactive element ions [Przybylski et al.,1988; Cotell et al., 1990] and (ii) inhibition of the cationic reaction step at the oxide/metal interface [Pieraggi and Rapp, 1993]. It should be noted that while the first mechanism needs the reactive element ions to be segregated to the oxide grain boundaries, the second requires the ions to be present at the oxide/metal interface. It is clear that since reactive element oxide particles act as a source of reactive element ions, the highest segregation level should be expected in reactive element rich sublayers, and this has been proven experimentally [Przybylski et al., 1988; Cotell et al., 1990]. In contrast, there is still no experimental evidence supporting the role of reactive elements at the oxide/metal interface. In a recent study performed using various systems, such as Ni/Ca, Co/Sr, Fe/Sr, and Cu/Ba, the greatest reduction in the oxidation rate was found for Ni coated with CaO [Strawbridge and Rapp, 1994]. At the same time, Ca was not detected by SIMS at the Ni/NiO interface but was found within the oxide [Strawbridge et al., 1995]. Similarly, for our system of NiO/CeO_2, the RBS presented in Fig. 9.2 and also the analysis conducted with AES and SIMS (Figs. 6.10, 7.3 and 10.3-10.7) did not detect the segregation of Ce to the Ni/NiO interface. Therefore, at this point, we should instead consider the role of reactive elements at NiO grain boundaries. Assuming the NiO grain boundary blocking by Ce^{+4}, one can explain the kinetic and microstructural observations.

The microchemical examinations reported in this study have proven the presence of Ce ion segregants at NiO grain boundaries (Figs. 6.13, 8.9). In oxide grain boundaries, the only possible sources of Ce ions are CeO_2 particles derived from coating or formed during the initial period by the oxidation of Ce implants. Although Ce is not soluble in the NiO lattice, it may dissolve at NiO grain boundaries. According to Duffy and Tasker [1983,1986] the high energy of the CeO_2 solution in NiO, about 9 eV, is considerably reduced at NiO grain boundaries by the interaction energy between large aliovalent Ce^{+4} ions (ionic radii 0.92 A), and charge density at appropriate boundary sites. Further decreases in the solution energy are possible when Ce^{+4} ion - Ni vacancy pairs are included as a dense array on the boundary plane. This theoretical prediction agrees with experimental findings of Ce ions segregated to NiO grain boundaries and the solution of CeO_2 particles at high temperatures (Figs. 6.13,6.14,8.8 and 8.9). The process of CeO_2 dissolution takes place according to the equation [Duffy and Tasker, 1986]:

$$CeO_2 + 2Ni_L{}^{2+} = Ce_L{}^{4+} + 2NiO + V_{Ni}{}^{''} \qquad (12.1)$$

where $Ni_L{}^{2+}$, $Ce_L{}^{4+}$, $V_{Ni}{}^{''}$ are nickel and cerium ions in lattice sites, and Ni vacancies, respectively (Kroger-Vink notation [Kroger, 1964]). It is clear from the equation (12.1) that the solution of CeO_2 will lead to an increase of the vacancies concentration in NiO grain boundaries, which should increase the diffusion rate. The discrepancy between this prediction and our experimental observations can be explained by the $Ce_L{}^{4+}$ ion - $V_{Ni}{}^{''}$ vacancy pairs formation on the grain boundary plane, as proposed by Duffy and Tasker [1986]. It appears that the existence of such pairs blocks the grain boundary diffusion of Ni^{2+} cation, to the extent that the mobility of O^{2-} anions along these grain boundaries exceeds that of Ni^{2+} cations. Thus, to suppress grain boundary diffusion, the network of grain boundaries in the CeO_2 dispersed part of the oxide should first be saturated with Ce ions. However, the activation energy of the CeO_2 solution, which is about 5 eV [Duffy and Tasker, 1986], is still too high to dissolve particles that are acting as sources of Ce ions. A possible way to achieve a significant reduction of the solution energy is to decrease the particle radii [Duffy and Tasker, 1986]. This observation offers an explanation of the lower effectiveness of Ce implants and CeO_2 coatings after vacuum annealing.

It is clear that some threshold of the reactive element concentration at oxide grain boundaries is necessary to inhibit diffusion, but there are no exact numbers in the literature. In general, the higher the reactive element concentration, the higher the expectation of blocking ion diffusion. Thus, keeping a high segregation level of Ce ions at NiO grain boundaries inside the CeO_2 dispersed sublayer, is crucial for stability of oxidation inhibition over time. Recent findings, however, demonstrate that reactive element ions are not statically doping the metal-oxide system, but actively diffuse in the oxide. For α-alumina and zirconia films doped with yttrium, the diffusion of yttrium from the yttrium rich zone towards the outer surface of the oxide due to oxygen gradient, is documented [Pint and Hobbs, 1993; Pint, 1994]. For the Ni-NiO system, there is also experimental evidence of the detection of Ce, at a great distance from the CeO_2 dispersed layer. After 120 h exposure at 1173 K, Ce was found at NiO grain boundaries, mainly in the outer [Chadwick and Taylor, 1984a,b], but also in the inner part of the oxide [Moon, 1989; Moon and Bennett, 1989]. To explain the experimental observations we propose the modified version of the segregation mechanism called "dynamic segregation mechanism".

According to theoretical predictions, Ce should be relatively immobile in NiO. Duffy and Tasker [1983,1986] have estimated that in the (310)/[001] tilt boundary in NiO, the activation energy for the Ce and vacancy to exchange is 3.0 eV, whereas for Ni, the energy was estimated to be 1.86 eV. According to tracer measurements [Atkinson and Taylor, 1986], the diffusion coefficient of Ce along grain boundaries of polycrystalline NiO is given by:

$$D(Ce) = 6.3x10^{-4} \exp\{-2.0(eV) / kT\} \qquad (cm^2/s) \qquad (12.2)$$

and is much smaller than the coefficient presented above for Ni diffusion along NiO grain boundaries, but larger than the lattice diffusion of Ni in NiO. The estimated square mean path for Ce in NiO after 4 h exposure is about 200 nm at 973 K, and about 600 nm at 1073 K. These values exceed the approximately 60 nm thick CeO_2 dispersed layer, and are comparable with the thicknesses of NiO produced on both Ni faces during the same time (Figs. 7.1, 7.2, and Table 7.1). Thus, despite such low mobility, Ce is able to diffuse away from the Ce rich sublayer if the easy diffusion paths are present.

Our microscopy data indicate that the CeO_2 dispersed part of NiO initially has the same structure on all the Ni substrates used, i.e. it is composed of polycrystalline NiO and CeO_2 phases with the random distribution of grain orientations. After the saturation of grain boundaries with Ce ions, the outward Ni^{+2} transport is blocked, and the inner layer of NiO starts to grow at the rate controlled by inward O^{2-} diffusion along the grain boundaries of the CeO_2 dispersed part (Figs. 10.4-10.7). Since for NiO, the grain boundary diffusion of O^{2-} is approximately the same as the lattice diffusion of Ni^{2+} [Atkinson and Taylor, 1986], this finding is in agreement with kinetic data presented in Figs. 7.1 and 7.2. Our results show that the microstructure of the subsequently developed inner oxide sublayer, in terms of the presence of easy paths for Ce^{+4} ions diffusion, affects the process of further growth. It is believed that the CeO_2 dispersed part controls the growth rate for the whole oxide. However, the Ce^{+4} concentration at grain boundaries in the Ce rich sublayer is controlled by the microstructure of the inner NiO sublayer (Fig. 12.3), which in turn is influenced by the Ni substrate nature. Thus, the inner oxide containing a low density of diffusion paths for Ce, as that which developed on CeO_2 coated (111)Ni or chemically polished Ni with a strong <111> texture component, will protect the Ce from diffusion away from the Ce-rich region. In contrast, in the oxide developed on (100)Ni or mechanically polished polycrystalline Ni with a large number of high angle grain boundaries, Ce will diffuse along these paths from the Ce-rich region. Therefore, in the latter NiO it is difficult to keep a high concentration of the reactive element at grain boundaries in the Ce-rich sublayer.

The above finding is of engineering importance. Namely, an essential drawback in the use of the surface applied reactive element for improving high temperature oxidation resistance, is the limited time period when the reactive element is effective. The early stage oxidation (Chapter 5), supported by long term experiments on polycrystalline Ni (Chapter 9), shows that this time period may be markedly extended when an appropriate surface texture of substrate is achieved. Since the oxidation anisotropy is also observed in other metals and alloys, including extremely important alumina formers [Schumann et al., 1992], controlling the surface texture may be a very effective way to extend the lifetime of reactive element coatings at high temperatures in corrosive environments.

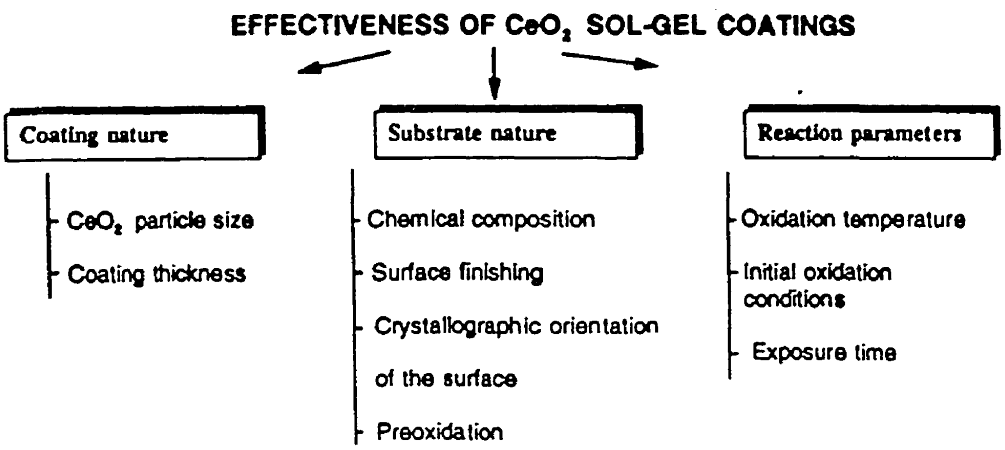

Fig. 12.1. Factors affecting the effectiveness of CeO_2 sol-gel coatings at high temperatures.

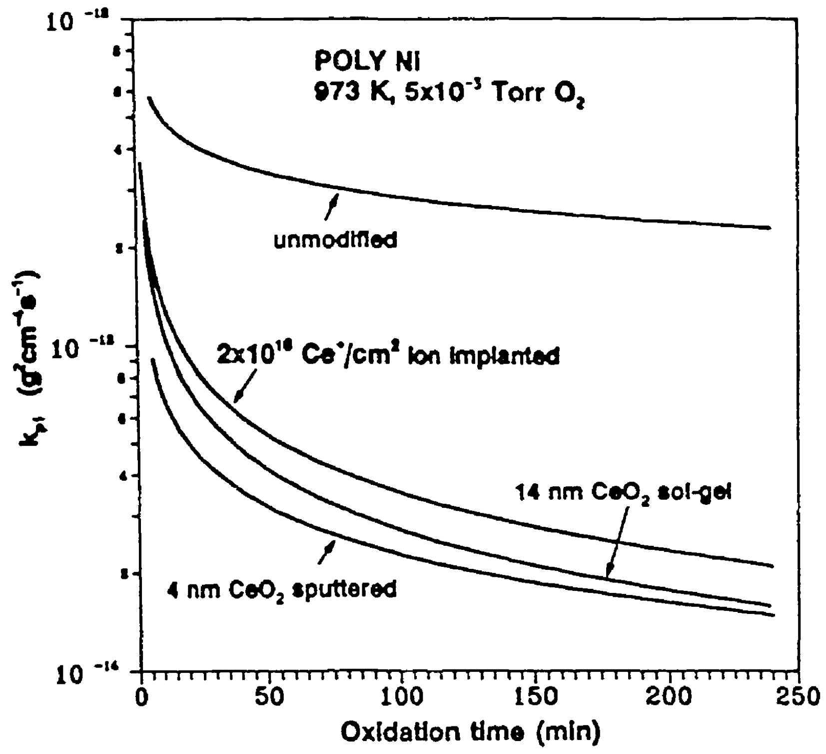

Fig. 12.2. Plot of instantaneous rate constant versus time for oxidation of Ni with surface modified with Ce by ion implantation and with CeO_2 by reactive sputtering and sol-gel technology.

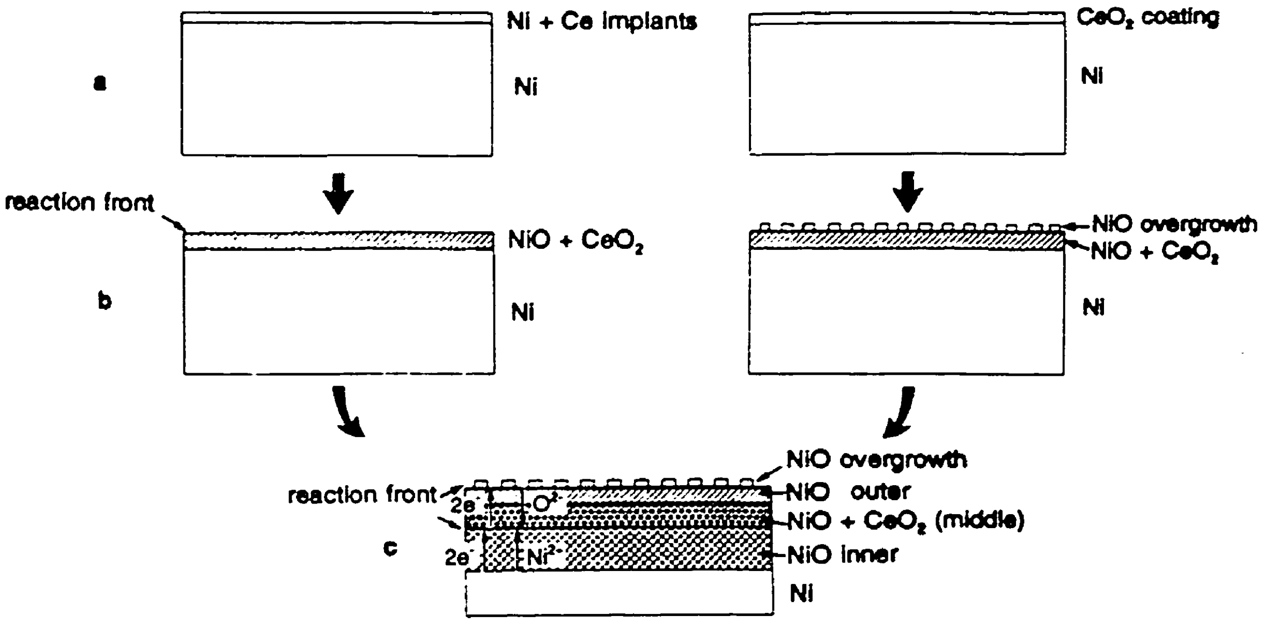

Fig. 12.3. Schematic diagram of oxide growth on CeO_2-coated and Ce-implanted Ni: (a) before oxidation, (b) initial stage of exposure to oxygen: incorporation of CeO_2 particles by outward Ni^{2+} diffusion, (c) steady stage of oxide growth by simultaneous Ni^{2+} and O^{2-} ion diffusion.

CHAPTER 13. CONCLUSIONS

1. The reactive element Ce, superficially applied in the form of ion-implants and CeO_2 coatings, significantly increases the oxidation resistance of Ni at temperatures in the range of 873-1073 K. The size of CeO_2 particles derived from coating, or formed by the oxidation of Ce implants is a decisive factor which controls improvement in oxidation resistance.

2. Inhibition of Ni oxidation by CeO_2 sol-gel coatings depends on the crystallographic orientation of the Ni surface. CeO_2 coatings deposited on (100)Ni significantly decrease the oxidation rate; however, the NiO growth rate on this coated face is still higher than that measured for uncoated (111)Ni. CeO_2 coatings on (111)Ni, when incorporated into growing NiO without the coarsening of CeO_2 particles, decrease the oxidation rate to the values predicted from the lattice diffusion. The beneficial effect of CeO_2 on (111)Ni is stable over the exposure time.

3. Surface modification of Ni with Ce implants and CeO_2 coatings changes the NiO surface morphology and internal microstructure. NiO films formed on Ce/CeO_2 modified Ni are composed of three sublayers, each with an essentially different microstructure. The reactive element Ce is present in a well defined middle sublayer which is composed of NiO grains and randomly distributed CeO_2 particles. Moreover, Ce^{4+} ions segregate to NiO grain boundaries in this sublayer. Although during the early-stages of oxidation this sublayer is located near the gas/oxide interface, its depth location changes with exposure time and depends mainly on substrate surface finishing, CeO_2 particle size and Ni grain orientation.

4. The structure and texture of NiO developed on both pure and CeO_2-coated Ni is influenced by the crystallographic orientation of the substrate. For (111)Ni, the initial epitaxially oriented NiO film with low dislocations density is transformed to polycrystalline film with a strong {111} texture. For (100)Ni, the epitaxial {100} film with a high dislocation density is transformed to polycrystalline film with two major texture components: <111> and {100}. Although the presence of CeO_2 introduces a three-layered structure of NiO, the structure of the inner sublayer is essentially the same as that observed without the coating.

5. The texture of NiO grown on polycrystalline Ni depends on the surface finishing and the presence of the CeO_2 coating. Oxidation of chemically-polished Ni with a {100}<023> texture leads to oriented nucleation and the epitaxial growth of NiO with a final {100}<013> texture. The presence of CeO_2 coatings on this substrate does not substantially change the texture of NiO. The oxidation of mechanically polished Ni in the absence of CeO_2, results in random nucleation and the growth of NiO with a <110> fibre texture. The CeO_2 coatings on this substrate change the NiO texture to a <100> fibre.

6. The reduction in the NiO growth rate and change in the NiO microstructure caused by the reactive element Ce, are not accompanied by changes in the grain boundary character distribution. The crystallographic orientation of the Ni substrate is the major factor which controls the grain boundary character distribution in both pure NiO and NiO modified with CeO_2 .

7. The growth mechanism of NiO films on polycrystalline Ni modified with Ce/CeO_2 depends on the surface finishing. CeO_2 sol-gel coatings deposited onto mechanically polished Ni significantly decrease the outward Ni^{2+} diffusion, but this mechanism is still predominant for NiO growth. The high inward diffusion of O^{2-} is observed for NiO formed on chemically polished Ni; this applies to both Ce ion-implanted and CeO_2 -coated Ni.

The mechanism of NiO growth on CeO_2 sol-coated Ni single crystals depends on crystallographic orientation. Of the two crystal faces studied, (100)Ni and (111)Ni, the higher contribution to growth by inward O^{2-} diffusion is observed for the CeO_2 sol-coated (111)Ni face.

8. A correlation exists between evolution of the topography of the oxide/gas interface and the mechanism of NiO growth. The surface roughness of NiO films growing predominantly by outward diffusion of Ni^{2+} cations increases significantly as the growth proceeds. Conversely, the changes of surface roughness of NiO films growing predominantly by inward diffusion of O^{2-} anions are small in the range of the oxide thicknesses studied.

9. This study suggests that at high temperatures the CeO_2 particles in NiO, derived from the coatings or formed by oxidation of Ce implants, dissolve and act as a source of Ce^{4+} ions in the NiO grain boundaries. It is believed that Ce^{4+} ion segregants impede Ni^{2+} diffusion, while allowing O^{2-} diffusion to continue, which results in change of the growth mechanism of NiO modified with CeO_2 compared to that of pure NiO. The size of the CeO_2 particle size play a key role in the dissolution process. The large CeO_2 particles are responsible for a lower effectiveness of Ce implants and CeO_2 coatings after vacuum annealing.

10. A modification of the "grain boundary segregation mechanism" is proposed in order to explain all the experimental findings of this study. A new "dynamic segregation mechanism" assumes that Ce^{4+} ions do not statically block the NiO grain boundaries, but actively diffuse along them. The Ce^{4+} diffusion from the CeO_2 containing a sublayer of NiO, in turn, affects the concentration level of Ce^{4+} ions in the NiO grain boundaries in this sublayer.

11. The microstructure and texture of NiO developed beneath the CeO_2 dispersed sublayer, play a key role in the "dynamic segregation mechanism" proposed, since they affect the depth distribution of Ce in NiO and the Ce concentration at NiO grain

boundaries. The presence of high diffusivity grain boundaries in NiO formed on polycrystalline Ni, with a surface deformed by mechanical polishing, and on the (100)Ni face, allows Ce to diffuse away from the CeO_2 dispersed sublayer. Conversely, the microstructure of NiO developed on (111)Ni containing grain boundaries with low diffusivity prevents the Ce from diffusing out, and extends the beneficial effect of surface applied CeO_2 on oxidation resistance over longer time intervals.

The study shows that controlling the surface texture of the metallic substrate may be a very effective way to extend the lifetime of reactive element coatings at high temperature in corrosive environments.

CONTRIBUTION TO ORIGINAL KNOWLEDGE

1. Measuring the early-stage growth kinetics of NiO thin films on Ni superficially modified with Ce and CeO_2 :

The oxidation kinetics of Ni modified with Ce/CeO_2 during the very early stages of NiO film formation, were measured at high accuracy. This was achieved by an application of the unique ultra-high vacuum manometric system. This apparatus is capable measuring reaction kinetics at oxygen uptakes at a finer level than that obtained from thermogravimetry.

2. Description of the microstructures of thin NiO films modified with Ce:

Because of experimental difficulties, the detailed microstructural characterization of thin oxide films with a complex depth-structure, grown on metals with surface modified with the reactive element, has not yet been done. The description of the microstructure of NiO thin films doped with Ce and the redistribution of Ce at high temperature, obtained using several advanced techniques, contributed primarily to the explanation of the mechanism responsible for oxidation inhibition. Secondly, these results may be utilized in the future to develop a computer model of oxide growth.

3. Description of the growth mechanism of NiO films modified with Ce:

An oxygen isotope experiment proves that the reactive element Ce, under certain conditions, changes the NiO growth mechanism from outward Ni^{2+} to inward O^{2-} diffusion. This is contrary to the existing literature data. An additional original finding of the oxygen isotope experiment is the location of a reaction front within NiO films modified with Ce.

4. The application of atomic force microscopy in the area of high-temperature oxidation:

In this research, the recently developed and powerful technique of surface imaging, AFM, was applied for the first time in the analysis of rough surfaces of oxides formed during high temperature oxidation. A correlation found, between the evolution of oxide surface roughness and the growth mechanism, is fully original.

5. The application of texture research in the area of high temperature oxidation:

Although the dependence of the oxidation rate on the crystallographic orientation of the metallic substrate was known in the past, until now this finding was unexplored for the purpose of improving oxidation resistance. The original contribution of this research is an application of texture and grain boundary character distribution in order to explain the effect of the reactive element on the oxidation process. The texture of NiO is critical for an explanation of the stability of the reactive element concentration inside NiO and the diffusion of Ni and O ions at high temperatures. This finding opens a new area of texture control for oxidation prevention.

6. Proposing a new "dynamic segregation mechanism" to explain the inhibition of the NiO growth rate by Ce additions:

Our results demonstrated that, to be effective, the reactive element must be concentrated in a thin layer inside the native oxide. But, according to our findings, the reactive element does not statically dope the native oxide but actively diffuses along specific paths, mainly along oxide grain boundaries. The new "dynamic segregation mechanism" proposed, which is based on the previous "grain boundary segregation theory" explains the improvement of Ni oxidation resistance by CeO_2 coatings and Ce implants.

7. Determining the factors controlling the protective properties of CeO_2 sol-gel coatings:

The critical question for application of the reactive element coating, as to what determines the conditions required to achieve a long lasting protection by trace amounts of the reactive element, until now remained unanswered. The results of this study provide an answer and allow us to establish all the important factors related to the coating nature, substrate nature, and oxidation conditions which control the effectiveness of the surface-applied reactive element. Moreover, the experiments permit us to compare the effectiveness of three different surface techniques: ion implantation, sol-gel technology, and reactive sputtering.

SUGGESTIONS FOR FUTURE WORK

1. <u>Further experimental study to explain the behaviour of the Ni-NiO-CeO_2 model system and to verify the assumptions of the "dynamic segregation mechanism"</u>:

When a progress in further deceasing the diameter of the electron beam in electron microscopes will be achieved, the following analyses of grain boundary segregation in NiO modified with Ce/CeO_2 will be of interest:

i) to determine a correlation between a level of Ce segregation in the NiO grain boundary and the grain boundary structure;

ii) to determine a level of Ce segregation in the NiO grain boundary of the same structure and containing the CeO_2 particles with different size; this analysis will allow to verify the critical role of the CeO_2 particle size in saturation NiO grain boundaries with Ce ions;

iii) to determine a stability of the level of Ce segregation in specific NiO grain boundaries with exposure time at high temperatures.

2. <u>Experimental study of the application of CeO_2 sol-gel coatings for oxidation protection of heat resistant alloys:</u>

The study of the Ni-NiO-CeO_2 model system should be extended to heat resistant alloys with complex chemical composition; especially alumina formers. The low rate of oxide formation on these alloys imposes difficulties on the application of the reactive element. The study should lead to design of the surface pretreatment, which will prevent the coarsening of the reactive element oxide particle. When this goal is achieved, the coatings would provide the further improvement of the oxidation resistance of alumina forming alloys.

3. Computer modelling the oxide growth on metals and alloys modified with reactive elements:

The present study provides a large number of experimental data from several advanced analytical techniques. These results are especially valuable as an input for computer modelling of NiO growth, diffusion processes within the oxide and the diffusion suppression by the reactive element Ce. The computer modelling should lead to the atomistic image of the interaction of reactive element ions in oxide grain boundaries.

REFERENCES

Ahmed, M. and Potter, D.I., 1987, *Acta Metall.*, **9**, 2341.

Anderson, A.B., Mehandru, S.P. and Smialek, J.L., 1985, *J. Electroch. Soc.*, **132**, 1695.

Atkinson, A., 1984, *Solid State Ionics*, **12**, 309.

Atkinson, A., 1985, *J. Phys. Paris Colloque* C4, **46**, 379.

Atkinson, A. and Taylor, R.I., 1979, *Philos. Mag.*, **39**, 581.

Atkinson, A. and Taylor, R.I., 1981, *Philos. Mag.*, **43**, 979.

Atkinson, A., Taylor, R.I. and Hughes, A.E., 1982, *Philos. Mag.*, **45**, 823.

Atkinson, A. and Taylor, R.I., 1986, *J. Phys. Chem. Solids*, **47**, 315.

Atkinson, A. and Smart, D.W., 1988, *J. Electroch. Soc.*, **135**, 2886.

Atomic Force Microscopy (operating manual), 1993, Digital Instruments Inc., Santa Barbara, CA.

Bennett, M.J., Houlton, M.R. and Dearnaley, G., 1980, *Corros. Sci.*, **20**, 69.

Bennett, M.J., Dearnaley, G., Houlton M.R. and Hawes, R.W.M., 1982, Ion Implantation into Metals, Pergamon, Oxford, 264.

Bennett, M.J., 1983, *High Temperature Corrosion*, NACE, **6**, 145.

Bennett, J.M. and Mattsson, L., 1989, Introduction to Surface Analysis and Scattering, Optical Soc. of America, Washington D.C.

Birks, N. and Meier, G.H., 1983, Introduction to High Temperature Oxidation of Metals, Edward Arnold Publ. Ltd., London.

Brandon, D.G., 1966, *Acta Metall.*, **14**, 1479.

Brinker, C.J. and Scherer, G.W., 1990, Sol-Gel Science, The Physics and Chemistry of Sol-Gel Processing, Academic Press Inc., New York.

Cannon, R.M., Rhodes, W.H. and Hener, A.H., 1980, *J. Amer. Ceram. Soc.*, **63**, 46.

Cathcart, J.V., Petersen, G.F., Sparks, C.J., 1969, *J. Electroch. Soc.*, **116**, 664.

Chadwick, A.T. and Taylor, R.I., 1984a, *Solid State Ionics*, **12**, 343.

Chadwick, A.T. and Taylor, R.I., 1984b, Proc. 9-th Inter. Congress on Metallic Corrosion, Toronto, Ottawa.

Chadwick, A.T. and Taylor, R.I., 1985, *J. Microscopy*, **140**, 221.

Chason, E., Falco, Ch.M., Ourmazd, A., Schubert, E.F., Slaughter, J.M. and Williams, R.S. in Evolution of Surface and Thin Film Microstructure, edited by Atwater, H.A., Chason, E., Grabow, M.H. and Legally, M.G., 1992, MRS Proc. Vol., **280**, Pittsburgh, PA, 203.

Chu, W.K., Mayer, J. and Nicolet, M.A., 1978, Backscattering Spectrometry, Academic Press, New York.

Cotell, C.M., Yurek, G.J., Hussey, R.J., Mitchell, D.F. and Graham, M.J., 1987, *J. Electroch. Soc.*, **134**, 1871.

Cotell, C.M., Yurek, G.J., Hussey, R.J., Mitchell, D.F. and Graham, M.J., 1990, *Oxid. Met.*, **34**, 173.

Dieter, G.E., 1976, Mechanical Metallurgy, McGraw-Hill Inc., New York.

Duffy, D.M. and Tasker, P.W., 1983, *Phil. Mag. A*, **47**, 817.

Duffy, D.M. and Tasker, P.W., 1984, *Phil. Mag. A*, **50**, 143.

Duffy, D.M. and Tasker, P.W., 1986, *Phil. Mag. A*, **54**, 759.

Funkenbusch., A.W., Smegill, J.G. and Bornstein, N.S., 1985, *Metall. Trans.*, **16A**, 1164.

Eror, N.G. and Wagner, J.B., 1969, *J. Phys. Stat. Sol.*, **35**, 641.

Feldman, L.C. and Mayer, J.W., 1988, Fundamentals of Surface and Thin Film Analysis, North-Holland, Amsterdam.

Field, D.P. and Adams, B.L., 1992, *Acta Metall. Mater.*, **40**, 1145.

Galerie, A., Caillet, M. and Pons M., 1985, *Mater. Sci. Eng.*, **69**, 329.

Garbacz, A. and Grabski, M.W., 1989, *Scripta Metall.*, **23**, 1369.

George, P.J., Bennett, M.J., Bishop, H.E., and Dearnaley, G., 1989, *Mater. Sci. Eng.*, **A116**, 111.

Gleiter, H. and Chalmers, B., 1972, Progress in Mater. Science, vol.16, Pergmon, Oxford.

Graham, M.J. and Cohen, M., 1972, *J. Electroch. Soc.*, **119**, 879.

Graham, M.J., Hussey, R.J., and Cohen, M.J., 1973, *J. Electroch. Soc.*, **120**, 1523.

Grimmer, H., Bollmann, M., and Warrington, D.H., 1974, *Acta Cristallogr.*, **30**, 197.

Hampikian, J.M., Devereux, O.F. and Potter, D.I., 1989, *Mater. Sci. Eng.*, **A116**, 119.

Hampikian, J.M. and Potter, D.I., 1992, *Oxid. Met.*, **38**, 139.

Harris, A.W. and Atkinson, A., 1990, *Oxid. Met.*, **34**, 229.

Harris, A.W., Brown, J.S. and Atkinson, A., 1990, Harwell Report AERE-R 13742.

Heart, E.W., 1957, *Acta Met.*, **5**, 597.

Hoshino, K. and Peterson, N.L., 1984, *J. Phys. Chem. Solids*, **45**, 963.

Hou, P.Y., and Stringer, J., 1988, *Oxid. Met.*, **29**, 45.

Hou, P.Y., Shui, Z.R., Chuang, G.Y. and Stringer, J., 1992, *J. Electroch. Soc.*, **139**, 1119.

Ikeda, Y., Nii, K., and Yata, M., 1993, *ISIJ Int.*, **33**, 298.

Johnson, C.A., 1987, Metallography Principles and Procedures, Leco Co., St. Joseph, MI.

Khoi, N.N., Smeltzer, W.W. and Embury, J.D., 1975, *J. Electroch. Soc.*, **122**, 1495.

Klug, H.P. and Alexander, L.E., 1974, X-ray Diffraction Procedures , John Wiley & Sons, New York.

Kofstad, P., 1972, Nonstoichiometry, Diffusion and Electrical Conductivity in Binary Metal Oxides, Wiley, New York.

Kofstad, P., 1986, High Temperature Corrosion, Elsevier, London.

Kramer, J.J., 1992, *Metall. Trans.* A, **23**, 1987.

Kroger, F.O., 1964, The Chemistry of Imperfect Crystals, North Holland Publ. Co., Amsterdam.

Landkof, M, Levy, A.V., Boone, D.H., Gray, R. and Yaniv, E., 1985, *Corrosion*, **41**, 344.

Leapman, R.D., Fiori, C.E. and Swyt, C.R., 1984, *J. Microscopy*, **133**, 239.

Loretto, M.H., 1984, Electron Beam Analysis of Materials, Chapman and Hall, New York.

Malis, T., Cheng, S.C. and Egerton, R.F., 1988, *J. Electron Micros. Technol.*, **8**, 193.

Meier, G.H. and Rapp, R.A., 1971, *Z. Phys. Chem. N.F.*, **74**, 168.

Merkle,K.L. and Smith, D.J., 1987, *Phys. Rev. Lett.*, **59**, 2887.

Moon, D.P., 1989, *Oxid. Met.*, **32**, 47.

Moon, D.P. and Bennett, M.J., 1989, *Mater. Sci. Forum*, **43**, 269.

Moosa, A.A. and Rothman, S.J., 1985, *Oxid. Met.*, **24**, 133.

Moosa, A.A., Rothman, S.J. and Nowicki, L.J., 1985, *Oxid. Met.*, **24**, 115.

Morawiec, A., Szpunar, J.A., and Hinz, D.A., 1993, *Acta. Metall. Mater.*, **41**, 2825.

Nath, P.J., Eyre, N. and Dearnaley, G., 1985, *Nucl. Instrum. Methods B*, **10/11**, 580.

Nelson, R.L., Ramsey, J.D., Woodhead, J.L., Cairns, J.A. and Crossley, J.A., 1981, *Thin Solid Films*, **81**, 329.

Neuman, J.P., Zhong, T. and Chang, Y.A., 1984, *Bull. Alloy Phase Diagrams*, **5**, 141.

Papaiacovou, P., Hussey, R.J., Mitchell, D.F. and Graham, M.J., 1990, *Corros. Sci.*, **30**, 451.

Perrow, J.M., Smeltzer, W.W. and Embury, J.D., 1968, *Acta Met.*, **16**, 1209.

Pieraggi, B. and Rapp, R.A., 1988, *Acta Metall.*, **36**, 1281.

Pieraggi, B. and Rapp, R.A., 1993, *J. Electroch. Soc.*, **140**, 2844.

Pint, B.A., 1994, *MRS Bulletin*, **10**, 26.

Pint, B.A., 1996, *Oxid. Met.*, **45**, 1.

Pint, B.A. and Hobbs, L.W., 1993, The Electroch. Soc. Ext. Abstracts, **93-1**, 1707.

Pfeil, L.B., 1937, U.K. Patent no. 459848.

Potter, D. and McCormick A., 1979, *Acta Metall.*, **27**, 933.

Przybylski, K. , Garatt-Reed, A.J. and Yurek, G.J., 1988, *J. Electroch. Soc.*, **135**, 509.

Rapp, R.A., 1984, *Metall. Trans.*, **15A**, 765.

Roure, S., Czerwinski, F. and Petric, A., 1994, *Oxid. Met.*, **42**, 75.

Roy, R., 1987, *Science*, **238**, 1164.

Saito, Y., Maruyama, T. and Amano, T., 1987, *Mater. Sci. Eng.*, **87**, 275.

Saito, Y. and Onay, B., 1990, *Surf. Coat. Technol.*, **43/44**, 336.

Schumacher, D., Schule, W. and Seeger, A., 1962, *Naturforsch.*, **A17**, 228.

Schumann, E, Schnotz, G., Trumble, K.P. and Ruhle, M., 1992, Acta Metall. Mater., 40, 1311.

Selvaray, U., Prasadarao, A.V., Komarneni, S. and Roy, R., 1992, *J. Am. Cer. Soc.*, **75**, 1167.

Smeggil, J.G. and Shuskus, A.J., 1987, *Surf. Coat. Technol.*, **32**, 57.

Smeggil, J.G., Shuskus, A.J., Burilla, C.T. and Cipolli, R.J., 1988, *Surf. Coat. Technol.*, **36**, 27.

Smeltzer, W.W., 1988, *Mater. Sci. Forum*, **29**, 151.

Smeltzer, W.W., Hearing, R.R. and Kirkaldy, J.S., 1961, *Acta Met.*, **9**, 880.

Smialek, J.L., 1987, *Metall. Trans.*, **18A**, 164.

Smialek, J.L., 1988, in High Temperature Materials Chemistry IV, Munir, Z. et al. eds., Electrochemical Society Inc., Pennington, N.J., p. 241.

Srnivasan, V., Meier, G.H., McCormic, A.W. and Rai, A.K., 1986, *Instrum. Met. Phys. Res.*, **B16**, 293.

Strawbridge, A. and Rapp. R.A., 1994, *J. Electroch. Soc.*, **141**, 1905.

Strawbridge, A., Rapp, R.A., Sproule, G.I., Hussey, R.I. and Graham, M.J., 1995, *J. Electroch. Soc.*, **142**, 2301.

Stringer, J., 1966, *Metall. Rev.*, **11**, 113.

Stringer, J., 1989, *Mater. Sci. Eng.*, **A120**, 129.

Sutton, A.P., and Balluffi, R.W., 1995, Interfaces in Crystalline Materials, Clarendon Press, Oxford, p. 318.

Wagner, C. and Gruenewald, K., 1938, *Z. Phys. Chem.*, **B40**, 455.

Whittle, D.P. and Stringer, J., 1980, *Phil. Trans. R. Soc. London* Ser. A, **295**, 309.

Young, E.W.A. and De Wit, J.H.W., 1985, *Solid State Ionics*, **16**, 39.

Young, F. W., Cathart, J.V. and Gwathemey, A.T., 1956, *Acta Metall.*, **4**, 145.

Ziegler, J.F, Biersack, J.P. and Littmark, U., 1985, The Stopping Power and Range of Ions in Solids, Pergamon Press, Oxford, U.K.

AUTHOR'S PAPERS RELATED TO THE SUBJECT OF THIS THESIS

The results published in the papers listed below were used during the preparation of this Ph. D. thesis. This was done with the kind permission of the following copyright holders: The Electrochemical Society (Pennington, NJ), Materials Research Society (Pittsburgh, PA), Elsevier Science Ltd. (Oxford, U.K.), Kluwer Academic Publishers (Norwell, MA), Plenum Press (New York, NY), The Government of Canada (Ottawa), The Institute of Materials (London, U.K.), The Minerals, Metals and Materials Society of AIME (Warrendale, PA), Transtec Publications Ltd. (Zurich, Switzerland).

Czerwinski, F. and Szpunar, J.A., 1997, The Nanocrystalline Ceria Sol-Gel Coatings for High-Temperature Applications,
J. Sol-Gel Sci. and Technol., **9**, 103.

Czerwinski, F. and Szpunar, J.A., 1997, Correlation Between the Growth Mechanism and Surface Roughness in Thin NiO Films Modified by CeO_2,
Corros. Sci., **39**, 147.

Czerwinski, F. and Szpunar, J.A., 1997, The Influence of Cerium Ion Implantation on Early-Stage Oxidation Kinetics of Nickel,
in Materials Modification and Synthesis by Ion Beam Processing edited by D.E. Alexander et al., Materials Research Society, Pittsburgh, PA, **438**, 217.

Czerwinski, F., Szpunar, J.A. and Smeltzer, W.W., 1996, The Growth and Structure of Thin Oxide Films on Cerium Ion-Implanted Nickel,
Metall. & Mater. Trans. A, **27**, 3649.

Czerwinski, F., Szpunar, J.A. and Smeltzer, W.W., 1996, Steady-Stage Growth of NiO Scales on Ceria-Coated Polycrystalline Nickel,
J. Electroch. Soc., **143**, 3000.

Czerwinski, F. and Szpunar, J.A., 1996, Optimizing Properties of CeO_2 Sol-Gel Coatings for Protection of Metallic Substrates Against High-Temperature Oxidation,
Thin Solid Films, **289**, 213.

Czerwinski, F. and Szpunar, J.A., 1996, Atomic Force Microscopy Study of Grain Evolution During Growth of Thin Oxide Films,
Mater. Sci. Forum, **204-206**, 729.

Czerwinski, F. and Szpunar, J.A., 1996, Influence of Annealing on Grain Growth in Nanocrystalline CeO_2 Ceramics,
Mater. Sci. Forum, **204-206**, 503.

Czerwinski, F. and Szpunar, J.A., 1996, Texture Development in Oxides Modified with Reactive Element Additions,
Mater. Sci. Forum, **204-206**, 497.

Czerwinski, F. and Szpunar, J.A., 1996, Texture Formation in Oxide Films Grown at High Temperatures on Ni Single Crystals,
in Textures of Materials - ICOTOM 11, edited by Z. Liang et al., International Academic Publ., Beijing, China, 1126.

Czerwinski, F. and Szpunar, J.A., 1996, A Role of Texture in Controlling High Temperature Oxidation Resistance of Metals and Alloys,
in Textures of Materials - ICOTOM 11, edited by Z. Liang et al., International Academic Publ., Beijing, China, 723.

Czerwinski, F., Sproule, G.I., Graham, M.J. and Smeltzer, W.W., 1995, An $^{18}O_2$-SIMS Study of Oxide Growth on Nickel Modified with Ce Implants and CeO_2 Coatings,
Corros. Sci., **37**, 541.

Czerwinski, F., Szpunar, J.A., Macaulay-Newcombe, R.G. and Smeltzer, W.W., 1995, Surface Analysis of Nickel Oxide Films Modified by Reactive Element,
Oxid. Met., **43**, 25.

Czerwinski, F. and Szpunar, J.A., 1995, Controlling Grain Boundary Diffusion in Oxide Films by Reactive Element Additions,
Canad. Metall. Quart., **34**, 243.

Czerwinski, F., Szpunar, J.A. and Smeltzer, W.W., 1995, Analytical Electron- and Atomic Force Microscopy Study of Multilayered Oxide Films Formed on Ce-doped Ni, in Structure and Properties of Multilayered Thin Films edited by T.D. Nguyen et al., Materials Research Society, Pittsburgh, PA, **382**, 135.

Czerwinski, F. and Szpunar, J.A., 1994, Atomic Force Microscopy Study of Nickel Oxide Films Modified by Reactive Element,
in Polycrystalline Thin Films - Structure, Texture, Properties and Applications, edited by M. Parker et al., Materials Research Society, Pittsburgh, PA, **343**, 529..

Czerwinski, F. and Szpunar, J.A., 1994, The Microstructural Characterization of Nanocrystalline CeO_2 Ceramics Produced by the Sol-Gel Method,
in Polycrystalline Thin Films - Structure, Texture, Properties and Applications edited by M. Parker et al., Materials Research Society, Pittsburgh, PA, **343**, 535.

Czerwinski, F. and Szpunar, J.A., 1994, Texture Development in Thin Nickel Oxide Films,
in Polycrystalline Thin Films - Structure, Texture, Properties and Applications edited by M. Parker et al., Materials Research Society, Pittsburgh, PA, **343**, 134.

Czerwinski, F. and Smeltzer, W.W., 1993,1994, The Early-Stage Oxidation Kinetics of CeO_2 Sol-Coated Nickel,
J. Electroch. Soc., **40**, 2606 (1993); **141**, L34 (1994).

Czerwinski, F. and Smeltzer, W.W., 1993, The Growth and Structure of Thin Oxide Films on Ceria Sol-Coated Nickel,
Oxid. Met., **40**, 503.

Czerwinski, F. and Smeltzer, W.W., 1993, The Analytical Electron Microscopy of Thin Oxide Films Formed on Cerium Implanted Nickel,
in Microscopy of Oxidation - 2, edited by S.B. Newcomb and M.J. Bennett, The Institute of Materials, London, 119.

Czerwinski, F. and Smeltzer, W.W., 1993, The Effect of Ceria Coatings on Early-Stage Oxidation of Nickel Single Crystals,
in Microscopy of Oxidation - 2, edited by S.B. Newcomb and M.J. Bennett, The Institute of Materials, London, 128.

Czerwinski, F. and Smeltzer, W.W., 1992, Influence of CeO_2 Sol Coatings on Early-Stage Oxidation Kinetics of Nickel,
in Oxide Films on Metals and Alloys, edited by B.R. MacDougall et al., The Electrochemical Society, Pennington, NJ, 81.
Partly in: The Extended Abstracts Volume of The Electrochemical Society, **92-2**, 1992, p. 211.

Papers Submitted and Accepted

Czerwinski, F. and Szpunar, J.A., The Effect of Reactive Element on Texture and Grain Boundary Character Distribution in Nickel Oxide,
Corros. Sci., accepted March 1997.

Czerwinski, F. and Szpunar, J.A., AFM Observations of Oxide Morphologies Formed at High Temperatures,
in Polycrystalline Thin Films III- Structure, Texture, Properties and Applications, edited

by B. Adams et al., Materials Research Society, Pittsburgh, PA, accepted April 1997.

Czerwinski, F. and Szpunar, J.A., The Influence of Crystallographic Orientation of Nickel Surface on Oxidation Inhibition by Ceria Coatings,
Acta Mater., submitted.

Czerwinski, F. and Szpunar, J.A., The Effect of Substrate Surface Nature on Texture Development in Nickel Oxide,
J. Mater. Sci., submitted.

Appendix A

Results of chemical analysiss of Nickel foil, 99.5% (metals basis) manufactured by Johnson Matthey Company, Ward Hill MA. Values in weight percent.
Stock number: 14193.

C	0.015%
Mn	0.11%
Si	0.03%
S	0.002%
Cr	< 0.01%
Ni	99.70%
Cu	0.01%
Fe	0.04%
Ti	0.005%
Co	0.03%
Mg	0.014%

Appendix B

This appendix contains the permissions of copyright owners to reproduce in this thesis the previously published results.

McGill

Department of Mining and Metallurgical Engineering

3450 University Street
Montreal, Canada
H3A 2A7

Département de Génie minier et métallurgique

3450, rue University
Montréal, Canada
H3A 2A7

Tel (514) 398-4352
Fax (514) 398-4492
dept@minmet.lan.mcgill.ca

APR 21

April 9, 1997.

Executive Director
Materials Research Society
9800 McKnight Road
Pittsburgh, Pa 15237-6006

re: copyright

Dear Sir:

I would like to ask you for permission to use the material published in the following papers, as a part of my Ph.D. Thesis entitled "The Growth and Structure of Thin Oxide Films on Nickel Superficially Modified with Ceria and Cerium".
Thesis will be submitted to the Department of Mining and Metallurgical Engineering, McGill University, Montreal, Canada.

1. ATOMIC FORCE MICROSCOPY STUDY OF NICKEL OXIDE FILMS MODIFIED BY REACTIVE ELEMENT,
F. Czerwinski and J.A. Szpunar, ok
in Polycrystalline Thin Films - Structure, Texture, Properties and Applications, edited by M. Parker, K. Barmak, R. Sinclair, D.A. Smith, and J. Floro (Materials Research Society, Pittsburgh, PA, 343, 1994), p. 529-534.

2. THE MICROSTRUCTURAL CHARACTERIZATION OF NANOCRYSTALLINE CeO_2 CERAMICS PRODUCED BY THE SOL-GEL METHOD,
F. Czerwinski and J.A. Szpunar, ok
in *Polycrystalline Thin Films - Structure, Texture, Properties and Applications* edited by M. Parker, K. Barmak, R. Sinclair, D.A. Smith, and J. Floro (Materials Research Society, Pittsburgh, PA, 343, 1994), p. 535-540.

3. TEXTURE DEVELOPMENT IN THIN NICKEL OXIDE FILMS,

F. Czerwinski and J.A. Szpunar,
in Polycrystalline Thin Films - Structure, Texture, Properties and Applications edited by M. Parker, K. Barmak, R. Sinclair, D.A. Smith, and J. Floro (Materials Research Society, Pittsburgh, PA, **343**, 1994), p. 131-136. OK
Partly in: *The Extended Abstracts Volume of The Electrochemical Society*, **94-2**, 1994, p. 849.

4. ANALYTICAL ELECTRON- AND ATOMIC FORCE MICROSCOPY STUDY OF MULTILAYERED OXIDE FILMS FORMED ON Ce-DOPED Ni,
F. Czerwinski, J.A. Szpunar, and W.W. Smeltzer, ok
in Structure and Properties of Multilayered Thin Films edited by T.D. Nguyen, B.M. Lairson, B.M. Clemens, S.C. Shin, and K. Sato (Materials Research Society, Pittsburgh, PA, **382**, 1995), p.135-140.

5. THE INFLUENCE OF CERIUM ION IMPLANTATION ON EARLY-STAGE OXIDATION KINETICS OF NICKEL,
F. Czerwinski and J.A. Szpunar, [illegible]
in *Materials Modification and Synthesis by Ion Beam Processing* edited by D.E. Alexander, B. Park, N.W. Cheung and W. Skorupa (Materials Research Society, Pittsburgh, PA) accepted December 1996.

Sincerely yours,
Czerwinski
F. Czerwinski

MRS
MATERIALS RESEARCH SOCIETY
9800 McKnight Road, Pittsburgh, PA 15237-6006
Telephone: (412)367-3003 • Facsimile: (412)367-4373 • http://www.mrs.org/

April 23, 1997

TO: F. Czerwinski
McGill
Dept of Mining & Metallurgical Eng.
3450 University Street
Montreal H3A 2A7, Canada

FROM: Shirley Krasa
phone: 412-367-3004 x 405
fax: 412-367-4373
e-mail: krasa@mrs.org

RE: Request for permission

You had sent the following letter asking if the articles you cited in your Ph.D. Thesis.

We grant permission provided you contact the author(s) and cite the source.

Shirley Krasa

Shirley Krasa

McGill

Department of Mining and Metallurgical Engineering
3450 University Street
Montreal, Canada
H3A 2A7

Département de Génie minier et métallurgique
3450, rue University
Montreal, Canada
H3A 2A7

Tel (514) 398-4352
Fax (514) 398-4492
dept@minmet.lan.mcgill.ca

March 6, 1997.

Executive Director
Elsevier Science Ltd.
The Boulevard, Langford Lane
Kidlington, Oxford OX5 1GB

re: copyright waiver

Dear Sir:

I would like to ask you for permission to use the material published in the following paper, as a part of my Ph.D. Thesis entitled "The Growth and Structure of Thin Oxide Films on Nickel Superficially Modified with Ceria and Cerium".
Thesis will be submitted to the Department of Mining and Metallurgical Engineering, McGill University, Montreal, Canada.

1. CORRELATION BETWEEN THE GROWTH MECHANISM AND SURFACE ROUGHNESS IN THIN NiO FILMS MODIFIED BY CeO_2,
F. Czerwinski and J.A. Szpunar,
Corrosion Science, 39 (1997) p. 147-158.

Sincerely yours,

F. Czerwinski

14 MAR 1997

thesis.

PLEASE TURN OVER

We hereby grant you permission to reprint the material specified in your letter (see recto) for the purpose you have indicated therein, at no charge, provided that:

1. The material to be used has appeared in our publication without credit or acknowledgement to another source.

2. Suitable acknowledgement to the source is given as follows:

For Books: "Reprinted from (Author/Title), Copyright (Year), Pages No., with kind permission from Elsevier Science Ltd, The Boulevard, Langford Lane, Kidlington 0X5 1GB, UK"

For Journals: "Reprinted from Journal title, Volume number, Author(s), Title of article, Pages No.,Copyright (Year), with kind permission from Elsevier Science Ltd, The Boulevard, Langford Lane, Kidlington 0X5 1GB, UK"

3. Reproduction of this material is confined to the purpose for which permission is hereby given.

For future permissions, please contact:
Frances Rothwell (Mrs)
Subsidiary Rights Manager
Elsevier Science Ltd
The Boulevard, Langford Lane
Kidlington 0X5 1GB, U.K.

Frances Rothwell

Should your thesis be published commercially, please repply for permission

McGill

Department of Mining and Metallurgical Engineering

Département de Génie minier et métallurgique

3450 University Street
Montreal, Canada
H3A 2A7

3450, rue University
Montréal, Canada
H3A 2A7

Tel (514) 398-4352
Fax (514) 398-4492
dept@minmet.lan.mcgill.ca

March 6, 1997.

Executive Director
Plenum Publishing Corporation
233 Spring St.
New York, NY 10013

PERMISSION GRANTED provided that material has appeared in our work without credit to another source; you obtain the consent of the author(s); you credit the original publication; and reproduction is confined to the purpose for which permission is hereby given.

4/2/97

Georgia Prince Date

Office of Rights/Permissions, Plenum Publishing Corp, 233 Spring Street. New York, NY 10013

re: copyright waiver

Dear Sir:

I would like to ask you for permission to use the material published in the following paper, as a part of my Ph.D. Thesis entitled "The Growth and Structure of Thin Oxide Films on Nickel Superficially Modified with Ceria and Cerium".
Thesis will be submitted to the Department of Mining and Metallurgical Engineering, McGill University, Montreal, Canada.

1. THE GROWTH AND STRUCTURE OF THIN OXIDE FILMS ON CERIA SOL-COATED NICKEL,
F. Czerwinski and W.W. Smeltzer,
Oxidation of Metals, 40 (1993) p. 503-527.

2. SURFACE ANALYSIS OF NICKEL OXIDE FILMS MODIFIED BY REACTIVE ELEMENT,
F. Czerwinski, J.A. Szpunar, R. Macaulay-Newcombe, and W.W. Smeltzer,
Oxidation of Metals, 43 (1995), p. 25-57.

Sincerely yours,

F. Czerwinski

[illegible]
MATERIALS TRANSACTIONS

MAR 20 1997

McGill

Department of Mining and Metallurgical Engineering

3450 University Street
Montreal, Canada
H3A 2A7

Département de Génie minier et métallurgique

3450, rue University
Montreal, Canada
H3A 2A7

Tel (514) 398-4352
Fax (514) 398-4492
dept@minmet.lan.mcgill.ca

March 6, 1997.

Executive Director
The Minerals, Metals & Materials Society of AIME
420 Commonwealth Drive
Warrendale, PA 15086

re: copyright waiver

Dear Sir:

I would like to ask you for permission to use the material published in the following paper, as a part of my Ph.D. Thesis entitled "The Growth and Structure of Thin Oxide Films on Nickel Superficially Modified with Ceria and Cerium".
Thesis will be submitted to the Department of Mining and Metallurgical Engineering, McGill University, Montreal, Canada.

THE GROWTH AND STRUCTURE OF THIN OXIDE FILMS ON CERIUM ION-IMPLANTED NICKEL,
F. Czerwinski, J.A. Szpunar, and W.W. Smeltzer,
Metallurgical and Materials Transactions A, **27** (1996), 3649-3661.

Sincerely yours,

F. Czerwinski

3/20/97 Permission is hereby granted for use of the above-mentioned material. Please be sure to give proper credit to the journal.

Dora Moscatello
Production Editor

John Bodt

PC 65

McGill

Department of Mining and Metallurgical Engineering

3450 University Street
Montreal, Canada
H3A 2A7

Département de Génie minier et métallurgique

3450, rue University
Montréal, Canada
H3A 2A7

Tel (514) 398-4352
Fax (514) 398-4492
dept@minmet.lan.mcgill.ca

March 6, 1997.

Executive Director
Kluwer Academic Publishers
1001 Philip Drive, Assinippi Pk.
Norwell, MA 02061

re: copyright waiver

Dear Sir:

I would like to ask you for permission to use the material published in the following paper, as a part of my Ph.D. Thesis entitled "The Growth and Structure of Thin Oxide Films on Nickel Superficially Modified with Ceria and Cerium".
Thesis will be submitted to the Department of Mining and Metallurgical Engineering, McGill University, Montreal, Canada.

THE NANOCRYSTALLINE CERIA SOL-GEL COATINGS FOR HIGH TEMPERATURE APPLICATIONS,
F. Czerwinski and J.A. Szpunar,
Journal of Sol-Gel Science and Technology, 9 (1997) p. 103-114.

Sincerely yours,

F. Czerwinski

PERMISSION GRANTED, PROVIDED THE COMPLETE ACKNOWLEDGEMENT IS GIVEN TO THE ORIGINAL SOURCE OF PUBLICATION

3/18/97 John Bodt

DATE **JOHN A. BODT, PUBLISHER**
KLUWER ACADEMIC PUBLISHERS

1 Carlton House Terrace
London SW1Y 5DB

Telephone: +44 (0)171 839 4071
Fax: +44 (0)171 839 2078

Patron: HM the Queen
Chief Executive: Dr B A Rickinson, CEng, MIM

email: peter@danckwerts compulink.co.uk

Book Publishing

18 April 1997

F. Czerwinski
Department of Mining and
Metallurgical Engineering
McGill University

Fax: 00 1 514 398 4492

Dear F Czerwinski,

Copyright Permission

Thank you for your letter of 9 April. Please accept this fax as permission to use the following papers from Microscopy of Oxidation 2 in your PhD thesis:

F. Czerwinski and W. W. Smeltzer, 'The analytical Electron Microscopy of Thin Oxide Films Formed on Cerium Implanted Nickel', pp 119 - 127.

F. Czerwinski and W. W. Smeltzer, 'The Effect of Ceria Coatings on Early-Stage Oxidation of Nickel Single Crystals', pp. 128–136.

Yours sincerely,

Peter Danckwerts,
Managing Editor, Books.

Registered with Charity number 269275

IMAGE EVALUATION
TEST TARGET (QA-3)

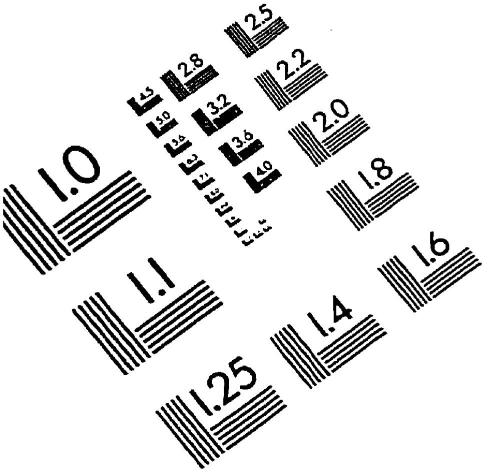

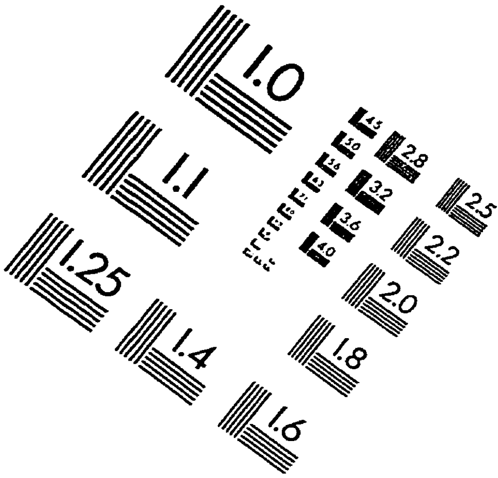

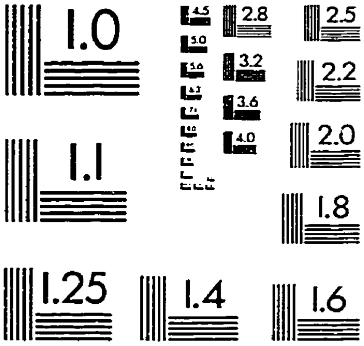

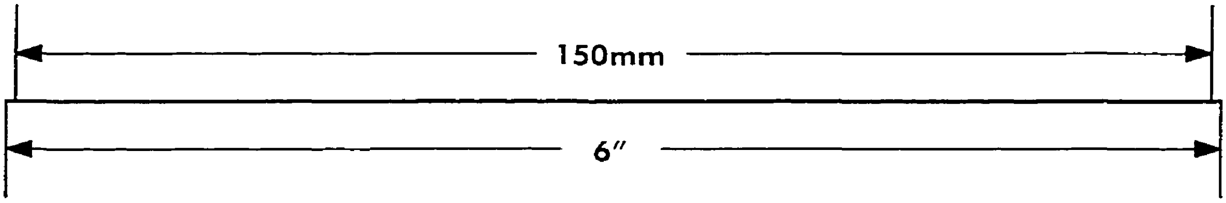

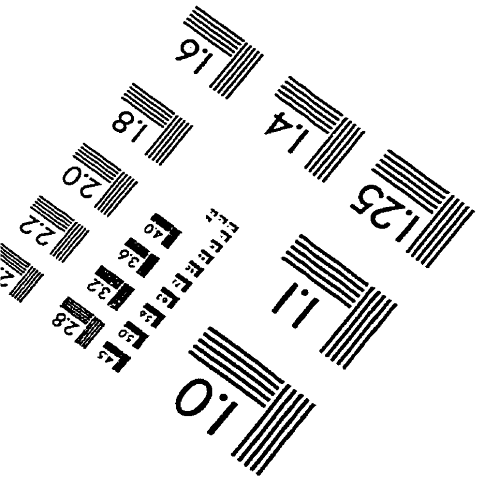

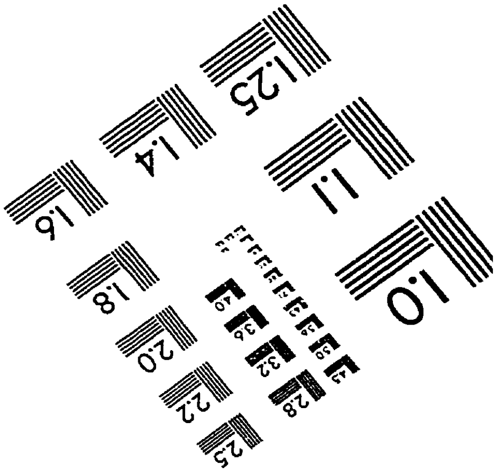

APPLIED IMAGE . Inc
1653 East Main Street
Rochester, NY 14609 USA
Phone: 716/482-0300
Fax: 716/288-5989